Complex band structure calculations of the electronic structure of nitride quantum wells

Bolland, Ian

Complex Band Structure Calculations of the Electronic Structure of Nitride Quantum Wells

Ian Bolland

A thesis submitted for the
degree of Doctor of Philosophy
at the University of Durham,
Department of Physics

2003

Abstract

This thesis is concerned with the electronic and structural properties of interfaces and quantum wells constructed from GaN, AlN, InN and their alloys. Calculations have been carried out on the electronic properties of the nitrides in the wurtzite crystal structure using the complex bandstructure method. Although this method has previously been applied to semiconductors with the zincblende crystal structure, the author believes that this is the first time the complex bandstructure method has been applied to systems with a wurtzite crystal structure. The complex bandstructures are derived from bulk bandstructures which have been calculated within the framework of the plane wave empirical pseudopotential method. The bound states of nitride quantum well heterostructures are calculated by the matching of complex bandstructure wavefunctions at the heterointerfaces. The effects of biaxial strain in the structures are taken into account by a suitable parameterisation of the pseudopotential form factors and the effects of alloying are described by the virtual crystal approximation. The method of matching the complex bandstructure wavefunctions at heterointerfaces has also been extended to wurtzite-zincblende homointerfaces and applied to a wurtzite-zincblende homostructure quantum well. The wurtzite-zincblende homointerface is further examined using first principles calculations based on density functional theory.

As a result of this work a complex bandstructure method for calculating the electronic properties of wurtzite-wurtzite and wurtzite-zincblende structures has been established as a calculational tool. Further, the efficacy of the method has been demonstrated by calculation of the bound state energies and carrier probability densities of GaN-InGaN-GaN and AlGaN-GaN-AlGaN quantum wells and the inter-subband absorption spectrum of an AlGaN-GaN-AlGaN conduction band well. The *ab-initio* calculations predict a small degree of interface reconstruction and very small band offsets for wurtzite-zincblende homointerfaces.

Declaration

The work presented in this thesis has been carried out by the candidate (except where otherwise acknowledged) and has not been previously submitted for any degree.

Acknowledgements

Firstly for supervision, advice and patience, I am indebted to my supervisor Dick Abram as well as Stuart Brand and my industrial supervisor Mike Burt for many very helpful discussions. In addition, the rest of the condensed matter theory group, past and present, have provided countless stimulating coffee-time discussions, although rarely about physics. I would therefore like to thank Derek Middlemiss, Stewart Clark, Paul Tulip, Andy Reeves and Gavin Crow for everything that made work as part of the group so enjoyable. Many other people at Durham and beyond have provided welcome distractions throughout the PhD, I am especially grateful to Hazel Robson, Lorna Stimson, Anna Charemza, Reuben McDonald and Alley Stoddart for all the help and good times they have provided. I would finally like to show my appreciation to my brother and sister, and mum and dad for all their unwavering support throughout.

Contents

List of Symbols

A List of symbols used throughout the text and their corresponding meaning. Quantities in bold type-face are vectors.

Symbol	Meaning
$\cdot$	dot product operator
$\wedge$	vector product operator
$\times$	multiplication
$\perp$	direction perpendicular to planes, i.e. in direction of growth (z-direction).
$\parallel$	direction parallel to growth planes (x,y direction in this work)
$\uparrow$	up spin
$\downarrow$	down spin
$\mathbb{R}$	Set of all real number
$\mathbb{C}$	Set of all complex numbers
α_{if}	absorption coefficient between band i and f
α_i	parameters for symmetric functional form of pseudopotential
β_i	parameters for antisymmetric functional form of pseudopotential
α_z	z component of straight bond
β_z	z component of diagonal bond
$\boldsymbol{\alpha}$	straight bond
$\boldsymbol{\beta}$	diagonal bond
Γ	Γ-point (centre of the Brillouin zone)
Δ_{CF}	crystal field splitting
Δ_{SO}	spin orbit splitting
ΔE_{VBO}	Valence band offset
ΔE_{CBO}	Conduction band offset

ΔE_v	Diference in valence band energies
ΔE_c	Diference in conduction band energies
$\Delta \overline{\overline{V}}^{B-A}$	difference in macroscopic average potential of material A and B
ϵ	strain
ε_0	absolute permittivity of free space
ε_r	relative dielectric constant of the material
ε_w	dielectric constant of the well
ε_b	dielectric constant of the barrier
$\epsilon_{\|\|}$	in-plain strain
$\epsilon_{\perp}$	growth direction strain
ϵ_j	column form of strain tensor
ϵ_{kl}	strain tensor
$\varepsilon_{xc}(\rho(\mathbf{r}))$	exchange-correlation energy of a uniform electron density.
η	$= (k' - k^* + g' - g)$
κ	bulk modulus
λ	interaction strength of spin orbit coupling component
λ_s	symmetric part of λ
λ_a	anti-symmetric part of λ
Λ	line in $\mathbf{k}_{\|\|}$-space within the 2D BZ
μ	Chemical potential
μ	refractive index
μ	spin orbit coupling parameter
ν	Poisson's ratio
σ	stress
$\boldsymbol{\sigma}$	Pauli spin matrix
σ_i	column form of stress tensor
σ_{ij}	stress tensor
σ_x	x component of Pauli spin matrices
σ_y	y component of Pauli spin matrices
σ_z	z component of Pauli spin matrices
ω	photon frequency

Ω	primitive unit cell volume
$\Omega_{\|\|}$	in-plane unit cell area
ϕ	bulk pseudo wavefunction
Φ	many electron wavefunction
Ψ	true wavefunction
Ψ_c	core wavefunction
ψ	layer (pseudo) wavefunction
ρ_n	charge density of band n
ρ_c	core energy parameter
$\rho(\mathbf{r})$	electron density (charge density)
$\overline{\rho}(z)$	planar charge density
$\overline{\overline{\rho}}(z)$	macroscopically averaged charge density
Υ, Υ'	period of potential in superlattice
$\xi^{(l)}$	momentum matrix integral
a	'in-plane' lattice constant
$\mathbf{a}$	lattice vector
$\mathbf{a}^*$	reciprocal lattice vector
a_e	bulk equilibrium growth layer 'in-plane' lattice constant
$a_{\mathbf{g},s}$	pseudo wavefunction coefficient
$a^{(l)}_{ksg}$	complex bandstructure pseudo wavefunction coefficient
a_s	substrate 'in-plane' lattice constant
A	A-point in wurtzite Brillouin zone
A	stacking location
$A^{(l)}$	unknown coefficient of general solution in layer l
$\mathbf{A}$	vector potential
$\mathbf{b}$	lattice vector
$\mathbf{b}^*$	reciprocal lattice vector
b_c	core state coefficients
$b^{(l)}_{ksg}$	complex bandstructure pseudo wavefunction coefficient
B	stacking location
$B^{(l)}$	unknown coefficient of general solution in layer l

c	'growth direction' lattice constant
$c_{supercell}$	supercell 'growth direction' lattice constant
c	speed of light
$\mathbf{c}$	lattice vector
$\mathbf{c}^*$	reciprocal lattice vector
c	Young's modulus / elastic modulus / elastic stiffness constant
c_{ijkl}	elastic stiffness tensor
c_{ij}	matrix form of elastic stiffness tensor
$\mathbf{c}_{cubic}$	elastic stiffness matrix for cubic symmetry
$\mathbf{c}_{hexagonal}$	elastic stiffness matrix for hexagonal symmetry
c_e	bulk equilibrium growth layer 'growth direction' lattice constant
c_g	relaxed value c-lattice constant for the epilayer strained on the substrate
$c_k^{(l)}$	heterostructure layer coefficient
c_s	substrate 'growth direction' lattice constant
C	stacking location
$\mathbf{d}$	unit cell displacement
$d_k^{(l)}$	heterostructure layer coefficient
e	charge of an electron
$e_{i,j}$	piezoelectric coefficients
E	energy
E_1	Heavy hole band energy at Γ
E_2	Light hole band energy at Γ
E_3	Crystal hole band energy at Γ
E_{Cor}	correlation energy
E_{HF}	Hartree Fock energy
E_C	Conduction band energy
E_V	Valence band energy
E_G	Band gap
E_{exact}	Exact total energy including all many body effects
E_{cut}	kinetic energy cutoff for plane wave expansion
$E_{\mathbf{k}}$	energy at wavevector $\mathbf{k}$

$E^{if}_{\mathbf{k}_\parallel}$	Energy separation of bands i and f
$E[\rho(\mathbf{r})]$	Total energy functional
$E_H[\rho(\mathbf{r})]$	Hartree energy functional
$E_K[\rho(\mathbf{r})]$	Kinetic energy functional
$E_{xc}[\rho(\mathbf{r})]$	Exchange correlation functional
E_z^{PZ}	Piezoelectric field strength
$E_z^{(l)}$	Piezoelectric field strength in layer l
$F[\rho(\mathbf{r})]$	energy functional
F_i	force acting on ion i
f	final band in transition
f_i, f_f	Fermi occupation factors
$f^{(l)}(z)$	one dimensional envelope function in region (l)
$\mathbf{g}$	reciprocal lattice vector
$\mathbf{g}_z$	z component of reciprocal lattice vector
$\mathbf{g}'$	reciprocal lattice vector
$\mathbf{G}$	reciprocal lattice vector
$g(E)$	density of states
$g_{if}(E)$	joint density of states
$\mathbf{H}$	Hamiltonian matrix
H	H-point in Brillouin zone
$\hat{H}$	Hamiltonian operator
$\hat{H}_{MB}$	many body Hamiltonian operator
$\mathbf{H}^P$	pseudo Hamiltonian matrix
$\mathbf{H}^0$	matrix of terms independent of k
$\mathbf{H}^1$	matrix of terms linear in k
$H^P_{\mathbf{g},\mathbf{g}'}$	individual component of pseudo Hamiltonian matrix
$H^P_{\mathbf{g},\mathbf{g}',s,s'}$	individual component of SOC pseudo Hamiltonian matrix
H^{SOC}	spin orbit coupling Hamiltonian operator
$H^{SOC}_{s,s'}$	spin orbit coupling term of Hamiltonian
$\hbar$	Planck's constant
h_c	critical layer thickness

i	square root of -1
i	initial band in transition
i, j, k, l	indices for vectors, matrices and tensors
$\mathbf{I}$	identity matrix
k	growth (z) direction component of wavevector
$\mathbf{k}_{tot}$	total complex wavevector
$\mathbf{k}$	wavevector
$\mathbf{k}_i$	imaginary part of wavevector $\mathbf{k}$
$\mathbf{k}_r$	real part of wavevector $\mathbf{k}$
$\mathbf{k}_{\|\|}$	in-plane component of wavevector
$\mathbf{K}$	$\mathbf{K} = \mathbf{k} + \mathbf{g}$
K	K-point in Brillouin zone
l	layer number
l	orbital angular momentum quantum number
l	integer component of g-vector in $\mathbf{a}^*$ direction
L	left barrier
$\mathbf{L}$	lattice vector
L	L-point in Brillouin zone
m	integer component of g-vector in $\mathbf{b}^*$ direction
m^*	effective mass of electron
m_e	rest mass of electron
M	number of bulk states used in layer wavefunction basis
M	M-point in Brillouin zone
n	integer component of g-vector in $\mathbf{c}^*$ direction
n	band index
n	number of atoms
n	number of interfaces
N	number of plane waves used in Fourier series
$N_{g\|\|}$	the number of different projections of g onto the growth plane
$\hat{\mathbf{p}}$	quantum mechanical momentum operator
$\mathbf{q}$	reciprocal space vector

$\mathbf{P}^{pz}$	piezoelectric polarisation vector
$\mathbf{P}^{sp}$	spontaneous polarisation vector
$\overleftarrow{\mathbf{P}}^{(l)}$	projection matrix for wavefunction to left interface of layer l
$\overrightarrow{\mathbf{P}}^{(l)}$	projection matrix for wavefunction to right interface of layer l
$\overleftarrow{\mathbf{Q}}^{(l)}$	projection matrix for derivative to left interface of layer l
$\overrightarrow{\mathbf{Q}}^{(l)}$	projection matrix for derivative to right interface of layer l
q	magnitude of reciprocal space vector
q	core cutoff
R	right barrier
$\pm\mathbf{R}_1$,$\pm\mathbf{R}_2$	atomic positions in wurtzite unit cell
$\pm\mathbf{R}$,	atomic positions in zinc blend unit cell
$\mathbf{r}$,$\mathbf{r}'$	general position
S_μ,S_α	spin orbit coupling pseudopotential parameters
$S(\mathbf{g}-\mathbf{g}')$	structure factor
s,s'	spin indices
s	elastic compliance constant
s_{ijkl}	elastic compliance tensor
s_{ij}	matrix form of elastic compliance tensor
t_b	barrier thickness
t_w	well thickness
$\hat{T}$	kinetic energy operator
$\hat{T}_e$	electron kinetic energy operator
$\hat{T}_N$	nucleus kinetic energy operator
$\mathbf{T}^{(l)}$	transfer matrix for layer l
$\mathbf{T}$	total transfer matrix
U	arbitrary energy shift
U	U-point in Brillouin zone
u	wurtzite internal parameter
U_j	local ideality at atom j
U^P	Atomic Pseudopotential
U_i^P	Atomic pseudopotential of atom i

$U_{\mathbf{g},j}$	Atomic pseudopotential form factor of atom j
$V^{(l)}$	Potential in region (l)
$V_0^{(l)}$	Potential in region (l) at zero field
$\overline{\overline{V}}$	Macroscopic average of potential
$\overline{V}(z)$	Planar microscopic average of the potential
$V, V(\mathbf{r})$	Potential
V^P	Crystal Pseudopotential
$V_\mathbf{g}$	Pseudopotential form factor
$V_H(\mathbf{r})$	Hartree potential
$V_{ion}(\mathbf{r})$	ionic potential (ab-initio pseudopotential)
$V_{KS}(\mathbf{r})$	Kohn Sham potential
V^R	Orthogonalisation potential
$V_{xc}(\mathbf{r})$	exchange - correlation potential
$\hat{V}_{NN}$	nucleus - nucleus potential energy operator
$\hat{V}_{eN}$	electron - nucleus potential energy operator
$\hat{V}_{ee}$	electron - electron potential energy operator
W	W-point in Brillouin zone
x	Alloy composition
x	x-axis
X	X-point in Brillouin zone
y	y-axis
z	z-axis

List of Acronyms

Where possible acronyms have been defined, in the main text, at the instance of their first use. However a list of the acronyms used and their meaning is presented below for clarity.

Acronym	Meaning
AES	Auger electron spectroscopy
BCC	Body centred cubic
BEF	Built-in electric field
BZ	Brillouin zone
CASTEP	A commercial DFT package
CB	Conduction band
CBM	Conduction band minimum
CBO	Conduction band offset
CBS	Complex band structure
CH	Crystal hole
CL	Cathodoluminescence
CMOS	Complimentary metal-oxide semiconductor
DFT	Density functional theory
DOS	Density of states
DVD	Digital versatile disc
EELS	Electron energy loss spectroscopy
EM	Electromagnetic
EMT	Effective mass theory
EPM	Empirical pseudopotential method
FCC	Face centred cubic
FFT	Fast fourier transform

GGA	Generalised gradient approximations
HBT	Heterojunction bipolar transistor
HCP	Hexagonal close packed
HF	Hartree Fock (theory)
HH	Heavy hole
HRXRD	High resolution x-ray diffraction
HVPE	Halide vapour phase epitaxy
IR	infrared
ISBT	Inter-subband transition
JDOS	Joint density of states
KS	Kohn Sham (equations)
LCAO	Linear combination of atomic orbitals
LDA	Local density approximation
LED	Light emitting diode
LEEBI	Low energy electron beam irradiation
LH	Light hole
MBE	Molecular beam epitaxy
MIS	Metal insulator semiconductor
ML	Mono-layer
MOSFET	Metal-oxide semiconductor field effect transistor
MOVPE	Metal-organic vapour phase epitaxy
MQW	Multiple quantum well
PD	Probability density
PL	Photoluminescence
PR	Photoreflectance
PZ	Piezoelectric
PWP	Plane wave pseudopotential (calculation)
QC	Quantum cascade
QCSE	Quantum confined stark effect
QW	Quantum well
QD	Quantum dot

RF	Radio frequency
RHEED	Reflection high energy electron diffraction
SAW	Surface acoustic wave
SOC	Spin orbit coupling
SP	Spontaneous polarisation
SQW	Single quantum well
SSO	Spin split off band
TBM	Tight binding method
USP	Ultrasoft pseudopotentials
VB	Valence band
VBM	Valence band maximum
VBO	Valence band offset
VCA	Virtual crystal approximation
WZ	Wurtzite
XPS	X-ray photoelectron spectroscopy
YAG	Yttrium aluminium garnet
ZB	Zincblende

List of Figures

List of Tables

Chapter 1

Introduction

1.1 Semiconductors

Semiconductors can be defined as materials possessing a fundamental energy gap of less than a few electron volts [1] and this is the origin of many of their characteristic properties which have not only formed the basis of much fascinating physics but are also exploited by the electronics industry. The semiconductor electronics revolution started with the invention of the bipolar junction transistor in 1947, followed by the integrated circuit, the MOSFET and the CMOS later in the twentieth century. Since then demand for increasingly sophisticated electronic components has steadily increased and today semiconductor electronic components feature in most of the technology we use every day. The most well known semiconductor is silicon (Si), a group IV element with a diamond crystal structure, because it has become the semiconductor of choice for the integrated circuit industry.

However, there are many other semiconductors that have found industrial application, although none to the same extent. Silicon is an indirect bandgap semiconductor and is therefore poorly suited in devices for light emission. To serve this purpose researchers have looked to other semiconducting materials, with direct band gaps, which are more effective in the efficient production of light. As well as Si, some group IV, V and VI elements are considered semiconductors, including germanium (Ge), phosphorus (P), tellurium (Te), selenium (Se) and sulphur (S). Binary compounds of two elements from groups III and V or groups II and VI of the periodic table, are also observed to be semiconducting. The compound semiconductors tend to exhibit larger fundamental energy gaps due to their increased ionicity,

which is a result of charge transfer from the group III (or II) atoms to the group V (or VI) atoms. GaAs is probably the most well known binary semiconductor and has found many commercial applications, primarily due to its high electron mobility compared to silicon and its direct band gap. Other materials have been shown to exhibit semiconductor behaviour, including layered semiconductors such as lead iodide (PbI_2), organic semiconductors, and compounds with the formulas I-III-VI_2 or II-IV-V_2. The properties of a semiconductor can be varied by doping or two or more semiconductors can be mixed to form an alloy. In addition the construction of interfaces and heterostructures, including quantum wells, superlattices and quantum dots enables the electronic and optical properties to be tailored in a way that provides great scope in the construction of electronic and optical devices. The need to understand the physics of these materials and structures based on them continues and is as important and challenging as ever.

One of the many semiconducting material systems experiencing a great deal of current interest is the group of binary compounds, comprising of group III elements and nitrogen, known collectively as the group III - nitrides.

1.2 Nitrides

The work of this thesis is focused on the III-V system of semiconductor materials known as the group III - nitrides. In particular we are concerned with gallium nitride (GaN), indium nitride (InN), aluminium nitride (AlN) and their alloys, which are currently generating a considerable level of research interest.

The lattice constants of the nitrides are considerably smaller than those of other III-V compounds, which is a direct result of the small covalent radius of nitrogen (e.g. 0.7 Å for GaN, c.f. 1.18 Å for GaAs). Large bond energies gives rise to high melting points which makes the crystal growth of nitrides more difficult. One of the most striking features is the ability of the nitrides to form stable crystals in either the zincblende (cubic) or wurtzite (hexagonal) crystal structure. The wurtzite structure is more thermodynamically stable and is the structure in which most of the devices are fabricated. The stability of the wurtzite phase for the nitrides is due to the small covalent radius of the nitrogen atom. A combination of the symmetry of the wurtzite crystal structure, and the partially ionic bonding, leads to very

strong ($\sim$ 1 MV/cm) piezoelectric fields when under strain, and a spontaneous polarisation of a similar order of magnitude, even without strain [2,3]. The total field, often referred to as a built-in electric field presents significant additional complications in experimental measurements of quantities such as band offsets.

However, the property that has attracted most attention is the size of the direct band gaps of the nitrides, which spans the range from 2.0 eV (InN) to 6.2 eV (AlN) and includes the whole of the visible spectrum and some of the ultraviolet region. Figure 1.1 gives an overview of the lattice constants and band gaps of some III-IV materials. The wide range of band gaps and efficient luminescence makes the nitrides attractive materials for light emitting devices, specifically for bright colour displays, for which the primary colours of red, green and blue are required. Large outdoor full colour displays have been demonstrated [4], and look to be commercially successful. Bright white LEDs based on blue GaN LEDs that excite an yttrium aluminium garnet (YAG) phosphor have also been produced [5] and are likely to be commercially attractive because of their high efficiency. Another important application for the nitride semiconductors will be as short wavelength laser diodes for optical storage devices. The next generation optical disc standard, the 'blu-ray' disc is expected be read by a GaN based laser and will have a storage capacity of 27Gb in comparison to the 4.7Gb of a digital versatile disc (DVD). Other optical device applications include visible-blind ultraviolet photodetectors, which are required to be selectively sensitive in the ultraviolet region of the spectrum. In addition the wide bandgap of GaN makes it a candidate material in the field of high frequency, high power electronic devices, important to the communications industry for satellite and terrestrial radio frequency electronics [5,6]. The high melting point and wide range of operating temperatures also makes GaN very suitable for high temperature electronics in the automotive and aerospace industries [6]. In fact the development of heat tolerant heterojunction bipolar transistors (HBTs) based on nitrides may allow the construction of an all electric aircraft. The strong piezoelectric properties of the hexagonal nitrides also makes them suitable for surface acoustic wave devices (SAW) in components such as filters, duplexers and resonators [5].

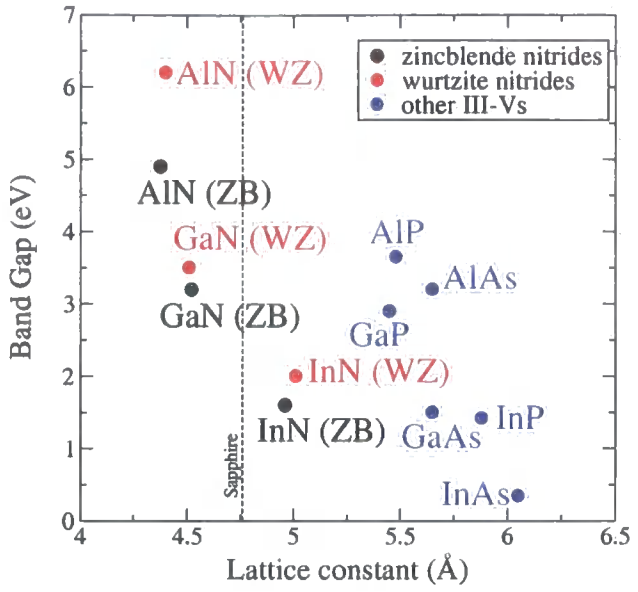

Figure 1.1: The band gaps and lattice constants of the nitrides and other common III-V compound semiconductors. The lattice constants are represented in zincblende equivalents for the wurtzite values to make a relevant comparison. The dashed line indicates the lattice constant of sapphire, which is commonly used as a growth surface [5,7,8]

1.3 History of nitrides research

Work on the synthesis of GaN began as early as 1938 when Juza and Hahn [9,10] passed ammonia over hot gallium, resulting in the growth of small crystals. The first GaN films were grown in 1969 when a number of workers attempted hetero-epitaxial growth on sapphire surfaces by applying the growth techniques developed for GaAs a decade earlier (see for example [11]). The growth was performed at a relatively high temperature of 1000 ^{o}C, which has the advantage of increasing the Ga mobility on the growing surface. The successful growth of GaN enabled the measurement of lattice constants [12] and other material properties such as the bandstructure, including the fundamental energy gap [13]. The first blue GaN LED (a metal insulator semiconductor (MIS) type diode) was fabricated in 1972 by Pankove *et al* [14]. Further device developments were not achieved until the next decade as the GaN available was not of sufficiently high quality. Higher quality GaN was realised by Yoshinda *et al* in 1983 and later by Amano *et al* [15,16] when the use of an AlN buffer layer initially grown at a lower temperature (500 ^{o}C) on sapphire, allowed the fabrication

of higher quality crystals. The higher quality layers exhibited the strong photoluminescence and high mobility that was expected of crystalline GaN. The production of p-type GaN, necessary for the p-n junction in LEDs and laser diodes, still eluded researchers until the modern growth techniques of metal-organic chemical vapour deposition (MOCVD), and later molecular beam epitaxy (MBE), were utilised. The first successful p-doping of GaN was by Amano *et al* [17] in 1989 through the Mg doping of MOCVD grown samples and the subsequent irradiation by low energy electron beam irradiation (LEEBI). $In_xGa_{1-x}N$ was first grown in 1990 when Matsuoka *et al* [18] achieved films of $In_xGa_{1-x}N$ on sapphire for the whole range of indium compositions $x = 0 \rightarrow 1$. At the start of the 1990s $Al_xGa_{1-x}N$ was grown as part of a layered heterostructure by Khan *et al* [19] and Itoh *et al* [20]. $In_xGa_{1-x}N$ layered structures are observed to possess a large ($\sim 10^{10}cm^{-2}$ [21]) dislocation density in the GaN epilayers. Most recently the 2.5% lattice mismatch between GaN and AlN, or GaN and InN has been used during MBE growth to grow 3D quantum dots that form naturally as a result of "islanding" [22].

The use of alloys allowed a range of different material layers to be used as the building blocks that workers in the 1990s have used to construct the commercially important devices described in section 1.2. Room temperature stimulated emission and lasing have been demonstrated and the thresholds of stimulated emission and lasing now improve every year (see [7] and references therein). This thesis is concerned with the heterostructure quantum well optical devices constructed from layers of GaN, $In_xGa_{1-x}N$ and $Al_xGa_{1-x}N$.

The quality of the nitride layers in the heterostructures that can currently be produced has come a long way from the first efforts at crystal growth. However, the materials are still of relatively poor quality. The large dislocation densities are a direct result of the lattice mismatch between the III-nitrides and the substrate (usually sapphire). Despite these dislocation densities, optical device performance is still very impressive. In other III-IV devices dislocation densities above $\sim 10^3cm^{-2}$ would significantly reduce the performance of the device and in most cases stop it entirely at $\sim 10^6cm^{-2}$ [7]. It has been suggested by Ponce [23] that the dislocations are clustered, leaving large regions dislocation free, and that the trapping/recombination centres may only be able to cope with a limited number of recombinations per unit time [7].

The poor quality of the nitride crystals has tended to inhibit the experimental determi-

nation of the material properties. In particular the band offsets and the built in electric field strengths are not accurately known for layered nitride heterostructures. This situation makes theoretical studies even more important in the role of determining the various quantities of interest.

1.4 Description of the work

The thesis is concerned with theoretical calculations of the electronic structure of quantum wells constructed from the nitrides. In order to achieve this the bulk electronic structure of the nitrides is also investigated. The division into chapters is primarily by theoretical technique and in each chapter a theory is introduced followed by a presentation of the results and a discussion.

Chapter 2 - Bandstructure Calculations

The existence of hexagonal (wurtzite) and cubic (zincblende) phases for nitride crystals is described in terms of stacking sequences. The hexagonal crystal structure of the nitrides is defined and discussed in some detail while a discussion of the cubic phase is deferred until chapter 5 in which calculations involving cubic GaN are first presented. The importance of the bandstructure is discussed and the empirical pseudopotential method (EPM) is introduced as an effective approach to bandstructure calculations which represents the wavefunctions as a Fourier series. The EPM is used because the accuracy with which it calculates both valence and conduction band states and the possibility of its application to alloys using the virtual crystal approximation. The empirical pseudopotential bandstructures for GaN, InN and AlN are presented as well as examples of the density of states and charge densities obtained for GaN. The effects of alloying, spin-orbit coupling and strain are considered, as is the choice of criterion for a convergent solution within the empirical pseudopotential scheme. The variations of the band gap and the effective masses for AlGaN and InGaN are presented as a function of alloy composition.

Chapter 3 - Complex Bandstructure

The advantages of using bandstructures with complex wavevector in the consideration of the electronic structure of finite spatial regions is explained. An eigenvalue method of generating bandstructures with a complex wavevector is outlined. Complex bandstructures of GaN, InN and AlN, within the empirical pseudopotential method are shown and the general topological features of these complex bandstructure are considered. The complex bandstructure of GaN with a non-zero wavevector in the growth plane, is investigated and the convergence of the complex bandstructure against number of plane waves, is considered. Finally the complex bandstructure of a strained alloy with the pseudopotential parameters derived from the virtual crystal approximation is also presented.

Chapter 4 - Heterostructures

The nature of nitride heterostructures is considered and a simple effective mass approach to modelling the bandstructure of a quantum well is outlined. The use of a transfer matrix method to establish the bound state energies and wavefunctions of a many layered heterostructure is discussed and a theoretical approach for calculating these bound states in a heterostructure using the complex bandstructure method is described. Bound state energies and probability densities are presented for GaN - InGaN conduction and valence band quantum wells for a range of electric field strengths and alloy compositions. The bound states are found to be very strongly affected by the built-in electric fields. Bound states of the AlGaN - GaN conduction band quantum well and the associated momentum matrix elements of conduction subband transitions are calculated and compared with experimental measurements. The complex bandstructure calculations of bound state energies are found to be in good general agreement with effective mass calculations.

Chapter 5 - Wurtzite - zincblende interface

The zincblende crystal structure is defined and the empirical pseudopotential bandstructure is presented along with the corresponding complex bandstructure. The convergence of the calculations is considered for both the bulk and the complex bandstructure. The concept of wurtzite crystals grown pseudomorphically on zincblende substrates is introduced and the possibility of a zincblende - wurtzite quantum well is considered. The nature of a

wurtzite - zincblende interface is considered and a quantum well of GaN in the wurtzite and zincblende phase is modelled using the empirical pseudopotential complex bandstructure method.

Chapter 6 - Ab-initio Calculations

A commonly used, plane wave, pseudopotential method using density function theory is outlined as a versatile and convenient *ab-initio* approach to electronic structure calculations of semiconductors. Calculations are carried out for the compounds GaN, InN and AlN. Lattice constants are obtained including the effect of strain. The lattice properties of zincblende GaN, InN and AlN are studied with the effect of biaxial strain included. Finally, the band discontinuities are calculated for the wurtzite-zincblende interface and interface structural properties are presented including the atomic relaxation at the interface.

Chapter 7 - Conclusions

A summary is presented of the calculations carried out and the results obtained. Conclusions are drawn and suggestions for future work are put forward.

Chapter 2

Bandstructure Calculations

2.1 Introduction

Bandstructure calculations remain at the heart of the theory of semiconductors and are an important starting point for the calculations performed in this work. This chapter is primarily concerned with an overview of bandstructure calculations using the empirical pseudopotential method for bulk GaN, AlN and InN in the wurtzite crystal structure. A discussion of the zincblende crystal structure is deferred until chapter 5 where the pseudopotential approach is applied to zincblende-wurtzite homostructures. The generation of pseudopotential form factors for the alloys is discussed and examples of bulk bandstructure are presented for GaN, AlN, InN and their alloys under the biaxial strain which occurs in epitaxial layers of a heterostructure with a lattice mismatch.

2.2 Crystal Structure

The nitrides, GaN, AlN, InN and their alloys, like many other semiconductors are covalently bonded by the overlap of s-p^3 hybrid bonding orbitals. These hybrid bonding orbitals have a tetrahedral geometry, with a bond angle of $\sim 109.5^o$. The bond lengths, determined by x-ray crystallography [24] are shorter than those of many other III-V semiconductors because of the smaller covalent radius of the nitrogen atom. The tetrahedral bond geometry can result in two different crystal structures, the exact structure depending on the stacking repeat sequence in which the layers of the crystal are built up. If the atoms of the

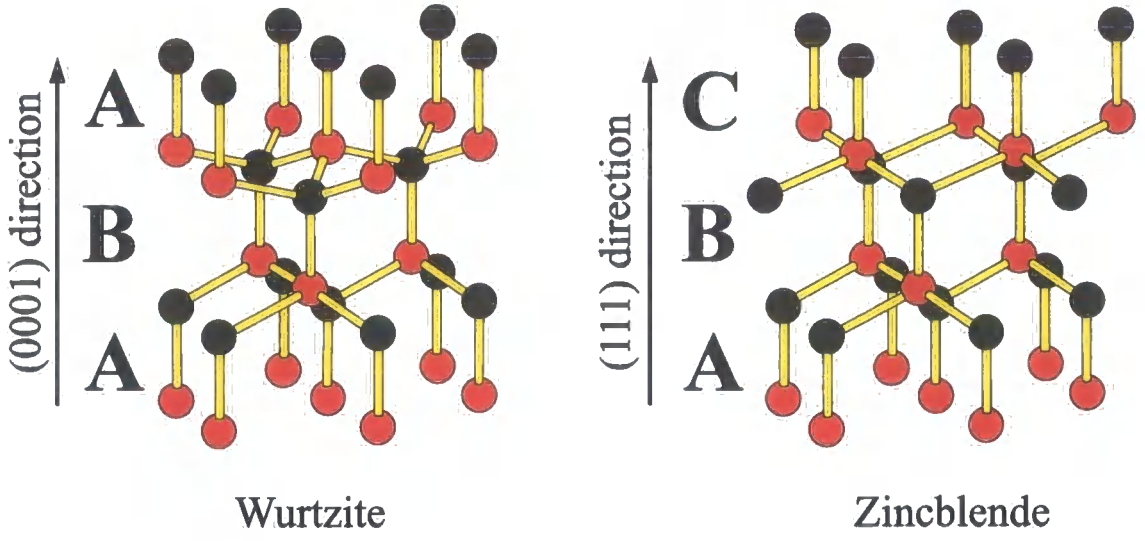

Figure 2.1: Wurtzite and zincblende crystal structures. The wurtzite structure is oriented along the (0001) direction and the zincblende along the (111) direction. The construction of the crystals through the stacking repeat sequence is indicated as $ABABAB$ for wurtzite and $ABCABC$ for zincblende.

layers are considered to be in the pattern of a close packed array of spheres, the atoms could align in one of three locations, labelled A,B and C. If the placing of the atoms repeats as $ABABAB$ then a wurtzite crystal structure results and if the repeat sequence is $ABCABC$ then the crystal has a zincblende structure. Figure 2.1 illustrates both crystal structures and the difference in repeat sequences. The wurtzite phase has hexagonal symmetry with space group $P6_3mc$ and the zincblende phase exhibits cubic symmetry with space group $F\bar{4}3m$. The nitrides considered here are thermodynamically stable in the wurtzite phase, although the zincblende phase can be achieved, under suitable growing conditions. The existence of two phases is unusual for a III-V semiconductor although it is commonly observed in the II-VI compounds, due to their more ionic bonding [25].

2.2.1 Wurtzite

The wurtzite structure can be considered as two interpenetrating hexagonal close packed (HCP) lattices. Each of the two lattices contains an atomic species of the two components labelled A and B. The two HCP lattices are displaced along the c-axis by uc where u is the 'internal parameter' and c is the lattice constant for the c axis. The crystal structure is described by a four atom basis and a Bravais lattice constructed using the primitive lattice

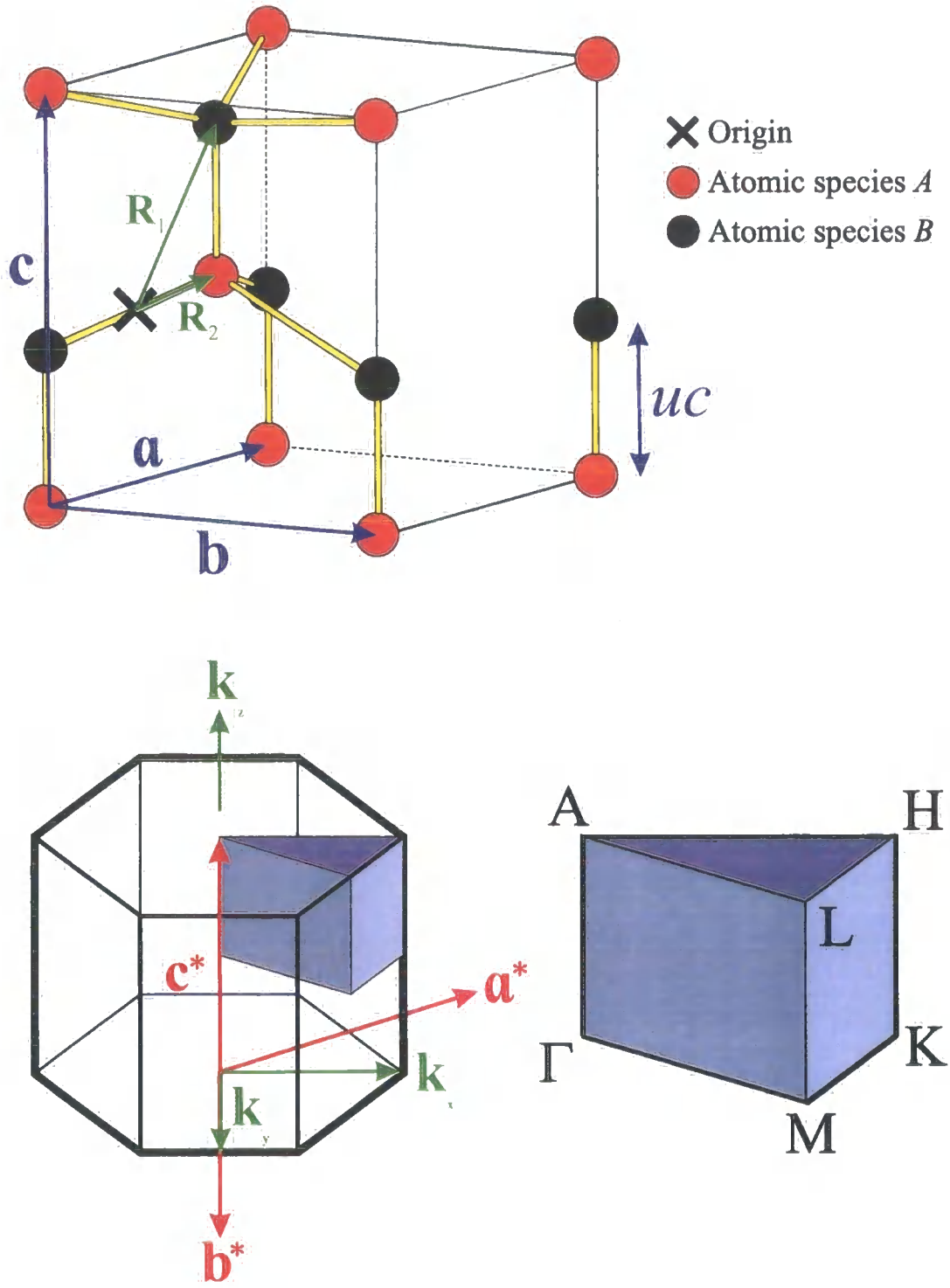

Figure 2.2: The wurtzite unit cell and 1st Brillouin zone indicating the irreducible wedge of the zone and points of high symmetry.

vectors

$$\mathbf{a} = \left(\frac{\sqrt{3}}{2}, \frac{1}{2}, 0\right) a \tag{2.1a}$$

$$\mathbf{b} = \left(\frac{\sqrt{3}}{2}, -\frac{1}{2}, 0\right) a \tag{2.1b}$$

$$\mathbf{c} = (0, 0, 1)c \tag{2.1c}$$

Therefore the crystal is defined by the internal parameter u and two lattice constants, a and c, where a refers to the hexagonal plane and c to its normal. The parameter a of wurtzite can only be meaningfully compared to the lattice parameter of zincblende if a factor of $\sqrt{2}$ is taken into account (i.e. $a_{ZB} = \sqrt{2}a_{WZ}$). Referring to figure 2.2, the four atoms that make up the basis, two of type A and two of type B are located at $\pm\mathbf{R}_1$ and $\pm\mathbf{R}_2$. By convention those denoted as type A are from group III (i.e. gallium, indium and aluminium in this work) and are found at $-\mathbf{R}_1$ and $\mathbf{R}_2$.

$$-\mathbf{R}_1 = -\frac{1}{6}(\mathbf{a} + \mathbf{b}) - \left(\frac{1}{4} + \frac{u}{2}\right)\mathbf{c} \tag{2.2a}$$

$$\mathbf{R}_2 = \frac{1}{6}(\mathbf{a} + \mathbf{b}) + \left(\frac{1}{4} - \frac{u}{2}\right)\mathbf{c} \tag{2.2b}$$

and those of type B are group V elements (i.e. nitrogen in this work) and are found at $-\mathbf{R}_2$ and $\mathbf{R}_1$.

$$-\mathbf{R}_2 = -\frac{1}{6}(\mathbf{a} + \mathbf{b}) + \left(-\frac{1}{4} + \frac{u}{2}\right)\mathbf{c} \tag{2.3a}$$

$$\mathbf{R}_1 = \frac{1}{6}(\mathbf{a} + \mathbf{b}) + \left(\frac{1}{4} + \frac{u}{2}\right)\mathbf{c} \tag{2.3b}$$

It follows that by convention the [0001] direction is given by a vector pointing from the gallium atom to the nearest neighbour nitrogen atom [26]. This convention in positioning is important in order to achieve a consistent agreement on the polarity of the crystal [27].

For the so called ideal wurtzite structure all the bond lengths are equal, the internal

parameter takes on the value $u = 3/8$ and the ratio of the lattice constants must then be $c/a = \sqrt{8/3}$. Real wurtzite crystals are not quite ideal, and have two slightly different bond lengths. The reciprocal lattice of a simple hexagonal lattice is also a simple hexagonal lattice, and the first Brillouin zone of a wurtzite crystal is a hexagonal prism of volume $2/\sqrt{3}(2\pi)/a^2c$ as shown in figure 2.2 with the following points of high symmetry marked.

$$\begin{aligned} A &= (0, 0, \tfrac{1}{2}) \\ L &= (\tfrac{1}{2}, 0, \tfrac{1}{2}) \\ M &= (\tfrac{1}{2}, 0, 0) \\ \Gamma &= (0, 0, 0) \\ H &= (\tfrac{2}{3}, \tfrac{1}{3}, \tfrac{1}{2}) \\ K &= (\tfrac{2}{3}, \tfrac{1}{3}, 0) \end{aligned} \tag{2.4}$$

2.2.2 Bandstructure calculations in semiconductor crystals

An accurate theoretical representation of the electronic structure (i.e. the bandstructure) of a semiconductor crystal is critical to realistic calculations of devices or heterostructures of that material. To define the problem more clearly, we require the electronic structure to be known as a function of position in k-space;

$$\begin{aligned} E &= E_n(\mathbf{k}) \\ \Psi &= \Psi_n(\mathbf{k}) \end{aligned} \tag{2.5}$$

where E is the energy, n is the band index and $\mathbf{k}$ is the wavevector. Ψ is the single electron wavefunction. The first step is therefore the reduction of the many body problem of electrons and ions, to that of solving the single electron (time-independent) Schrödinger equation,

$$\hat{H}\Psi(\mathbf{r}) = \left(-\frac{\hbar^2}{2m_e}\nabla^2 + V\right)\Psi(\mathbf{r}) = E\Psi(\mathbf{r}) \tag{2.6}$$

The reduction is achieved, firstly by application of the Born-Oppenheimer approximation [28] which assumes that due to the differences in mass, the nuclear response to electron-

nuclei interactions is very small and therefore the nuclei can be considered stationary. Secondly the Hartree or mean-field approximation assumes that each electron experiences an identical *mean-field* potential V, as a result of all the other electrons and nuclei. The full wavefunction can then be approximated by a Slater determinant of the one electron wavefunctions, solved using this mean-field potential (see for example [29]). All the difficulty in solving equation (2.6) lies in knowing the exact form of the potential V. This potential does however have the periodicity of the lattice. From Bloch's theorem [30] the eigenstates $\Psi(\mathbf{r})$ of the one electron Hamiltonian in 2.6 have the form of a plane wave multiplied by a function with the periodicity of the Bravais lattice:

$$\Psi_{n\mathbf{k}}(\mathbf{r}) = e^{i\mathbf{k}\cdot\mathbf{r}} u_{n\mathbf{k}}(\mathbf{r}) \tag{2.7}$$

where $u_{n\mathbf{k}}(\mathbf{r}+\mathbf{L}) = u_{n\mathbf{k}}(\mathbf{r})$ for all $\mathbf{L}$ in the Bravais lattice. There are several different approaches to bandstructure calculations in semiconductors, one of the most commonly employed being the use of *pseudopotentials* in combination with a Fourier series basis set for the wavefunction. The pseudopotential approximation allows computationally efficient calculations to be performed while retaining a realistic description of the electronic structure of valence and conduction electrons. In this work the empirical pseudopotential method (EPM) is used to calculate bulk bandstructures which are later used in a model for the bound states of heterostructures.

2.3 Pseudopotential Method

The pseudopotential approach was proposed by Fermi in 1934 [31] for the study of high energy atomic states and refined a year later by Hellman [32] for calculating alkali metal energy levels. However, most of the progress in applying pseudopotentials to metals and semiconductors occurred from the 1950s onwards (see for example [33], [34] and [35]). There are many excellent reviews and books about the pseudopotential method, its history and its application, see for example [25,35,36].

The pseudopotential bandstructure method considers the electrons to be grouped as either core electrons, tightly bound to the nucleus, or delocalised valence electrons which

are free-electron-like. For example Si has the electronic configuration $1s^2 2s^2 2p^6 3s^2 3p^2$, of which the $1s$, $2s$ and $2p$ form the core orbitals. The $3s$ and $3p$ orbitals are those responsible for the bonding between atoms and can be modelled by a so called pseudowavefunction, which differs from the true wavefunction only in the ionic cores that occupy a small fraction of the crystal volume, and obeys a Schrödinger-like equation with only a relatively weak potential. This assumption of a weak potential can be understood in terms of the fact that the valence electrons experience a nuclear potential that is screened by the core electrons and, in addition, the effect of the Phillips-Kleinman cancellation theorem [37]. The latter demonstrates that since the true wavefunction must be orthogonal to the core states, the pseudowavefunction behaves as if there is a repulsive "orthogonality potential". It turns out that the repulsive orthogonality potential and the attractive core potential almost cancel.

2.3.1 Orthogonalised Plane Waves

A mathematical formulation of the above argument is now presented. First of all the true wavefunction Ψ must be expressed as a smooth wavefunction ϕ, which is to be determined, and a linear combination of occupied core state wavefunctions Ψ_c

$$\Psi = \phi + \sum_c b_c \Psi_c, \tag{2.8}$$

The true wavefunction is forced to be orthogonal to the core requiring that

$$\langle \Psi_c | \Psi \rangle = 0, \tag{2.9}$$

for all c. Then solving for b_c yields

$$|\Psi\rangle = |\phi\rangle - \sum_c |\Psi_c\rangle\langle\Psi_c|\phi\rangle, \tag{2.10}$$

which can be substituted into the Schrödinger equation $\hat{H}|\Psi\rangle = E|\Psi\rangle$ to give

$$\hat{H}|\phi\rangle - \sum_c \hat{H}|\Psi_c\rangle\langle\Psi_c|\phi\rangle = E|\phi\rangle - \sum_c E|\Psi_c\rangle\langle\Psi_c|\phi\rangle \tag{2.11}$$

Now the Hamiltonian has the core states as its eigenstates, with energy E_c. Further, the Hamiltonian can be written as the sum of the kinetic $\hat{T}$ and potential V energy operators ($\hat{H} = \hat{T} + V$)

$$\hat{T}|\phi\rangle + V|\phi\rangle - \sum_c E_c|\Psi_c\rangle\langle\Psi_c|\phi\rangle = E|\phi\rangle - \sum_c E|\Psi_c\rangle\langle\Psi_c|\phi\rangle \tag{2.12}$$

which can be rearranged to produce;

$$\hat{T}|\phi\rangle + (V + V^R)|\phi\rangle = E|\phi\rangle \tag{2.13}$$

where the orthogonalisation potential V^R has been defined as

$$V^R = \sum_t (E - E_t)\phi_t\langle\phi_t|\phi\rangle \tag{2.14}$$

If this potential is combined with the core potential V, the resulting total potential (or pseudopotential V^P) is normally very weak [25]. The Schrödinger-like equation with a pseudo-Hamiltonian H^P now becomes

$$\hat{H}^P\phi = \left(-\frac{\hbar^2}{2m_e}\nabla^2 + V + V^R\right)\phi = \left(-\frac{\hbar^2}{2m_e}\nabla^2 + V^P\right)\phi = E\phi \tag{2.15}$$

where ϕ is a pseudo-wavefunction. The true wavefunction is related to ϕ by equation (2.10).

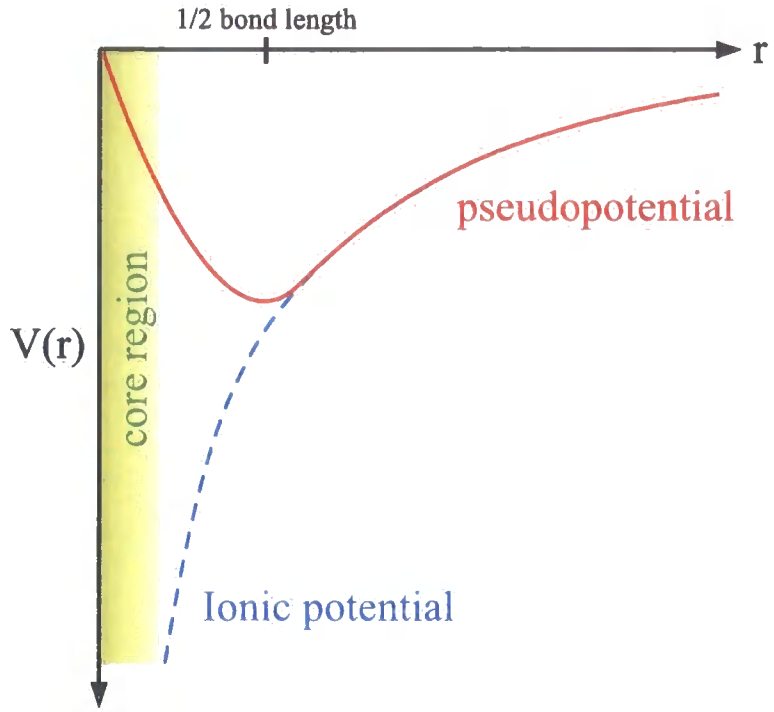

Figure 2.3: Schematic representation of an actual potential and pseudopotential.

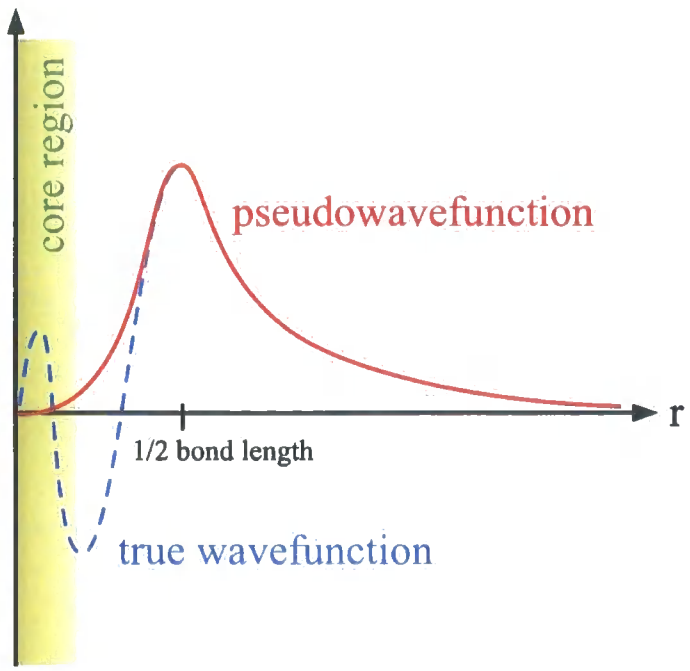

Figure 2.4: Schematic representation of an actual wavefunction and corresponding pseudo-wavefunction

2.3.2 Concept of a pseudopotential

The cancellation of terms in equation (2.15) results in a pseudopotential which is weaker than the original ionic potential as illustrated in figure 2.3. Near the nucleus the ionic potential diverges, but the pseudopotential weakens, as a result the true wavefunction for the ionic potential has rapid spatial oscillations near the core, but the pseudo-wavefunction is quite smooth. Both the potential and pseudopotential, and the wavefunction and pseudo-wavefunction become identical far away from the core. Note that although the true wavefunction and pseudo-wavefunction differ near the ionic cores, the ionic cores only constitute a small fraction of the crystal volume.

2.3.3 Empirical pseudopotentials

In this chapter we are concerned with pseudopotentials that have been determined by experimental measurements or more fundamental calculations. These pseudopotentials are said to be empirical, however it is possible to define pseudopotentials, from first principles without empirical input, using an all-electron calculation of the core states. Such an approach is often used self-consistently in combination with density functional theory (DFT) to provide accurate ground state properties of a system. In such an "*ab-initio*" calculation the pseudo-wavefunction would be used in turn to generate a new potential. The new potential would be again used to generate a wavefunction, and the process would be repeated until the potential and wavefunction remained unchanged. The use of DFT is however, not an appropriate theory for the excited states of a system. First principles self-consistent calculations are a powerful tool in the calculation of the electronic structure of solids, but the restriction to ground state properties means that they have limitations in the calculation of optical properties.

Unlike *ab-initio* pseudopotentials, empirical pseudopotentials consider the pseudopotential to include the mean field seen by a single electron due to all the other electrons. This information is included by parameterising the pseudopotential and fitting by comparison with experimental bandstructure data. In this way the effects of temperature, exchange and correlation are all included, although only because they were present in the experiments from which the data is taken. The use of experimental information should in principle make the pseudopotential self-consistent, but this is not explicitly enforced. Studies of the na-

ture of empirical pseudopotentials have been performed and suggest a reasonable level of self-consistency can be achieved [38].

The form of equation (2.14) suggests that the pseudopotential will generally be spatially non-local in nature [39]. In practice, for wurtzite materials the non-local contribution is normally small [40] and is not included in these calculations. The total pseudopotential of the lattice is periodic and can be written in a Fourier representation.

$$V^P(\mathbf{r}) = \sum_{\mathbf{g}} V_{\mathbf{g}} e^{i\mathbf{g}\cdot\mathbf{r}} \tag{2.16}$$

$V^P(\mathbf{r})$ is the local crystal pseudopotential and is parameterised by the Fourier coefficients $V_{\mathbf{g}}$ whose $\mathbf{g}$ are reciprocal lattice vectors. The coefficients $V_{\mathbf{g}}$ of equation (2.16) are often referred to as the "pseudopotential form factors". It follows from the theory of Fourier analysis that

$$V_{\mathbf{g}} = \frac{1}{\Omega}\int_{\Omega} V^P(\mathbf{r}) e^{-i\mathbf{g}\cdot\mathbf{r}} d^3\mathbf{r} \tag{2.17}$$

Here Ω is the lattice unit cell volume. $V(\mathbf{r})$ can be rewritten in terms of 'atomic' pseudopotentials of each atom in the unit cell.

$$V^P(\mathbf{r}) = \sum_{\mathbf{L}_j}\sum_{\mathbf{R}_i=1}^{4} U_i^P(\mathbf{r} - \mathbf{L}_j - \mathbf{R}_i) \tag{2.18}$$

Here U_i^P is the atomic pseudopotential, $\mathbf{R}_i$ is the atomic positions within the wurtzite unit cell, as defined by equations (2.2) and (2.3) for atom i and $\mathbf{L}_j$ is the jth lattice vector. Combining (2.17) and (2.18) gives

$$V_{\mathbf{g}} = \frac{1}{\Omega}\sum_{i=1}^{4}\int_{\Omega} U_i^P(\mathbf{r} - \mathbf{R}_i) e^{-i\mathbf{g}\cdot\mathbf{r}} d^3\mathbf{r} \tag{2.19}$$

The atomic form factors for each of the A and B atomic species can now be defined as

$$U_{\mathbf{g},j} = \frac{4}{\Omega}\int_{\Omega} U_j^P(\mathbf{R}_j)e^{-i\mathbf{g}\cdot\mathbf{r}'}d^3\mathbf{r} \tag{2.20}$$

where $j = A$ or B. Equation (2.19) can now be simplified in terms of the atomic form factors

$$V_{\mathbf{g}} = \frac{1}{4}\left[e^{i\mathbf{g}\cdot\mathbf{R}_1}U_{\mathbf{g},A} + e^{-i\mathbf{g}\cdot\mathbf{R}_2}U_{\mathbf{g},A} + e^{i\mathbf{g}\cdot\mathbf{R}_1}U_{\mathbf{g},B} + e^{-i\mathbf{g}\cdot\mathbf{R}_2}U_{\mathbf{g},B}\right] \tag{2.21}$$

It is convenient to express $V_{\mathbf{g}}$ in terms of symmetric $V_{\mathbf{g}}^S$ and antisymmetric $V_{\mathbf{g}}^A$ form factors:

$$V_{\mathbf{g}} = V_{\mathbf{g}}^S S_{\mathbf{g}}^S + iV_{\mathbf{g}}^A S_{\mathbf{g}}^A \tag{2.22}$$

where $V_{\mathbf{g}}^S = \frac{1}{2}[U_{\mathbf{g},A} + U_{\mathbf{g},B}]$ and $V_{\mathbf{g}}^A = \frac{1}{2}[U_{\mathbf{g},A} - U_{\mathbf{g},B}]$. The structure factors; $S_{\mathbf{g}}^S$ and $S_{\mathbf{g}}^A$, contain the terms which are dependent on the crystal structure and are defined as

$$S_{\mathbf{g}}^S = \cos(\mathbf{g}\cdot\mathbf{R}_1) + \cos(\mathbf{g}\cdot\mathbf{R}_2) = \cos\left[2\pi\left(\frac{l}{6}+\frac{m}{6}+\frac{n}{4}\right)\right]\cos\left[2\pi\left(\frac{nu}{2}\right)\right] \tag{2.23a}$$

$$S_{\mathbf{g}}^A = \cos(\mathbf{g}\cdot\mathbf{R}_1) - \cos(\mathbf{g}\cdot\mathbf{R}_2) = \cos\left[2\pi\left(\frac{l}{6}+\frac{m}{6}+\frac{n}{4}\right)\right]\sin\left[2\pi\left(\frac{nu}{2}\right)\right] \tag{2.23b}$$

where l,m,n are the integer components of reciprocal lattice vector $\mathbf{g}$ such that $\mathbf{g} = l\mathbf{a}^* + m\mathbf{b}^* + n\mathbf{c}^*$. Note that although the lattice constants do not appear in the definition of the structure factors, $S_{\mathbf{g}}^S$ and $S_{\mathbf{g}}^A$ are functions of u and are therefore changed by any deviation of u from its ideal value of 3/8.

The atomic pseudopotentials are taken to be spherically symmetric, and it follows that the pseudopotential form factors depend only on the magnitude of the reciprocal lattice vector. The symmetric and antisymmetric form factors can now simply be described by $U_{g,A}$ and $U_{g,B}$ where $g = |\mathbf{g}|$. This greatly reduces the number of independent form factors that define the pseudopotential and therefore the number that have to be determined. $V_{\mathbf{g}=(000)}$ is spatially independent, contributing only to a uniform potential and is usually set to zero. The structure factors for $\mathbf{g} = (003)$, $\mathbf{g} = (211)$ and $\mathbf{g} = (213)$ and the antisymmetric structure

g	g^2	S_g^S	S_g^A
(100)	$2\frac{2}{3}$	$\frac{1}{2}$	0 †
(002)	3	0.71	0.71
(101)	$3\frac{5}{12}$	0.33	0.80
(102)	$5\frac{2}{3}$	0.35	0.35
(210)	8	1	0 †
(103)	$9\frac{5}{12}$	0.80	0.33
(200)	$10\frac{2}{3}$	$\frac{1}{2}$	0 †
(212)	11	0.71	0.71
(201)	$11\frac{5}{12}$	0.33	0.80
(004)	12	0.00*	1.00
(202)	$13\frac{2}{3}$	0.35	0.35
(104)	$14\frac{2}{3}$	0.00*	0.50

Table 2.1: The reciprocal lattice vectors used in Fourier expansion of a wurtzite pseudopotential. The values of $\mathbf{g}^2$ and the structure factors $S_\mathbf{g}^S$ and $S_\mathbf{g}^A$ are displayed for ideal wurtzite, $u = 3/8$ and $c/a = \sqrt{8/3}$ and will vary slightly for the non ideal case. $*$ The symmetric structure factors for (004) and (104) are only exactly zero for ideal wurtzite. † the antisymmetric structure factors for (100), (200) and (210) are zero for all u

factors for $\mathbf{g} = (100)$, $\mathbf{g} = (210)$ and $\mathbf{g} = (200)$ are also zero and the corresponding form factors are not required.

The Fourier expansion of the lattice pseudopotential is truncated and it is found that for the wurtzite structure 21 form factors, (12 symmetric and 9 antisymmetric) are sufficient to adequately describe the potential. The complete list is given in table 2.1.

In summary, we may write the pseudopotential of the crystal lattice as;

$$V^P(\mathbf{r}) = \sum_\mathbf{g} \left(V_g^S S_\mathbf{g}^S + iV_g^A S_\mathbf{g}^A\right) e^{i\mathbf{g}\cdot\mathbf{r}} \tag{2.24}$$

2.3.4 EPM calculations of electronic structure

Having considered the nature of the pseudopotential and the general form of the empirical pseudopotential for wurtzite materials, the application of the pseudopotential method to the calculation of electronic structure of a nitride semiconductor will now be discussed. A pseudo-energy eigenfunction for the crystal will still satisfy Bloch's theorem and can be

written as a Fourier series expansion;

$$\phi_n \mathbf{k}(\mathbf{r}) = e^{i\mathbf{k}\cdot\mathbf{r}} \sum_{\mathbf{g}} a_{\mathbf{g}} e^{i\mathbf{g}\cdot\mathbf{r}} \tag{2.25}$$

Where $a_{\mathbf{g}}$ is the Fourier coefficient for the reciprocal lattice vector $\mathbf{g}$. The energy eigenvalues and their associated pseudo-wavefunction, can be obtained by solving the Schrödinger equation which, in the representation of equation (2.25), is the matrix equation with the pseudo-Hamiltonian in a plane wave basis.

$$H^P_{\mathbf{g},\mathbf{g}'} a_{\mathbf{g}} = E_n a_{\mathbf{g}} \tag{2.26}$$

The pseudo-Hamiltonian matrix is given by

$$H^P_{\mathbf{g},\mathbf{g}'} = \frac{\hbar^2}{2m_e}(\mathbf{k}+\mathbf{g})^2 \delta_{\mathbf{g},\mathbf{g}'} + V_{|\mathbf{g}-\mathbf{g}'|} \tag{2.27}$$

where $V_{|\mathbf{g}-\mathbf{g}'|}$ is the coefficient of $e^{i(\mathbf{g}-\mathbf{g}')\cdot\mathbf{r}}$ on the right hand side of equation (2.24).

2.3.5 Spin-orbit coupling

Spin-orbit coupling (SOC) is the interaction of the electron spin and its orbital angular momentum which causes the degeneracy of some of the electron states in the crystal to be lifted. It is a relativistic phenomenon and is therefore more pronounced in the heavier elements. The electronic states of nitrogen are known to dominate the electronic structure at the top of the valence band [40], where the effect of spin-orbit coupling is expected to be most noticeable. Although nitrogen is a light element, the spin-orbit splitting cannot be ignored without undue error. The spin-orbit coupling is described by a contribution to the Hamiltonian

$$H^{SOC} = \frac{\hbar}{4m_e^2c^2}\boldsymbol{\sigma}\left(\nabla V(\mathbf{r}) \wedge \mathbf{p}\right) \tag{2.28}$$

where here c is the speed of light, and $\boldsymbol{\sigma}$ is the Pauli spin matrix, with

$$\sigma_x = \begin{bmatrix} 0 & 1 \\ 1 & 0 \end{bmatrix} \qquad \sigma_y = \begin{bmatrix} 0 & -i \\ i & 0 \end{bmatrix} \qquad \sigma_z = \begin{bmatrix} 1 & 0 \\ 0 & -1 \end{bmatrix} \tag{2.29}$$

Spin-orbit coupling has been incorporated into the pseudopotential scheme by Weisz [41] and others [42,43] and here we make use of the simplest form of the approach. Weisz has shown that H^{SOC} can be parameterised within the pseudopotential scheme as

$$H^{SOC}_{\mathbf{g},\mathbf{g}'} = -i\lambda S(\mathbf{g}-\mathbf{g}')\boldsymbol{\sigma}\cdot(\mathbf{K}\wedge\mathbf{K}') \tag{2.30}$$

where $\mathbf{K} = \mathbf{k} + \mathbf{g}$ and λ is an adjustable parameter for interaction strength. It can be shown that

$$-i\lambda S_{\mathbf{g}-\mathbf{g}'} = -i\lambda^S\left(\cos(\mathbf{g}\cdot\mathbf{R}_1)+\cos(\mathbf{g}\cdot\mathbf{R}_2)\right) + \lambda^A\left(\sin(\mathbf{g}\cdot\mathbf{R}_1)+\sin(\mathbf{g}\cdot\mathbf{R}_2)\right) \tag{2.31}$$

where the parameters λ^S and λ^A are determined empirically and are usually expressed in terms of two more factors S_μ and S_α by

$$\lambda^A = \frac{S_\mu(1-S_\alpha)}{2} \tag{2.32}$$

$$\lambda^S = \frac{S_\mu(1+S_\alpha)}{2} \tag{2.33}$$

S_μ determines the strength of the spin-orbit coupling and S_α gives the relative strengths of

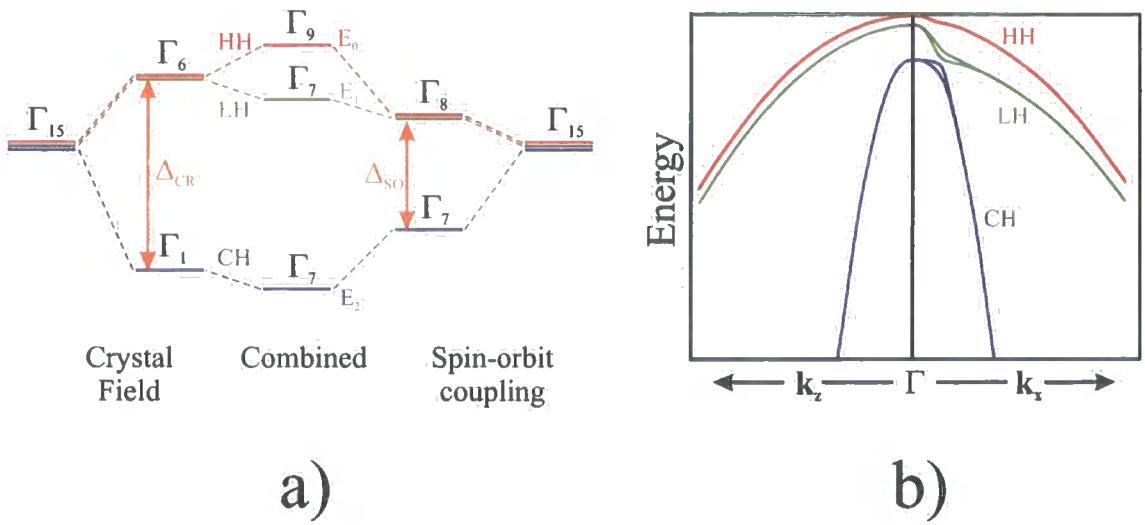

Figure 2.5: (a) Schematic illustration of the spin-orbit splitting and crystal field splitting in wurtzite materials. (b) Schematic illustration of the resulting valence bandstructure near the zone centre. The heavy hole (HH), light hole (LH) and crystal hole (CH) bands are indicated.

the spin-orbit interaction for the two atomic species A and B.

With the inclusion of spin-orbit effects the states of the system are now spinors and the wavefunction of equation (2.25) must be modified to include spin up and spin down components.

$$\phi(\mathbf{r}) = \sum_{\mathbf{g}} \begin{pmatrix} a_{\mathbf{g}\uparrow} \\ a_{\mathbf{g}\downarrow} \end{pmatrix} e^{i(\mathbf{k}+\mathbf{g})\cdot\mathbf{r}} \tag{2.34}$$

2.3.6 Crystal Field Splitting

Spin-orbit coupling has a significant effect on the bandstructure at the top valence band in nitride semiconductors. Fig 2.5a shows schematically how some splitting of bands occurs due to the spin-orbit interaction. Additional splitting is observed due to the symmetry of the crystal, known as crystal field splitting. The crystal field splitting is a function of the deviation of the crystal from ideality, i.e. a function of the change in u from the ideal internal parameter $u = 3/8$ and the deviation from the ideal ratio of lattice constants $a/c = \sqrt{8/3}$ [44]. The crystal field splitting (also shown in fig 2.5a) is given by

$$\begin{aligned} \Delta_{CF} &\equiv E_{\Gamma_6} - E_{\Gamma_1} \\ \Delta_{CF} &= \Delta_{CF}^0 + \alpha\left(u - \tfrac{3}{8}\right) + \beta\left(\tfrac{c}{a} - \sqrt{\tfrac{8}{3}}\right) \end{aligned} \tag{2.35}$$

where $\alpha = -17$eV and $\beta = 2$eV for GaN [44], indicating that Δ_{CF} is strongly effected by changes in u. The combination of these spin-orbit coupling and crystal field splitting gives rise to the valence bandstructure shown in fig 2.5b. A schematic representation of the three bands is shown in figure 2.5. The energies at the top of the three valence bands are given by [45]

$$\begin{aligned} E_0 &= 0 \\ E_1 &= -\tfrac{1}{2}(\Delta_{SO} + \Delta_{CF}) + \tfrac{1}{2}\sqrt{(\Delta_{SO} + \Delta_{CF})^2 - \tfrac{8}{3}\Delta_{SO}\Delta_{CF}} \\ E_2 &= -\tfrac{1}{2}(\Delta_{SO} + \Delta_{CF}) - \tfrac{1}{2}\sqrt{(\Delta_{SO} + \Delta_{CF})^2 - \tfrac{8}{3}\Delta_{SO}\Delta_{CF}} \end{aligned} \tag{2.36}$$

where Δ_{SO} is the splitting due to spin-orbit coupling alone, and E_1,E_2 and E_3 are the energies of the top three valence bands.

2.3.7 Fitting of Pseudopotentials

Experimental information is incorporated into the pseudopotentials through the symmetric and antisymmetric pseudopotential form factors. Bandstructure information for a particular material is obtained from experiment and/or from more fundamental calculations. This bandstructure data is used to determine a set of $V_{\mathbf{g}}^S$ and $V_{\mathbf{g}}^A$ that define the pseudopotential for the specific reciprocal lattice vectors of the material in question. The simplest approach is to fit the set of $V_{\mathbf{g}}^S$ and $V_{\mathbf{g}}^A$ directly to the bandstructure data. Data for form factors established in this way are available in the literature (see for example [45]). This approach is well established and has proved to be a very successful tool in the calculation of electronic structure [25,46], but there is no ready way to use the results to obtain the form factors of the material when strained, or of alloys made from the material.

An alternative approach, which is used throughout this thesis, is to parameterise the functions $V_{\mathbf{q}}^S$ and $V_{\mathbf{q}}^A$, for a range of continuous $\mathbf{q}$ values, such that the form factors could be obtained for any reciprocal lattice in that range. This approach provides more flexibility,

as the reciprocal lattice vectors can be varied as the lattice constant changes with strain or alloying. The symmetric and antisymmetric functional forms of the pseudopotentials used in this work are given below [47,48]

$$V_q^S = \frac{\alpha_1 q^2 + \alpha_2}{1 + e^{[\alpha_3(\alpha_4 - q^2)]}} \tag{2.37}$$

$$V_q^A = (\beta_1 q^2 + \beta_2) e^{[\beta_3(\beta_4 - q^2)]} \tag{2.38}$$

where $\alpha_i, i = 1-4$ and $\beta_i, i = 1-4$ are the parameters to be adjusted in the fitting procedure and q (in units of $2\pi/a_{ZB}$) is the magnitude of the reciprocal space vector at which the form factors are required. The values of α_i and β_i are fitted using a Monte-Carlo approach in which the values α_i or β_i are varied randomly until the pseudopotential reproduces the experimental bandstructure data to within the required accuracy. The experimental data is in the form of typically between three and six band energies at three different points of high symmetry. A weighting is applied to the fitting to ensure the more important transitions are fitted more accurately (e.g. those across the principal band gap). Specifically the fitting procedure attempts to minimise the function:

$$\epsilon = \sum_{n\mathbf{k}} w(n, \mathbf{k}) \left| E_{\text{EPM}}(n, \mathbf{k}) - E_{\text{TARGET}}(n, \mathbf{k}) \right|^2 \tag{2.39}$$

where the index n refers to the band energy information at each of the $\mathbf{k}$-points. In each loop of the algorithm the weighted error ϵ is calculated for a new changed set of α_i or β_i and the changes are only retained if ϵ is reduced. The algorithm for this approach is described by the flow chart in figure 2.6. Care must be taken to avoid the procedure becoming trapped in a local minimum of ϵ.

The lattice parameters and the internal parameter u are set to the experimental values or those obtained from a first principles calculation. Spin-orbit splitting parameters are usually fitted after the procedure has minimised ϵ for a bandstructure with spin-orbit effects ignored. A single spin-orbit parameter is then manually fitted to the experimental values of Δ_{SO}.

As well as agreeing with the experimental data at the three points of high symmetry, several other constraints were placed on the resultant functional forms of the pseudopoten-

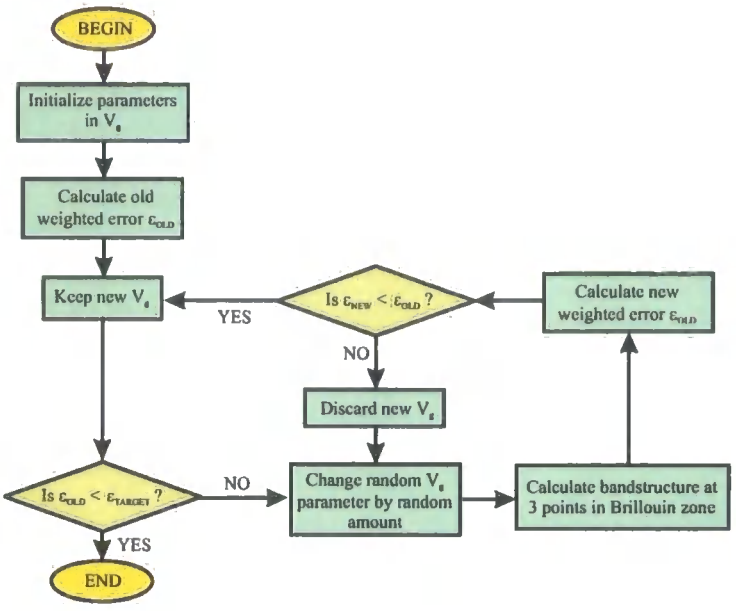

Figure 2.6: Flowchart describing the procedure for fitting of a parameterised pseudopotential to experimental values.

tials.

1. The V_q functional forms must be smooth and physically reasonable

2. The V_q functional form for a particular material should bear some resemblance to that of its zincblende counterpart

3. Reasonable deformation potentials should be obtained

By physically reasonable we mean constraints such as the requirement that the potential decays away from the atom. The second point is a result of the concept of atomic pseudopotentials and attempts to maintain a consistency between the two structures. It is logical to expect two different crystal pseudopotentials derived from the same atomic species to have a similar form. The recent method adopted by Goano *et al* [49] for the functional form of nitride pseudopotentials takes this idea a stage further. In the scheme of Goano *et al* [49], the functional form is applied to the atomic pseudopotential and the bandstructure data is used to fit the atomic pseudopotentials which in turn are then used for the production of the pseudopotential form factors. The atomic functional forms generated in this way are however still dependent on the structure they are part of, e.g. there are three nitrogen atomic function forms, one for each of AlN, GaN and InN. In the calculations performed by Goano

	V^S				V^A			
	α_1	α_2	α_3	α_4	β_1	β_2	β_3	β_4
GaN	0.0837	-0.5643	-0.5485	10.5076	0.0148	0.0869	0.1265	9.3214
InN	0.0843	-0.6104	-0.5851	10.3746	0.0079	0.0857	0.0492	9.6443
AlN	0.0767	-0.4478	-0.4831	10.7550	0.0018	0.1005	0.1736	10.7369

Table 2.2: The α_i and β_i parameters for the functional form of the symmetric and anti-symmetric form factors for wurtzite GaN, InN and AlN. [47,50,51]

et al [49], nonlocal corrections are included which although often important are not compatible with the complex bandstructure techniques used later on in this work. No data was available on the effectiveness of this method without the nonlocal components and therefore the approach outlined in figure 2.6 is adopted. The α_i and β_i parameters as well as the spin parameter μ used in this work for wurtzite materials were obtained by Pugh *et al* [47] and are presented in table 2.2.

The symmetric and antisymmetric V_q curves are displayed in figure 2.7. As Dugdale [40] and Goano *et al* [49] point out the antisymmetric form factors for AlN are significantly larger than those of GaN and InN leading to some disagreement with pseudopotentials produced by other workers [45,49,52–54]. The larger antisymmetric form factors are quite obvious from inspection of the curves in fig 2.7. However, the general form of the curves is consistent with other similar studies of zincblende and wurtzite systems [25,40,46].

2.4 Nitride Bandstructures

The bandstructures of GaN, InN and AlN are presented in figures 2.8-2.10. 263 plane waves per spin orientation were used in the calculations, the choice of this number is discussed in section 2.4.4. All three materials are direct gap semiconductors, with the valence band maximum at Γ. It is worth noting that the band ordering of AlN at the top of the valence band is different to that of GaN and InN in that AlN has a negative crystal field splitting.

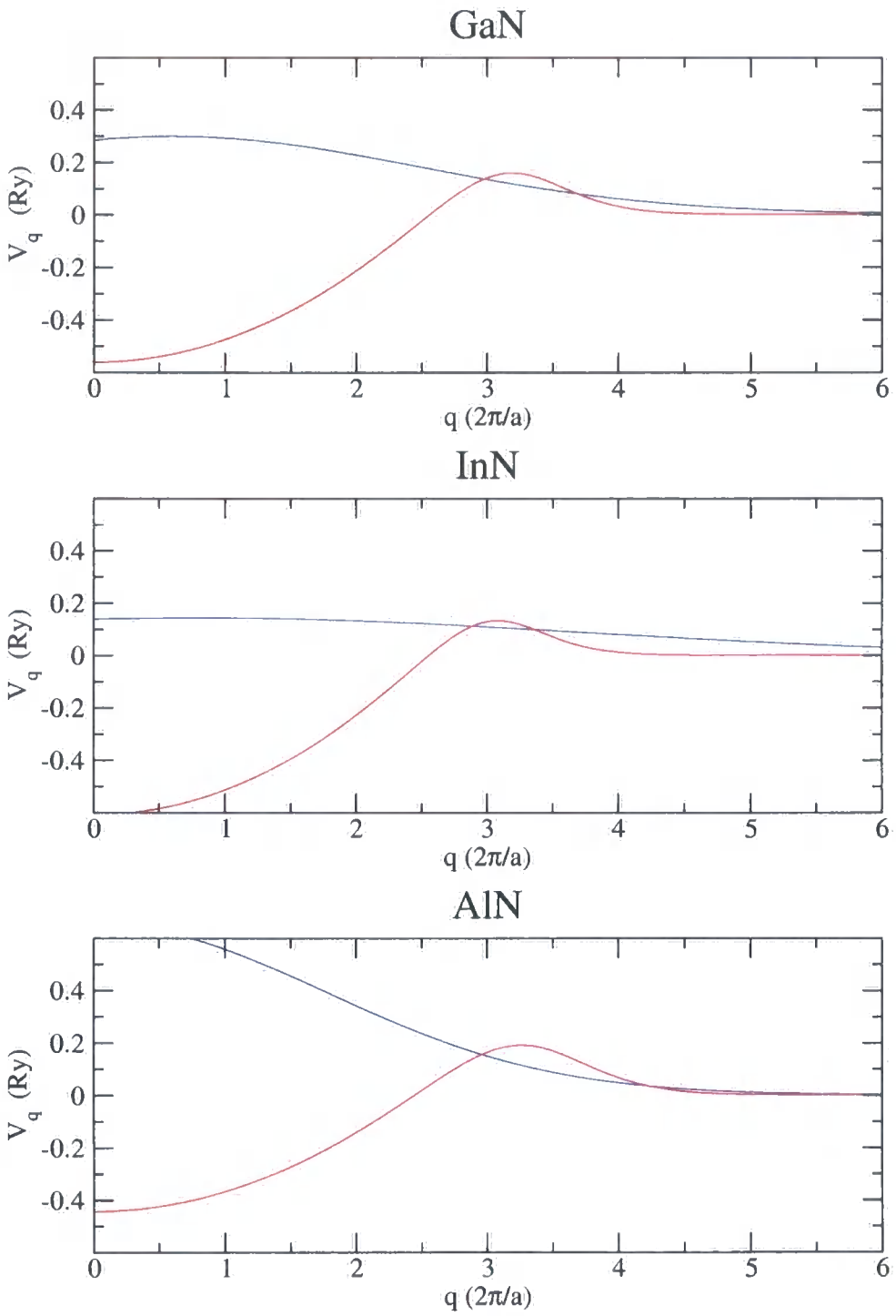

Figure 2.7: The symmetric (blue) and antisymmetric (red) V_q curves for wurtzite GaN, InN and AlN using the parameters from table 2.2.

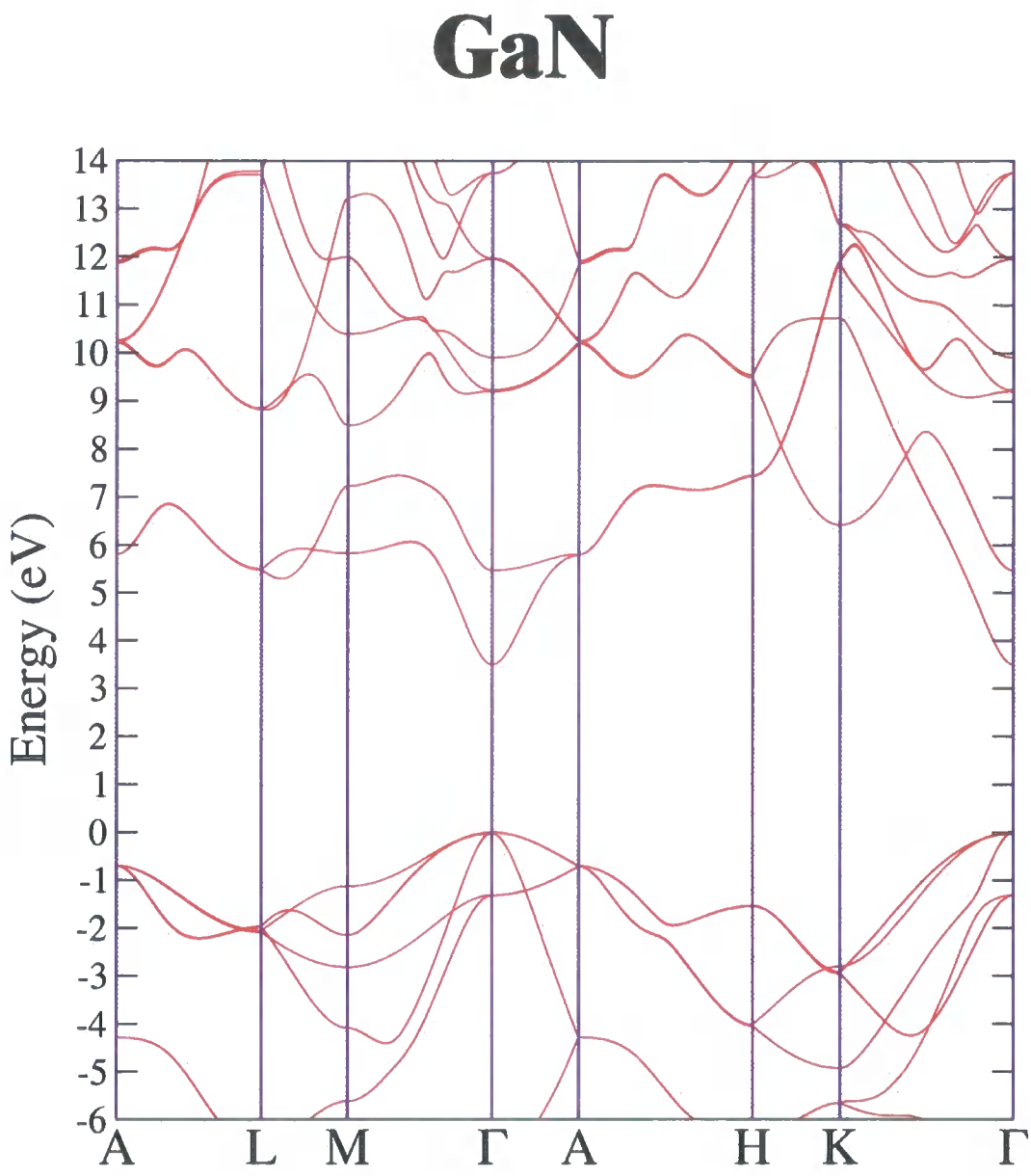

Figure 2.8: Empirical pseudopotential bandstructure of wurtzite GaN

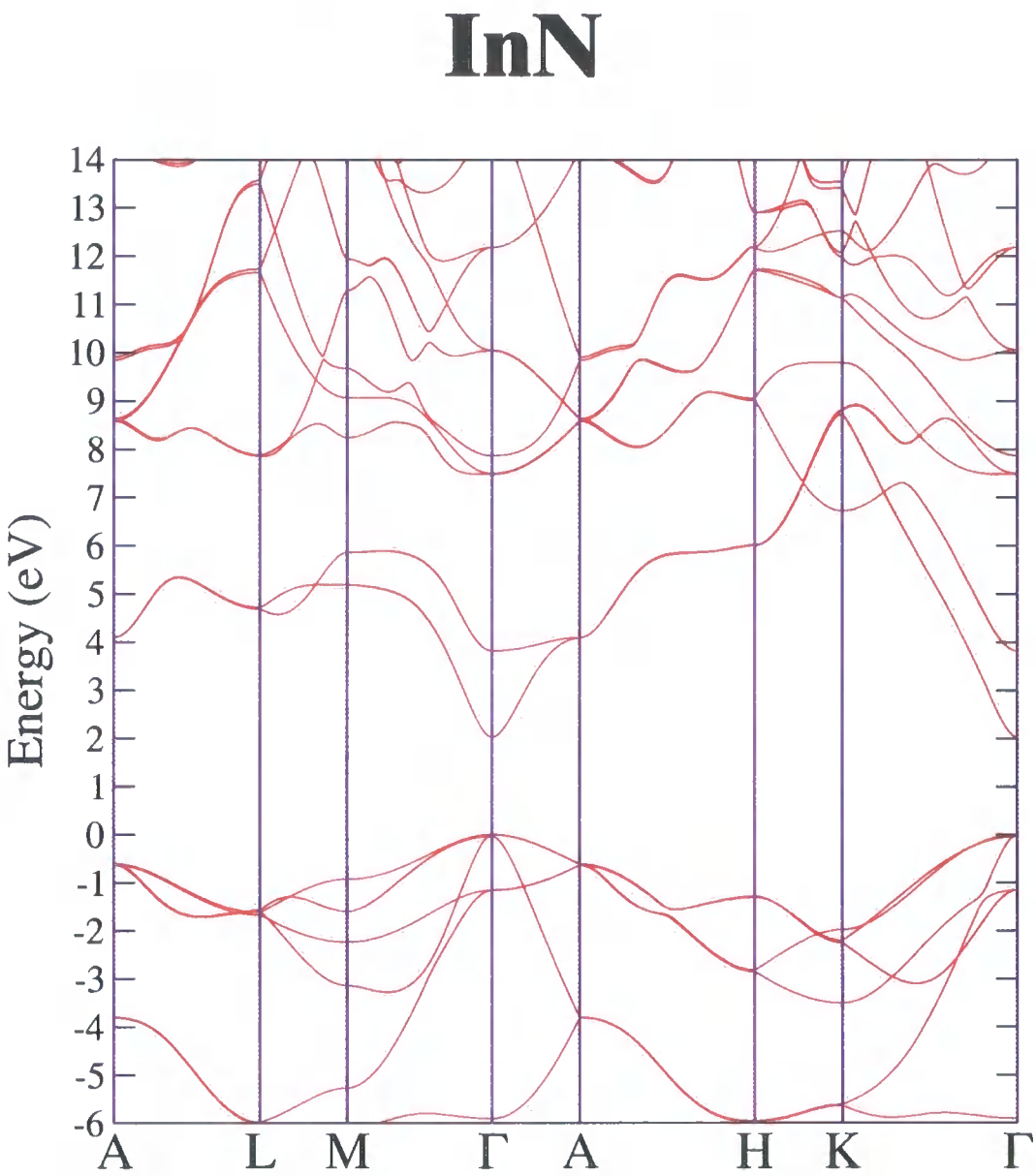

Figure 2.9: Empirical pseudopotential bandstructure of wurtzite InN

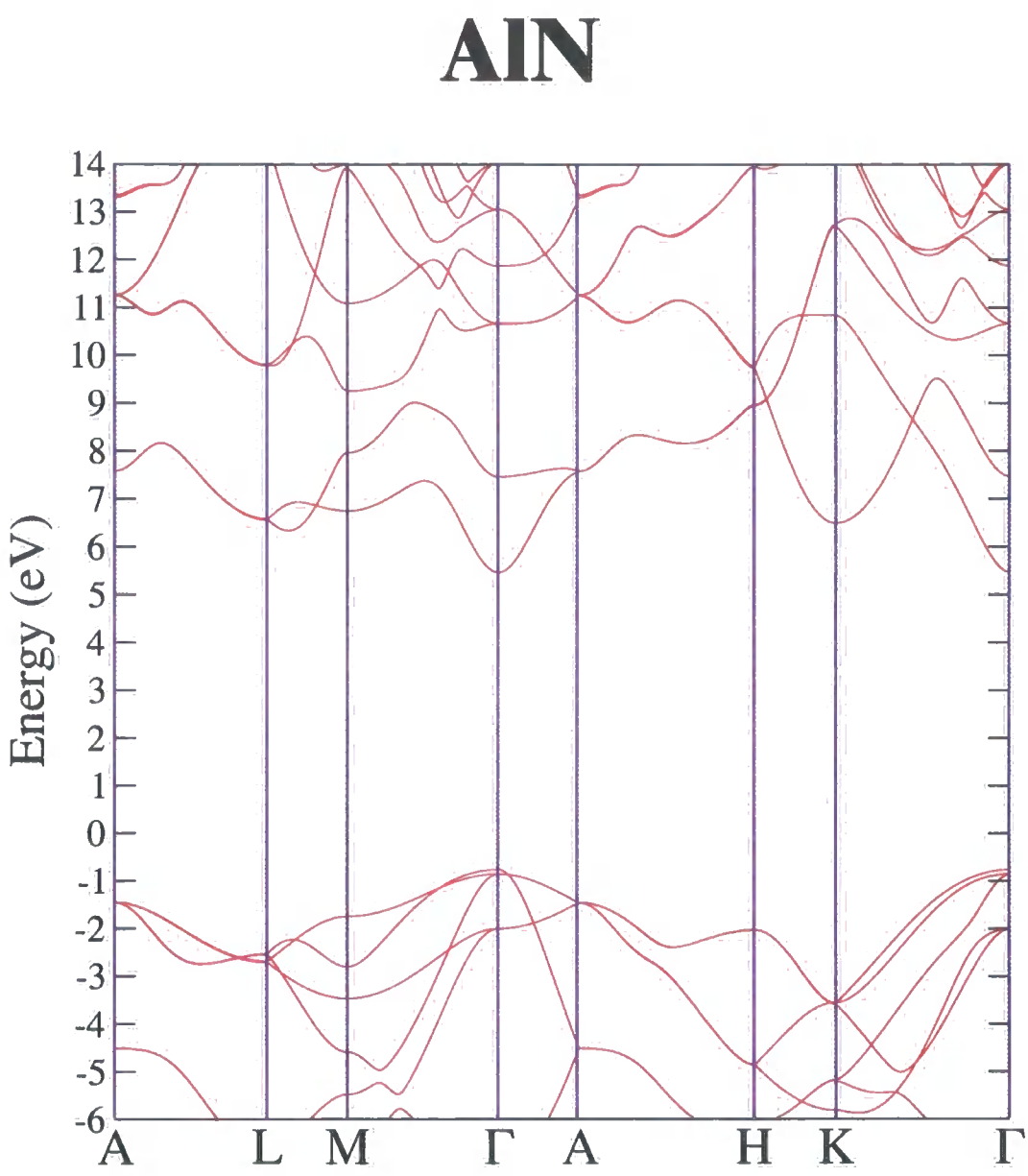

Figure 2.10: Empirical pseudopotential bandstructure of wurtzite AlN

2.4.1 Accuracy of EPM bandstructures

Unfortunately the details of the electronic structure at the top of the valence band for the nitrides are still contentious. In particular, the values of Δ_{CF} and Δ_{SO} to be found in the literature vary considerably [8]. Most of the valence bandstructure information comes from first principles calculations and very little experimental information is available to support these. Even the commonly accepted values of the band gap are not beyond dispute, and notably for InN where the measurements of band-gap vary widely [55]. Analysis of the optical absorption of crystals grown by different techniques gives rise to band gaps from less than 1eV to above 2eV [56]. Wu *et al* [55] recently examined the optical properties of a series of MBE-grown InN films and found the band gap of InN to be below 1.0 eV rather than the accepted value of 1.95 eV.

The bandstructure information derived by Pugh *et al* [47] and used to construct the pseudopotentials in this work is in general agreement with much of the data in the literature and is considered adequate. However, as with any calculation based on empirical input the results are only as reliable as experimental data used as input. Further progress in obtaining reliable data for nitride bandstructures can be put to use in calculations as appropriate. The experimental results upon which these bandstructures are based are examined in detail by Dugdale [40] and Pugh *et al* [47]. A review of band parameters for a range of III-V semiconductors including the nitrides can be found in [8].

2.4.2 Density of states

The density of electronic states at energy E is given by

$$g(E) = \sum_n g_n(E) = \sum_n \int \frac{d^3\mathbf{k}}{(2\pi)^3} \delta(E - E_n) \tag{2.40}$$

where the summation is over all energy bands n and the integral is over a single Brillouin zone. Evaluation of equation 2.40 requires only a knowledge of the relationship between E and $\mathbf{k}$ for each band and the integral is carried out numerically by a sampling of $\mathbf{k}$ throughout the Brillouin zone. As an illustration, the density of states for GaN is plotted in figure 2.11.

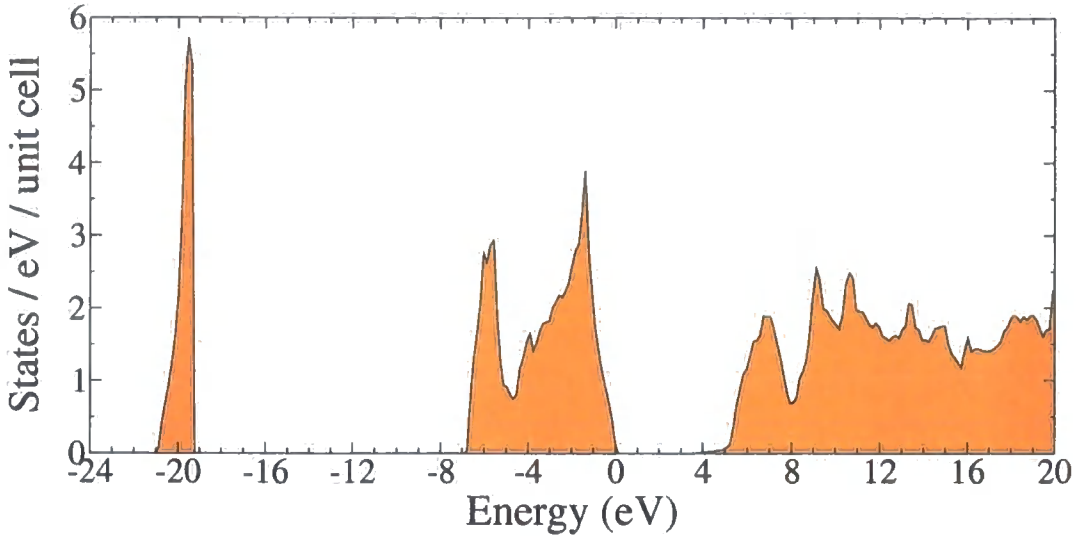

Figure 2.11: Density of states for GaN

2.4.3 Pseudo-wavefunction

The pseudo-wavefunction is important in calculations of overlap integrals, matrix elements of quantum mechanical operators and the dielectric function for a bulk material. In this work we are concerned with the calculation of properties such as the quantum well bound states constructed from bulk pseudo-wavefunctions. However it is also interesting to use the pseudo-wavefunction to calculate the charge density for a unit cell of bulk GaN. The (pseudo) charge density for the n^{th} band is defined as:

$$\rho_n(\mathbf{r}) = e \sum_{\mathbf{k}} |\phi_{n\mathbf{k}}(\mathbf{r})|^2 \tag{2.41}$$

In which e is the charge of an electron and the summation is again over all states in the Brillouin zone. The $\mathbf{k}$-space summation can be made computationally more efficient by summing the charge at several representative "special" $\mathbf{k}$-points [57,58], (see [25] for more details). The total valence charge density can be obtained by summing over all the individual valence bands. The calculated valence charge density of GaN is shown in figure 2.12. The highest concentration of charge is situated between the atoms as would be expected for a covalently bonded material. Some ionic character is apparent with significantly greater charge density observed near the anion (N) than the cation (Ga).

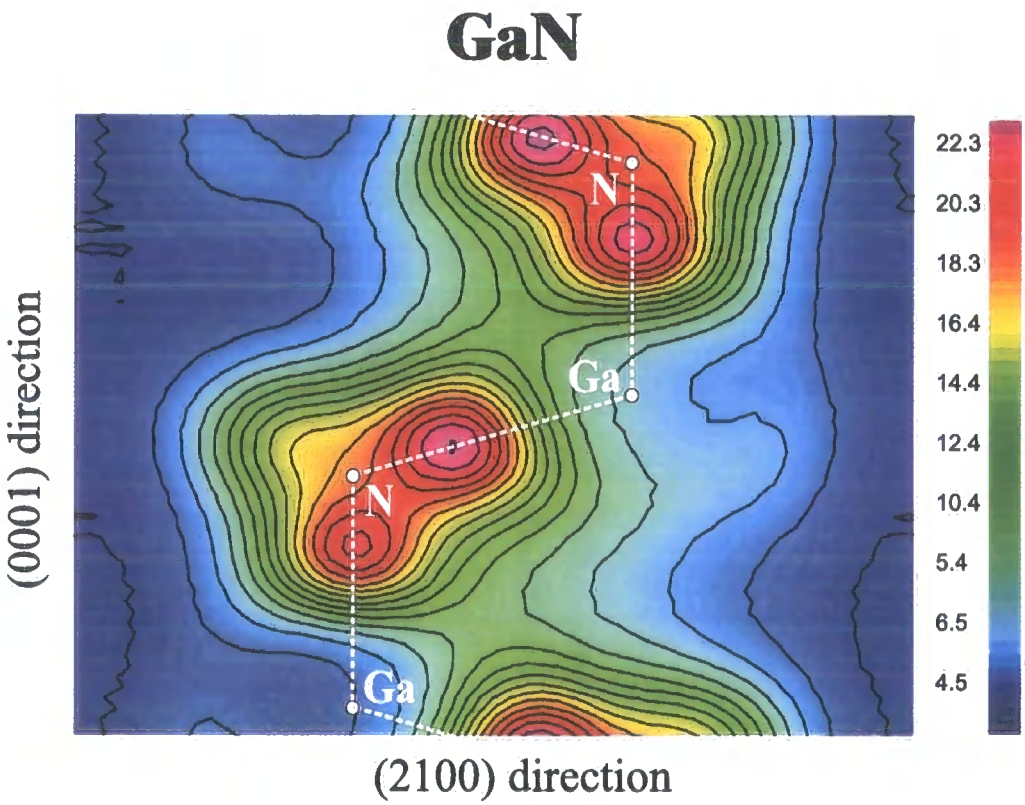

Figure 2.12: Valence charge density for GaN along the bond plane. The y-axis is the growth direction and the x-axis defines the plane to cut through the core sites and the bonds between them. The contours are in units of electrons per unit cell volume

2.4.4 Convergence

In section 2.3 it was stated that the pseudopotential wavefunction was expanded as a Fourier series, also referred to as an expansion *in plane waves*. In this section we consider at what point the Fourier series can be truncated and still be an adequate approximation to the pseudo-wavefunction. Figure 2.13 shows the change in the calculated energy eigenvalues of the conduction and valence bands with increasing number of plane waves. The plane waves are added in groups of equal energy in order to ensure there is a closed set of reciprocal lattice vectors [49]. As can be seen from the figures, the energies are converged to within about 0.02eV per unit cell, at 263 plane waves per spin direction, and no significant benefit is observed for any higher values up to 496 plane waves. Although convergence of energies does not provide definitive evidence for convergence of the pseudo-wavefunction, it is generally accepted as a strong indicator.

It is worth noting that the computational time taken to diagonalise the Hamiltonian matrix varies with the cube of its size. For calculations that include spin the matrix size is doubled. It is clear that very significant savings in computational effort are achieved by choosing the lowest acceptable number of plane waves. For this reason 263 plane waves have been chosen for our calculations. The truncation of the Fourier series is often described in terms of the maximum kinetic energy of the plane waves used, the *kinetic energy cutoff*. For the lattice parameters of GaN, 263 plane waves corresponds to a kinetic energy cutoff of 183eV.

2.5 Alloys

An important benefit of including an alloy as part of a heterostructure is the ability to tune the properties of the alloy through the choice of alloy composition x. However, the use of alloys leads to the need for a theoretical description of material properties that is valid for a range of alloy compositions. In this work we are concerned with the ternary nitride alloys $In_xGa_{1-x}N$ and $Al_xGa_{1-x}N$.

To describe successfully the electronic structure of an alloy any theoretical technique must take account of the local strains present due to the lattice mismatch of the constituent materials. Two *ab-initio* approaches commonly employed are the use of cluster expansions

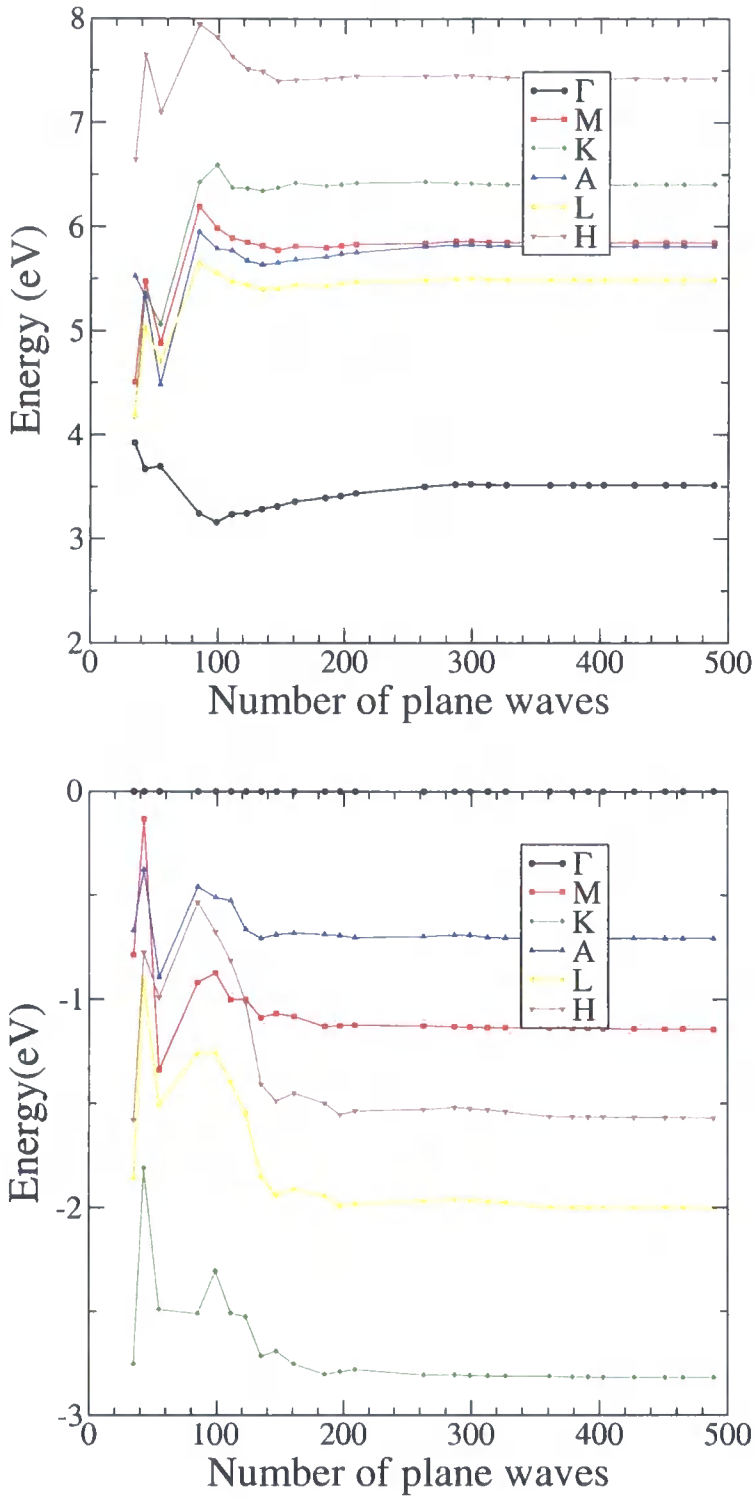

Figure 2.13: The convergence of conduction band (top) and valence band (bottom) energies at various points of high symmetry with increasing number of plane waves N. The top of the valence band is considered to be zero for all energies.

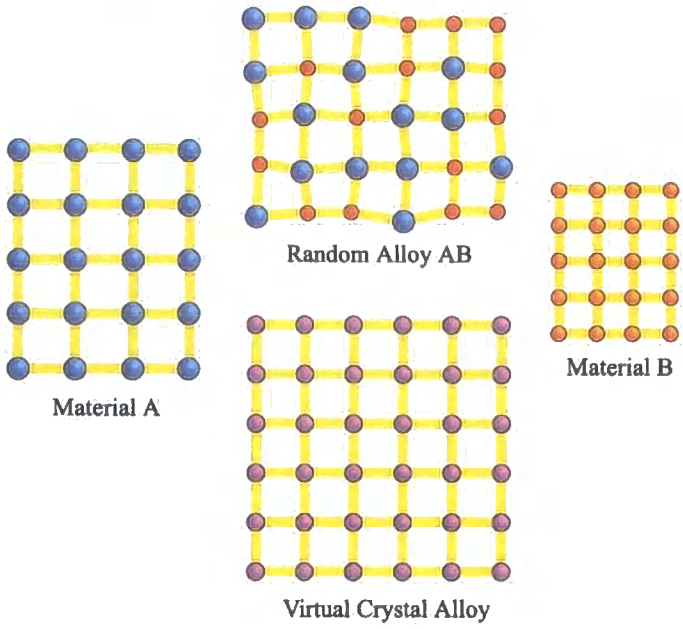

Figure 2.14: The virtual crystal concept. Schematic illustration of a random alloy with randomly positioned atomic species, and the corresponding virtual crystal with a single species representing the average of the constituents in the alloy. The atomic sites in the random alloy are clearly subject to local strain fields resulting from the different lattice constants of A and B.

[59] and supercells [60]. A cluster expansion involves the study of a set of ordered crystal structures, which are in turn used to infer the properties of a disordered alloy. The second approach involves the use of supercells with atomic species of the alloy randomly placed at the lattice sites and normally involves considerable computational effort as 1000s of atoms are required in a supercell.

One successful empirical approach involves the use of parameterised force fields and potentials with large supercells [61] to approximate the local strains, but this is still relatively computationally expensive. $\mathbf{k} \cdot \mathbf{p}$ parameters have been derived from EPM calculations and can provide a continuum model of the alloy [51]. However the virtual crystal approximation (VCA) within the framework of the pseudopotential approach is employed in this work.

2.5.1 Virtual crystal approximation

The virtual crystal approximation considers the alloy to be a uniform crystal composed of one atomic species for each lattice site that displays the characteristics of the alloy [47, 50] as illustrated in figure 2.14. The characteristics are modelled by choosing parameters

that are a concentration dependent function of those of the real atoms. For example the In and Ga atoms in the alloy $In_xGa_{1-x}N$ would be approximated by a single "virtual" atom. The In-N and the Ga-N bond lengths are assumed to be the same in the virtual crystal and therefore local strain fields are ignored. The virtual lattice constants $a(x)$ and $c(x)$ can be approximated by Vegard's Law [40] which approximates the lattice constants as the mean of the lattice constants of the binary compound, weighted by their relative compositions. For the alloys considered here

$$\begin{aligned} a_{AlGaN}(x) &= (3.190 - 0.080x)\text{Å} \\ a_{InGaN}(x) &= (3.190 + 0.354x)\text{Å} \\ a_{AlInN}(x) &= (3.544 - 0.434x)\text{Å} \\ c_{AlGaN}(x) &= (5.189 - 0.080x)\text{Å} \\ c_{InGaN}(x) &= (5.189 + 0.529x)\text{Å} \\ c_{AlInN}(x) &= (5.718 - 0.735x)\text{Å} \end{aligned} \tag{2.42}$$

A combination of Rutherford, HRXRD and elastic recoil detection analysis that the predictions of Vegard's law and measured lattice constants agree to better than 2% [62–65] for the nitride alloys. No consistent experimental data exists for the variation of u with alloy composition x so it is assumed to vary linearly with x. Note however that the crystal field splitting of the valence bands is not expected to vary linearly with x because of the nature of the strong dependence on u.

Chemical and electronic clustering

The assumption of a completely randomly disordered alloy is implicit in the adoption of the virtual crystal approximation. However, for $In_xGa_{1-x}N$ in particular, the clustering of In atoms has been observed [61,66,67]. The effect of this chemical clustering or phase separation is to introduce local regions of high indium concentration that may act like quantum dots and confine the carriers. As well as changing the electronic structure, it has been proposed that this effect could give rise to high efficiency of optical emission even in the presence of dislocations [7].

In addition to chemical clustering, Bellaiche *et al* [68] have used large supercell empir-

ical pseudopotential calculations to predict an "electronic clustering". This is in the form of In-localised hole wavefunctions for low In concentration alloys. The existence of localised states is thought to have a strong effect on the effective band gap of the alloy and its variation with alloy composition.

Clearly the VCA is a simplistic approximation to the complexities of a real alloy, but it has been successfully applied to several III-V alloys that do not contain nitrogen. Given the existence of both chemical and electronic clustering in the nitride alloys the VCA is used here with an understanding of its limitations.

2.5.2 Empirical pseudopotentials for alloys

The simplest approach to applying the empirical pseudopotential method to alloys within the VCA is to fit the pseudopotentials of a virtual crystal to experimental information on the alloy at that composition. However this approach relies on experimental information being available at all alloy compositions of interest, rather than providing a means to predict the properties of alloys.

In this work the pseudopotential for the virtual crystal is assumed to be the composition weighted average of the pseudopotentials of the alloy constituents and the symmetric and antisymmetric form factors are averaged using Vegard's Law. The symmetric and antisymmetric form factors for $In_xGa_{1-x}N$ are therefore given by

$$V_g^{alloy} = V_g^{InN} x + V_g^{GaN}(1-x) \tag{2.43}$$

where V_g^{In} and V_g^{Ga} relate to bulk InN and AlN, but at the g values relevant to the alloy and the new alloy volume.

2.6 Strain

Strain can arise in semiconductors in a number of ways, including growth on a lattice-mismatched substrate, applied stress, thermal expansion and the piezoelectric effect. In the case of heterostructures, strain due to lattice mismatch is often deliberately introduced. If one

material is grown on a crystal substrate with a different equilibrium lattice constant then the atoms of the growth layer try to match up neatly with the atoms of the substrate. Depending on the growth conditions and the thickness of the growth layer one of several outcomes is possible:

1. The strain causes the growth atoms to collect together into "islands" or other strained nanostructures. Island formation is used in the preparation of self assembled quantum dots and is the subject of much current research [69].

2. If the in-plane strain does not cause islanding, then up to a certain critical layer thickness the layer grows "pseudomorphically" with the same in-plane lattice constants as the substrate and is said to be a strained layer.

3. If the layer thickness is too large then the formation of dislocations is energetically favoured and further layer growth is relaxed towards the equilibrium lattice constant of the growth material. The layer thickness when this begins to occur is known as the critical layer thickness, denoted by h_c.

If a strained layer results from the growth then a relaxation of the lattice constant in the growth direction is observed to compensate for the in-plane strain. For an epitaxial layer with an in-plane lattice constant larger than that of the substrate, the resulting in-plane (biaxial) compression gives rise to an increase in the perpendicular lattice constant of the growth material. Conversely for an in-plane expansion (biaxial tensile strain) caused by a smaller lattice constant, a reduction in perpendicular lattice constant would be observed. This is illustrated schematically in figure 2.15.

2.6.1 Elastic Theory

The relationship between the stress applied to a crystal and the resultant strain is described by elastic theory and is important to an understanding of strained systems and strain related effects such as piezoelectricity. A brief account of the relevant parts of elastic theory is given below, but for a more detailed study, see for example [72].

When subjected to a stress a solid body changes its shape. Below the elastic limit this change is reversible and can be considered linear. The fourth rank elastic stiffness tensor c_{ijkl} relates the stress tensor σ_{ij} to the strain tensor ϵ_{kl}

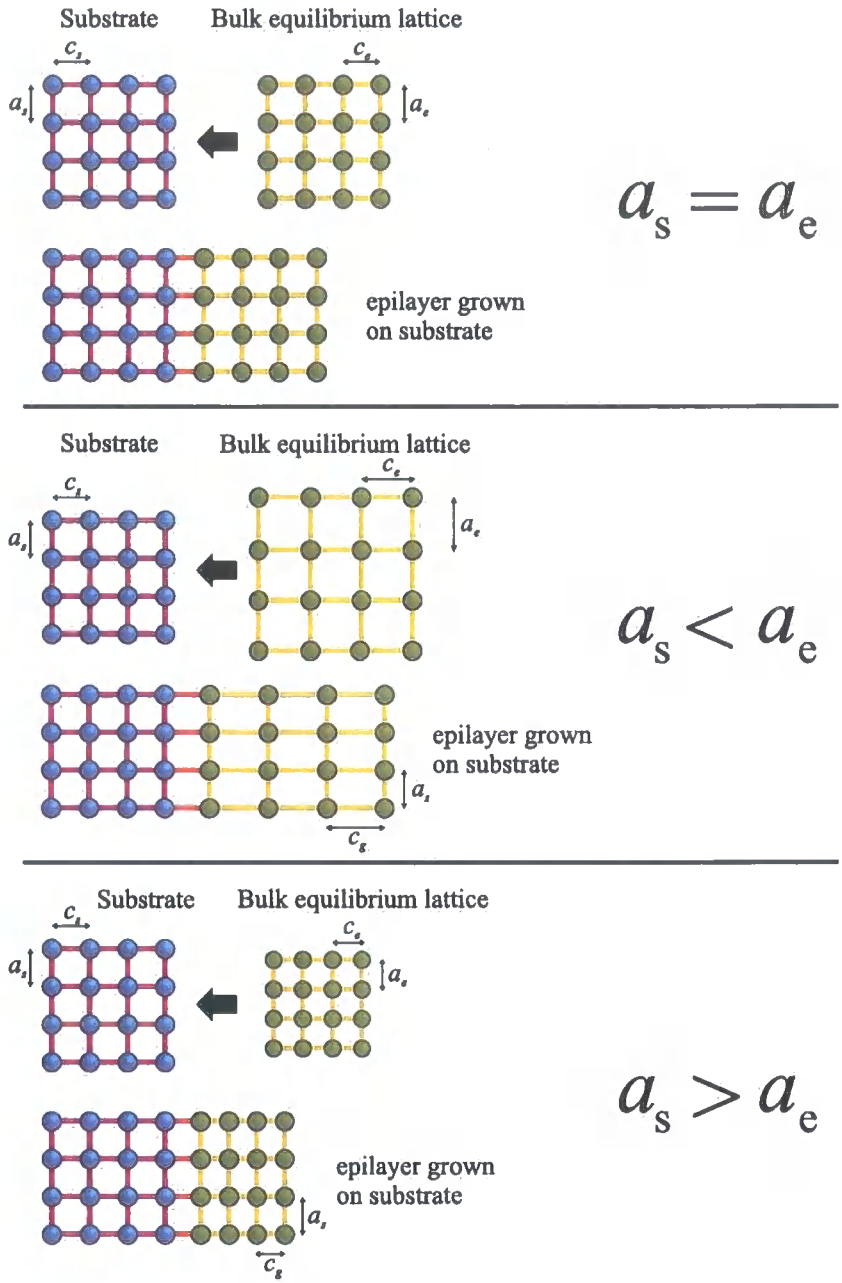

Figure 2.15: Schematic representation of the growth of an epilayer on a substrate and the resulting relaxation of lattice constant. a_s is the substrate in-plane lattice constant and a_e is the epilayer in-plane lattice constant. i) $a_s = a_e$ - growth of epilayer without strain. ii) $a_s < a_e$ - in-plane compression results in growth direction relaxation of epilayer with $c_g > c_e$. iii) $a_s > a_e$ - in-plane tension results in growth direction relaxation of epilayer with $c_g < c_e$.

$$\sigma_{ij} = \sum_{kl} c_{ijkl}\epsilon_{kl} \tag{2.44}$$

In the absence of body-torques the tensors for stress and strain are symmetric [72] and therefore can be represented by 6 independent components.

$$\begin{bmatrix} \sigma_{11} & \sigma_{21} & \sigma_{31} \\ \sigma_{12} & \sigma_{22} & \sigma_{32} \\ \sigma_{13} & \sigma_{23} & \sigma_{33} \end{bmatrix} \Longrightarrow \begin{bmatrix} \sigma_1 & \sigma_6 & \sigma_5 \\ \sigma_6 & \sigma_2 & \sigma_4 \\ \sigma_5 & \sigma_4 & \sigma_3 \end{bmatrix} \tag{2.45}$$

$$\begin{bmatrix} \epsilon_{11} & \epsilon_{21} & \epsilon_{31} \\ \epsilon_{12} & \epsilon_{22} & \epsilon_{32} \\ \epsilon_{13} & \epsilon_{23} & \epsilon_{33} \end{bmatrix} \Longrightarrow \begin{bmatrix} \epsilon_1 & \frac{1}{2}\epsilon_6 & \frac{1}{2}\epsilon_5 \\ \frac{1}{2}\epsilon_6 & \epsilon_2 & \frac{1}{2}\epsilon_4 \\ \frac{1}{2}\epsilon_5 & \frac{1}{2}\epsilon_4 & \epsilon_3 \end{bmatrix} \tag{2.46}$$

It follows that the number of independent components in c_{ijkl} drops from 81 to 36. It is often convenient to represent this simpler situation with a matrix notation where stress and strain are expressed as column matrices σ_i,ϵ_j with 6 components and c_{ijkl} is expressed as a square matrix c_{ij} of order 6.

$$\sigma_i = \sum_{j} c_{ij}\epsilon_j \tag{2.47}$$

In a crystal c_{ij} can be reduced further due to symmetry. For all crystal structures the matrix is found to be symmetric and in addition further reductions in number of independent components for crystal structures of higher symmetry are noted. For hexagonal crystal structures five independent components exist; c_{11},c_{33},c_{44},c_{12} and c_{13}. [73]

$$\mathbf{c}_{hexagonal} = \begin{bmatrix} c_{11} & c_{12} & c_{13} & 0 & 0 & 0 \\ c_{12} & c_{11} & c_{13} & 0 & 0 & 0 \\ c_{13} & c_{13} & c_{33} & 0 & 0 & 0 \\ 0 & 0 & 0 & c_{44} & 0 & 0 \\ 0 & 0 & 0 & 0 & c_{44} & 0 \\ 0 & 0 & 0 & 0 & 0 & \frac{1}{2}(c_{11} - c_{12}) \end{bmatrix} \tag{2.48}$$

The independent components of c_{ij} (called stiffness constants) are usually determined experimentally for each bulk material. The inverse relation between stress and strain is expressed in terms of the compliance constants s_{ij}

$$\epsilon_i = \sum_j s_{ij}\sigma_j \tag{2.49}$$

2.6.2 Uniaxial Stress

Uniaxial stress is an important experimental tool because it can be used to break crystal symmetry. It can also be used to define Poisson's ratio. Consider a uniaxial stress in the z-direction (growth direction), the only non-zero stress tensor element is then $\sigma_{33} = \sigma$

$$\epsilon_i = \begin{cases} s_{13}\sigma & i = 1, 2 \\ s_{33}\sigma & i = 3 \\ 0 & \text{otherwise} \end{cases} \tag{2.50}$$

Poisson's ratio ν is defined as minus the ratio of the strains perpendicular and parallel to the stress axis,

$$\nu = -\frac{\epsilon_2}{\epsilon_1} = -\frac{s_{13}}{s_{33}} \tag{2.51}$$

Poisson's ratio is a property of the material and for tetrahedral semiconductors it typically

has a value of about 1/3.

2.6.3 Biaxial Stress

In the case of planar heterostructures we are mainly interested in biaxial stress. The strains in both in-plane directions (i.e. parallel to the growth plane) are equal and given by

$$\epsilon_{\parallel} = \epsilon_1 = \epsilon_2 = \frac{a_s - a_e}{a_e} \tag{2.52}$$

which gives rise to a relaxation (strain) perpendicular to the growth plane

$$\epsilon_{\perp} = \epsilon_3 = \frac{c_g - c_e}{c_e} = -\frac{c_{13}}{c_{33}}(\epsilon_1 + \epsilon_2) \tag{2.53}$$

The strain is often written in terms of Poisson's ratio ν

$$\epsilon_{\parallel} = -\frac{2\nu}{1-\nu}\epsilon_{\perp} \tag{2.54}$$

For a value of $\nu = \frac{1}{3}$, equation (2.54) gives $\epsilon_{\parallel} \sim \epsilon_{\perp}$

Critical Layer Thickness

The heterostructures in this work are assumed to be continuous defect free crystals made up of strained layers that normally only exist below the critical layer thickness h_c (sometimes referred to as the critical film thickness). It is therefore important to have an idea of the size of h_c for relevant materials. A brief discussion is presented here, but for a more complete review, see the work of Jain [7,74,75].

The critical layer thickness is a function of the in-plane strain and the material properties. There exist two main approaches to modelling this behaviour; the energy minimisation approach and the force balance approach [74]. The energy minimisation approach was first proposed by Frank and Van der Merwe [76] in 1949 and, as is suggested by the name, relies on the minimisation of the system's energy [77]. The force balance approach was developed

by Matthews and Blakeslee in 1974 [78] and is based on thermodynamic assumptions and represents an elasticity theory approach [79]. The two approaches can be shown to be equivalent if the same values of dislocation energies are used [74,75]. From the force balance approach, the critical layer thickness is given as [40]

$$h_c = \frac{1-\nu/4}{4\pi(1+\nu)} b\epsilon_{\|}^{-1}\left(\ln\left(\frac{\rho_c h_c}{q}\right)\right) \tag{2.55}$$

Here ν is Poisson's ratio, b is the length of the dislocation Burgers vector and q is the core cutoff parameter, assumed to be equal to b. ρ_c is the core energy parameter, which is usually fitted to experiment and typically has values between 1 and 4 [79]. Equation 2.55 is clearly transcendental and is normally solved numerically, but recently it has been shown that its solution can be written analytically [79]. When compared to experimental values, equation 2.55 tends to underestimate the value of h_c, primarily because real growing conditions are less favourable to the propagation of dislocations.

Experimental measurements of h_c vary considerably. For AlN grown on GaN, values of h_c measured by RHEED vary from 4 Å to 30 Å [75,80,81]. For InN on GaN, h_c is estimated to be 6 Å [81]. Larger values of h_c occur for the alloys when the strain is significantly reduced. For example Akasaki and Amano looked at the critical layer thickness of $In_xGa_{1-x}N$ and $Al_xGa_{1-x}N$ grown on GaN, and observed h_c of 300 nm - 700 nm [82–84]. No significant variation with indium alloy composition was noted, over the range of low indium alloy composition ($x = 0 - 0.2$) studied, however h_c is usually thought to be a very strong function of alloy composition [5].

2.6.4 Strain in pseudopotential theory

Strain is included in the empirical pseudopotential method through i) alterations to the pseudopotential formfactors V_g, and ii) the change in the lattice constants and hence the reciprocal lattice vectors **g**. The concept of transferable pseudopotentials, requires that the form of the atomic pseudopotentials should not change under the influence of strain. The values of the form factors V_g will therefore only be different in that **g** will have changed. The advantages of a functional form for the pseudopotential are fully appreciated at this point,

as the new strained form factors are immediately available from equation (2.37). The curves for the functional form of the pseudopotentials are continuous in reciprocal space, and in principle any amount of strain can be modelled in this way.

An alternative approach is to consider the form factors to vary linearly in the region of each reciprocal lattice vector [85]. The gradients of the form factor curves can be fitted in a similar way to the form factors themselves. This approach can accurately reproduce the changes in bandstructure for very small ($\sim 1\%$) values of strain. The change in energy with strain for a particular band is known as the deformation potential and the strength of this approach is the ability to fit the form factor gradients to these deformation potentials. However, the restriction to small values of strain is not appropriate for the modelling of nitride quantum wells and therefore we adopt the first approach.

2.6.5 Effect on bandstructures

Unlike a zincblende or diamond structure, the symmetry of a wurtzite crystal is not lowered by the introduction of a lattice relaxed biaxial strain, in the hexagonal plane. As a consequence there is no splitting of degenerate bands as a result of the biaxial strain. However, an important consequence of strain is the effect on the principal band gap. Under compressive strain the semiconductor band gap is generally observed to reduce in size. Biaxially strained materials also tend to exhibit a reduced band gap. Other features of a bandstructure may also be effected, with the shape and even the ordering of the bands being altered.

2.7 Nitride Alloy Bandstructures

This work is concerned with nitride alloys grown on a GaN substrate for use in quantum wells. The alloys are biaxially strained and therefore it is as important to consider the effect of strain on the bandstructure as it is the effect of the alloying. Of primary importance to the modelling of a quantum well is the band gap and the effective mass. Figure 2.16 displays the variation of conduction band and valence band energies changing with alloy composition for both $Al_xGa_{1-x}N$ and $In_xGa_{1-x}N$. The band gap is seen to vary from more than 6eV for strained AlN right down to 0.5eV for strained InN. The dashed line indicates the variation for a strain free alloy and provides some indication of the importance of strain.

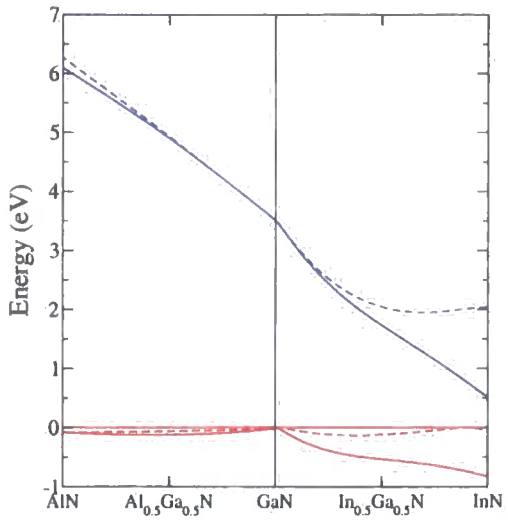

Figure 2.16: The variation of band energy with different alloy concentrations of Al (left) and In (right) for both unstrained (dashed line) and biaxially strained to GaN (solid line). The blue line is the conduction band minima and the red lines are the valence bands. The zero of energy is taken as the valence band maxima.

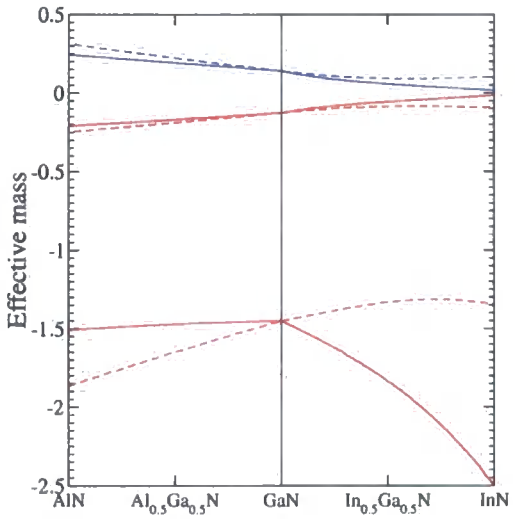

Figure 2.17: The variation of the conduction and valence band effective masses with alloy composition of Al (left) and In (right) for both unstrained (dashed line) and biaxially strained to GaN (solid line).

The variation of effective mass with alloy composition is considered in figure 2.17. The effective mass will be used in chapter 4 for simple calculations of quantum well states based on a single parabolic band model. Note that $In_xGa_{1-x}N$ exhibits a greater change in effective mass with alloy composition than $Al_xGa_{1-x}N$.

Figures 2.18i)-2.18iii) describe the valence bandstructure of GaN and $In_xGa_{1-x}N$ for $x = 0.05$ and $x = 0.1$. There is a a flip in the normal ordering of the valence band at an alloy composition $x = 0.02 - 0.03$. This change in ordering is not observed for $Al_xGa_{1-x}N$. Figures 2.19i)-2.19iii) describe the valence bandstructure of GaN and $Al_xGa_{1-x}N$ for $x = 0.2$ and $x = 0.4$.

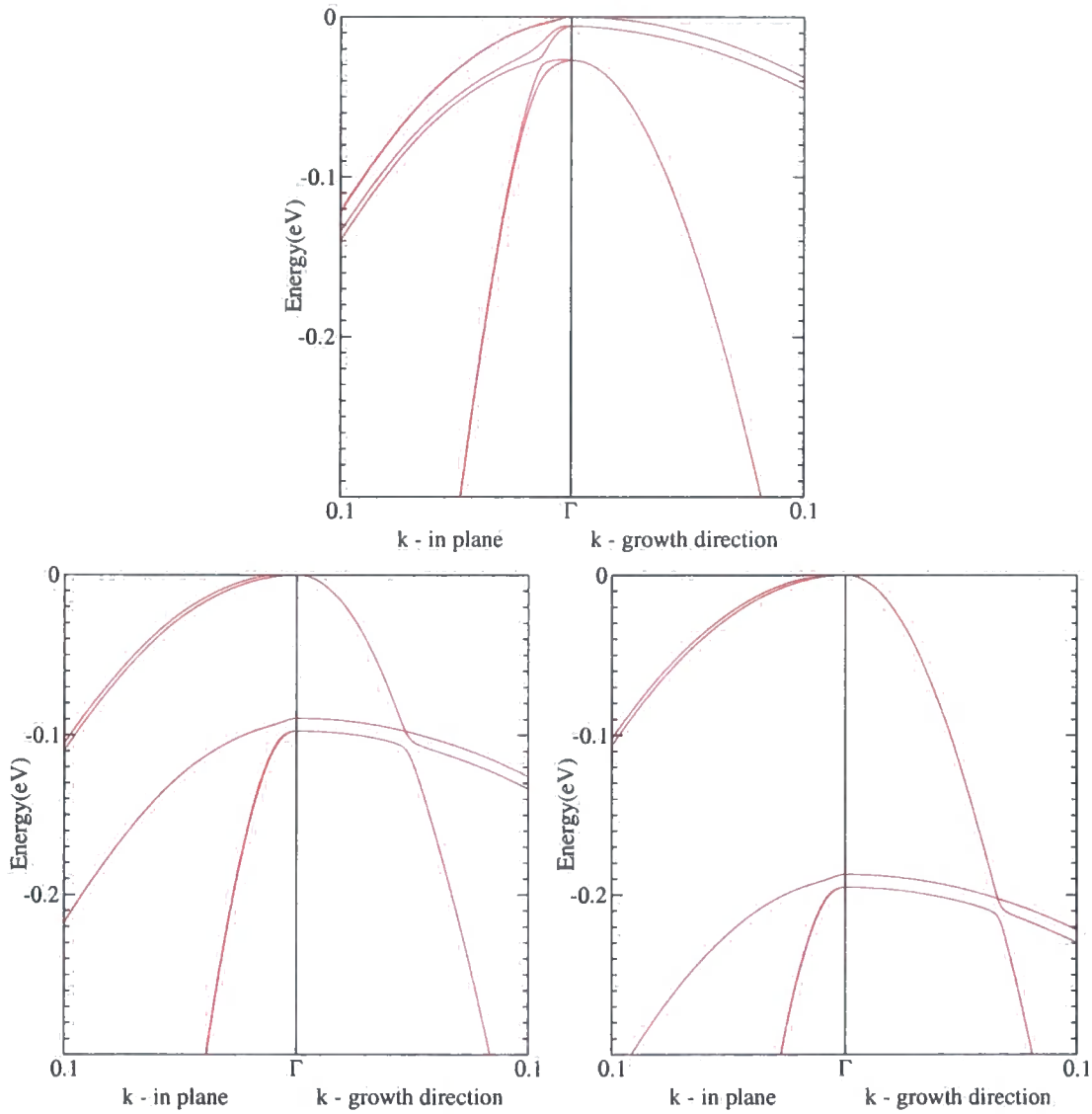

Figure 2.18: Valence bandstructure near the Γ point for i) GaN, ii) $In_{0.05}Ga_{0.95}N$ and iii) $In_{0.1}Ga_{0.9}N$

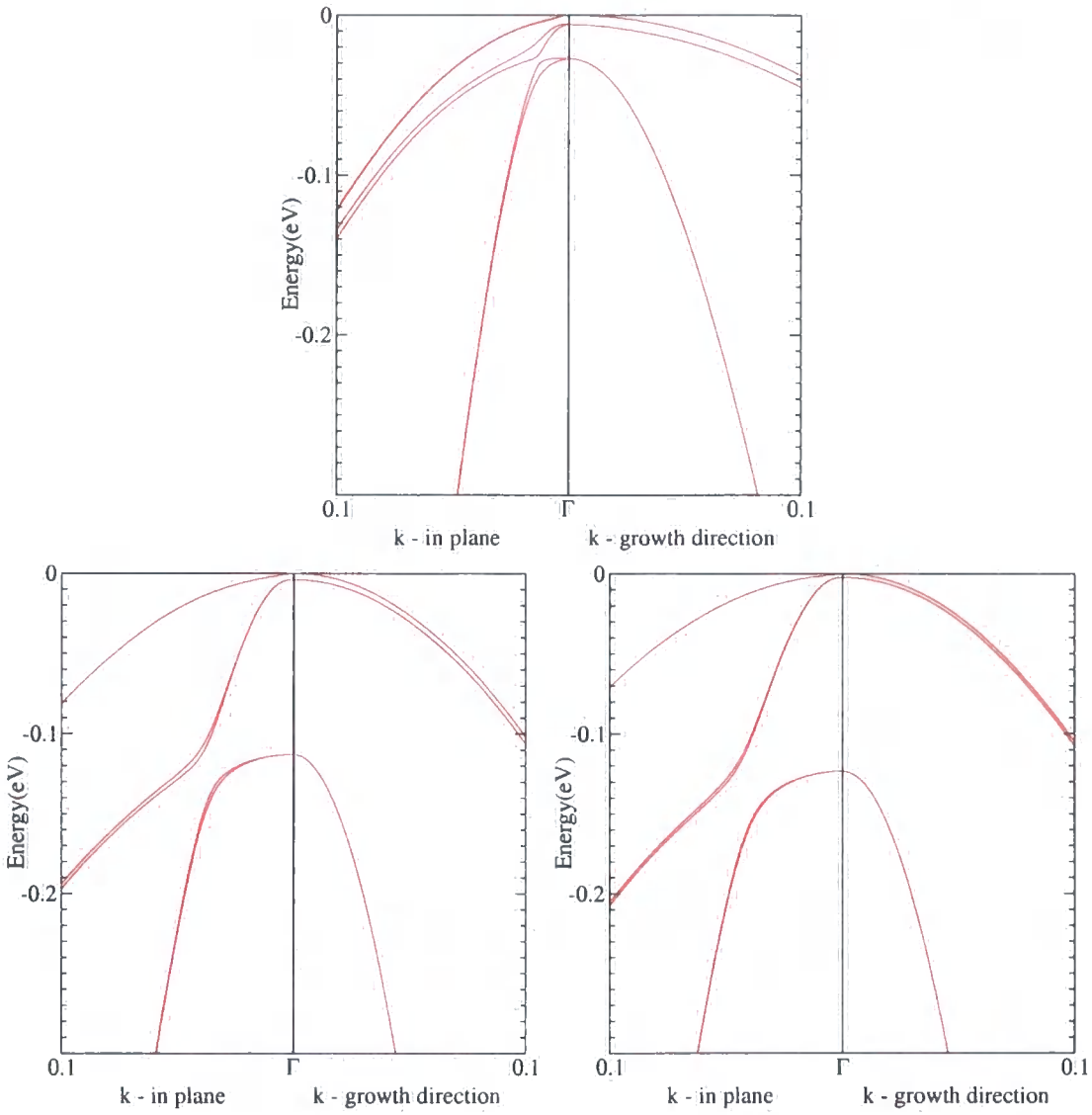

Figure 2.19: Valence bandstructure near the Γ point for i) GaN, ii) $Al_{0.2}Ga_{0.8}N$ and iii) $Al_{0.4}Ga_{0.6}N$

Chapter 3

Complex Bandstructure

3.1 Introduction

The complex bandstructure is a generalisation of the bulk bandstructure that is discussed in chapter 2. The empirical pseudopotential method acts as a starting point for the generation of complex bandstructures, which can be used in the study of heterostructure bound states. In this chapter the complex bandstructures of the nitrides in the wurtzite crystal structure are generated using a pseudopotential approach.

3.2 Complex wavevector

The bulk bandstructure is usually presented as the set of allowed real energies for all real wavevectors in the whole first Brillouin zone. *Complex* bandstructure is the set of real, imaginary and complex wavevectors (within the first Brillouin zone) for *all* real energies. A complex wavevector is defined as being within the first Brillouin zone if its real component $\mathbf{k}_r$ is in the zone. Any wavevector with a real component outside the first Brillouin zone is a repeated solution within Bloch's theorem. Bloch states with complex wavevectors are evanescent and are not valid solutions for bulk semiconductors because they are not finite everywhere. However, evanescent states can exist in a region of space that is limited in some way so that they do not diverge. For example, evanescent states are possible in a region of finite spatial extent or in an infinite half-space, states that decay away from the surface of the half-space are allowed. Therefore in the case of a planar heterostructure, the

wavevector is only allowed to have a complex component in the direction perpendicular to the interfaces, i.e. the growth direction. In the plane parallel to the surface the wavevector must be real. The components of wavevector parallel and perpendicular must therefore be considered separately. The growth direction is described as *perpendicular* ($\perp$) because it is perpendicular to the plane of the interface and will always be defined as the z axis in this work. Vectors parallel to the interface are referred to as being in the *in-plane* or *parallel* ($\|$) directions and will always be in the xy plane. In general we can write the wavevector $\mathbf{k}_{tot}$ as

$$\mathbf{k}_{tot} = \mathbf{k}_{\|} + k \tag{3.1}$$

where

$$\begin{aligned} k &\in \mathbb{C} \\ \mathbf{k}_{\|} &\in \mathbb{R} \\ E_{\mathbf{k}_{tot}} &\in \mathbb{R} \end{aligned} \tag{3.2}$$

3.3 Bandstructure with imaginary wavevectors

The empirical pseudopotential method has been shown to provide an effective approach to calculations of bulk bandstructure in semiconductors, and it provides a good basis for the calculation of complex bandstructures. However, it is worth noting that complex bandstructures can be generated from other bandstructure techniques such as the tight binding method [86], although the pseudopotential approach, with a plane wave basis set, is applied in this work. The most rudimentary approach is to calculate the energy eigenvalues and eigenvectors from the normal pseudopotential Hamiltonian for complex values of k. This approach will in general yield *complex* energy eigenvalues of which any real eigenvalues can be considered to be associated with valid solutions and used to form part of the complex bandstructure. For example, for GaN the energy solutions for a range of imaginary wavevectors can quickly be computed and the results are shown in figure 3.1.

A significant feature is a branch of the bandstructure spanning the band gap corresponding to evanescent states. This bandstructure for imaginary k is only a subset of the

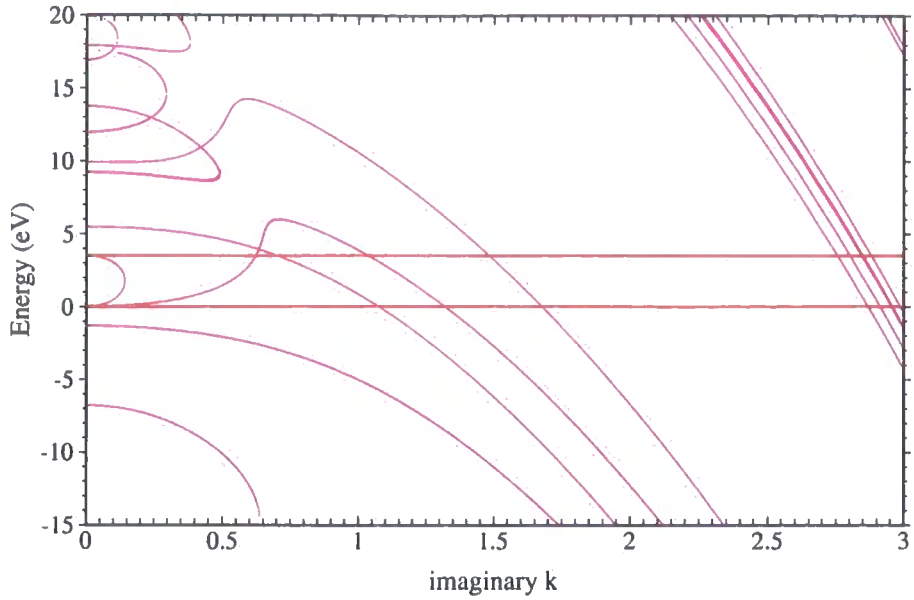

Figure 3.1: Bandstructure for GaN with imaginary wavevector. The horizontal red lines indicate the band gap. k is in units of $2\pi/c$

bandstructure for complex k. To generate the complete complex bandstructure, a search over a range of complex k would be required which would be computationally very inefficient.

3.4 Eigenvalue method

Ideally a complex bandstructure calculation would provide a set of all the possible wavevectors (real, imaginary and complex) for any given real energy. This objective can be achieved by rearranging the matrix elements of the Schrödinger equation (2.26) to provide an eigenvalue problem with k as the eigenvalue [86–89]. The Schrödinger equation is written as a quadratic function of k, with terms independent of k and those dependent on k and k^2.

$$(\mathbf{H}^0 + k\mathbf{H}^1 + k^2\mathbf{I})\phi = 0 \tag{3.3}$$

where the elements of $\mathbf{H}^0$ and $\mathbf{H}^1$ are from (2.26-2.27) and (2.30-2.33) are given by

$$
\begin{aligned}
H^0_{\mathbf{g},\mathbf{g}',s,s'} &= \left[(\mathbf{k}_{||}+\mathbf{g}_{||})^2 + g_z^2 - E\right]\delta_{\mathbf{g},\mathbf{g}'}\delta_{s,s'} \\
&+ V_{|\mathbf{g}-\mathbf{g}'|}\delta_{s,s'} \\
&+ \text{terms from } H^{soc} \text{ that are independent of } k \qquad (3.4) \\
H^1_{\mathbf{g},\mathbf{g}',s,s'} &= 2g_z\delta_{\mathbf{g},\mathbf{g}'}\delta_{s,s'} \\
&+ \text{terms from } H^{soc} \text{ that are linear in } k
\end{aligned}
$$

where g_z is the z component of $\mathbf{g}$, and s, s' label the elements of the spin matrix. The inclusion of the trivial identity, $0\phi + k\phi = k\phi$, to equation (3.3) gives

$$
\begin{bmatrix} 0 & \mathbf{I} \\ -\mathbf{H}^0 & -\mathbf{H}^1 \end{bmatrix} \begin{bmatrix} \phi \\ k\phi \end{bmatrix} = k \begin{bmatrix} \phi \\ k\phi \end{bmatrix} \qquad (3.5)
$$

The solution of equation (3.5) yields complex eigenvalues k and associated eigenvectors for a given energy E and in-plane wavevector $\mathbf{k}_{||}$. In this way the complete complex bandstructure can be generated by sweeping through E and $\mathbf{k}_{||}$. However, note that the matrix is now twice the dimension it was for the standard bandstructure calculation of equation (2.26), with an associated increase in computational cost.

3.4.1 Calculation of complex bandstructure

The complete complex bandstructure would contain an infinite number of wavevectors, the majority of them with increasingly large imaginary components. In practice since a finite basis set is used only a finite number of wavevectors are computed. For a given E and $\mathbf{k}_{||}$ there are $2N$ solutions to the eigenvalue problem (3.5) where N is the number of reciprocal lattice vectors used in the plane wave basis. Many of the k values represent equivalent solutions, separated by a reciprocal lattice vector. The number of independent solutions is given by $4N_{\mathbf{g}_{||}}$, where $N_{\mathbf{g}_{||}}$ is the number of distinct projections of the N reciprocal lattice vectors $\mathbf{g}$ onto the growth plane [88]. The $4N_{\mathbf{g}_{||}}$ unique solutions must therefore be identified, and the out of zone or repeated solutions discarded, before the complex bandstructure can be plotted. Solutions that are separated by a reciprocal lattice vector can be easily identified

as being out of the first Brillouin zone. Solutions exactly on the zone edge are related to a solution on the opposite side of the zone by the g-vector (0001) and must also be accounted for.

3.5 GaN, InN, AlN

The complex bandstructures of GaN, InN and AlN for zero in-plane wavevector are presented in figures 3.2-3.4. The plots show the real bandstructure (in the growth direction) between Γ and A, as well as the states for imaginary and complex k. The limited extent of the k-axis means that not all the solutions with imaginary k are shown. Notable features are the imaginary k which spans the principal band gap and, in the case of InN, a link with the third conduction band. For GaN and AlN this link is still present, but is more complicated as the part of the link involves complex k rather than purely imaginary solutions. Lines of complex k are only found between a maximum and a minimum away from the origin. The complex solutions in this valence-third conduction band link, join a maximum and minimum at imaginary values of wavevector. Another example that is seen in all three materials is the complex solutions that originate at the maximum in the first and second conduction bands.

An imaginary or complex wavevector is connected to any extremum in the bandstructure and this ensures that the number of solutions at any given energy remains constant. This "rule" was proposed by Heine [90] and implies that the energy bands never terminate, but are continuous in the complex k-space. All the complex bandstructures considered in this work behaved in that manner. For example, consider a maximum on the real axis that is connected to bands in the complex plane. Lines with an imaginary and real component represent four different k corresponding to $\pm k_r$ and $\pm k_i$. For a given energy below the maxima there are *two* lines of $\pm k_r$ (i.e. 4 k-states) that come together to form a maxima. The number of solutions for the complex branch is conserved.

The conservation of the number of solutions provides a useful checking mechanism when attempting to identify unique and repeated solutions to equation (3.5). A further check on the consistency of the computed bandstructure can be made by comparing the numerical output for a given energy with the energies calculated from the standard pseudopotential with a general complex k.

GaN

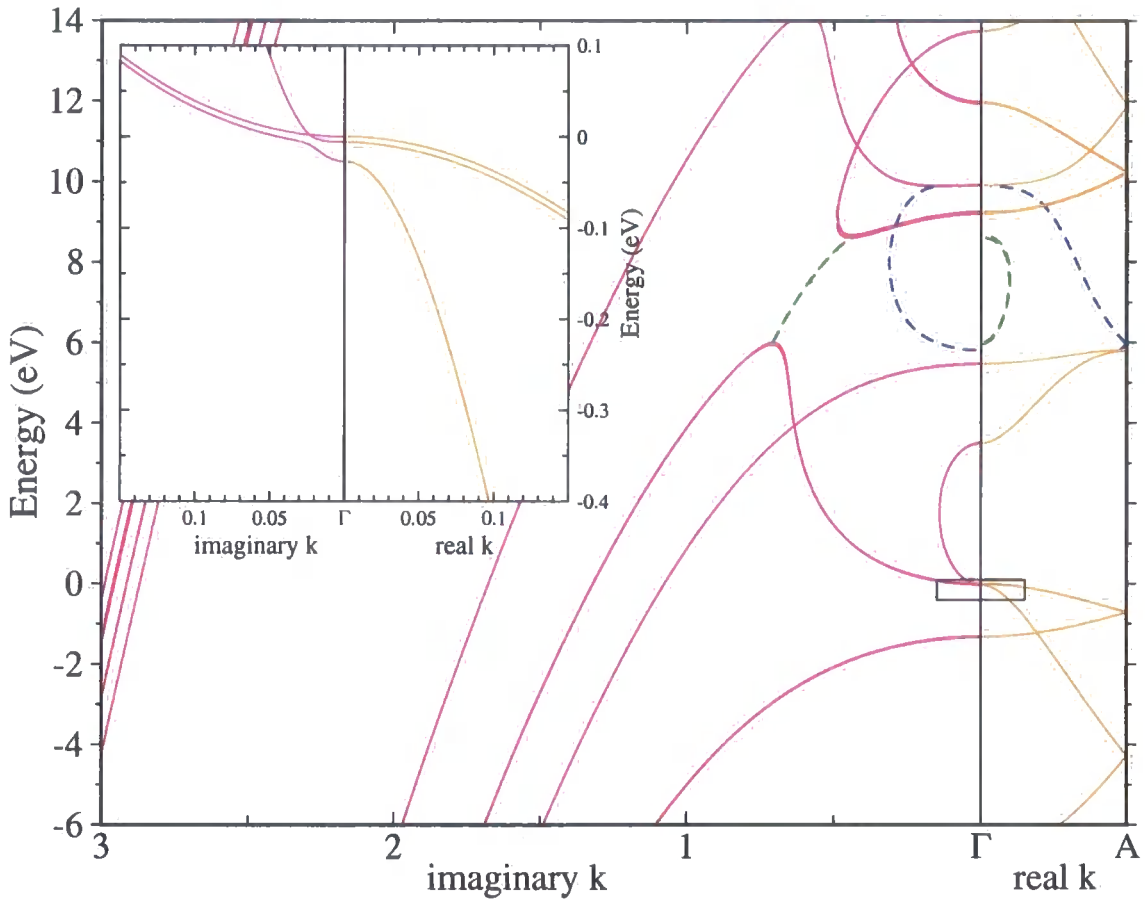

Figure 3.2: Complex Bandstructure for GaN. The solid pink lines to the left of Γ represent purely imaginary solutions. The solid orange lines to the right are the lines of real bandstructure between Γ and A. Complex solutions have a real and imaginary component of k, which are represented by a pair of dashed lines. The colours of the complex solutions identify which imaginary component matches up with which real component of the complex k. The inset shows a magnified view of the region around the Γ point and is indicated on the main graph by a black rectangle. k is in units of $2\pi/c$. In-plane wavevector of zero.

InN

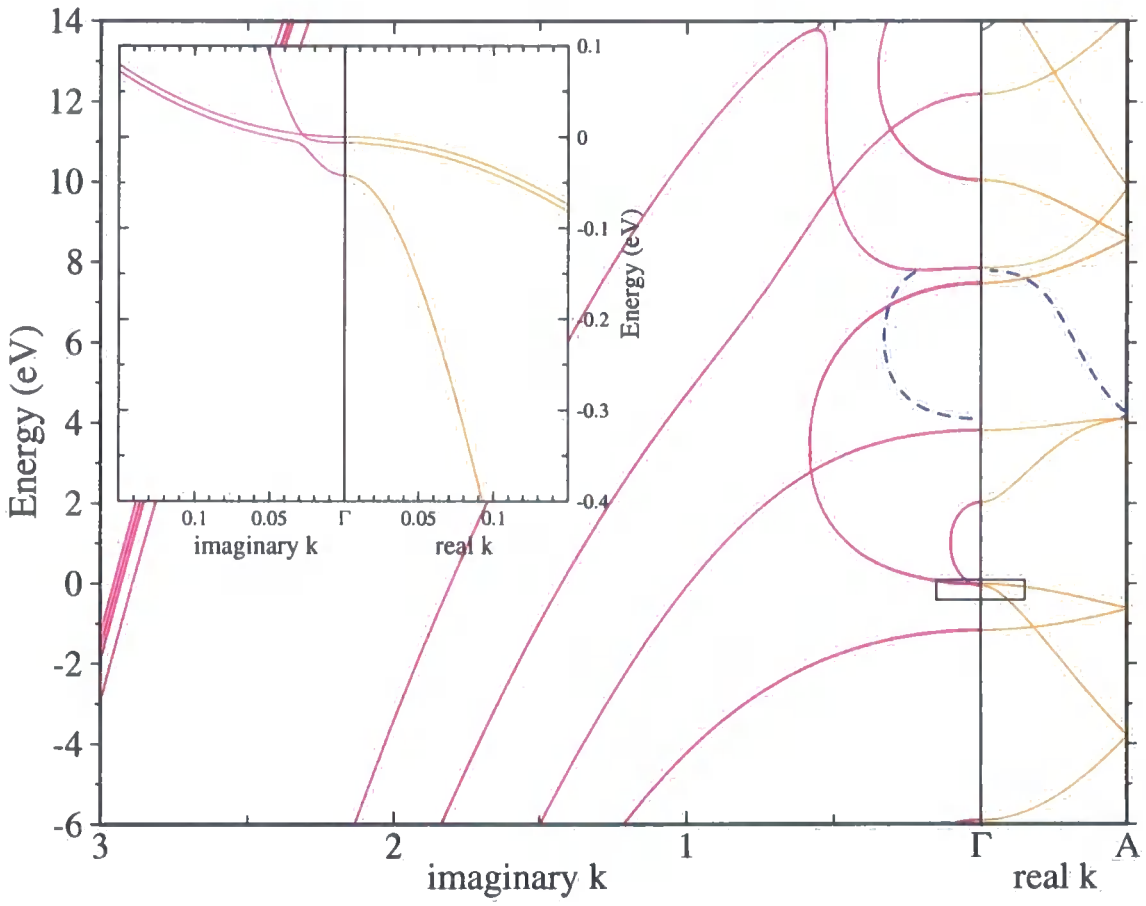

Figure 3.3: Complex Bandstructure for InN with an in-plane wavevector of zero. See figure 3.2 for details.

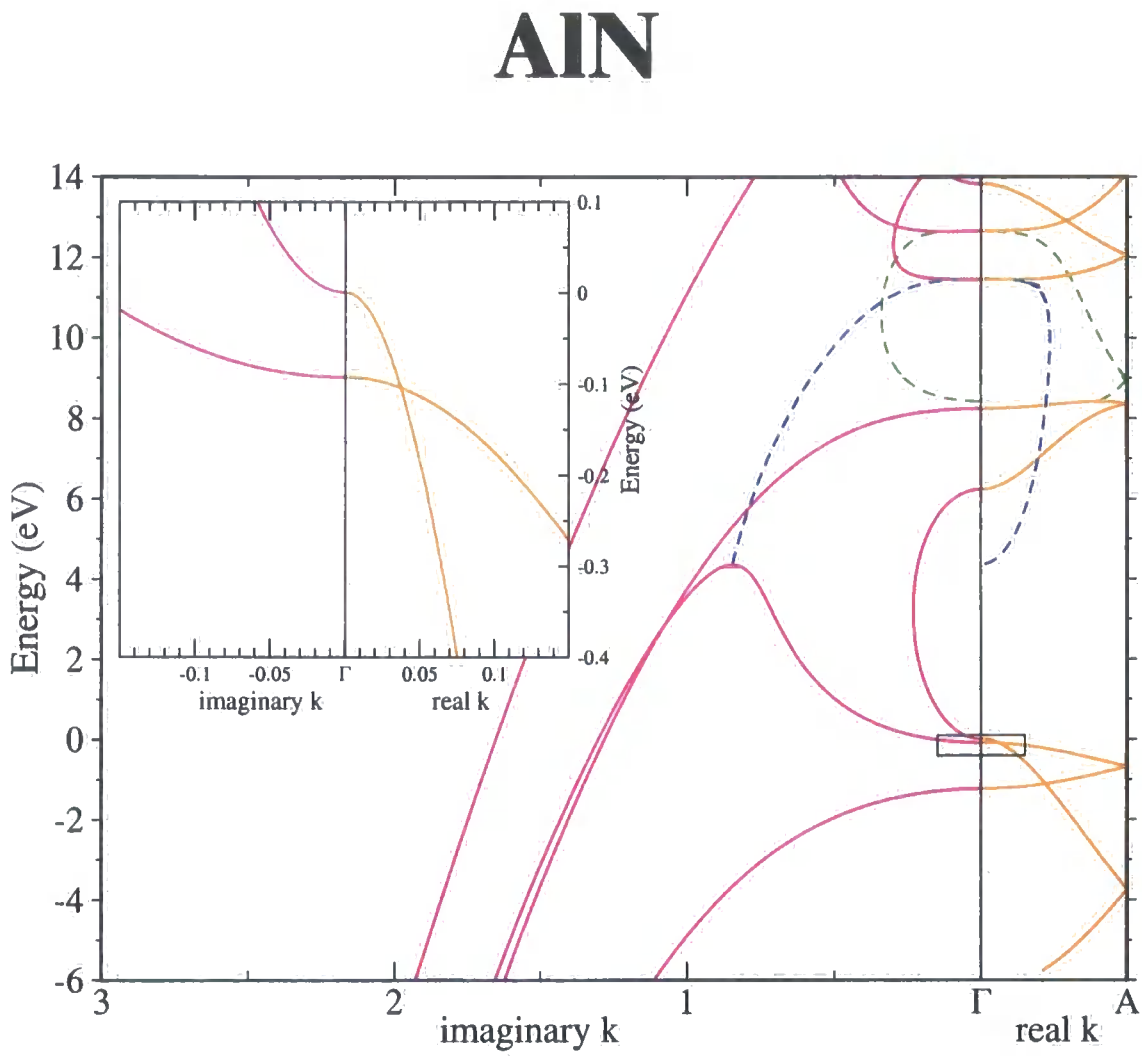

Figure 3.4: Complex Bandstructure for AlN with an in-plane wavevector of zero. See figure 3.2 for details.

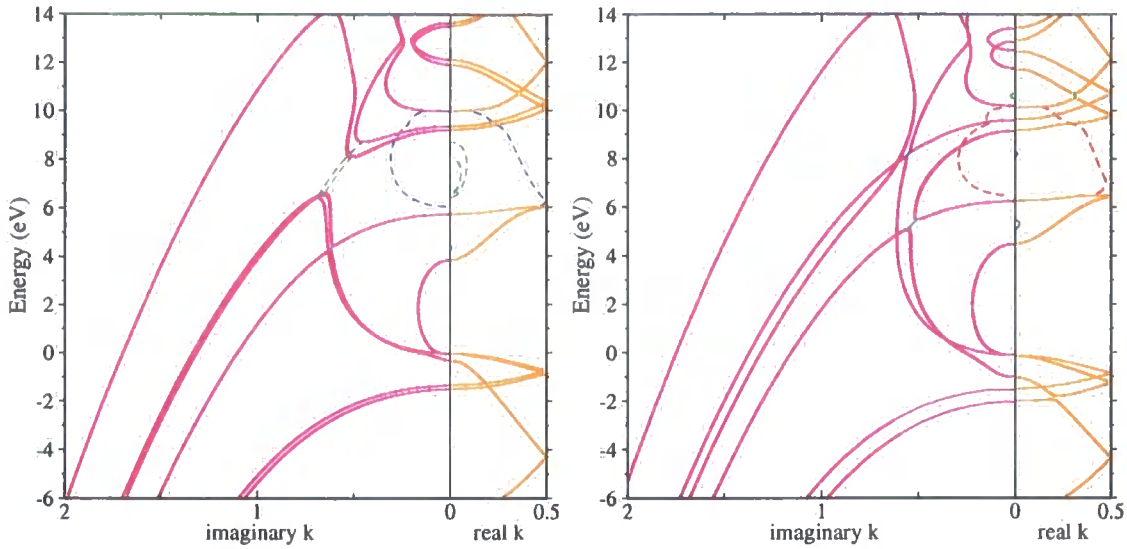

Figure 3.5: In-plane Complex Bandstructure for GaN with i) $k_{||} = (0.05, 0)$ and ii) $k_{||} = (0.1, 0)$

To our knowledge, calculations of complex bandstructure of wurtzite crystals have not been reported previously and no published bandstructures are available to confirm the topological features we have observed. A comparison of the zincblende and wurtzite crystal structures suggests that the bandstructure along the (111) direction in zincblende should have similarities to that along the c-axis in wurtzite. Zincblende complex bandstructures have been studied extensively, although the (111) direction has received little attention. However, Chang [91] used a 10-band tight binding model to produce the complex bandstructures for 14 zincblende materials, including consideration of the (111) direction. Chang's zincblende (111) complex bandstructures share many features with those presented here, including the complex loops between maxima and minima on the imaginary axis.

3.6 In-plane Complex Bandstructure

The complex bandstructure calculations can be performed for different values of in-plane wavevector (see figures 3.5 and 3.6). This is important in the consideration of heterostructures, because for the bound states of a quantum well it is the in-plane bandstructure that produces the subbands. The introduction of a non-zero in-plane wavevector moves the wavevector off a point of high symmetry and splits the degeneracy of some of the complex bandstructure. The "band gap" at a particular in-plane wavevector, increases with increasing

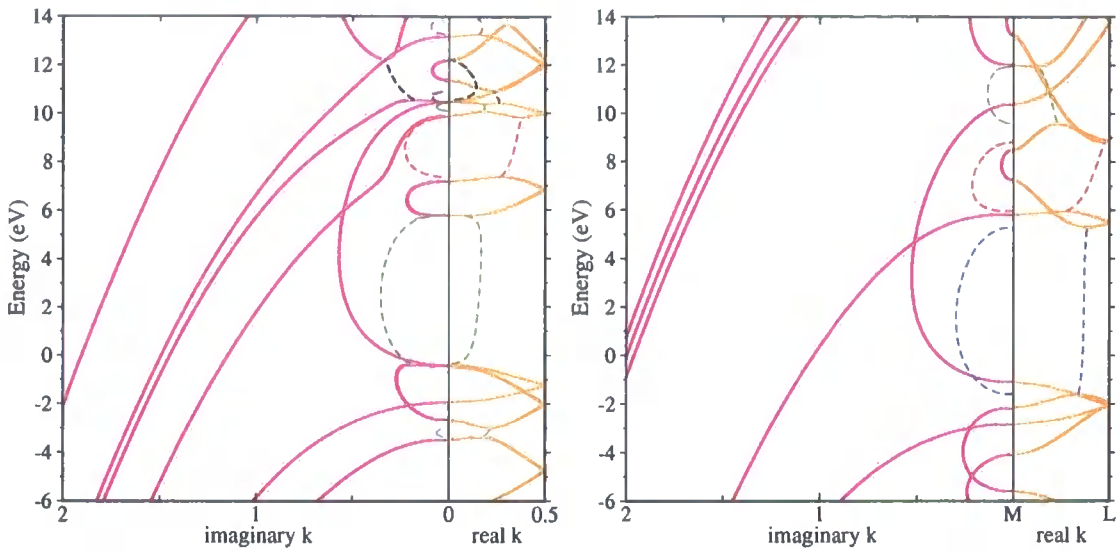

Figure 3.6: In-plane Complex Bandstructure for GaN with i) $k_{||} = (0.2, 0)$ and ii) $k_{||} = (0.5, 0)$ (i.e. the M-point)

in-plane wavevector (figures 3.5-3.6), and is "indirect" at the zone edge $k_{||} = (0.5, 0)$ (figures 3.6i and 3.6ii). The "indirect band gap" gives rise to a complex, rather than imaginary loop over the gap. With more bands due to the splitting of some of the degeneracy, the complex bandstructure is increasingly complicated and many more examples of maxima and minima and their corresponding branches into the complex plane are seen.

3.7 Convergence

It was reported in chapter 2 that the convergence for the bulk bandstructure was better than 0.02eV. However, there is no guarantee that the complex bandstructure is converged to the same degree. The convergence for the bulk bandstructure was tested by considering the changes in the band energies with number of plane waves. A corresponding test for the complex bandstructure is to plot the energy of a significant feature of the complex bandstructure against the number of plane waves. The energy difference between the maximum and minimum along the imaginary axis of the GaN complex bandstructure seems an appropriate choice in that it is a feature that is not part of the real bandstructure, for which the convergence has already been tested. Figure 3.7 shows the convergence in the complex bandstructure to be slightly slower than for the real bandstructure, but broadly in agreement. The energy difference measured was seen to be converged to better than 0.05eV at 263 plane

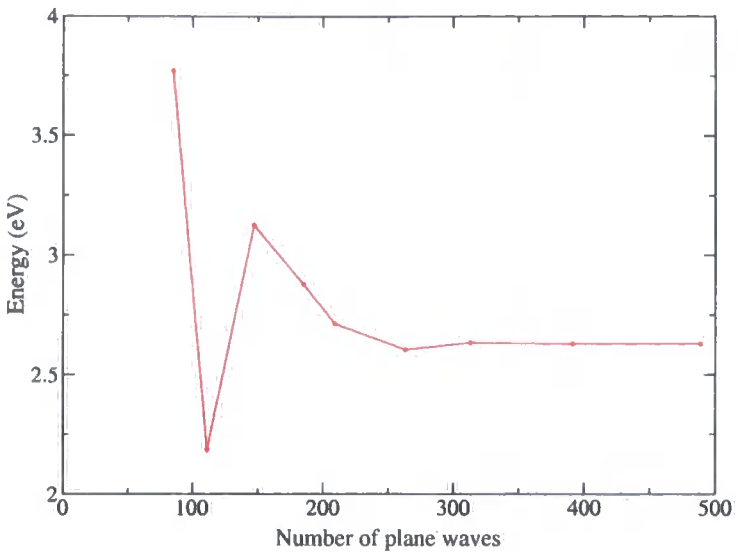

Figure 3.7: Convergence of complex bandstructure vs N for GaN

waves.

3.8 Alloy complex bandstructure

The method of generation of the complex bandstructures of the alloys only requires the input of the calculated pseudopotential form factors from the functional forms, discussed in chapter 2. As with the bulk bandstructure, the observed alloy bandstructures gradually change from being that of GaN to that of biaxially strained AlN or InN with the increase of In or Al composition. Shown in figure 3.8 is the complex bandstructure of $In_{0.15}Ga_{0.85}N$, grown on GaN. This should be compared to that of GaN (figure 3.2) and unstrained InN (figure 3.3) while remembering that the alloy is under biaxial strain. The relaxed biaxial strain has had the effect of changing the ordering of the top valence bands and the associated loops for imaginary wavevector. The inset of figure 3.8 provides an interesting comparison with InN (figure 3.3) because the same anti-crossing behaviour is observed between the crystal hole and light hole bands, when the anti-crossing occurs at both real wavevectors and imaginary wavevectors.

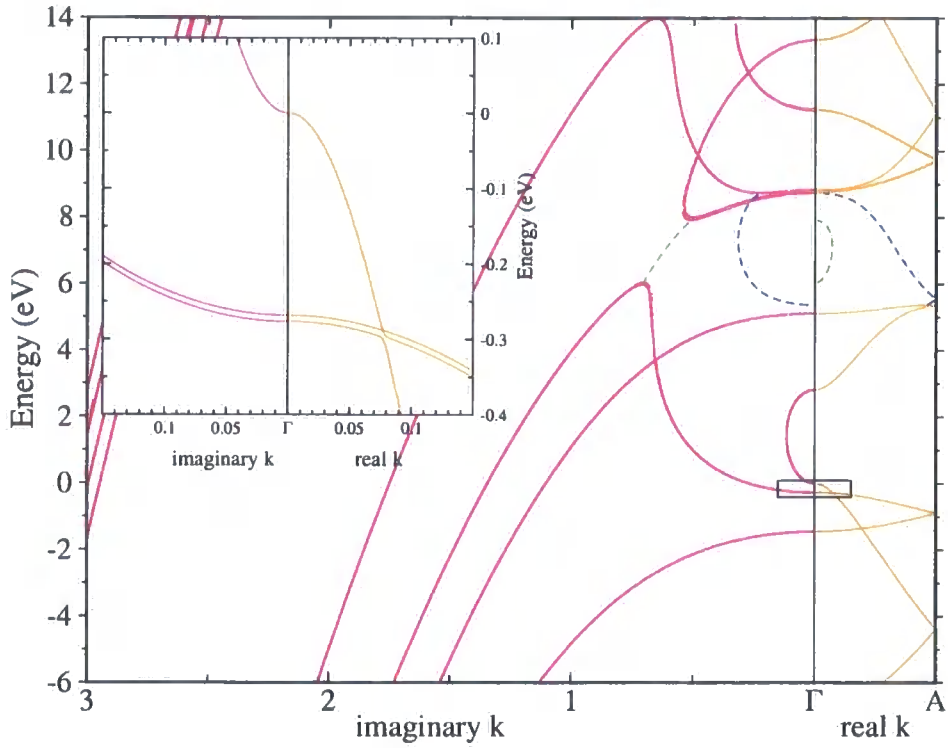

Figure 3.8: Complex Bandstructure for $In_{0.15}Ga_{0.85}N$

Chapter 4

Complex bandstructure method applied to heterostructures

4.1 Introduction

A semiconductor heterostructure can be defined as a structure comprising two or more different semiconducting materials. For the purposes of this work it is assumed that there is an abrupt change of chemical composition at the interface. A heterojunction is the simplest heterostructure, and consists of a single planar interface between two different materials. The introduction of more than one interface allows the construction of more complicated heterostructures and makes possible the confinement of any charge carriers. The confinement can be in one, two or three directions, resulting in quantum wells, quantum wires or quantum dots. In this work we are concerned with quantum wells constructed from two or more parallel interfaces. Quantum wells like this are usually grown using molecular beam epitaxy (MBE) or metal-organic chemical vapour deposition (MOCVD), and depending on the materials involved, some of the layers may be under the influence of a biaxial strain which will have an effect on their properties.

4.2 Band offsets

The bandstructures of two materials forming a heterojunction will not match at the interface. Around the principal energy gap, this leads to discontinuities in both the valence and

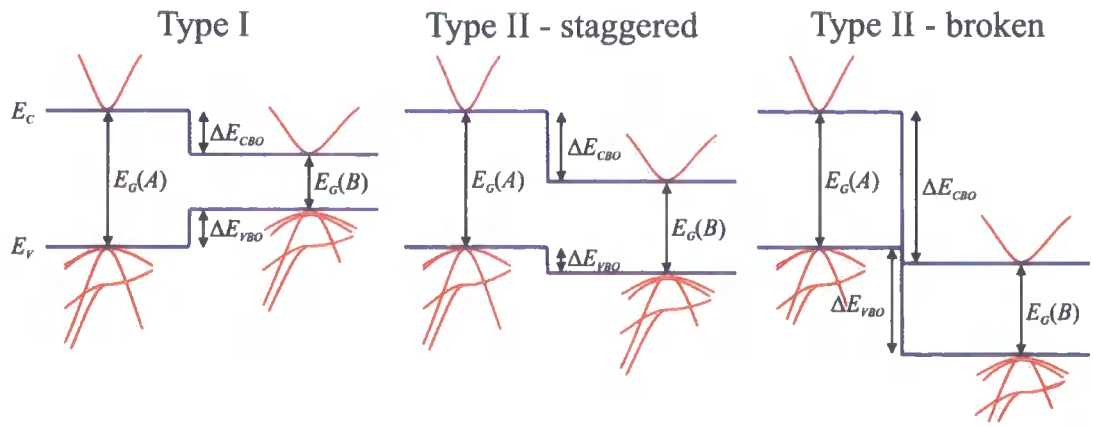

Figure 4.1: Schematic illustration of three types of heterojunction. The type I heterojunction has material B's conduction and valence band entirely within the principal band gap of material A. The type II - staggered has either the conduction or valence band of material B within the energy range of material A's band gap. The final type of heterojunction (type II - broken) has no overlap of band gap energy between the two materials. The blue lines represent the principal energy gap as a function of position and the red lines illustrate the relative offsets of the bandstructures.

conduction bands, referred to as the valence band offset (VBO) and the conduction band offset (CBO). The existence of a valence band and conduction band offsets is the origin of most of the useful properties of a heterojunction. The relative positions of two bandstructures are characteristic of the two materials present and are affected by the strain of the layers. Since the strain is caused by the lattice parameter of whichever material on which the heterostructure is grown, the band offsets may not be symmetric; i.e. the offset of A grown on B may not be the same as B grown on A. Furthermore, it is thought that for lattice matched systems the band offsets between two materials A and B can be inferred by the offsets of both A and B with a third material C.

$$\Delta E^{AB}_{VBO,CBO} = \Delta E^{AC}_{VBO,CBO} + \Delta E^{CB}_{VBO,CBO} \tag{4.1}$$

This property is known as *transitivity* and has been verified experimentally [92,93] to within the experimental precision. Valence band offsets can be calculated with first principles approaches and can be determined experimentally with techniques such as x-ray photoelectron spectroscopy, although such measurements are often prone to large uncertainties.

Trends in the change of valence band offset between the common II-VI and III-V semiconductors are mainly due to cation d orbital to anion coupling; in aluminium nitride, the cation d orbital is unoccupied and above the anion p orbital and therefore p-d repulsion pushes the anion valence band maximum (VBM) down in energy. Ga and In have occupied $3d$ (Ga) and $4d$ (In) orbitals which are below the anion p energy so p-d repulsion moves the anion p VBM up in energy [44,94]. The observed valence band offsets for the nitrides are larger than comparable III-V systems because, due to the shorter bond lengths and the smaller cation d and nitrogen $2p$ energy differences, the p-d repulsion is stronger [44].

Heterojunctions can be classified into three basic types depending on the band offset and the relative size of their principal band gaps. Figure 4.1 describes the three types of interface. In this work we are concerned with nitride interfaces which, for GaN, AlN and InN and their alloys, are all of type I.

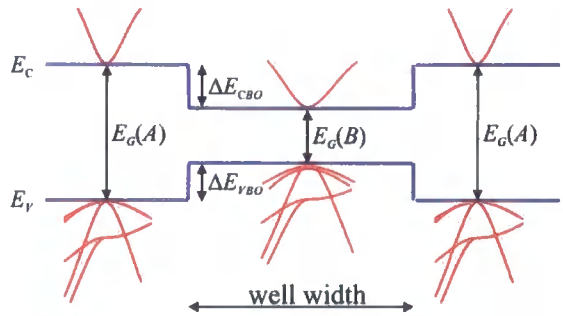

Figure 4.2: Schematic illustration of a quantum well formed by two heterojunctions. The blue lines represent the principal energy gap as a function of position and the red lines illustrate the relative offsets of the bandstructures.

4.3 Quantum Wells

A heterostructure with quantum wells in both the conduction and valence bands can be constructed from two type I heterojunctions, formed by a layer of material sandwiched between layers of a semiconductor of larger band gap (figure 4.2). The width of the well is of the order of the de-Broglie wavelength of the charge carriers, and the carrier confinement to the layer gives rise to quantum mechanical effects. In particular, the confinement causes the carrier's kinetic energy associated with motion normal to the quantum well layer to be quantised. Then the in-plane bandstructure resulting from the unconfined in-plane motion of

the charge carriers takes the form of one or more subbands.

Nitride quantum wells are most easily fabricated through the same methods by which the nitride bulk semiconductors are grown. In particular molecular beam epitaxy (MBE) allows the precise growth of layers of material and by changing the chemical composition during growth, different layers are built up. The atoms of the new layers try to crystallise at the same in-plane positions as the previous layers, which can give rise to a strained layer. The growth of high quality layered heterostructures is the subject of much research for all materials, including the nitrides [7].

4.4 Effective mass calculations

Effective mass theory (EMT) [95–100] simplifies the problem of describing the physics of a crystal by abandoning the periodic potential. The physics of the periodic potential is approximated by an effective mass and the rapidly oscillating true wavefunction becomes a smooth envelope function. The idea of an effective mass and the concept of an envelope function can be used to provide a rudimentary initial approximation for calculating the quantum mechanical bound states of a quantum well. An approach such as this has the advantage of simplicity and provides a 'baseline' comparison for more complicated techniques such as the complex bandstructure approach employed in this work. Within effective mass theory the bandstructure of the semiconductor can be approximated as a single parabolic band. We will refer to this as the effective mass single parabolic band model. This single band is considered in isolation and no interactions with other bands are considered. Heterostructures can be modelled in this approach by employing the same techniques of a wave-mechanics calcu-

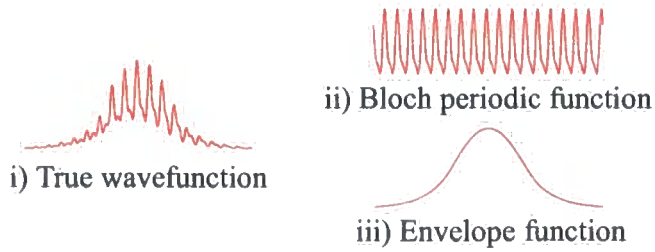

Figure 4.3: Concept of an envelope function. The true wavefunction (i) can be considered to compose of two components, the rapidly varying Bloch periodic function (ii) and the slowly varying envelope function (iii)

lation found in any standard quantum mechanics textbook [101] with the free electron mass m_e replaced by an effective mass m^*. Implicit in the approximation of an effective mass is the consideration of just the envelope function rather than the full wavefunction which includes the Bloch periodic part as illustrated in figure 4.3.

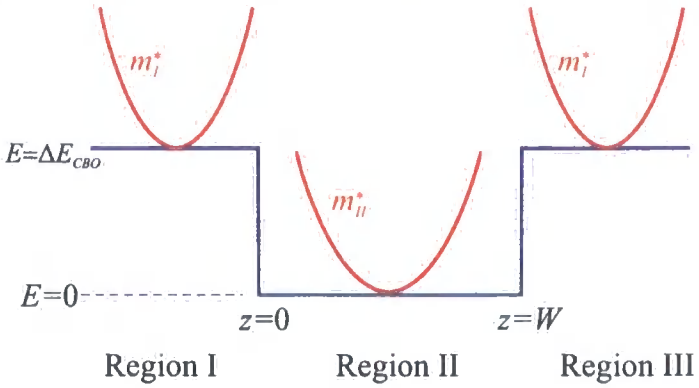

Figure 4.4: A simple quantum well with two barrier regions and a well region.

For a layered heterostructure such as the quantum well in figure 4.4 the one-dimensional Schrödinger equation for the envelope function $f^{(l)}(z)$ of each separate material layer (l) is

$$\left(-\frac{\hbar^2}{2m^*}\frac{\partial^2}{\partial z^2} + V^{(l)}\right) f^{(l)}(z) = E_k f^{(l)}(z) \tag{4.2}$$

where $V^{(l)}$ is a constant potential in layer (l) and E_k is the energy. General solutions of (4.2) have the familiar form

$$f^{(l)}(z) = A^{(l)}e^{ikz} + B^{(l)}e^{-ikz} \tag{4.3}$$

where $A^{(l)}$ and $B^{(l)}$ are constants and the wave vector k is given by

$$k = \frac{\sqrt{2m^*(E_k - V^{(l)})}}{\hbar} \tag{4.4}$$

The boundary conditions across the interfaces however cannot be derived from (4.2) as this is only valid for the bulk. For a rigorous derivation of the boundary conditions across the in-

terfaces, a microscopic model such as that proposed by Burt [98,99] is required. Burt shows that both envelope function and derivative of envelope function, weighted by the effective mass, are continuous across the interfaces.

$$f^{(I)}(0) = f^{(II)}(0) \tag{4.5a}$$

$$f^{(II)}(W) = f^{(III)}(W) \tag{4.5b}$$

$$\frac{1}{m_I^*}\frac{\partial f^{(I)}}{\partial z}\bigg|_{z=0} = \frac{1}{m_{II}^*}\frac{\partial f^{(II)}}{\partial z}\bigg|_{z=0} \tag{4.5c}$$

$$\frac{1}{m_{II}^*}\frac{\partial f^{(II)}}{\partial z}\bigg|_{z=W} = \frac{1}{m_{III}^*}\frac{\partial f^{(III)}}{\partial z}\bigg|_{z=W} \tag{4.5d}$$

For the case of bound states the six unknowns from equation (4.3) is reduced to four by setting one of the coefficients in each barrier region to zero, to prevent $f(z)$ from diverging. The boundary conditions of (4.5) then allow the solutions to be identified. This is usually achieved by writing equations (4.3) and (4.5) as an eigenvalue problem and searching for a zero in the determinant of the resulting matrix M. Figure 4.5 gives an example of the determinant as a function of energy and the resulting envelope functions are described in figure 4.6. Heterostructures with more than three layers can be modelled in much the same way by making use of a transfer matrix.

4.5 Complex bandstructure transfer matrix approach

The same general approach as described in section 4.4 for envelope functions can be applied to the pseudowavefunctions generated by the empirical pseudopotential complex bandstructure method. Monaghan *et al* [87] and Brand *et al* [88,89] describe examples of this approach for zincblende quantum wells and superlattices. In essence, the complex bandstructures replace the single parabolic band of the envelope function approximation and the matching conditions are well defined for this microscopic approach.

4.5.1 Matching of pseudo-wavefunction at interfaces

Consider a general heterostructure grown as a series of layers sandwiched between two barrier regions of thickness much greater than the layers. Each of the different layers

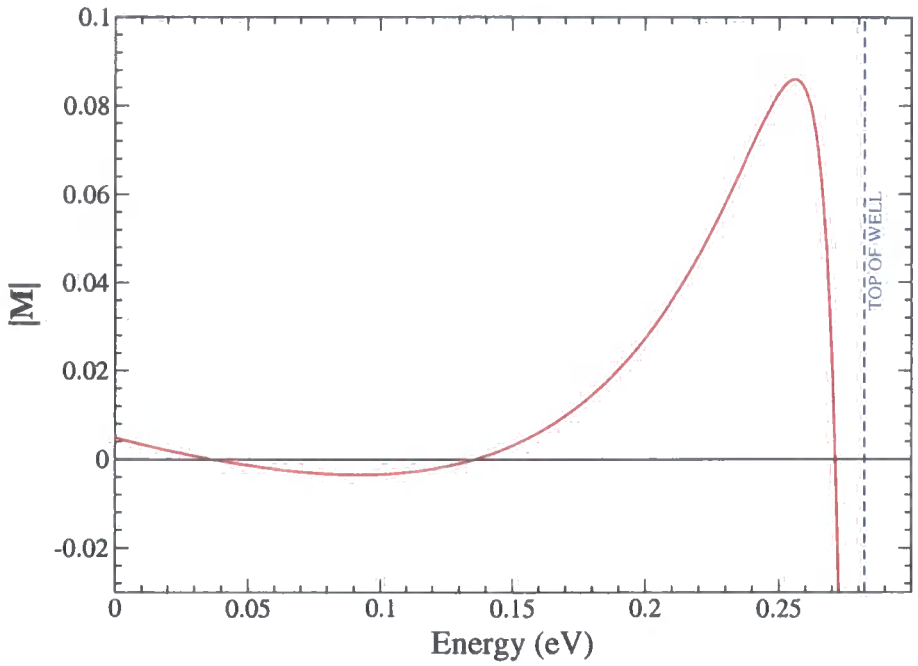

Figure 4.5: Graph showing scan over energy range for zeros in the determinant, used to identify bound state solutions of a $Al_{0.4}Ga_{0.6}N$ / GaN / $Al_{0.4}Ga_{0.6}N$ quantum well within the effective mass approximation.

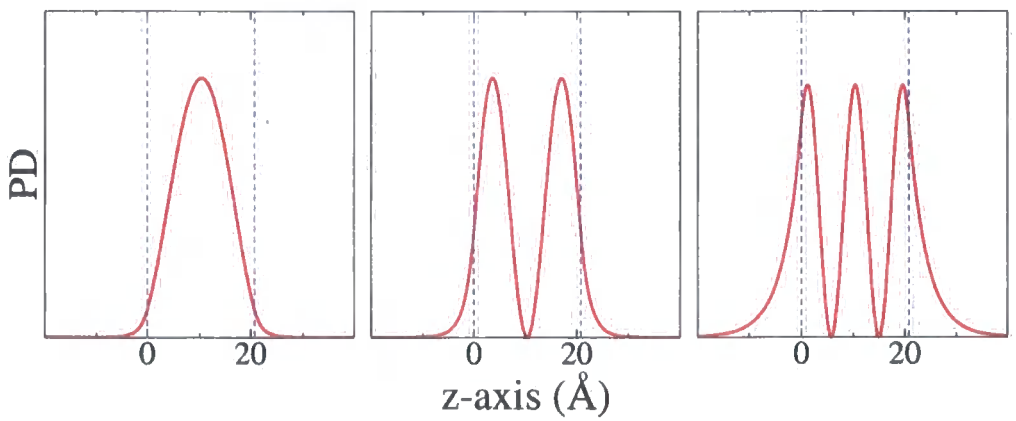

Figure 4.6: The probability densities (PD) of the ground state and first two excited state envelope functions for a $Al_{0.4}Ga_{0.6}N$ / GaN / $Al_{0.4}Ga_{0.6}N$ quantum well.

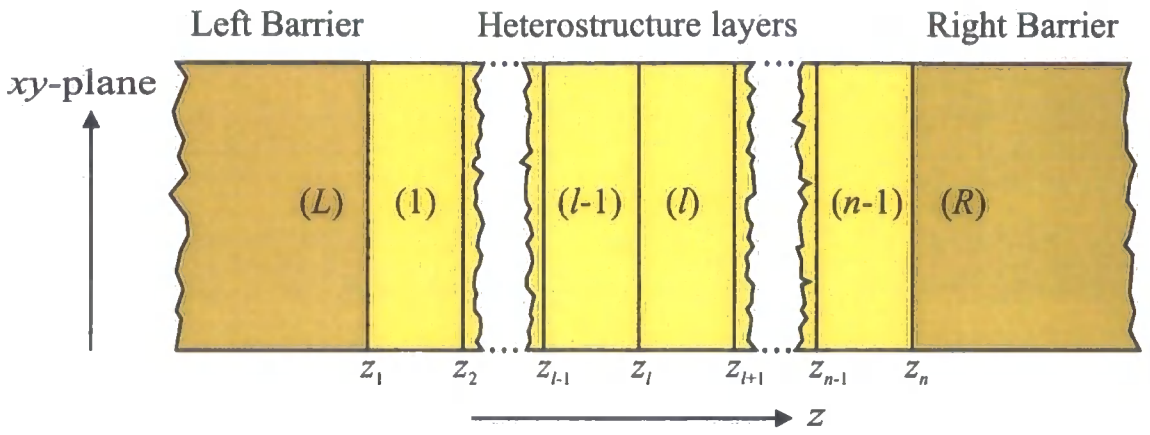

Figure 4.7: Schematic describing the relative positions of n interfaces in a general heterostructure. The material layers are labelled L, 1, 2, ... ,$l-1$,l, ... $n-1$ and R, where L and R are the left and right hand barriers.

and barrier regions may be a different material. The most general wavefunction in a given layer is the sum of all complex bandstructure states for that material at a given energy E and in-plane wavevector, $\mathbf{k}_{||}$, which we write as

$$\psi_{E\mathbf{k}_{||}}(\mathbf{r}) = \sum_{k} c_{kE\mathbf{k}_{||}} \phi_{kE\mathbf{k}_{||}}(\mathbf{r}) \tag{4.6}$$

where $c_{kE\mathbf{k}_{||}}$ are coefficients, yet to be determined and $\phi_{kE\mathbf{k}_{||}}(\mathbf{r})$ is the pseudo wavefunction determined by the complex bandstructure calculation at energy E and in-plane wavevector, $\mathbf{k}_{||}$. Henceforth, the wavefunction is assumed to be dependent on E and $\mathbf{k}_{||}$, and for clarity and notational compactness the subscripts indicating this dependence are no longer included. For layer l we write $\phi_{kE\mathbf{k}_{||}}(\mathbf{r})$ as $\phi^{(l)}(\mathbf{r})$ which is itself an expansion of a Fourier series given by

$$\phi^{(l)}(\mathbf{r}) = \sum_{\mathbf{g}} a^{(l)}_{\mathbf{g}sk} e^{i(\mathbf{k}+\mathbf{g})\cdot\mathbf{r}} \tag{4.7}$$

where $a^{(l)}_{\mathbf{g}sk}$ are the Fourier components (spinors, with spin index s) of state k for the material in layer (l).

Now consider the general layered heterostructure, grown in the z direction, with n

interfaces as shown in figure 4.7. The interfaces are labelled from left to right, starting with interface 1 at $z = z_1$, which separates the left barrier material and layer $l = 1$. There are $n-1$ layers between the two barriers, finishing on the right with interface N_I at $z = z_n$, separating layer $l = n - 1$ and the right barrier. The barriers are considered to extend infinitely in the z direction. The wavefunction in layer l can now be written as

$$\psi^{(l)}(z, \mathbf{r}_{\|}) = \sum_{k} c_k^{(l)} \sum_{\mathbf{g}} a_{\mathbf{g}sk}^{(l)} e^{i(k+g)z} e^{i(\mathbf{k}_{\|}+\mathbf{g}_{\|})\cdot\mathbf{r}_{\|}} \tag{4.8}$$

the superscripts in parenthesis denote the layer and the wavevector $\mathbf{k}$ and reciprocal lattice vector $\mathbf{g}$ have been split into inplane and growth direction components $\mathbf{k} = k + \mathbf{k}_{\|}$, $\mathbf{g} = g + \mathbf{g}_{\|}$.

Now consider general interface l which joins layers $l - 1$ on the left to l on the right. The boundary conditions of continuity of wavefunction and continuity of derivative can be applied to the wavefunctions of both layers at $z = z_l$.

$$\psi^{(l-1)}(z_l, \mathbf{r}_{\|}) = \psi^{(l)}(z_l, \mathbf{r}_{\|}) \tag{4.9}$$

$$\frac{\partial}{\partial z}\psi^{(l-1)}\bigg|_{z_l,\mathbf{r}_{\|}} = \frac{\partial}{\partial z}\psi^{(l)}\bigg|_{z_l,\mathbf{r}_{\|}} \tag{4.10}$$

For continuity of wavefunction (4.9) applied to equation (4.8) this gives

$$\sum_{k} c_k^{(l-1)} \sum_{\mathbf{g}} a_{\mathbf{g}sk}^{(l-1)} e^{i(k+g)z_l} e^{i(\mathbf{k}_{\|}+\mathbf{g}_{\|})\cdot\mathbf{r}_{\|}} = \sum_{k'} c_{k'}^{(l)} \sum_{\mathbf{g}'} a_{\mathbf{g}'s'k'}^{(l)} e^{i(k'+g')z_l} e^{i(\mathbf{k}'_{\|}+\mathbf{g}'_{\|})\cdot\mathbf{r}_{\|}} \tag{4.11}$$

where k represents the wavevectors for layer $l - 1$ and k' for layer l. The in-plane translation symmetry is maintained throughout the heterostructure layers. The in-plane wavevector must therefore be the same in the different layers in order to conserve momentum; i.e. $k_{\|} = k'_{\|}$. Equation (4.11) is multiplied by $e^{-i\mathbf{g}''_{\|}\cdot\mathbf{r}_{\|}}$ and then integrated over the in-plane unit cell face

in the plane of the interface. Integrating in this way has the effect of equating the sum of all coefficients that project onto each given 2D projection. [88,89]

$$\sum_k c_k^{(l-1)} \sum_{\mathbf{g}} a_{\mathbf{g}sk}^{(l-1)} e^{ikz_l} \delta_{\mathbf{g}_\parallel \mathbf{g}''_\parallel} = \sum_{k'} c_{k'}^{(l)} \sum_{\mathbf{g}'} a_{\mathbf{g}'s'k'}^{(l)} e^{ik'z_l} \delta_{\mathbf{g}'_\parallel \mathbf{g}''_\parallel} \tag{4.12}$$

z_l is assumed to be an integer number of unit cells. Defining $\overrightarrow{P}^{(l)}_{\mathbf{g}_\parallel sk}$ and $\overleftarrow{P}^{(l)}_{\mathbf{g}_\parallel sk}$, the projection of the wavefunction in layer (l) on to the right and left interface respectively as

$$\overrightarrow{P}^{(l)}_{\mathbf{g}_\parallel sk} = \sum_{\mathbf{g}'} a_{\mathbf{g}'sk}^{(l)} e^{ikz_{l+1}} \delta_{\mathbf{g}'_\parallel \mathbf{g}_\parallel} \tag{4.13}$$

$$\overleftarrow{P}^{(l)}_{\mathbf{g}_\parallel sk} = \sum_{\mathbf{g}'} a_{\mathbf{g}'sk}^{(l)} e^{ikz_l} \delta_{\mathbf{g}'_\parallel \mathbf{g}_\parallel} \tag{4.14}$$

now equation (4.12) becomes

$$\sum_k c_k^{(l-1)} \overrightarrow{P}^{(l-1)}_{\mathbf{g}_\parallel sk} = \sum_{k'} c_{k'}^{(l)} \overleftarrow{P}^{(l)}_{\mathbf{g}_\parallel sk'} \tag{4.15}$$

The same procedure can be followed for equation (4.10), the continuity of derivative, resulting in

$$\sum_k c_k^{(l-1)} \overrightarrow{Q}^{(l-1)}_{\mathbf{g}_\parallel sk} = \sum_{k'} c_{k'}^{(l)} \overleftarrow{Q}^{(l)}_{\mathbf{g}_\parallel sk'} \tag{4.16}$$

where $\overrightarrow{Q}^{(l)}_{\mathbf{g}_\parallel sk}$ and $\overleftarrow{Q}^{(l)}_{\mathbf{g}_\parallel sk}$, the projection of the derivative of the wavefunction to the right and left, are defined by

$$\overrightarrow{Q}^{(l)}_{\mathbf{g}_{\|}sk} = \sum_{\mathbf{g}'} (k + g'_z) a^{(l)}_{\mathbf{g}'sk} e^{ikz_{l+1}} \delta_{\mathbf{g}'_{\|}\mathbf{g}_{\|}} \tag{4.17}$$

$$\overleftarrow{Q}^{(l)}_{\mathbf{g}_{\|}sk} = \sum_{\mathbf{g}'} (k + g'_z) a^{(l)}_{\mathbf{g}'sk} e^{ikz_{l}} \delta_{\mathbf{g}'_{\|}\mathbf{g}_{\|}} \tag{4.18}$$

$\overrightarrow{P}_{\mathbf{g}_{\|}sk}(l)$, $\overrightarrow{Q}_{\mathbf{g}_{\|}sk}(l)$, $\overleftarrow{P}_{\mathbf{g}_{\|}sk}(l)$ and $\overleftarrow{Q}_{\mathbf{g}_{\|}sk}(l)$ are now best represented as a pair of $2M$ by $4M$ matrices, where M is the number of inplane projections of $\mathbf{g}$ being used

$$\overrightarrow{\mathbf{P}}^{(l)} = \begin{bmatrix} \overrightarrow{P}^{(l)}_{(00)\uparrow k_1} & \overrightarrow{P}^{(l)}_{(00)\uparrow k_2} & \cdots & \overrightarrow{P}^{(l)}_{(00)\uparrow k_{4M}} \\ \overrightarrow{P}^{(l)}_{(11)\uparrow k_1} & \overrightarrow{P}^{(l)}_{(11)\uparrow k_2} & \cdots & \overrightarrow{P}^{(l)}_{(11)\uparrow k_{4M}} \\ \vdots & \vdots & & \vdots \\ \overrightarrow{P}^{(l)}_{(00)\downarrow k_1} & \overrightarrow{P}^{(l)}_{(00)\downarrow k_2} & \cdots & \overrightarrow{P}^{(l)}_{(00)\downarrow k_{4M}} \\ \overrightarrow{P}^{(l)}_{(11)\downarrow k_1} & \overrightarrow{P}^{(l)}_{(11)\downarrow k_2} & \cdots & \overrightarrow{P}^{(l)}_{(11)\downarrow k_{4M}} \\ \vdots & \vdots & & \vdots \end{bmatrix} \quad \mathbf{c}^{(l)} = \begin{bmatrix} c^{(l)}_{k_1} \\ c^{(l)}_{k_2} \\ \vdots \\ c^{(l)}_{k_{4M}} \end{bmatrix} \tag{4.19}$$

Combining equations (4.16) and (4.15) in matrix form,

$$\begin{bmatrix} \overrightarrow{\mathbf{P}}^{(l-1)} \\ \overrightarrow{\mathbf{Q}}^{(l-1)} \end{bmatrix} \mathbf{c}^{(l-1)} = \begin{bmatrix} \overleftarrow{\mathbf{P}}^{(l)} \\ \overleftarrow{\mathbf{Q}}^{(l)} \end{bmatrix} \mathbf{c}^{(l)} \tag{4.20}$$

where the combined matrices are square ($4M \times 4M$). A transfer matrix $\mathbf{T}^{(l)}$ can now be defined which relates the wavefunction on layer l to that on layer $l-1$

$$\mathbf{c}^{(l)} = \mathbf{T}^{(l)} \mathbf{c}^{(l-1)} \tag{4.21}$$

where $\mathbf{T}^{(l)}$ is given by

$$\mathbf{T}^{(l)} = \begin{bmatrix} \overleftarrow{\mathbf{P}}^{(l)} \\ \overleftarrow{\mathbf{Q}}^{(l)} \end{bmatrix}^{-1} \begin{bmatrix} \overrightarrow{\mathbf{P}}^{(l-1)} \\ \overrightarrow{\mathbf{Q}}^{(l-1)} \end{bmatrix} \tag{4.22}$$

The wavefunctions between the two layers l and $l+m$ are therefore related by

$$\mathbf{c}^{(l+m)} = \mathbf{T}^{(l+m)}\mathbf{T}^{(l+m-1)} \ldots \mathbf{T}^{(l+2)}\mathbf{T}^{(l+1)}\mathbf{c}^{(l)} \tag{4.23}$$

The use of a transfer matrix is only valid in this way when applied to the finite layers and is not valid for the barriers on the left and right hand sides of the structure.

4.5.2 Barrier Regions

The barrier regions are for the purposes of the calculation considered to be infinite in extent. The purpose of the calculation is to identify *bound states*, which by definition are restricted to some finite region of space. In order for the wavefunction to remain finite in the barrier regions it must not be allowed to grow exponentially, *away from the barriers.* To ensure this, only wavevectors that provide solutions that decay away from the barrier are allowed. Since the wavefunction is of the form $\psi \propto e^{i\mathbf{k}\cdot z}$ k-solutions in the left barrier are required to have only negative imaginary components. Conversely k-solutions in the right barrier are required to have only positive imaginary components.

$$\text{left barrier} \qquad \lim_{z\to-\infty}\left(e^{i(k_r+ik_i)z}\right) = 0 \qquad \text{if} \quad k_i < 0 \tag{4.24}$$

$$\text{right barrier} \qquad \lim_{z\to+\infty}\left(e^{i(k_r+ik_i)z}\right) = 0 \qquad \text{if} \quad k_i > 0 \tag{4.25}$$

The energy range of the quantum well, coincides with the band gap of the semiconductor of the barrier regions, for which there are only states with imaginary or complex wavevector. Exactly half of these states will have either a positive or negative imaginary component of wavevector in the growth direction and therefore exactly half the total number of states will be used in the matching of the wavefunctions at the barriers.

The same interface boundary conditions as were applied to a general well interface, apply to the interface between the left barrier (L) and the first finite layer ($l = 1$)

$$\sum_{k=k^-} c_k^{(L)} \sum_{\mathbf{g}} a_{\mathbf{g}sk}^{(L)} e^{i(k+g)z_1} e^{i(\mathbf{k}_\parallel+\mathbf{g}_\parallel)\cdot\mathbf{r}_\parallel} = \sum_{k'} c_{k'}^{(1)} \sum_{\mathbf{g}'} a_{\mathbf{g}'s'k'}^{(1)} e^{i(k'+g')z_1} e^{i(\mathbf{k}'_\parallel+\mathbf{g}_\parallel)\cdot\mathbf{r}_\parallel} \tag{4.26}$$

where again, the wavevectors used are those appropriate to the material layer in question. An analogous equation can be written down for the right barrier and similarly for the matching of the derivative at the left and right barriers, giving four equations in total. As with equation (4.12) both sides are multiplied by $e^{-i\mathbf{g}''_\parallel\cdot\mathbf{r}_\parallel}$ and integrated over the in-plane unit cell face. This produces four equations for the projections of the wavefunction and derivative onto the the left and right barrier interfaces.

$$\sum_{k=k^-} c_k^{(L)} P_{\mathbf{g}_\parallel sk}^{(L)} = \sum_{k'} c_{k'}^{(1)} \overleftarrow{P}_{\mathbf{g}_\parallel sk'}^{(1)} \tag{4.27}$$

$$\sum_{k=k^-} c_k^{(L)} Q_{\mathbf{g}_\parallel sk}^{(L)} = \sum_{k'} c_{k'}^{(1)} \overleftarrow{Q}_{\mathbf{g}_\parallel sk'}^{(1)} \tag{4.28}$$

$$\sum_{k=k^+} c_k^{(R)} P_{\mathbf{g}_\parallel sk}^{(R)} = \sum_{k'} c_{k'}^{(n-1)} \overrightarrow{P}_{\mathbf{g}_\parallel sk'}^{(n-1)} \tag{4.29}$$

$$\sum_{k=k^+} c_k^{(R)} Q_{\mathbf{g}_\parallel sk}^{(R)} = \sum_{k'} c_{k'}^{(n-1)} \overrightarrow{Q}_{\mathbf{g}_\parallel sk'}^{(n-1)} \tag{4.30}$$

The projections of the wavefunction are again represented by matrices. In order to relate the wavefunction in the right barrier to that in the left barrier the total transfer matrix between the first and last finite layer needs to be defined.

$$\mathbf{T} = \mathbf{T}^{(n-1)}\mathbf{T}^{(n-2)} \ldots \mathbf{T}^{(3)}\mathbf{T}^{(2)}\mathbf{I} \tag{4.31}$$

where $\mathbf{I}$ is the identity matrix. If there is only one finite layer then $\mathbf{T} = \mathbf{I}$. Equations (4.27)(4.28)(4.29)(4.30) and the total transfer matrix (4.31) can be put together to form two matrix equations.

$$\begin{bmatrix} \mathbf{P}^{(L)} & 0 \\ 0 & \mathbf{P}^{(R)} \end{bmatrix} \begin{bmatrix} \mathbf{c}^{(L)} \\ \mathbf{c}^{(R)} \end{bmatrix} = \begin{bmatrix} \overleftarrow{\mathbf{P}}^{(1)} \\ \overrightarrow{\mathbf{P}}^{(n-1)} \mathbf{T} \end{bmatrix} \begin{bmatrix} \mathbf{c}^{(1)} \\ \end{bmatrix} \tag{4.32}$$

$$\begin{bmatrix} \mathbf{Q}^{(L)} & 0 \\ 0 & \mathbf{Q}^{(R)} \end{bmatrix} \begin{bmatrix} \mathbf{c}^{(L)} \\ \mathbf{c}^{(R)} \end{bmatrix} = \begin{bmatrix} \overleftarrow{\mathbf{Q}}^{(1)} \\ \overrightarrow{\mathbf{Q}}^{(n-1)} \mathbf{T} \end{bmatrix} \begin{bmatrix} \mathbf{c}^{(1)} \\ \end{bmatrix} \tag{4.33}$$

which may be combined into a single eigenvalue equation with an eigenvalue of 1 and eigenvector $\mathbf{c}^{(1)}$. [46,88]

$$\begin{bmatrix} \overleftarrow{\mathbf{Q}}^{(1)} \\ \overrightarrow{\mathbf{Q}}^{(n-1)} \mathbf{T} \end{bmatrix}^{-1} \begin{bmatrix} \mathbf{Q}^{(L)} & 0 \\ 0 & \mathbf{Q}^{(R)} \end{bmatrix} \begin{bmatrix} \mathbf{P}^{(L)} & 0 \\ 0 & \mathbf{P}^{(R)} \end{bmatrix}^{-1} \begin{bmatrix} \overleftarrow{\mathbf{P}}^{(1)} \\ \overrightarrow{\mathbf{P}}^{(n-1)} \mathbf{T} \end{bmatrix} \begin{bmatrix} \mathbf{c}^{(1)} \\ \end{bmatrix} = \begin{bmatrix} \mathbf{c}^{(1)} \\ \end{bmatrix} \tag{4.34}$$

$$\mathbf{M}\mathbf{c}^{(1)} = \mathbf{c}^{(1)} \tag{4.35}$$

Bound states therefore exist if solutions to equation (4.34) exist for a given energy and in-plane wavevector. The bound states can therefore be located by scanning over the energy range of the quantum well and looking for eigenvalues of unity. Equivalently solutions will be found when the determinant of $\mathbf{M} - \mathbf{I}$ vanishes.

4.5.3 Practicalities

The calculations of the complex bandstructure and the associated wavefunction coefficients is usually performed separately from that of the matching which requires that the wavefunction and wavevector information for a range of given energies is stored. This initial calculation is computationally quite expensive, taking up to a day on a standard workstation. However, once stored, this data can be used for any heterostructure that uses that material over that energy range. This allows quantum wells to be studied very easily over a range

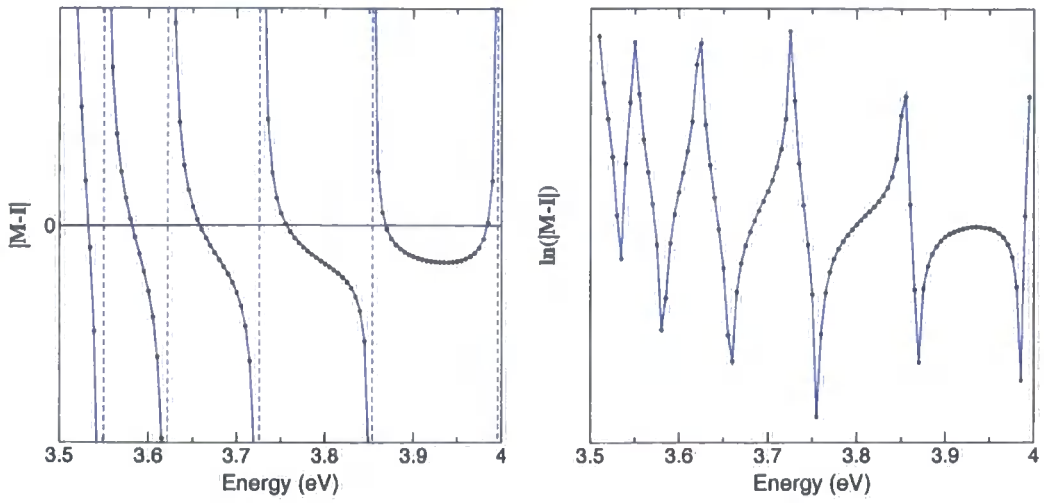

Figure 4.8: Example of the graph of determinant of matrix vs E for a 0.5eV deep, 20 unit cells wide, GaN, conduction band quantum well. i) Without spin-orbit coupling. Bound state solutions are found where the solid line crosses the $|\mathbf{M} - \mathbf{I}| = 0$ line ii) With spin-orbit coupling. Solutions are found at downward spikes in the value of $|\mathbf{M} - \mathbf{I}|$. The y axis is plotted on a log scale for clarity.

of thicknesses at very little additional computational cost. The precision of a search over the energy range for a zero in the determinant is dependent on the energy sampling used in the complex bandstructure. Clearly a greater level of sampling requires a computationally more expensive complex bandstructure calculation and greater storage requirements. For the purposes of this work the energy sampling was chosen such that between about 100 and 200 energy points were calculated for each quantum well. Interpolation schemes allow the bound state energy to be estimated to an accuracy which is enhanced by a further order of magnitude, giving a precision of three significant figures in the bound state energies. If necessary the storage requirements can be further reduced by calculating the projection matrices and storing these rather than the complete wavefunctions.

Identification of solutions

An example of a determinant as a function of energy is given in figure 4.8 for a quantum well with and without the effects of spin-orbit coupling. The locations of the bound states are indicated by $|\mathbf{M}-\mathbf{I}|$ crossing the abscissa for the calculation without spin-orbit coupling and by sharp dips in the curve if spin-orbit coupling is included. Asymptotic changes in sign can be seen on the non spin-orbit coupling graph that become sharp upwards peaks

if spin-orbit coupling is included. These features correspond to energies where the infinite well solutions for a quantum well of that width are valid. Examination of the corresponding wavefunction coefficients for the barrier regions at one of these crossover energies, confirms this. The wavefunctions in the barrier becomes smaller and smaller as the crossover energy is approached.

Numerical Problems

The e^{ikz} terms in the projection matrices can produce a numerically ill-conditioned problem for the evaluation of a determinant. For anything larger than the smallest quantum wells, for complex k, the e^{ikz} terms contribute to very large or very small values in the projection matrices. This is handled in two ways, firstly the evanescent solutions are normalised for each layer to ensure that they decay from numerically the same value. Secondly a limit on the decay of the e^{ikz} term is imposed by truncating any e^{ikz} terms smaller than this limit $e^{E_{LIM}}$ [88,102]. This truncation can be justified physically, because any solutions that have decayed excessively will effectively make no difference to the matching conditions.

Convergence

The bulk and complex bandstructures were tested separately for convergence against number of plane waves in sections 2.4.4 and 3.7. Given that the pseudo wavefunction was considered adequately converged in those instances it is reasonable to consider the number of plane waves adequate for the process of identification of bound states. However, the number of complex k basis states used in the two dimensional projections M will affect the accuracy of the quantum well state energies and eigenfunctions and requires justification. The microscopic hexagonal in-plane symmetry allows the use of $M = 1, 7, 13, 19 \ldots$ as the matching must be performed for a complete set of in-plane g-vectors. Figure 4.9 describes the variation of bound state energy for the ground state and first and second excited states of a test quantum well for different values of M. Figure 4.9 shows that the energies are converged to within the precision of the energy sampling at $M = 7$. From the complex bandstructure graphs in chapter 3, it is clear that after the first few states the imaginary component of the wavevectors gets too large for the associated states to play any meaningful role in the matching.

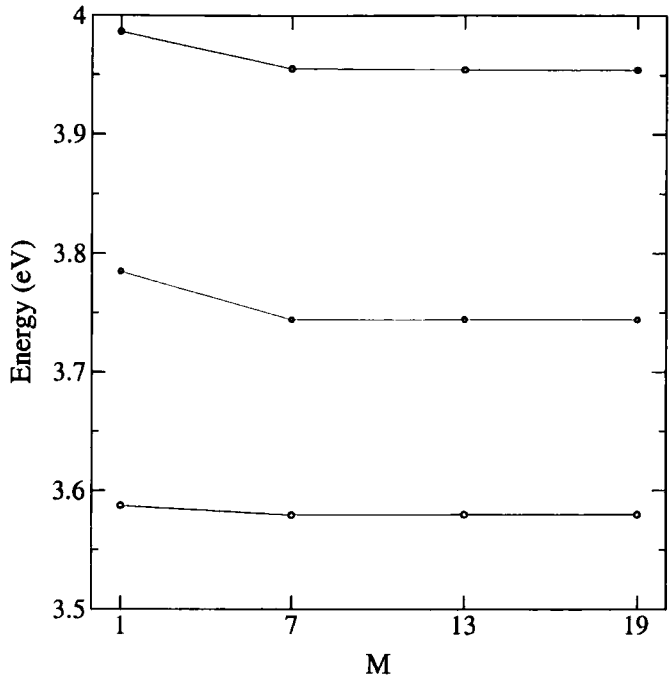

Figure 4.9: The convergence of bound state energy with M for the ground state and first and second excited states for a 0.5eV GaN quantum well.

4.5.4 Probability Density

Having identified an energy at which a bound state exists, the complex bandstructure wavefunctions and the eigenvectors of equation (4.34) can be used to construct the bound state wavefunction. The eigenvector from the solution of (4.34) contains the wavefunction coefficients for the bulk k-states used to construct the bound state wavefunction for region $l = 1$. The transfer matrix (4.22) for each layer can then be used to calculate the wavefunction coefficients in all the other layers and equation (4.32) yields the wavefunction coefficients in the barrier regions. The probability density (PD) can then easily be generated as

$$\psi^{(l)*}(\mathbf{r})\psi^{(l)}(\mathbf{r}) = \sum_{k}\sum_{k'} c_{k}^{(l)} c_{k'}^{(l)*} \sum_{\mathbf{g}}\sum_{\mathbf{g}'} \left(a_{\mathbf{g}\uparrow k}^{(l)} a_{\mathbf{g}'\uparrow k'}^{(l)*} a_{\mathbf{g}\downarrow k}^{(l)} a_{\mathbf{g}'\downarrow k'}^{(l)*} \right) \times e^{i(\mathbf{k}_{\parallel}+\mathbf{g}_{\parallel})\cdot\mathbf{r}_{\parallel}} e^{i(\mathbf{k}'_{\parallel}+\mathbf{g}'_{\parallel})\cdot\mathbf{r}_{\parallel}*} e^{i(k+g)z} e^{i(k'+g')z*} \tag{4.36}$$

For a convenient comparison with the envelope function solutions the probability can be

integrated over the in-plane unit cell to produce a two dimensional average of the three dimensional probability density.

$$\int_{-\infty}^{+\infty}\int_{-\infty}^{+\infty} \psi^{(l)*}(\mathbf{r})\psi^{(l)}(\mathbf{r})dxdy \propto \sum_{k}\sum_{k'}\sum_{\mathbf{g}}\sum_{\mathbf{g}'} c_k^{(l)} c_{k'}^{(l)*} \left(a_{\mathbf{g}\uparrow k}^{(l)} a_{\mathbf{g}'\uparrow k'}^{(l)\,*} a_{\mathbf{g}\downarrow k}^{(l)} a_{\mathbf{g}'\downarrow k'}^{(l)\,*}\right) \times e^{i(kz+gz-k'^{*}z-g'z)}\delta_{\mathbf{g}_{\|}\mathbf{g}'_{\|}} \quad (4.37)$$

Figure 4.10 shows the probability density of a slice through the bond plane of a AlGaN-GaN-AlGaN valence band quantum well, the resulting in-plane averaged probability density and the envelope function corresponding to an effective mass calculation of the same well. The "bond plane" can be defined by the 4 atoms in a single unit cell and the bonds between them, and has one axis in the growth direction. The in-plane averaged PD is an average of the whole of the in-plane unit cell. All the probability densities are for zero in-plane wavevector. The PD is noticeably asymmetric about the well centre, especially when compared to the envelope function. This is partly a result of the inherent asymmetry of the polar wurtzite crystal and partly because of the microscopic ordering of the atomic layers and their corresponding band offsets. Consider a hypothetical AlN - GaN - AlN quantum well in which we have atomic layers in the order:

$$\cdots \mathrm{Al}\cdot\mathrm{N}\cdot\mathrm{Al}\cdot\mathrm{N} \,\big|\, \mathrm{Ga}\cdot\mathrm{N}\cdot\mathrm{Ga}\cdot\mathrm{N} \,\big|\, \mathrm{Al}\cdot\mathrm{N}\cdot\mathrm{Al}\cdot\mathrm{N}\cdots$$

For a *polar* crystal the N · Al layers are not mirror images of the Al · N layers and the asymmetry is clearly a physical feature. However, for a *non-polar* crystal any asymmetry in the theoretical well is solely a result of the approximation of the N atoms at the interface being either part of GaN or AlN, because in a real crystal such an artificial designation doesn't exist and the well is in reality perfectly symmetrical. In an EPM calculation for a non-polar crystal, the asymmetry can be removed by a suitable choice of matching plane:

$$\cdots \mathrm{Al}\cdot\mathrm{N}\cdot\mathrm{Al} \,\big|\, \mathrm{N}\cdot\mathrm{Ga}\cdot\mathrm{N}\cdot\mathrm{Ga}\cdot\mathrm{N} \,\big|\, \mathrm{Al}\cdot\mathrm{N}\cdot\mathrm{Al}\cdot\mathrm{N}\cdots$$

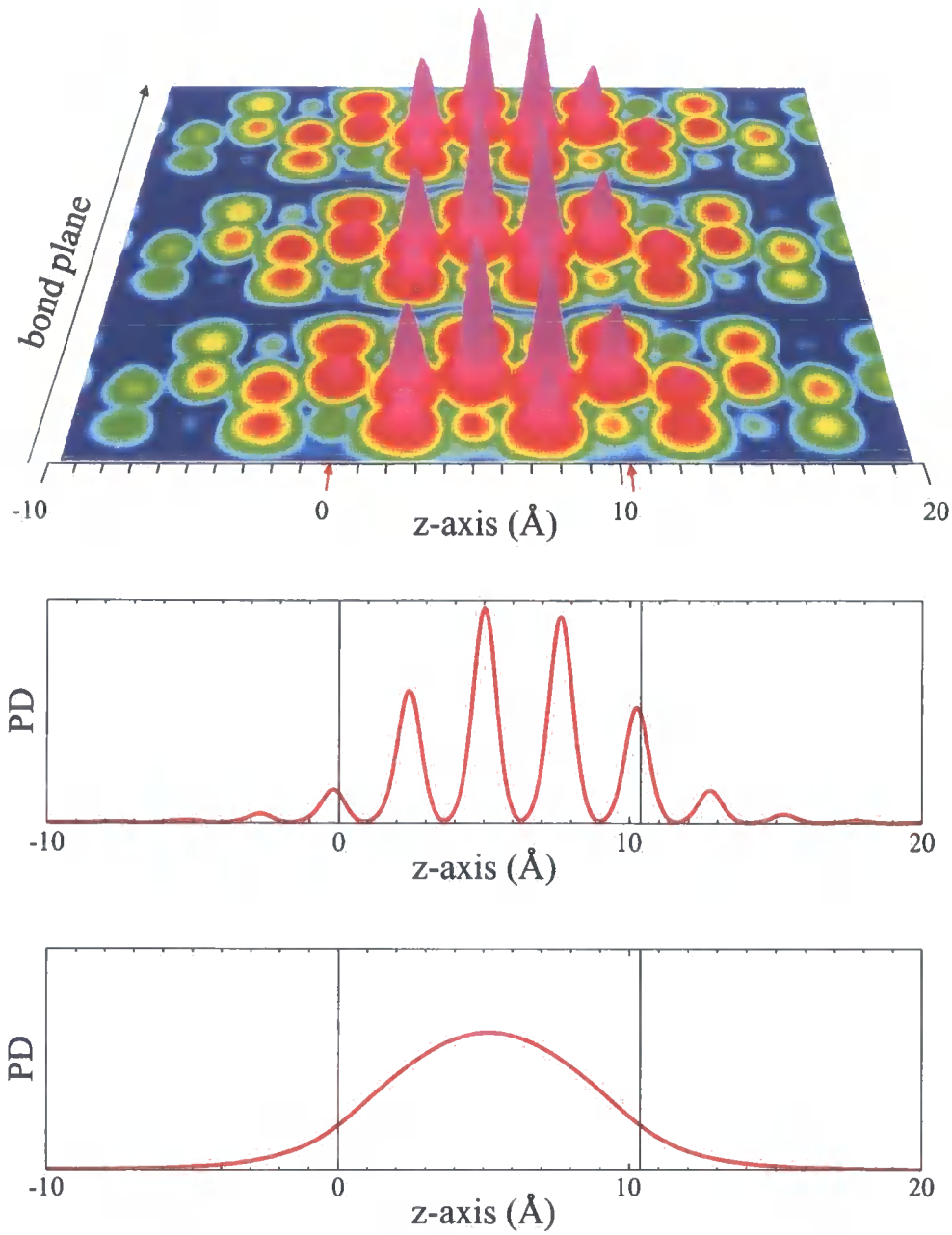

Figure 4.10: Top: Probability density of a slice through the bond plane of a 10.38Å wide $Al_{0.4}Ga_{0.6}N$-GaN-$Al_{0.4}Ga_{0.6}N$ quantum well. **Middle:** the resulting in-plane averaged probability density. **Bottom:** The corresponding envelope function from an effective mass calculation.

However, for wurtzite materials, the polar nature of the crystal provides the dominant contribution to the asymmetry and therefore such considerations are not required. The effect is especially noticeable for such a small well.

4.6 Electric fields

Quantum well systems are often subject to an electric field which can have a dramatic effect on the electronic and optical properties. An electric field, can be either applied as part of the working of the device, or it can be a *built-in* electric field due to an inherent polarisation or that derived from the piezoelectric or pyroelectric properties of the semiconductor layers. The field strength will normally vary in the different layers due to their different properties.

An electric field can be considered to produce a linear change with position z in the band profile of the quantum well, thus

$$V^{(l)}(z) = V_0^{(l)} - E_z^{(l)} z \tag{4.38}$$

where $V^{(l)}(z)$ is the potential when $E_z^{(l)}$ is the field strength in layer l, $V_0^{(l)}$ is the zero field potential. The sloped band profile causes any symmetry of the well to be broken and changes the bound state energies. This change of carrier energy is manifested in the quantum confined Stark effect (QCSE) which is the observed redshift (lowering) in the valence to conduction band energy transition of bound states due to the presence of an electric field. The redshift results from the decrease in energy difference, with increasing field, between the bottom of the valence band quantum well and the bottom of the conduction band quantum well. The asymmetric well profile gives rise to asymmetric wavefunctions, with an associated change in the optical transition rates.

4.6.1 Piezoelectricity

When strained, piezoelectric materials have a polarisation $\mathbf{P}^{pz}$ which is given in terms of the piezoelectric constants $e_{i,j}$ and the column form of the strain tensor ϵ_j (see equations (2.49)) by

$$\begin{bmatrix} P_x^{PZ} \\ P_y^{PZ} \\ P_z^{PZ} \end{bmatrix} = \begin{bmatrix} 0 & 0 & 0 & 0 & e_{15} & 0 \\ 0 & 0 & 0 & e_{15} & 0 & 0 \\ e_{31} & e_{31} & e_{33} & 0 & 0 & 0 \end{bmatrix} \cdot \begin{bmatrix} \epsilon_1 \\ \epsilon_2 \\ \epsilon_3 \\ \epsilon_4 \\ \epsilon_5 \\ \epsilon_6 \end{bmatrix} \tag{4.39}$$

4.6.2 Spontaneous polarisation

Spontaneous polarisation is also known as equilibrium polarisation or as pyroelectricity. The polarisation is caused by a movement of positive and negative charge to opposite ends of a crystal's polar axis due to a change in temperature. Spontaneous polarisation will therefore give rise to an electric field even if there is no strain. Pyroelectricity is observed to some extent in all crystals having a polar axis, although it is particularly strong in the nitrides, especially for AlN.

Experimental measurements of the strength of the electric field and therefore the level of spontaneous polarisation and the piezoelectric constants for the nitrides are still not particularly consistent. The temperature dependence of the pyroelectric contribution probably accounts for some of the disagreement. Different defect densities will also give rise to different effective strains and therefore different piezoelectric fields. The measurements are often based on photoluminescence measurements of a quantum well, and infer the polarisation induced electric field from comparisons with envelope function calculations. This approach requires the valence band offset and effective masses to be known accurately, which for a given alloy they may not be. In any case for many quantum well structures the envelope function approximation may not be entirely valid. Furthermore, it has been reported that the piezoelectric properties are non-linear with respect to strain and therefore alloy composition [26] and that there is a barrier and well width dependence on the field strength in nitride quantum wells [103]. However, most reports in the literature agree on one thing, that the fields are large. Fields of over 2.5MV/cm [84] are reported for InGaN quantum wells and even higher for AlGaN wells.

Experimental measurements tend to underestimate the polarisation induced sheet charge

densities and therefore the field strengths by about 50% [26,104] compared to theoretical predictions. The reasons for the reduced field strength found in practice are not entirely clear, but could be a result of indium alloy fluctuations [26], free carrier screening [26,105], partial neutralisation of charges at the sample surface by some adsorbates [106–108] or segregation of species at the quantum well boundaries during growth, giving non-planar interfaces [26,106]. This reduced field manifests itself in the quantitative disagreement between the experimental ground excitonic states and the values based on a theoretical field strength [109].

The theoretical calculations are not without problems, because the dipole of a periodic charge distribution is ill defined [110,111], which makes consistent theoretical calculations of the polarisation model-dependent [110]. *Ab-initio* calculations of polarisation have been performed [112,113] on the nitrides, and provide piezoelectric and pyroelectric coefficients, but still compare poorly to experimental measurements [26].

The total polarisation P_z due to spontaneous and piezoelectric polarisations, for a well layer, is given by [103]

$$P_z = P_b^{SP} - P_w^{SP} + P_z^{PZ} \tag{4.40}$$

where P_b^{SP} and P_w^{SP} are the barrier and well spontaneous polarisations and P_z^{PZ} is the piezoelectric polarisation in the z-direction. The corresponding electric field for a quantum well is given by [103]

$$E_z^b = -\frac{t_w P_z}{t_b \varepsilon_w + t_w \varepsilon_b} \tag{4.41}$$

$$E_z^w = -\frac{t_b P_z}{t_w \varepsilon_b + t_b \varepsilon_w} \tag{4.42}$$

with P_z given by (4.40). t_w and t_b are the well and barrier thicknesses and ε_w and ε_b are the dielectric constants. Equation (4.41) introduces a barrier thickness dependence for the field. However, in the limit of the barriers being considered infinite in extent, the field in the well region becomes:

$$E_z^w = -\frac{P_z}{\varepsilon_w} \tag{4.43}$$

The electric field in a nitride quantum well can be tuned to a certain extent by the barrier width dependence of the field strength [103], using temperature to affect the free carrier screening, modulation doping to screen the field [114] or simply the application of an external electric field [115]. Given the uncertainty in the field strengths and the possibility of tuning them to a certain extent the heterostructures treated in this work consider the field to be a parameter and the resultant effect of various field strengths on the heterostructures is explored.

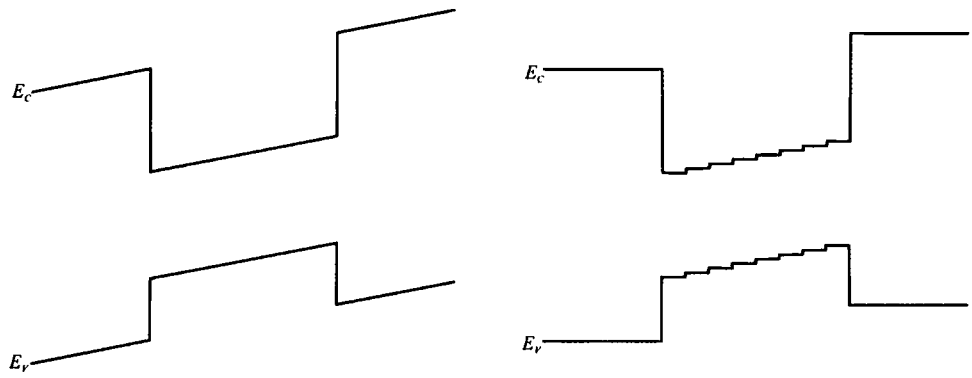

Figure 4.11: Schematic diagram showing the stepped approximation of the electric field.

4.6.3 Electric Fields within the EPM

Electric fields are included within the matching schemes of the EPM and envelope function methods by approximating the slope in the band edge caused by the fields as a series of small steps. Figure 4.11 illustrates this approach. In order to achieve truly bound states the barrier regions are kept field free, which is not a bad approximation provided the bound state wavefunction is concentrated in the well region. For the approximation to be accurate, the widths of the steps should be as small a possible. For the envelope function approach this is not a problem, but the EPM calculation includes the microscopic information of the atomic positions. While mathematically matching at the ionic cores is possible, from a physical point of view it can be argued that this is unphysical since the

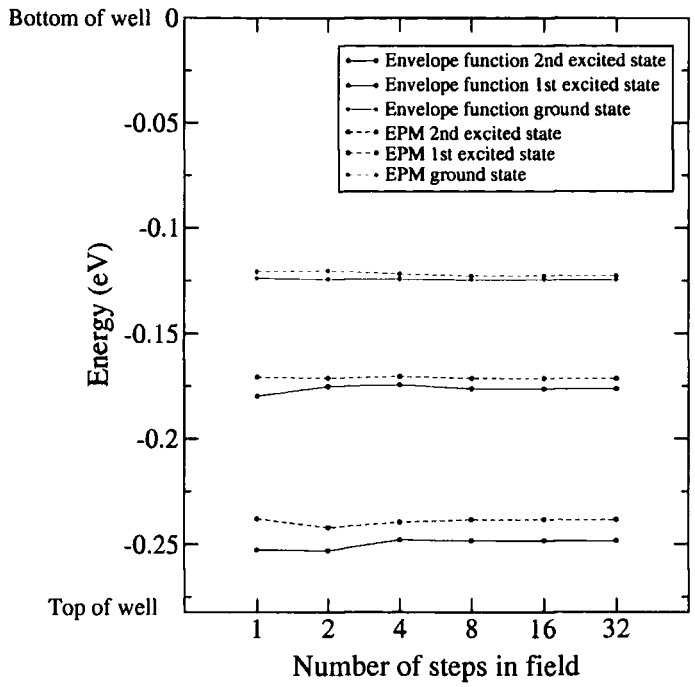

Figure 4.12: Convergence of bound state energy with increasing number of field steps for both an envelope calculation and an EPM calculation.

pseudopotential is only strictly valid away from the ionic cores. If the matching is only performed at the bond centre locations then this imposes a lower limit on the minimum width of a field step. In practice is is found that this is more than enough to make the approximation valid, even for the strong fields encountered in nitride quantum wells. Figure 4.12 describes the convergence of bound state energy with increasing number of field steps for both an envelope calculation and an EPM calculation. The variation of bound state energy with number of steps is surprisingly small, with adequate convergence achieved using just 8 steps. For the calculations presented in this work as many steps as is possible for the size of well under consideration will be used, while only performing the matching at the bond centre locations.

4.7 InGaN wells

$In_xGa_{1-x}N$ is primarily of interest as the active region in blue-green, single quantum well (SQW) light emitting diodes [5,116,117] and multiple quantum well laser diodes [5, 116,118]. In this work we concentrate on the $In_xGa_{1-x}N$ single quantum well system.

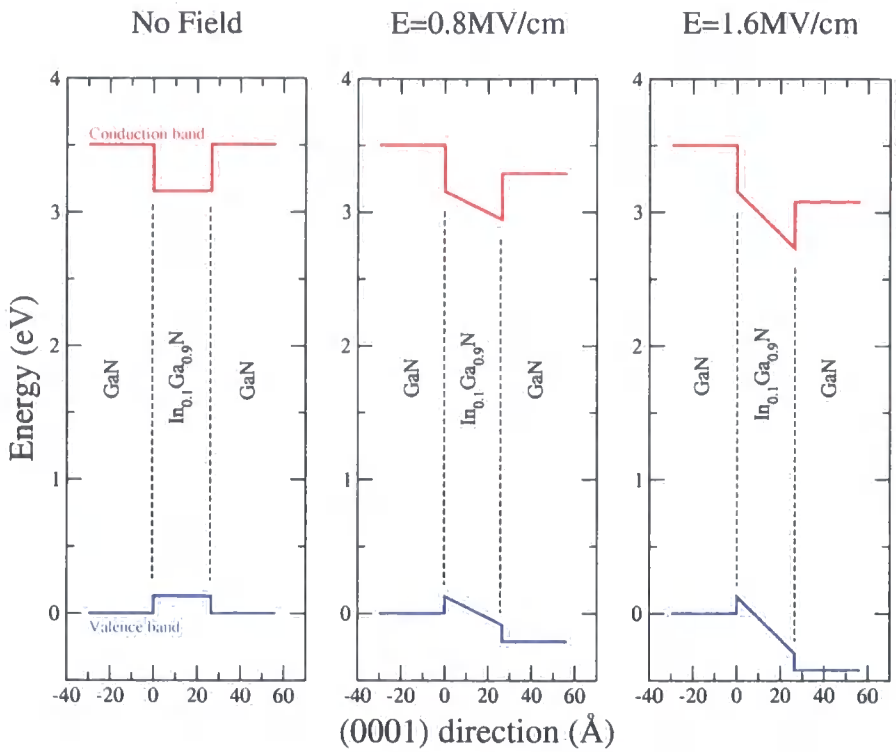

Figure 4.13: The profiles of a 5 unit cell wide $In_{0.1}Ga_{0.9}N$ conduction and valence band quantum well for a) No field b) 0.7MV/cm c) 1.6MV/cm

The GaN - $In_xGa_{1-x}N$ single quantum well system comprises an $In_xGa_{1-x}N$ well layer between two layers of GaN grown on a buffer layer, as shown by figure 4.13. The GaN region acts as a barrier confining the electron and hole bound states to the $In_xGa_{1-x}N$ well region, with the latter under biaxial compression. The difference in the GaN and InN a-lattice parameters, which are 3.19 Å and 3.544 Å respectively, lead to considerable strain in the quantum well even at low indium compositions. The resulting built-in electric field is dominated by the piezoelectric contribution, which is a function of the strain and therefore of the alloy composition. In practice the large InN/GaN lattice mismatch restricts GaN - $In_xGa_{1-x}N$ quantum wells to low indium compositions, with x rarely outside the 0.03-0.25 range. Within this range of compositions, wells up to 40nm thick can be grown pseudomorphically [83]. However, in most cases, the wells are considerably narrower to reduce the redshift of the quantum confined Stark effect.

Measured values for the built-in electric field within the well region of $In_xGa_{1-x}N$ quantum wells vary considerably. Experimental values are usually based on photoreflectance or photoluminescence measurements of the excitonic energy for a range of well widths, from

Material	Band Gap (eV)	VBO (eV)	CBO (eV)
$In_{0.2}Ga_{0.8}N$	2.612	0.252	0.636
$In_{0.15}Ga_{0.85}N$	2.810	0.189	0.501
$In_{0.1}Ga_{0.9}N$	3.028	0.126	0.346
$In_{0.05}Ga_{0.95}N$	3.267	0.063	0.170

Table 4.1: The barrier principal band gap and resultant band offsets for the InGaN quantum well system.

which envelope function or similar calculations are used to extract a field strength. These calculations require the band offset between the well and barrier materials, the principal band gap of both materials and the effective masses of both materials. Examples of derived electric fields for an $In_{0.1}Ga_{0.9}N$ quantum well, assuming a linear variation of field strength with x, include 0.62MV/cm [2,83,119], 0.9MV/cm [120], 0.6MV/cm [116], 0.8MV/cm [84,121], 0.98MV/cm [122], 1.25MV/cm [22] and 1.4MV/cm [123]. Theoretical values, based on *ab-initio* calculations of bulk materials consistently overestimate the experimental results; for example the field in a $In_{0.1}Ga_{0.9}N$ quantum well is given as 1.63MV/cm [3,105,112,113,124]. The profile of a quantum well with electric fields of 0.8MV/cm and 1.6MV/cm is illustrated in figure 4.13.

The band offsets between the well region and the barriers used in this work are derived from the photoluminescence measurements of Manz *et al* [125] and assume a linear variation of offsets with indium composition x. The value of the valence band offset for $x = 0.1$ is 0.126eV and corresponds to a type I quantum well with a valence band offset to conduction band offset ratio of 27% to 73%. All the band offsets used are given in table 4.1.

4.7.1 Energy vs well width

Figures 4.14-4.17 show plots of bound state energy against well width for a range of values of electric field calculated by both the complex bandstructure method outlined in this chapter and a single band effective mass mass model. In order to make a relevant comparison, the effective masses used in the single band effective mass mass model were derived from the empirical pseudopotential bulk bandstructures used in the generation of the the complex bandstructures. The valence band quantum wells do not include heavy and

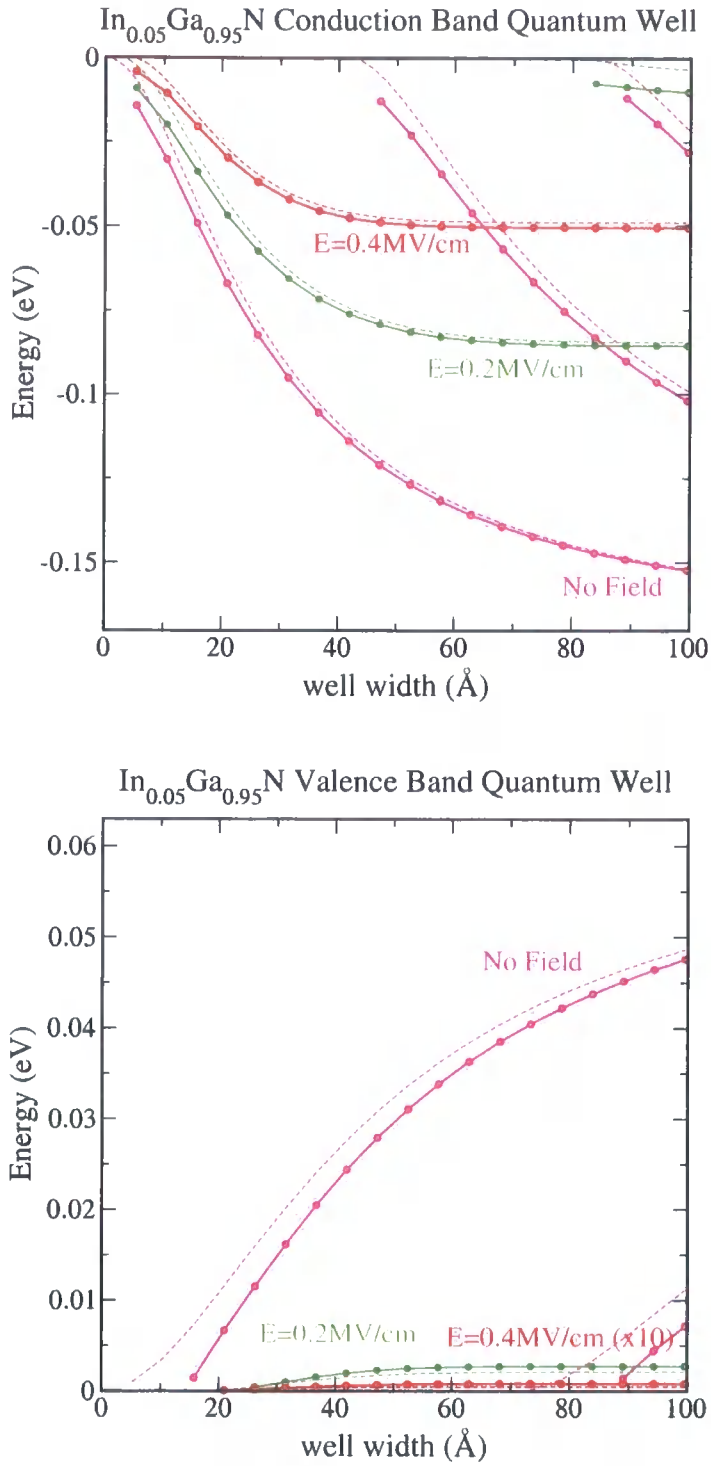

Figure 4.14: The variation of bound state energy with well width of a conduction (top) and valence band (bottom) $In_{0.05}Ga_{0.95}N$ quantum well, for different strengths of built-in electric field. The solid lines represent EPM calculations and the dashed lines represent envelope function calculations with effective mass derived from the EPM. Energies are in eV, with 0eV as the top of the well, 0.063eV at the bottom of the valence band well and -0.170eV at the bottom of the conduction band well. The valence band energies for E=0.4MV/cm are magnified by a factor of 10.

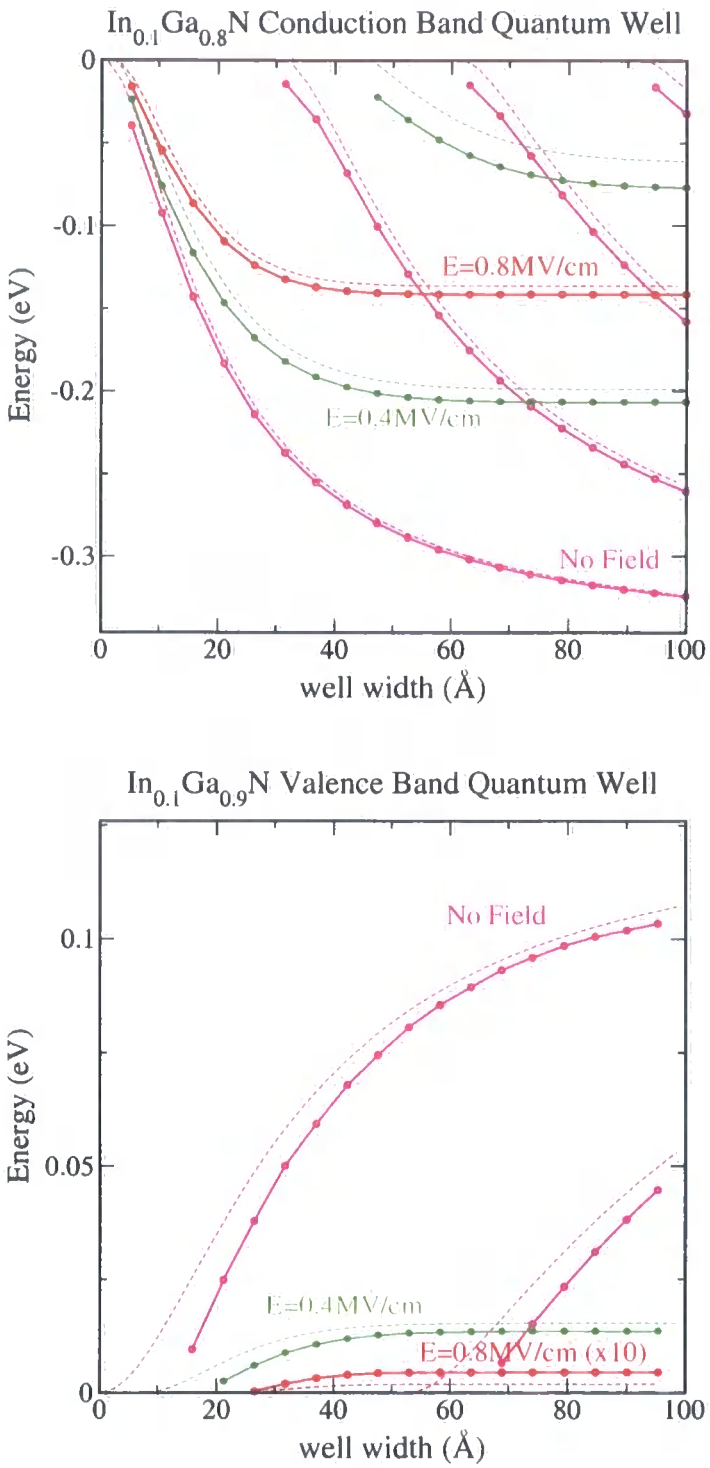

Figure 4.15: The variation of bound state energy with well width of a conduction (top) and valence band (bottom) $In_{0.1}Ga_{0.9}N$ quantum well, for different strengths of built-in electric field. The solid lines represent EPM calculations and the dashed lines represent envelope function calculations with effective mass derived from the EPM. Energies are in eV, with 0eV as the top of the well, 0.126eV at the bottom of the valence band well and -0.3465eV at the bottom of the conduction band well. The valence band energies for E=0.8MV/cm are magnified by a factor of 10.

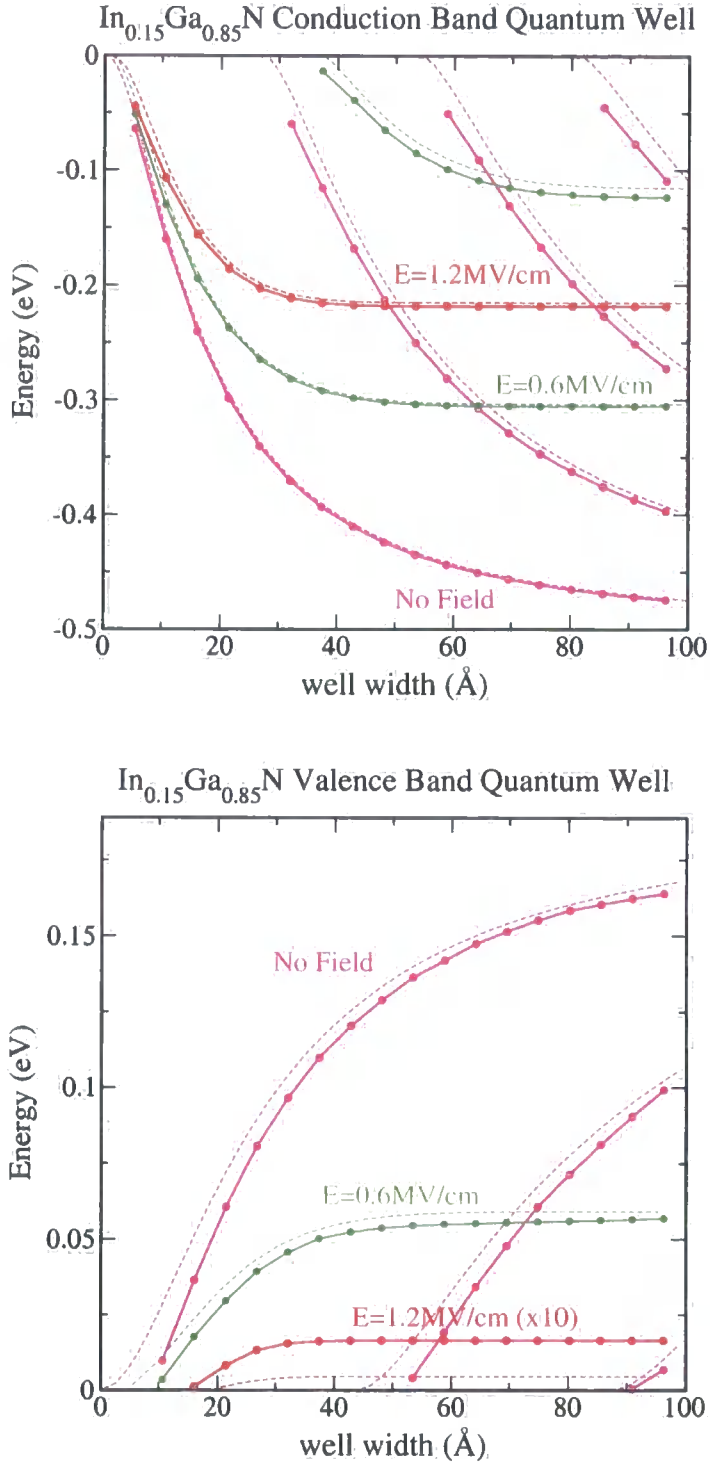

Figure 4.16: The variation of bound state energy with well width of a conduction (top) and valence band (bottom) $In_{0.15}Ga_{0.85}N$ quantum well, for different strengths of built-in electric field. The solid lines represent EPM calculations and the dashed lines represent envelope function calculations with effective mass derived from the EPM. Energies are in eV, with 0eV as the top of the well, 0.189eV at the bottom of the valence band well and -0.5005eV at the bottom of the conduction band well. The valence band energies for E=1.2MV/cm are magnified by a factor of 10.

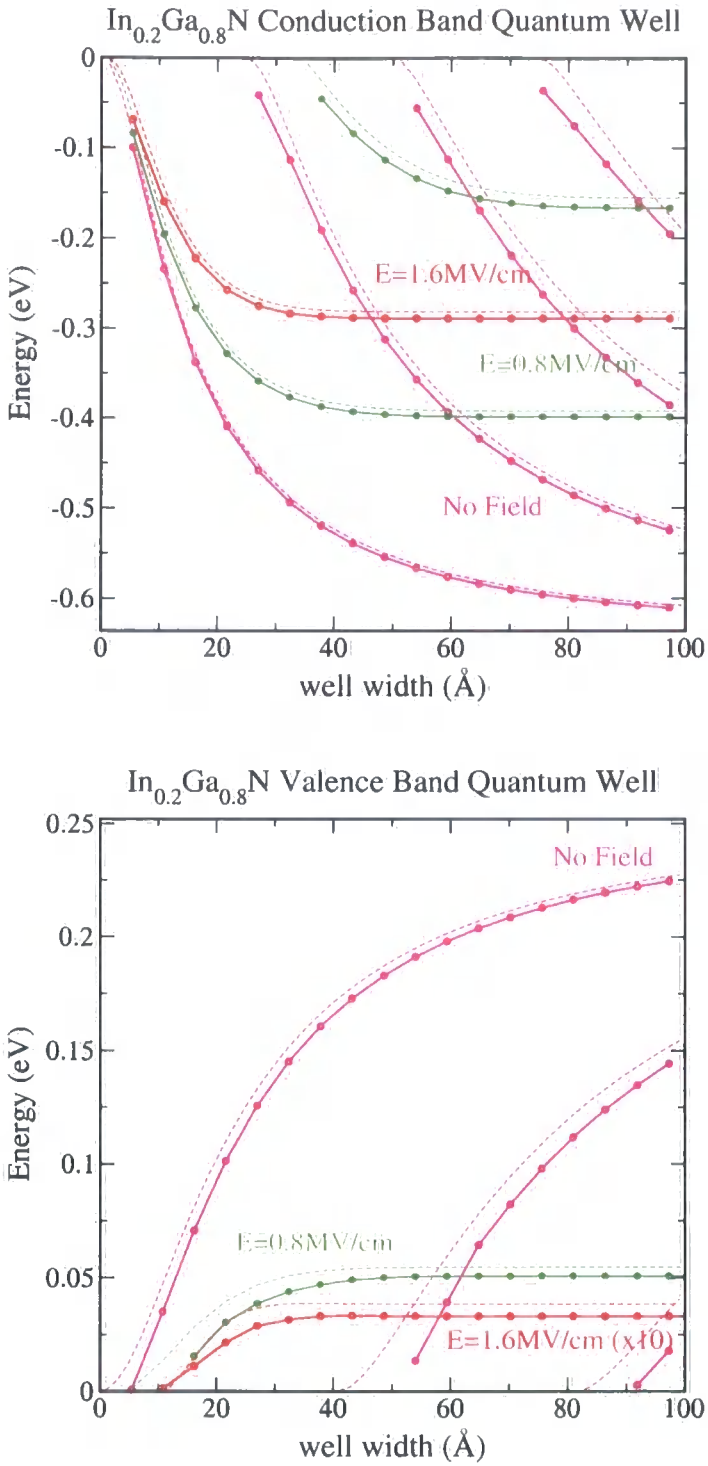

Figure 4.17: The variation of bound state energy with well width of a conduction (top) and valence band (bottom) $In_{0.2}Ga_{0.8}N$ quantum well, for different strengths of built-in electric field. The solid lines represent EPM calculations and the dashed lines represent envelope function calculations with effective mass derived from the EPM. Energies are in eV, with 0eV as the top of the well, 0.252eV at the bottom of the valence band well and -0.6359eV at the bottom of the conduction band well. The valence band energies for E=1.6MV/cm are magnified by a factor of 10.

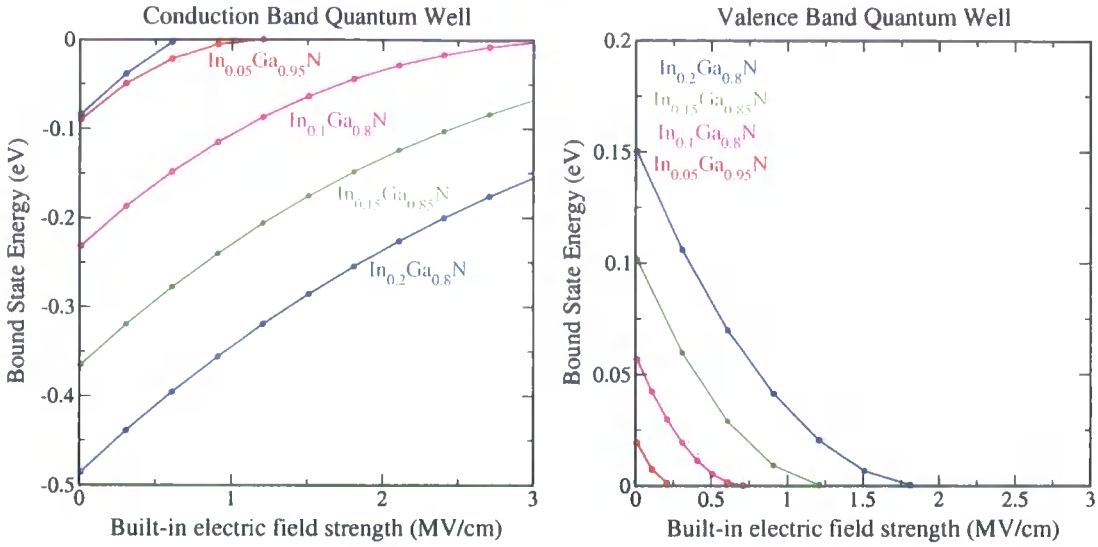

Figure 4.18: The variation of bound state energies with increasing electric field for a 6 unit cell wide $In_xGa_{1-x}N$ quantum well.

light hole bound states because the valence band offset is smaller than the energy difference between the crystal-hole band as the top valence band and the heavy hole band. The quantum well bound states are therefore entirely due to the crystal hole and very little band mixing is present. The deviation of the complex bandstructure energies from the single band effective mass energies is a measure of the non-parabolic bandstructure and the extent of band mixing that occurs. It can be seen from figures 4.14-4.17 that, in general, the complex bandstructure results are in good agreement with the single band effective mass energies. The agreement is better near the bottom of the well for the ground states and for larger well widths. At the top of the well the deviation of the well region bandstructure from a parabolic form is more noticeable and results in a less accurate effective mass bound state energy. The same argument is true for thinner wells in which the energies are closer to the top of the well.

The quantum wells with higher indium composition have a larger valence band offset and both deeper valence and conduction band quantum wells. The deeper wells give rise to bound state energies further from the tops of the wells and for the lower values of built-in electric field more than one bound state is predicted.

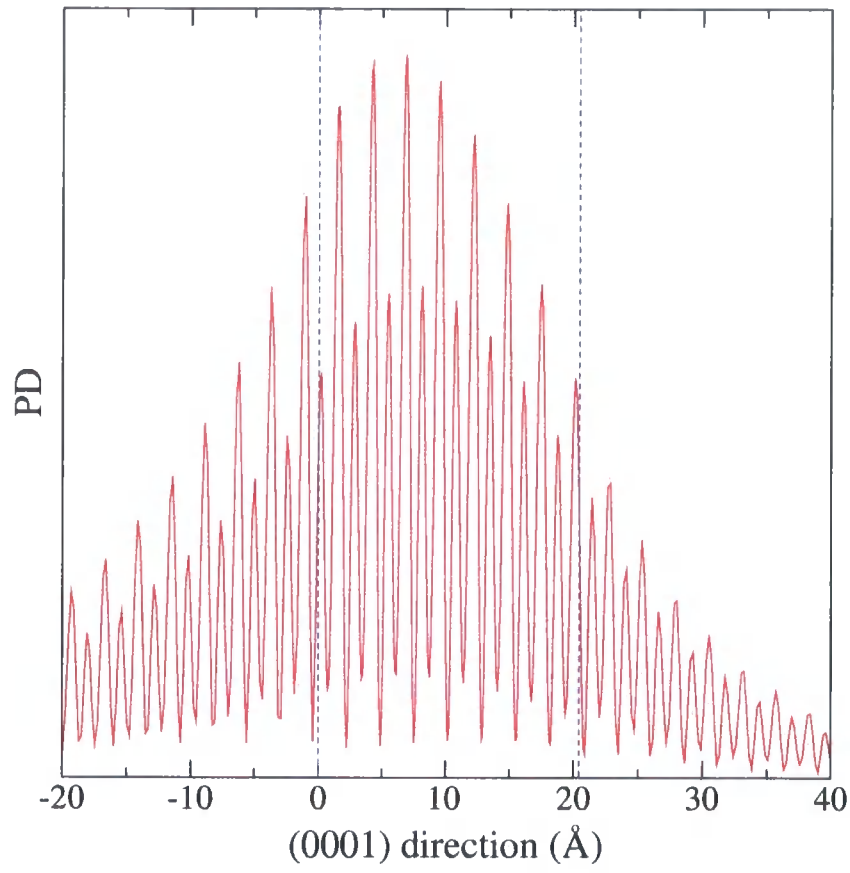

Figure 4.19: The in-plane averaged probability density for the ground state of a 4 unit cell wide $In_{0.1}Ga_{0.9}N$ quantum well.

4.7.2 Effect of built in electric-field

Figures 4.14-4.17 show the bound state energies for zero field and two different values of built-in electric field. The field values are increased linearly with increasing indium composition to allow a meaningful comparison between wells composed of different alloys. The field strengths used are approximately at 50% and 100% of the experimentally observed values. For instance the field strengths used for $In_{0.1}Ga_{0.9}N$ are 0.4MV/cm and 0.8MV/cm.

For wells with a built-in field the variation of bound state energy with well width is observed to level off and much less change in the energy is observed for the wider wells. The presence of the electric field causes the triangular well region to act as its own barrier confining the bound state to one side of a triangular quantum well. The barrier on the other side is therefore less and less important for the confinement as the width of the well increases.

The bound states in the presence of a field are at considerably higher confinement energies, i.e. closer to the top of the quantum well. This is most noticeable for the valence band wells where for the higher value of field the states are at the very top of the well. States so close to the top of a quantum well are only very loosely bound and are likely to result in large fraction of the integrated probability density in the barrier regions. Accurately establishing the energy of these states proved problematic as only a finite grid of energies was employed and often this was not accurate enough to detect a state so close to the top of the well. In these cases a finer grid was employed in over a small energy range near the top of the well, but this was computationally quite expensive. The higher values of electric field give rise to states closer to the top of the well and therefore were more problematic in this respect. Figure 4.18 illustrates this by showing the variation of bound state energies with increasing field strength for a quantum well with a width of 6 unit cells.

The wavefunction of a bound state in a strongly asymmetric well is itself strongly asymmetric and this effect is quite dramatic for the nitride quantum wells. Under the influence of a field the well profile is clearly asymmetric and the resultant probability densities are shifted by the field to one side of the well (see figure 4.19).

4.7.3 In-plane bandstructure

In chapter 3 the complex bandstructure was described for a range of non-zero in-plane wavevectors. This complex bandstructure can be used to calculate the in-plane subband-

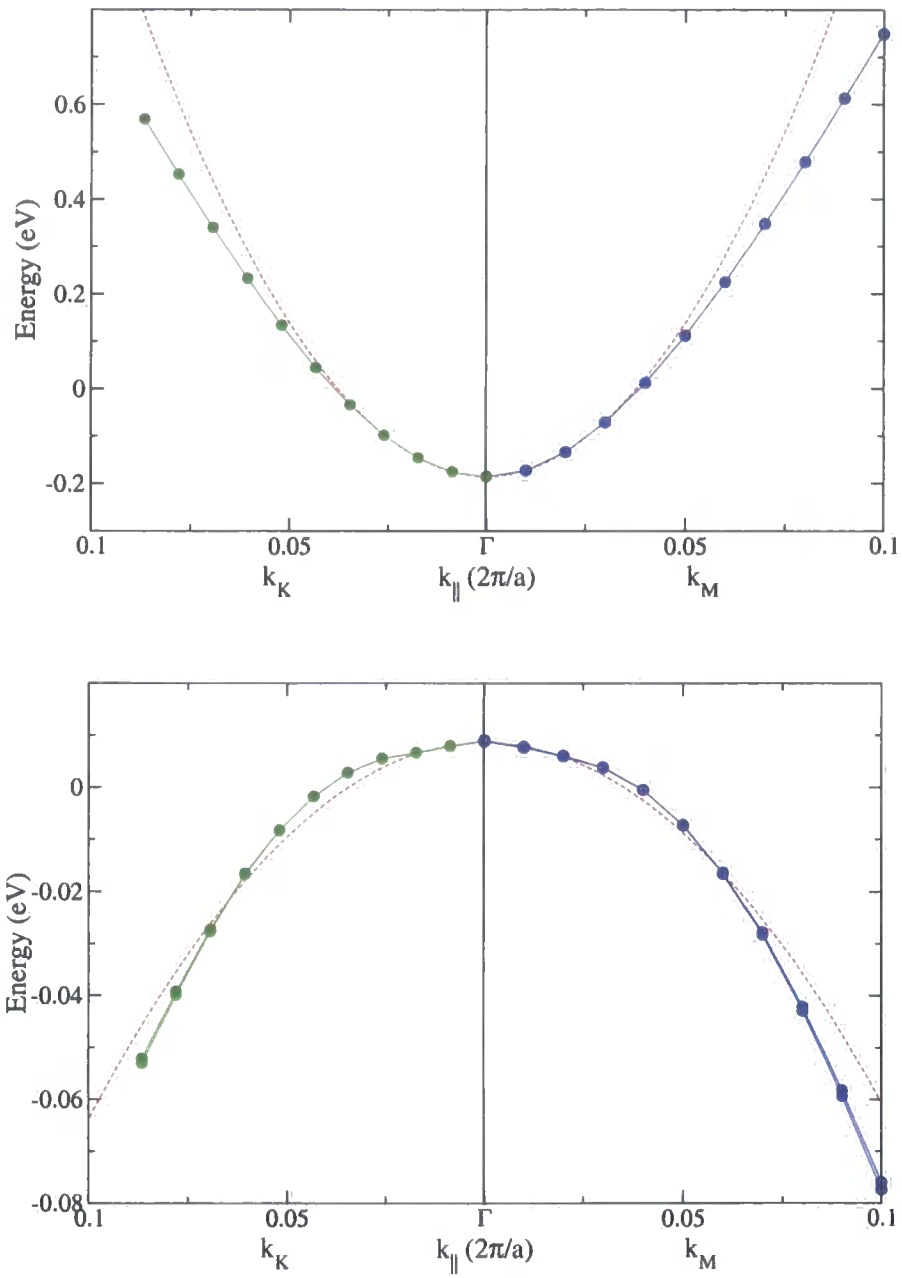

Figure 4.20: The in-plane bandstructure for a 6 unit cell wide conduction (top) and valence (bottom) band $In_{0.1}Ga_{0.9}N$ quantum well. The green circles mark the in-plane bound state energy (in eV), with respect to the top of the well at Γ, for $\mathbf{k}_{||}$ in the in-plane direction of high symmetry point M and the red circles in the in-plane direction of high symmetry point K. The dashed lines display a parabola for comparison.

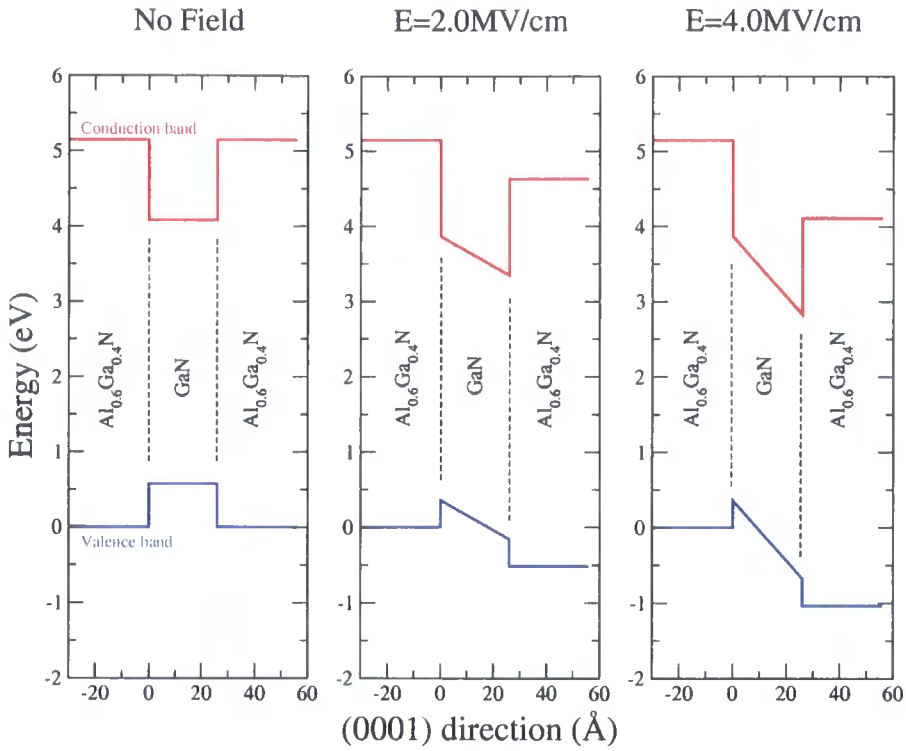

Figure 4.21: The profiles of a $Al_{0.6}Ga_{0.4}N$ conduction and valence band quantum well for a) No field b) 2MV/cm c) 4MV/cm

structure of a given quantum well by simply applying the same matching procedures as described in section 4.5.1 and scanning over an appropriate energy range. The resultant in-plane bandstructure for an $In_{0.1}Ga_{0.9}N$ quantum well with a width of 6 unit cells is displayed in figure 4.20. The energy dispersion is plotted as a function of the magnitude of the in-plane wavevector. The in-plane energies in the $\Gamma-A$ and $\Gamma-K$ directions is very similar, indicating an essentially isotropic in-plane bandstructure. Some splitting is observed for values of $\mathbf{k}_{||}$ away from the high symmetry point of Γ, although this is very small and to a good approximation the system can be considered spin degenerate. The subband energies vary quadratically for very small $k_{||}$ but deviate noticeably at larger values. The non-parabolicity of the in-plane energy dispersion is illustrated by comparison to parabolic curves which were fitted to values of the subband energy close to Γ.

4.8 AlGaN wells

One of the motivations for studying the high Al content, $Al_xGa_{1-x}N$ - GaN quantum well system, is because the deep (~1-2eV) conduction band well gives rise to multiple subbands between which inter-subband transitions (ISBT) have been observed [126]. Unlike the InGaN system, the strong built-in electric fields due to piezoelectricity and pyroelectricity do not always adversely affect the transition probabilities and in fact allow what would otherwise be forbidden transitions to take place due to the symmetry breaking of the well potential. ISBTs in GaAs quantum wells have possible application for infrared (IR) detectors and quantum cascade (QC) lasers [126–128] and similar applications are possible for ISBTs in the $Al_xGa_{1-x}N$ - GaN quantum well system. It has also been suggested that a technologically important terahertz frequency laser could be based on $Al_{0.75}Ga_{0.25}N$ quantum well ISBTs [129].

The $Al_xGa_{1-x}N$ - GaN quantum well system is, like the $In_xGa_{1-x}N$-GaN system, grown on a GaN buffer and so the whole system is still held at the in-plane lattice constant of GaN. However, unlike the $In_xGa_{1-x}N$-GaN system, the alloy $Al_xGa_{1-x}N$ forms the barrier region for both the conduction and valence bands and GaN forms the well region (see figure 4.21). The smaller a-lattice constant of AlN mean that the barriers are under biaxial tensile strain, while the GaN well layers are unstrained. The magnitude of lattice mismatch between GaN and AlN, and therefore the magnitude of strain, is significantly less in an $Al_xGa_{1-x}N$ - GaN system than the $In_xGa_{1-x}N$ system. The alloy therefore often has substantial aluminium fraction, with quantum wells across the whole composition range reported. Piezoelectric fields occur in the barrier regions and spontaneous polarisation is considered to contribute significantly. The resultant field in the well region can be very strong indeed; up to 4MV/cm. As with $In_xGa_{1-x}N$, there is strong disagreement between the experimentally determined built-in electric fields and those based on theoretical calculations of bulk materials [5]. Examples of experimental estimates of the field in an $Al_{0.6}Ga_{0.4}N$ quantum well include 3.75MV/cm [130], 2.5MV/cm [22,131], 3.42MV/cm [129], 2MV/cm [132], 1.6MV/cm [126] and 3.33MV/cm [106]. The theoretical calculations predict a field of 4.0MV/cm [3,112,113,124,132,133]

The difference between the band gap of AlN and GaN is generally considered to be contained mostly in the conduction band offset, with the valence band offset being compar-

Material	Band Gap (eV)	VBO (eV)	CBO (eV)
AlN	6.083	0.568	2.015
$Al_{0.8}Ga_{0.2}N$	5.627	0.468	1.659
$Al_{0.6}Ga_{0.4}N$	5.141	0.361	1.280
$Al_{0.4}Ga_{0.6}N$	4.625	0.247	0.877
$Al_{0.2}Ga_{0.8}N$	4.104	0.133	0.471

Table 4.2: The barrier principal band gap and resultant band offsets for the AlGaN quantum well system.

atively small [5]. Conduction band offset to valence band offset ratios of between 94% : 6% [40,134] 65% : 35% and [44,81] are reported. In this work we use a conduction band offset to valence band offset ratio of 78% : 22% consistent with the x-ray photoemission spectroscopy measurements of Martin *et al* [81]. This gives rise to conduction band wells as deep as 2eV for AlN/GaN quantum wells, as shown in Table 4.2.

4.8.1 Bound States

The bound states of conduction band $Al_xGa_{1-x}N$ quantum wells as a function of width, alloy composition and field strength are presented in figures 4.22-4.24. The deep (0.877eV-1.659eV) wells give rise to more than one conduction subband, even at the strongest field and with zero field up to 8 subbands are predicted. Unlike the $In_xGa_{1-x}N$ quantum well system, the $Al_xGa_{1-x}N$ alloy is in the barrier regions and therefore the changing alloy has less of an effect on the bound states. The effect of the changing band offset and therefore well depth dominates the variation of bound state energy with increasing aluminium composition.

The results are in good general agreement with those calculated by an effective mass model (indicated by dashed lines on figures 4.22-4.24). The complex bandstructure bound state energies are consistently lower (further from the top of the well) than the effective mass energies and consequently any predicted intra-subband transitions (ISBTs) have slightly lower energies. The good agreement with effective mass theory is again because off the highly parabolic conduction band and general lack of mixing between the states. As with the InGaN quantum wells, the presence of a field gives rise to a levelling out of the bound state energies as the well width increases. The fields applied in figures 4.22-4.24 correspond

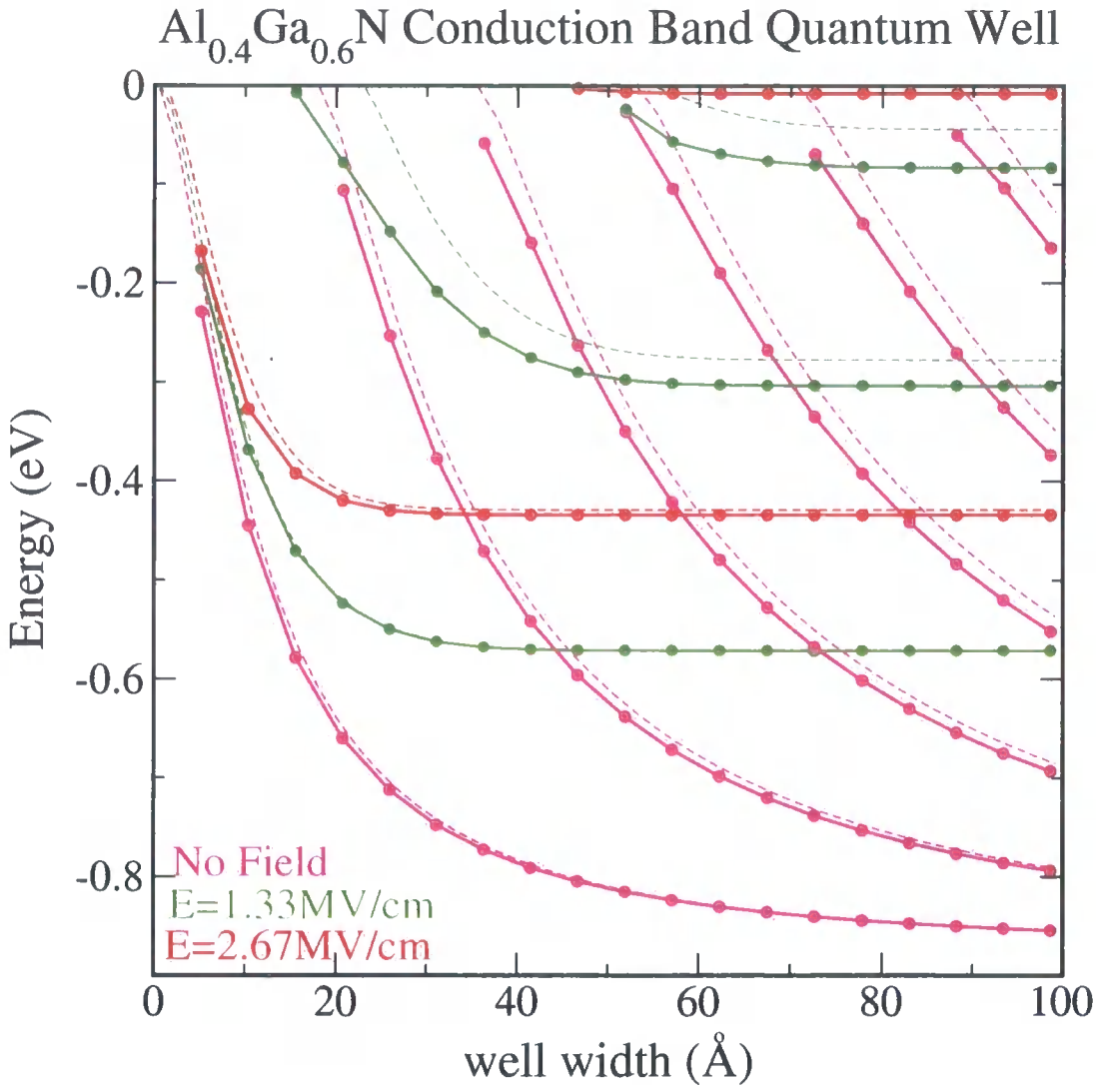

Figure 4.22: The variation of bound state energy with well width of a conduction band $Al_{0.4}Ga_{0.6}N$ quantum well, for different strengths of built-in electric field. The solid lines represent EPM calculations and the dashed lines represent envelope function calculations with effective masses derives from the EPM. Energies are in eV, with 0eV as the top of the well, -0.877eV at the bottom of the conduction band well.

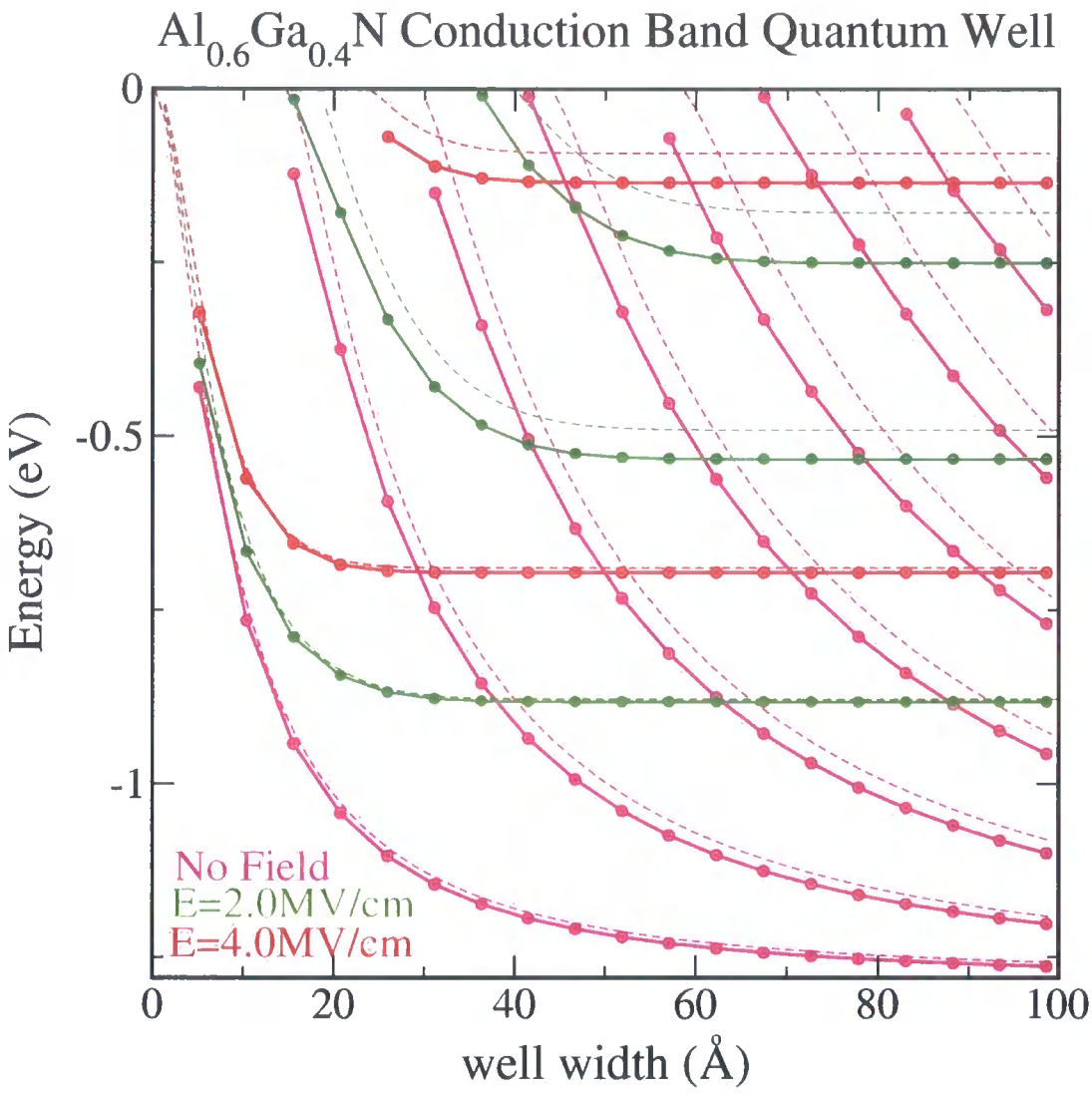

Figure 4.23: The variation of bound state energy with well width of a conduction band $Al_{0.6}Ga_{0.4}N$ quantum well, for different strengths of built-in electric field. The solid lines represent EPM calculations and the dashed lines represent envelope function calculations with effective masses derives from the EPM. Energies are in eV, with 0eV as the top of the well, -1.280eV at the bottom of the conduction band well.

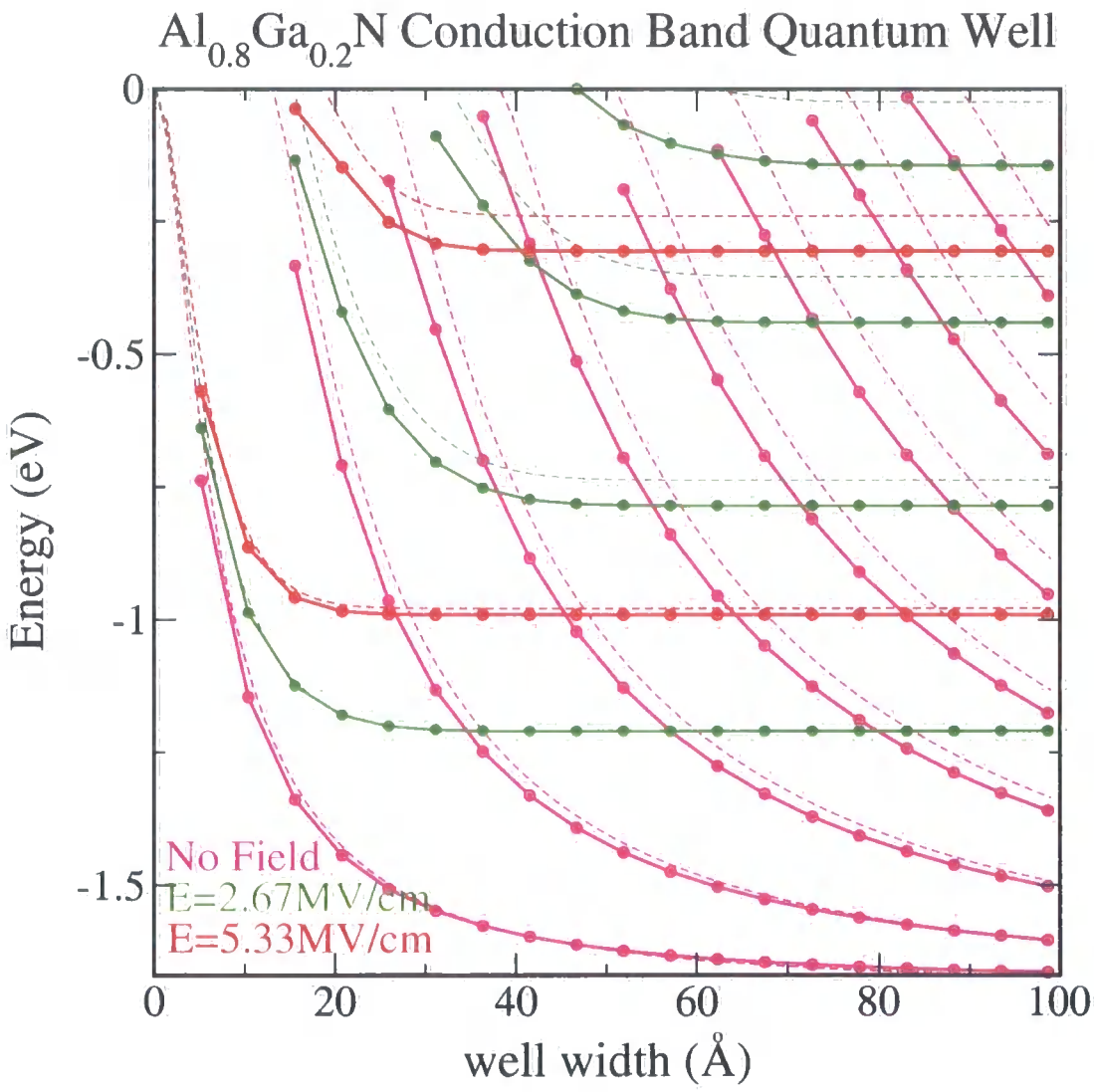

Figure 4.24: The variation of bound state energy with well width of a conduction band $Al_{0.8}Ga_{0.2}N$ quantum well, for different strengths of built-in electric field. The solid lines represent EPM calculations and the dashed lines represent envelope function calculations with effective masses derives from the EPM. Energies are in eV, with 0eV as the top of the well, -1.659eV at the bottom of the conduction band well.

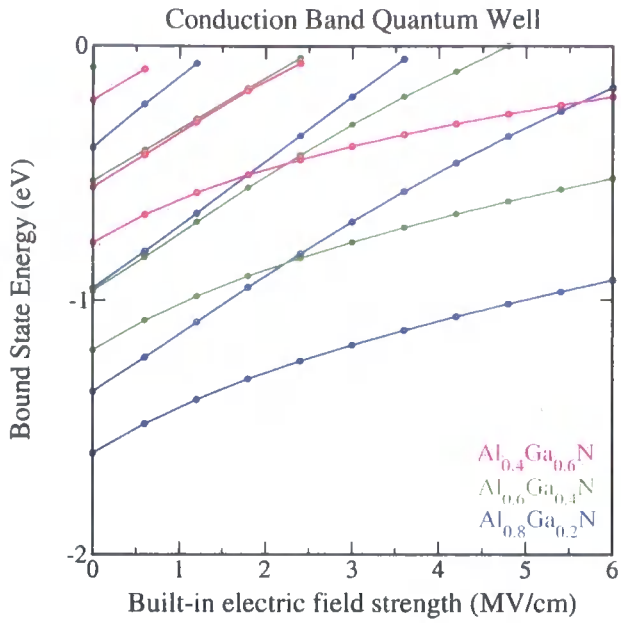

Figure 4.25: The variation of bound state energies with increasing electric field for a 8.5 unit cell wide $Al_xGa_{1-x}N$ quantum well.

to approximately 50% and 100% of the theoretically predicted values. As was noted in sections 4.6.3 and 4.8 the experimental observed fields in AlGaN quantum wells vary considerably and are of the order ~50% of the theoretical values. Therefore the two different field strengths in figures 4.22-4.24 approximately correspond to the theoretical and experimental values. It would appear that the theoretical field is incorrect because transitions between the ground and 2nd excited state have been observed in an $Al_{0.56}Ga_{0.44}N$ quantum well and both the complex bandstructure and effective mass calculations only predict 2 conduction subband states at the higher value of field (4MV/cm) [126]. Three subbands are predicted for 2MV/cm, in agreement with experiment.

A stronger value of field raises the bound state energies, but the deeper AlGaN wells do not suffer the same pinning by the field, of the ground state to the top of the well, observed in the InGaN wells. Figure 4.25 shows the variation of bound state energy with built-in electric field, for an $Al_{0.6}Ga_{0.4}N$ quantum well which is 8.5 units cells wide, and indicates the rise in the bound state energy as the field increases. It is interesting to note the effect of the field on the ISBT energies (figure 4.26). The 1st, 2nd and 3rd subbands are labelled E_1, E_2 and E_3 respectively and figure 4.26 shows a reduction in the $E_2 - E_3$ transition energy as the $E_1 - E_3$ and $E_1 - E_2$ transition energies increase. At approximately the experimentally

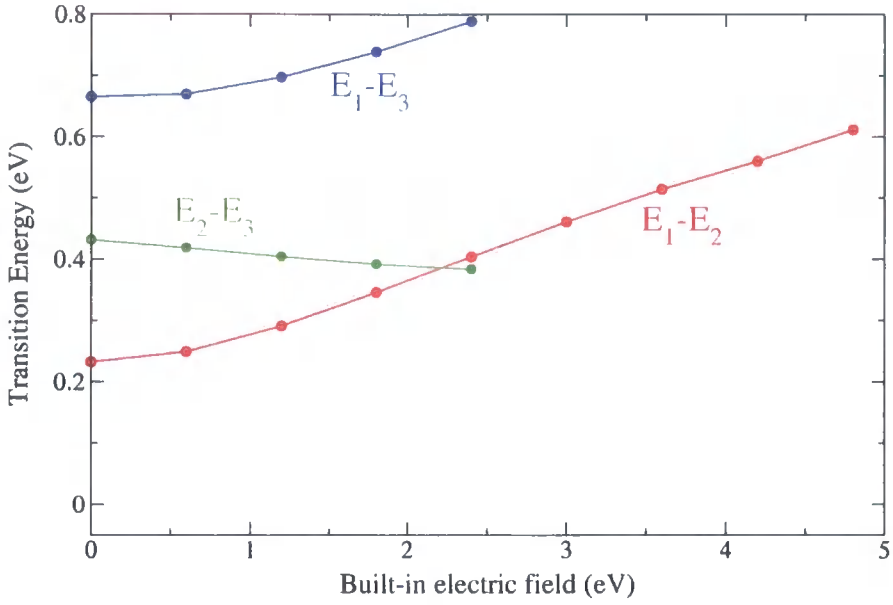

Figure 4.26: The inter-subband transition energies as a function of built-in electric field for a 8.5 unit cell wide conduction band $Al_{0.6}Ga_{0.4}N$ quantum well.

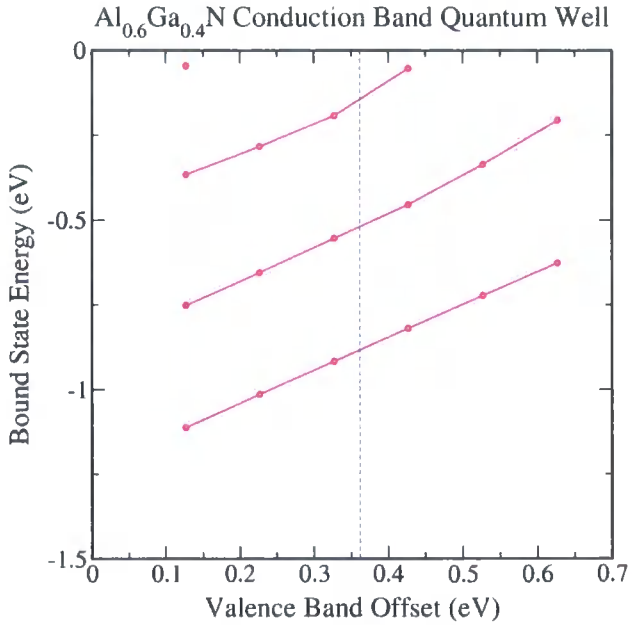

Figure 4.27: The bound state energies as a function of valence band offset for a 8.5 unit cell wide conduction band $Al_{0.6}Ga_{0.4}N$ quantum well. The value of valence band offset for $Al_{0.6}Ga_{0.4}N$ used in this work is indicated by the dashed line.

observed field strength of 2MV/cm the $E_1 - E_2$ and the $E_2 - E_3$ transitions are of similar values (i.e. the subbands are approximately evenly spaced in energy).

Comparison with experimental measurements is difficult because of the uncertainty in the parameters used in the theoretical model, especially the field strength and the band offset. The problem is principally in what field strength to use for the comparison, since the experimental value is obtained by fitting effective mass model energies to experimental transitions by varying the field. Consequently a comparison between the complex bandstructure transition energies to experimental values at the experimentally quoted field implicitly involves the effective mass model. For instance, Suzuki and Iizuka [132] observed an $E_1 - E_2$ transition energy of 0.35eV for 6nm $Al_{0.65}Ga_{0.35}N$ quantum wells. A complex bandstructure calculation with a field of 2.2MV/cm predicts the same transition energy, which can be compared to their effective mass derived field of 2.0MV/cm. Similarly the results of Hoshino *et al* indicate an $E_1 - E_2$ transition energy of 0.3eV and an $E_1 - E_3$ transition energy of 0.61eV for 4.4nm wide, $Al_{0.56}Ga_{0.44}N$ quantum wells. A complex bandstructure calculation with a field of 1.5MV/cm gives rise to an $E_1 - E_2$ transition energy of 0.3eV and an $E_1 - E_3$ transition of 0.7eV. Hoshino *et al* estimate the field as 1.6MV/cm from effective mass calculations. Any comparison of theory and experiment is also somewhat confused by the value of band offset and therefore the well depth used. Figure 4.27 describes the calculated bound state energies as a function of valence band offset for a 8.5 unit cell wide conduction band $Al_{0.6}Ga_{0.4}N$ quantum well. The band offset strongly affects the bound state energies and will clearly have an impact on any estimated field strength.

Very few theoretical calculations have been performed on the conduction band $Al_xGa_{1-x}N$ single quantum well system with which to make a relevant comparison. One interesting approach taken by Liu *et al* [129] is to calculate the potential of an $Al_{0.75}Ga_{0.25}N$ quantum well self-consistently. With such an approach they predict some band bending and and estimate the field to be approximately 4.28MV/cm. From these values they report an $E_1 - E_3$ transition energy of 0.795eV compared to a complex bandstructure calculated transition of 0.88eV at the same field strength, width and well depth.

The complex bandstructure calculations of bound state energies are in excellent agreement with effective mass calculations, and in good qualitative agreement with experimental measurements and self-consistent calculations. It is therefore reasonable to suggest that, due

to the more complete bandstructure informations used in the complex bandstructure calculations, the field strengths inferred by this approach are likely to be more accurate that those based on the simple effective mass calculations. The difference in the field values predicted from experimental data is small and not, however enough to account for the wide discrepancy in the theoretical and experimental values.

4.8.2 Probability densities

Figure 4.28 shows the in-plane averaged probability densities for the ground state, and 1st and 2nd excited states of a 8.5 unit cell wide $Al_{0.6}Ga_{0.4}N$ quantum well under the influence of a built-in electric field of 2MV/cm. The overall shapes of the densities are notably asymmetric as a result of the triangular potential caused by the field.

4.8.3 In-plane Bandstructure

Figure 4.29 displays the in-plane bandstructure for an 8.5 unit cell wide $Al_{0.6}Ga_{0.4}N$ conduction band quantum well. As with the InGaN quantum well, the in-plane energy dispersion is almost isotropic. Any splitting for in-plane wavevectors away from the Γ point was not resolved in the finite energy sampling used to locate the bound state solutions and is therefore less than 20meV. The dashed lines of parabolic dispersion indicate the degree of non-parabolicity. Figure 4.30 indicates the ISBT energies as a function of magnitude of in-plane wavevector, and at the larger wavevectors these clearly deviate strongly from those of parabolic subbands.

Joint Density of States

The joint density of state (JDOS) is related to the density of states and represents the "density of transitions" between two subbands in a quantum well. It is required for calculation of the rate of transitions between the two subbands, that might result from optical excitation or some other perturbing influence. For an ideal quantum well with parabolic subbands, the form of the joint density of states $g_{if}(E)$ is that of a step function. For the quantum wells considered in this work the subbands may not even be approximately parabolic and therefore $g_{if}(E)$ must be calculated over a range of in-plane wavevectors. The joint density of states

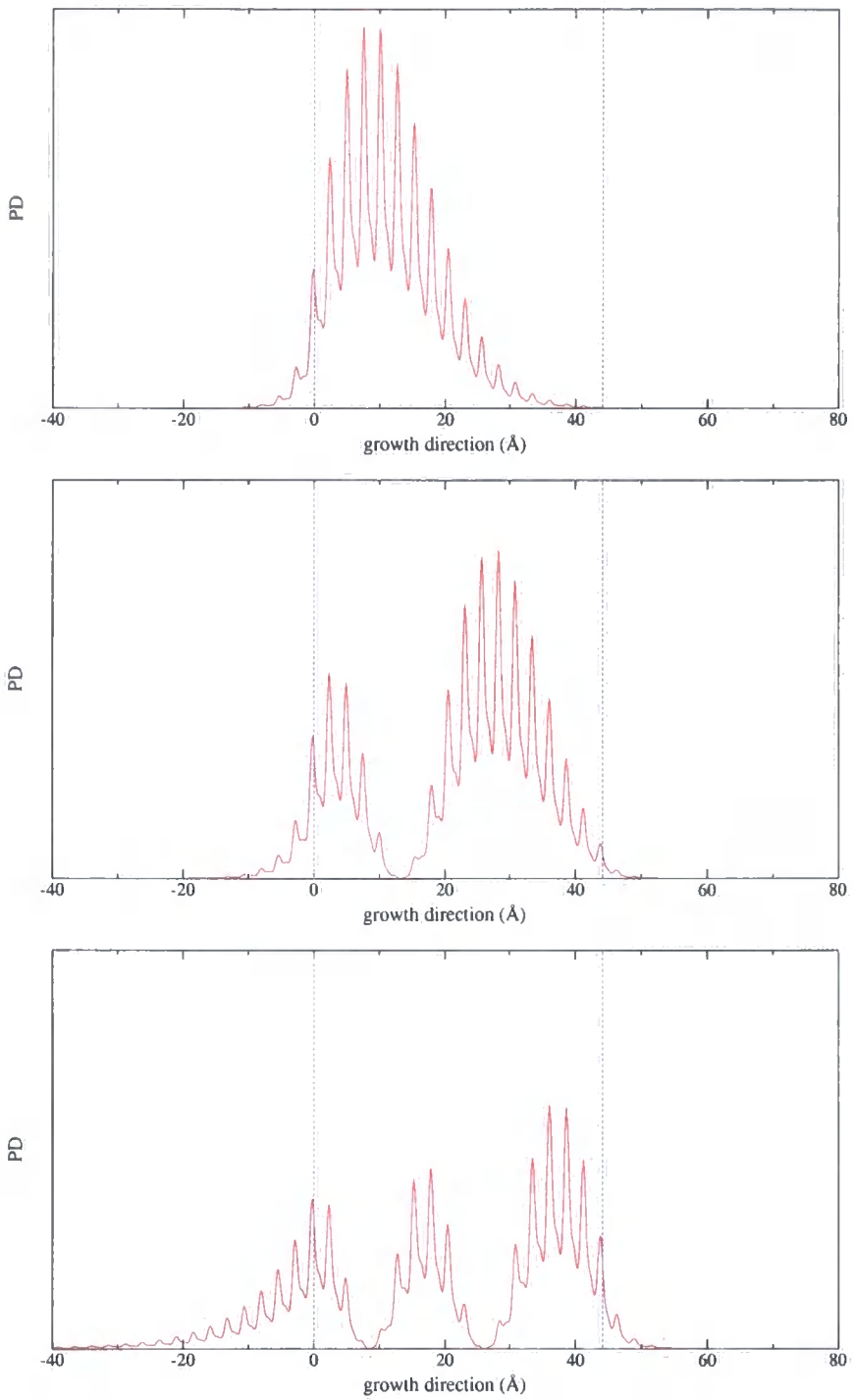

Figure 4.28: The in-plane averaged probability density for the ground state, and 1st and 2nd excited states of a 8.5 unit cell wide $Al_{0.6}Ga_{0.4}N$ quantum well under the influence of a built-in electric field of 2MV/cm.

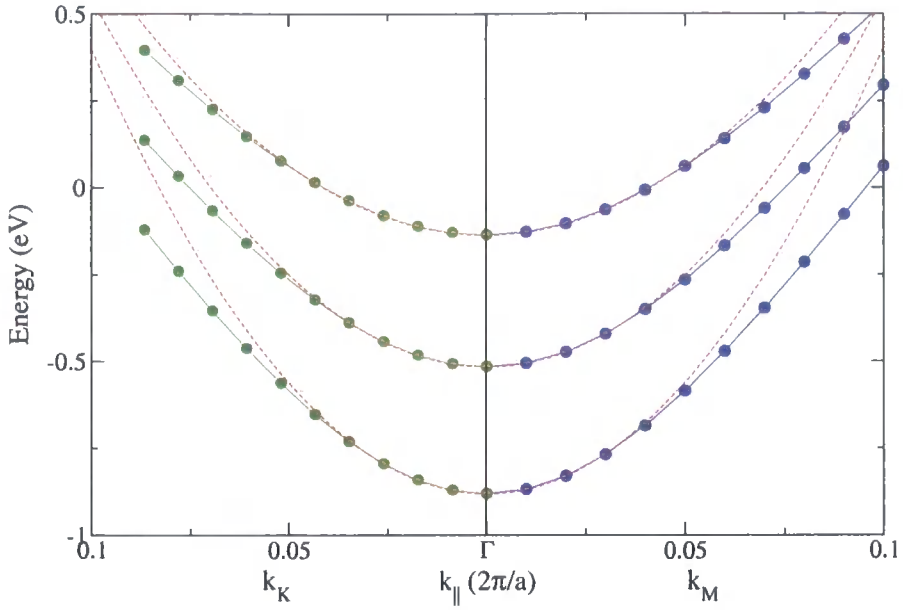

Figure 4.29: The in-plane bandstructure for a 8.5 unit cell wide conduction band $Al_{0.6}Ga_{0.4}N$ quantum well with 2MV/cm built-in electric field. The green circles mark the in-plane bound state energy (in eV), with respect to the top of the well at Γ, for $\mathbf{k}_{||}$ in the in-plane direction of high symmetry point M and the red circles in the in-plane direction of high symmetry point K. The dashed lines display a parabola for comparison.

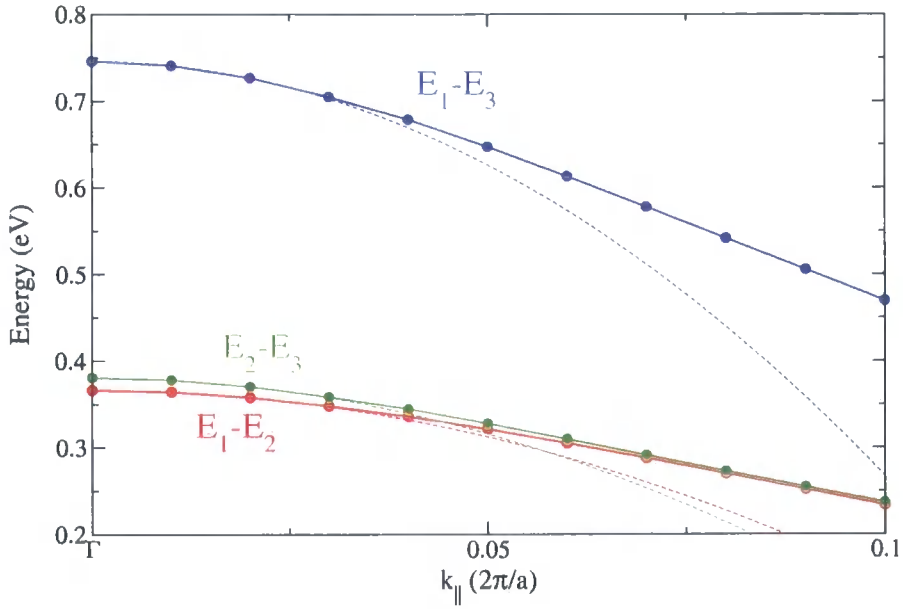

Figure 4.30: The average in-plane inter-subband transition energies for a 8.5 unit cell wide conduction band $Al_{0.6}Ga_{0.4}N$ quantum well with 2MV/cm built-in electric field. The dashed lines display a parabola for comparison.

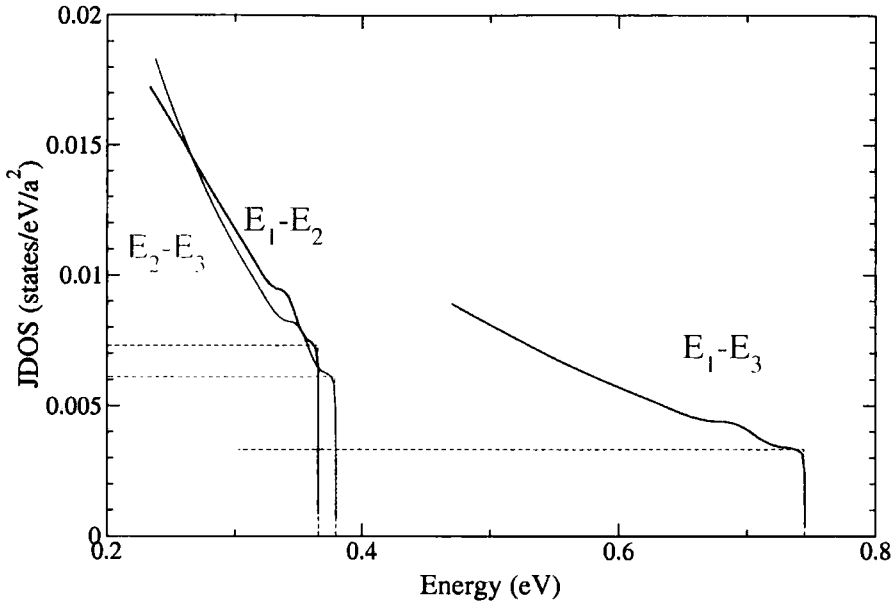

Figure 4.31: The joint density of states for the inter-subband transition of an 8.5 unit cell wide conduction band $Al_{0.6}Ga_{0.4}N$ quantum well with 2MV/cm built-in electric field. The dashed lines display the JDOS for parabolic subbands.

for a quantum well is given by

$$g_{if}(E) = \frac{2}{4\pi^2} \int_{\Lambda(E)} \frac{d\Lambda}{|\nabla_{\mathbf{k}_{||}} E^{if}_{\mathbf{k}_{||}}|} \tag{4.44}$$

Here $E^{if}_{\mathbf{k}_{||}}$ is the energy separation of bands i and f, $E^{if}_{\mathbf{k}_{||}} = E^{f}_{\mathbf{k}_{||}} - E^{i}_{\mathbf{k}_{||}}$. The integral is over $\Lambda(E)$, which is the line of constant energy E, through two dimensional $\mathbf{k}$-space, within the 2D Brillouin zone. To evaluate (4.44) over the whole energy range E requires a knowledge of the complete in-plane bandstructure. This can prove computationally very costly as a separate complex bandstructure calculation is required for many directions of $\mathbf{k}_{||}$. However, since the approximation of an isotropic bandstructure can often be made, the path $\Lambda(E)$ is approximated by a circle, and

$$\int_{\Lambda(E)} d\Lambda \approx 2\pi k_{||}(E) \tag{4.45}$$

where $k_{||}(E)$ is the value of $k_{||}$ at energy E. There may be more than one value of $k_{||}$ for

a given energy, in which case all the values must be summed over. The JDOS can now be calculated from the complex bandstructure for a discrete set of points along a single line in 2D **k**-space and using a cubic spline fit to interpolate the values in-between. The JDOS is then given by

$$g(E)_{if} = \frac{k_{\|}(E)}{\pi |\nabla_{k_{\|}} E_{\|}^{if}|} \tag{4.46}$$

Figure 4.31 shows the joint density of states for an 8.5 unit cell wide $Al_{0.6}Ga_{0.4}N$ quantum well with the equivalent step function for parabolic subbands marked by a dashed line. A clear departure from the JDOS of parabolic subbands is noted.

4.9 Optical Transitions

Optical properties of semiconductors are of considerable interest, because of the wide range of applications that can result from them. For the nitrides, we are particularly interested in the absorption and emission of light in the visible part of the electromagnetic spectrum.

The transition probability λ_{if} between two states, i and f is given by Fermi's Golden rule (see for example [29])

$$\lambda_{if} = \frac{2\pi}{\hbar} |M_{if}|^2 \, g(E)_{if} \tag{4.47}$$

where $g(E)_{if}$ is the joint density of states and M_{if} is the transition matrix element. The electron-radiation matrix element has the form

$$M_{if} = \langle \Psi_i | \frac{|e|}{2m_e} \mathbf{A} \cdot \hat{\mathbf{p}} \, | \Psi_f \rangle \tag{4.48}$$

where e the electron charge, m_e the mass of the electron, $\hat{\mathbf{p}} = -i\hbar\nabla$ is the momentum operator and $\mathbf{A}$ is the vector potential of the electromagnetic field. For bound states in quantum wells, equation (4.48) becomes

$$M_{if} = \int_{z=-\infty}^{z=+\infty} \int_{\Omega_{||}} \psi_i^* \frac{|e|}{2m_e} \mathbf{A} \cdot \hat{\mathbf{p}} \psi_f d\mathbf{r}_{||} dz \tag{4.49}$$

Here M_{if} is the momentum matrix element per unit cell area. For a layered heterostructure, this is easiest to achieve layer by layer and then sum to get the final value. The contribution from layer l is therefore given by

$$M_{if} = \int_{z_l y}^{z_{(l+1)}} \int_{\Omega_{||}} \left[\sum_{k} \sum_{\mathbf{g}} c_k^{(l)*} \begin{pmatrix} a_{k\uparrow\mathbf{g}}^{(l)\,*} \\ a_{k\downarrow\mathbf{g}}^{(l)\,*} \end{pmatrix} e^{-i(\mathbf{k}^*+\mathbf{g})\cdot\mathbf{r}} \frac{|e|}{2m_e} \mathbf{A} \cdot \hat{\mathbf{p}} \right.$$
$$\left. \times \sum_{k'} \sum_{\mathbf{g}'} d_{k'}^{(l)} \begin{pmatrix} b_{k'\uparrow\mathbf{g}'}^{(l)} \\ b_{k'\downarrow\mathbf{g}'}^{(l)} \end{pmatrix} e^{-i(\mathbf{k}'+\mathbf{g}')\cdot\mathbf{r}} \right] d\mathbf{r}_{||} dz \tag{4.50}$$

$$M_{if} = \hbar\Omega_{||} \sum_{k,k'} \sum_{\mathbf{g},\mathbf{g}'} \sum_{s,s'} c_k^{(l)*} d_{k'}^{(l)} a_{ks\mathbf{g}}^{(l)\,*} b_{k's'\mathbf{g}'}^{(l)} \frac{|e|}{2m_e} \mathbf{A} \cdot (\mathbf{k}' + \mathbf{g}') \delta_{\mathbf{g}\mathbf{g}'} \delta_{ss'} \times \xi^{(l)} \tag{4.51}$$

where $c_k^{(l)}$ and $a_{ks\mathbf{g}}^{(l)}$ are the coefficients for the initial state and $d_k^{(l)}$ and $b_{ks\mathbf{g}}^{(l)}$ are for the final state. $\xi^{(l)}$ is an integral that depends on the layer type

$$\xi^{(l)} = \int_{z_l}^{z_l+1} e^{i(k'-k^*+g'-g)z} dz \tag{4.52}$$

and

$$\xi^{(L)} = \frac{e^{i\eta z_1}}{i\eta} \tag{4.53}$$

$$\xi^{(l)} = \begin{cases} \frac{e^{i\eta z_{l+1}} - e^{i\eta z_l}}{i\eta} & \eta \neq 0 \\ z_{l+1} - z_l & \eta = 0 \end{cases} \tag{4.54}$$

$$\xi^{(R)} = -\frac{e^{i\eta z_n}}{i\eta} \tag{4.55}$$

where

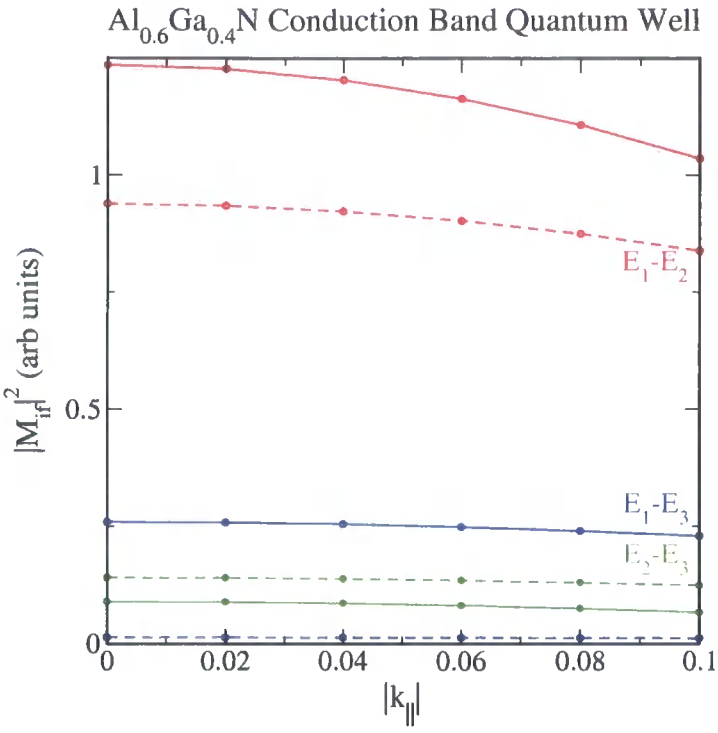

Figure 4.32: Squared magnitude of the momentum matrix elements for the transition between i) E_1-E_2 (red), ii) E_2-E_3 (green) and iii) E_1-E_3 (blue). The dashed lines indicate the values in the absence of a field and the solid lines represent the values with a field of 2MV/cm. Matrix elements are for z polarised transitions.

$$\eta = (k' - k^* + g' - g) \tag{4.56}$$

Figure 4.32 shows an example of the calculated momentum matrix elements for an $Al_{0.6}Ga_{0.4}N$ quantum well, with both zero field and a built-in electric field of 2MV/cm. In agreement with the experimental observations of Hoshino *et al* [126], the normally forbidden transition, E_1-E_3 has non-zero matrix elements for the asymmetric potential caused by the built-in electric field. The E_1-E_2 transition has the largest momentum matrix elements both with and without the field, and is slightly enhanced by the presence of a field. The small but non-zero momentum matrix elements for the forbidden transition E_1-E_3 with zero field is due to a combination of the slight intrinsic asymmetry of the well discussed in section 4.5.4 and the band mixing present in the states [46].

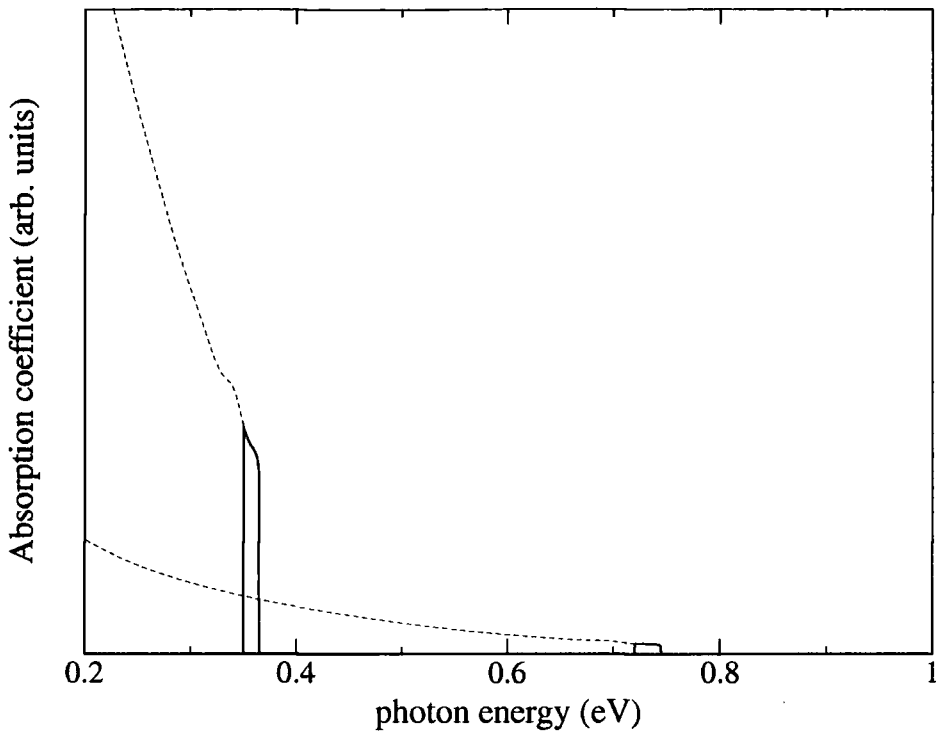

Figure 4.33: The theoretical absorption spectra for an 8.5 unit cell wide $Al_{0.6}Ga_{0.4}N$ quantum well. The dashed red line indicates the contribution from the E_1-E_2 transition and the dashed blue line from the E_1-E_3 transition. The solid lines indicate the 0K spectra for a quantum well with the lowest subband containing 10^{12} electrons/cm^2.

4.9.1 Absorption Coefficients

The calculated momentum matrix elements and joint density of states can be together used to predict the optical absorption spectra of the quantum well. The absorption coefficient resulting from electronic transitions between initial state i and final state f can be written as [135,136]

$$\alpha_{if}(\hbar\omega) = \int \frac{\pi e^2 \hbar}{m_e \varepsilon_0 \mu \hbar\omega c W} |M_{if}|^2 (f_i - f_f)\delta(E_{if} - \hbar\omega) d\mathbf{k}_{||} \qquad (4.57)$$

where μ = refractive index of well material, $\hbar\omega$ = photon energy, c = speed of light, W = well width, M_{if} = optical matrix element, E_{if} = energy separation of subbands i and f, ε_0 = permittivity of free space. f_i and f_f are the Fermi occupation factors which are the probabilities that the states i and f are occupied. The measured optical absorption will be

a result of the transitions between a number of subbands and is obtained by summing the individual absorption coefficients of the transitions concerned.

We are assuming that the bands are isotropic in the x-y plane, in which case equation (4.57) can be written as

$$\alpha_{if}(\hbar\omega) = \int \frac{\pi e^2 \hbar}{m_e \varepsilon_0 \mu \hbar\omega c W} |M_{if}|^2 (f_i - f_f)\delta(E_{if} - \hbar\omega) \frac{4\pi k_{||}}{(2\pi)^2} dk_{||} \qquad (4.58)$$

which can be expressed in terms of the joint density of states g_{if} through a change of variables to an integration over energy

$$\alpha_{if}(\hbar\omega) = \int \frac{\pi e^2 \hbar}{m_e \varepsilon_0 \mu \hbar\omega c W} |M_{if}|^2 (f_i - f_f)\delta(E_{if} - \hbar\omega) g_{if} dE_{if} \qquad (4.59)$$

Equation (4.59) predicts that transitions only occur when $E_{if} = \hbar\omega$ and gives rise to a step like structure similar to the joint density of states that is modulated by the affect of the Fermi occupation factors. For a simplistic demonstration of an absorption spectra, the lowest subband can be filled with a given number of electrons at 0K. Figure 4.33 shows the calculated absorption spectrum for a conduction band AlGaN quantum well with 10^{12} electrons/cm^2 filling the lowest subband. The dashed lines indicate the shape of the spectra for more and more electrons. In reality, finite temperature effects would considerably broaden the spectra. However, despite the simplistic assumptions, figure 4.33 is broadly similar to experimental spectra of similar quantum wells, for example [126].

4.10 Summary

A matching technique for the complex bandstructure approach is presented and has been demonstrated on InGaN and AlGaN wurtzite quantum wells for a range of field strengths and alloy compositions. The results for both quantum well systems have been shown to be in excellent agreement with effective mass envelope function calculations, therefore justifying to some extent the use of the simplistic effective mass approach in these systems. Comparison with experiment in these systems in not always possible or valid because of the large

uncertainties in the model parameters especially the built-in electric field strength. It is suggested that the complex bandstructure approach could be used as a more accurate method for the fitting of these fields to experimental data. Finally the calculation of momentum matrix elements has been demonstrated and suggests that the electric field strongly effects in the optical performance of a device based on AlGaN ISBTs, enhancing the $E_1 - E_2$ and the normally forbidden $E_1 - E_3$ transition and slightly reducing the matrix elements for the $E_2 - E_3$ transition.

Chapter 5

Wurtzite-Zincblende Interface

5.1 Introduction

In previous chapters, studies were performed on nitride heterostructures with the wurtzite crystal structure using the empirical pseudopotential method. However, crystal growth in the zincblende phase is also possible. In this chapter, the zincblende phase, which for the nitrides is characterised by marginally smaller band gaps, is considered. First the empirical pseudopotential method is used to calculate the bulk and complex bandstructures of zincblende GaN. The wurtzite (0001) crystal face and the zincblende (111) crystal face are analogous faces in the two crystals. The structure and electronic properties of zincblende GaN in the (111) direction, therefore makes an interesting comparison with those of wurtzite GaN. The smaller band gap of zincblende GaN and the concept of a *homointerface* between the wurtzite (0001) face and the zincblende (111) face of GaN, allows the construction of a quantum well entirely from GaN; a *homostructure*. The wavefunction matching methods employed in chapter 4 are adapted for matching between the two crystal structures and the approach is demonstrated for a GaN conduction and valence band quantum well.

5.2 Zincblende Crystal Structure

The cubic zincblende crystal structure can be thought of as two interpenetrating face centred cubic (FCC) lattices separated by $(1/4, 1/4, 1/4)a$, where a is the lattice constant. Each of the two lattices contains atomic species of the two components labelled A and B.

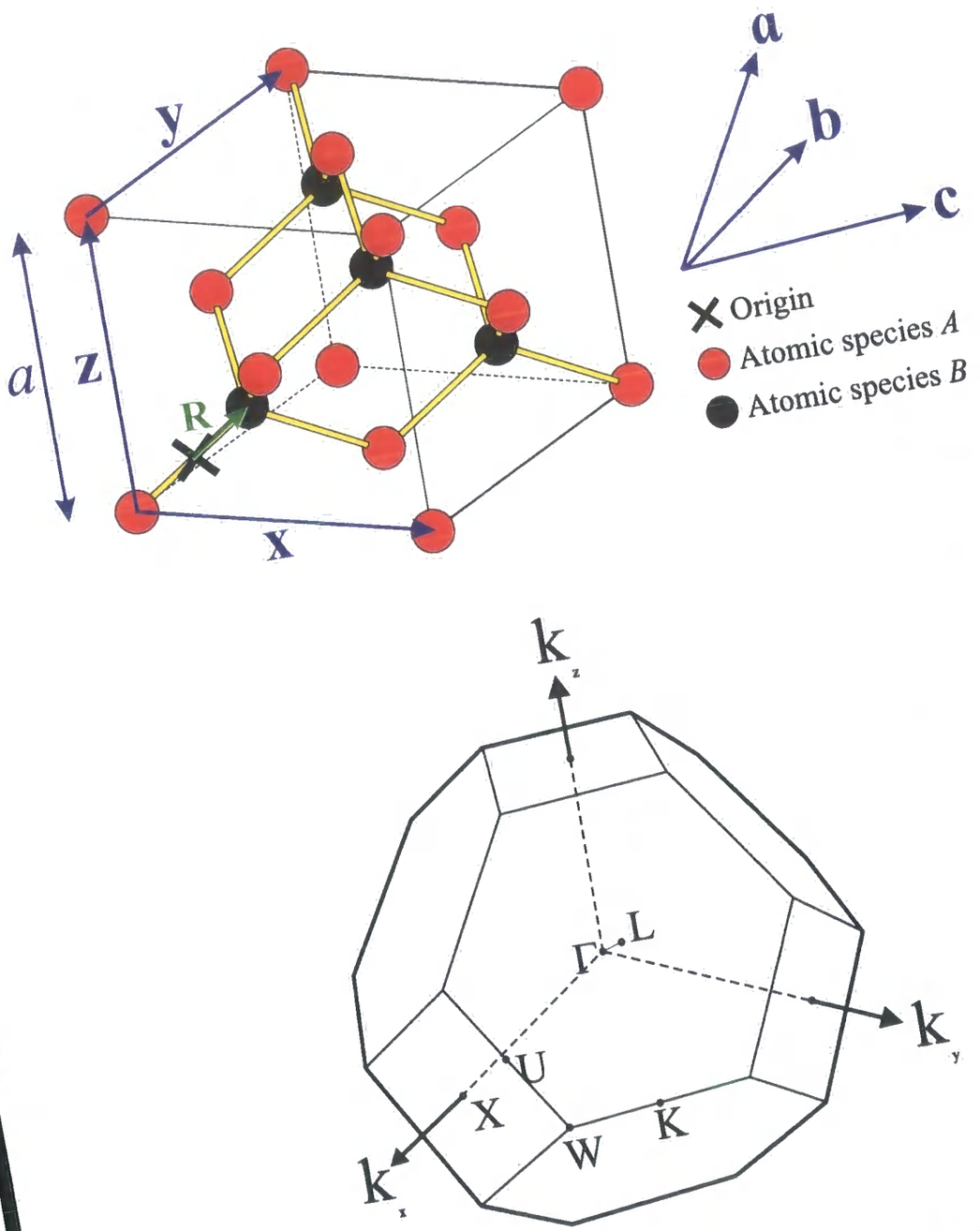

Figure 5.1: The zincblende unit cell and 1st Brillouin zone indicating points of high symmetry.

More formally, the structure is described by a face centred cubic Bravais lattice with a two atom (A and B) basis. The two atoms are located at positions $+\mathbf{R}$ and $-\mathbf{R}$ relative to the lattice points, where

$$\mathbf{R} = \frac{(1,1,1)a}{8} \tag{5.1}$$

The resulting conventional cubic unit cell in figure 5.1 describes the geometry of the crystal. The primitive lattice vectors are

$$\begin{aligned} \mathbf{a} &= (0, \tfrac{1}{2}, \tfrac{1}{2})a \\ \mathbf{b} &= (\tfrac{1}{2}, 0, \tfrac{1}{2})a \\ \mathbf{c} &= (\tfrac{1}{2}, \tfrac{1}{2}, 0)a \end{aligned} \tag{5.2}$$

The reciprocal lattice for a face centred cubic lattice is a body centred cubic (BCC) lattice and the first Brillouin zone is therefore a truncated octahedron of volume $4(2\pi/a)^3$. Figure 5.1 shows the first Brillouin zone and the following points of high symmetry.

$$\begin{aligned} L &= (\tfrac{1}{2}, \tfrac{1}{2}, \tfrac{1}{2}) \\ \Gamma &= (0,0,0) \\ X &= (1,0,0) \\ U &= (1, \tfrac{1}{4}, \tfrac{1}{4}) \\ K &= (\tfrac{3}{4}, \tfrac{3}{4}, 0) \\ W &= (1, \tfrac{1}{2}, 0) \end{aligned} \tag{5.3}$$

5.3 Pseudopotentials

The empirical pseudopotential approach has been widely applied to the zincblende crystal structure. The basic approach is very similar to that described in chapter 2 for the wurtzite crystal structure. The principal difference comes from the pseudopotential term which has the periodicity of the lattice. The symmetric and antisymmetric structure factors for a zincblende crystal are given by [25,46]

$$S_{\mathbf{g}}^{S} = \cos(\mathbf{g} \cdot \mathbf{R})$$
$$S_{\mathbf{g}}^{A} = \sin(\mathbf{g} \cdot \mathbf{R}) \tag{5.4}$$

For the bandstructure calculations presented here 6 form factors, 3 symmetric and 3 anti-symmetric are found to be sufficient to describe the pseudopotential and are given in table 5.1. Clearly the g-vectors appropriate to the zincblende reciprocal lattice must be used in the Fourier expansions.

g	g^2	S_g^S	S_g^A
(111)	3	$\frac{\sqrt{2}}{2}$	$\frac{\sqrt{2}}{2}$
(200)	4	0	1
(220)	8	1	0
(311)	11	$\frac{\sqrt{2}}{2}$	$\frac{\sqrt{2}}{2}$

Table 5.1: The reciprocal lattice vectors used in Fourier expansion of a zincblende pseudopotential [40].

5.3.1 Local Pseudopotentials

To use the complex bandstructure method employed in this work, the pseudopotentials must be local. However, unlike wurtzite, most empirical pseudopotential work on zincblende semiconductors makes use of non-local pseudopotentials and it is generally believed that accurate zincblende bandstructures require the non-local contribution [39]. As a result the majority of pseudopotential form factors available in the literature are non-local. Fan *et al* [137,138] and Kassali and Bouarissa [139] do quote local form factors for zincblende GaN, but the two bandstructures are in strong disagreement with each other and also with those that include a non-local contribution, such as Pugh *et al* [50].

For this work, local form-factors were instead derived by making Monte-Carlo fits to the accepted bandstructure, as outlined in chapter 2. The bandstructure targets used by Dugdale [40] for his non-local calculations were used with an increased weighting between Γ and L in an effort to provide an accurate representation of the bandstructure for the region

g	g^2	V_g^S	V_g^A
(111)	3	-0.36626	0.20355
(200)	4	0	0.20069
(220)	8	0.05316	0.14339
(311)	11	0.014339	0

Table 5.2: The local pseudopotential form factors (in Rydbergs) for zincblende GaN, derived by Monte-Carlo fitting.

	Local	Non-local	Quasiparticle	Expt.
$\Gamma_{15}^v \rightarrow \Gamma_1^c$	3.301	3.370	3.1	3.2 [140,141] 3.3 [142]
$X_5^v \rightarrow X_1^c$	7.191	7.191	7.7	
$L_3^v \rightarrow L_1^c$	6.943	6.966	7.3	

Table 5.3: Comparison of energy gap transitions (in eV) calculated by i) local parameters presented here, ii) non-local parameters [40,50], ii) quasiparticle calculations within the GW approximation [143] and experiment.

of particular interest, despite the use of local pseudopotentials. The resultant form factors are given in table 5.2. A value for the zincblende lattice constant of $a_{zb} = 4.511$Å is used to ensure exact lattice matching with wurtzite GaN.

Table 5.3 contains the values of the transition energies obtained from the local pseudopotential calculations, along with the non-local and GW-quasiparticle values for comparison. Surprisingly the local pseudopotential values are very similar to the non-local values, and will be considered sufficient accuracy for this work. Table 5.4 gives the values of effective mass calculated from the local and non-local bandstructures. Figure 5.2 shows the actual local bandstructure calculated with 137 plane waves. Very little experimental information is available for the spin-orbit splitting energy of zincblende GaN, and therefore the spin-orbit parameter is assumed to be the same as for the wurtzite structure $\mu = 0.00325$. The top of the valence band for the zincblende structure is more degenerate than for the wurtzite structure because of the additional crystal field splitting in the latter. A close up of the top of the valence bandstructure (figure 5.3) illustrates this and should be compared to the close-up of the GaN in the wurtzite bandstructure in figure 2.18.

	Local	Non-local [40]
m_{so}	0.33	0.33
m_{lh}	0.20	0.21
m_{hh}	0.86	0.81
m_{hh}^{L}	2.11	2.41
m_c	0.13	0.13

Table 5.4: Comparison of the relative effective masses for the local calculation with those including a non-local contribution.

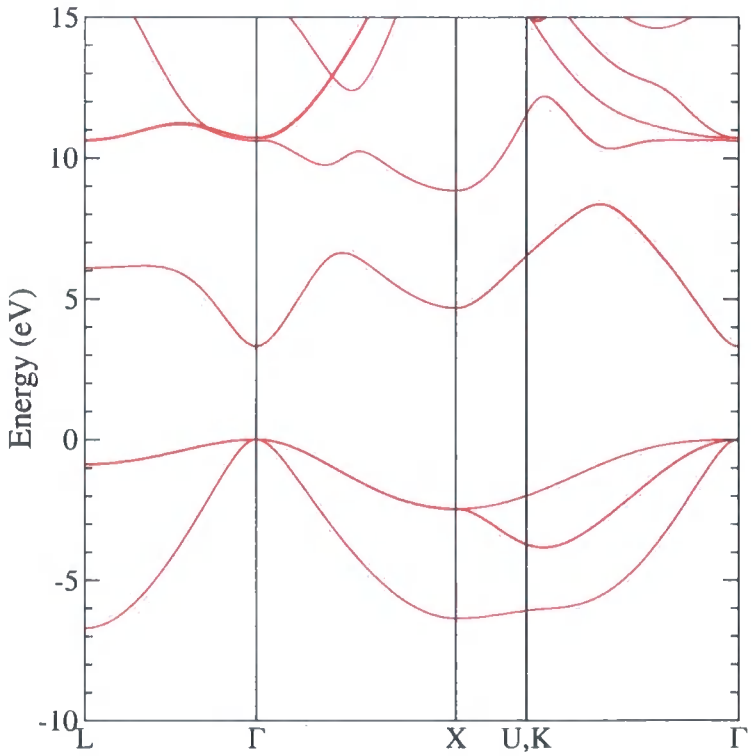

Figure 5.2: The empirical local-pseudopotential bandstructure for zincblende GaN.

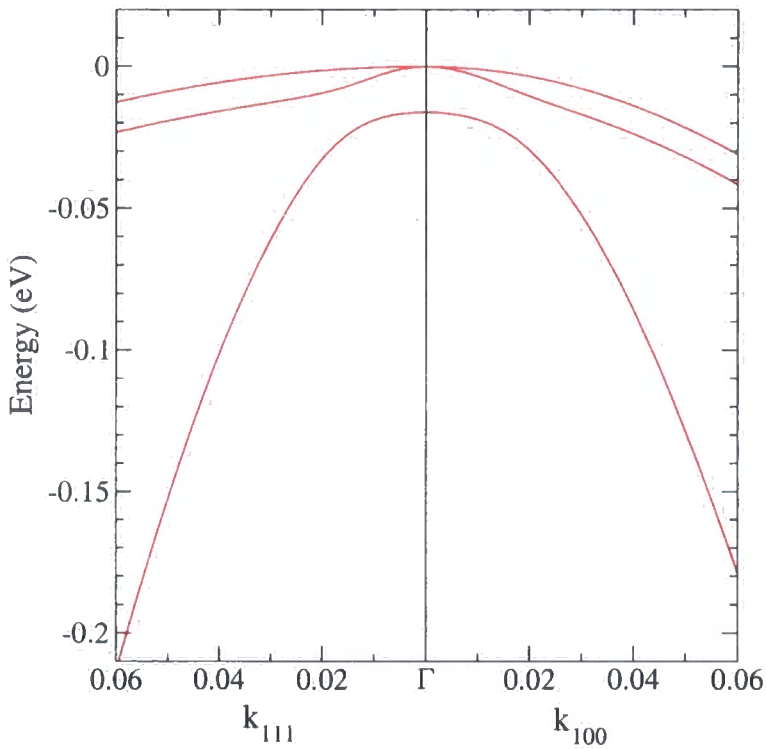

Figure 5.3: A close-up of the empirical local-pseudopotential bandstructure around Γ for zincblende GaN.

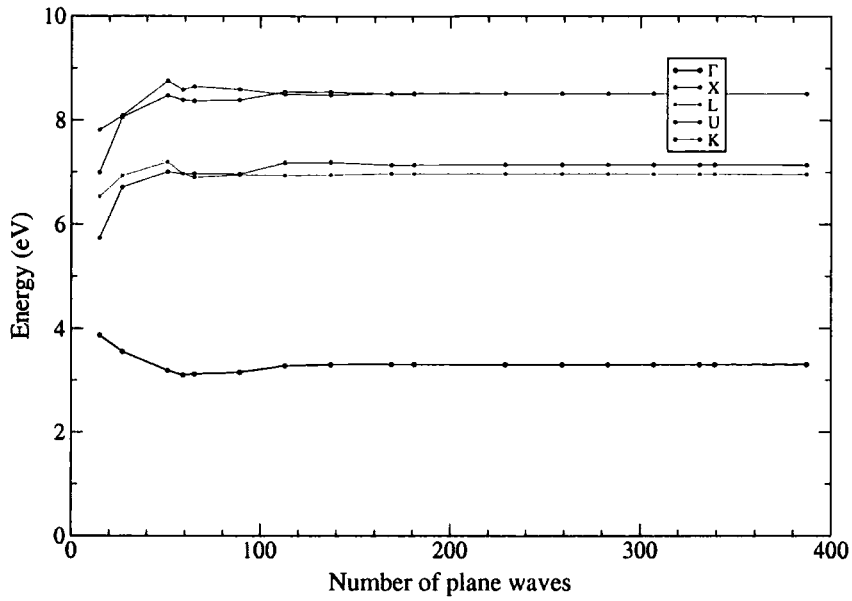

Figure 5.4: The convergence, against number of plane waves, of the conduction band of zincblende GaN at various points within the first Brillouin zone.

5.3.2 Convergence

The convergence of energy eigenvalues for the expansion of pseudo-wavefunction against number of plane waves, has to be tested separately for zincblende GaN. The zincblende unit cell is smaller than that of wurtzite and only contains two atoms. Therefore, the pseudo-wavefunction should achieve the same level of convergence as for the wurtzite structure with significantly fewer plane waves.

Figure 5.4 describes the convergence of the zincblende GaN first conduction bands for several points of high symmetry throughout the zone. For symmetry reasons, the energies at the K and U points of the Brillouin zone should be equal. It can be seen that for less than 113 plane waves they are significantly different. The energies seem to be converged to within about 0.05eV at 113 or 137 plane waves, which is accurate enough for this work. Similar calculations by other workers (e.g. [46]) on zincblende semiconductors make use of 89 or even 65 plane waves in calculations. However, in comparison to the computational cost of the wurtzite calculations, 137 plane waves is very efficient. For bulk bandstructure calculations, a value of 137 plane waves is therefore considered adequate.

5.4 Complex Bandstructure

The complex bandstructure of a zincblende crystal is constructed in an analogous way to that for a wurtzite crystal. The g-vectors appropriate to zincblende must be used, and in the construction of $H^0_{\mathbf{g},\mathbf{g}',s,s'}$ and $H^1_{\mathbf{g},\mathbf{g}',s,s'}$, the appropriate terms from the zincblende H^{soc} should be included. Zincblende materials are also usually grown in the (100) direction and most complex bandstructure calculations are for this direction. However, for this work the complex bandstructure is primarily required in the (111) direction. Wurtzite bandstructures are 'folded' in the (0001) direction in the plane of the A, L and H points when compared to zincblende. Therefore wurtzite bandstructures do not have stationary points at the zone edge in the (0001) direction. In contrast zincblende does have stationary points at the zone edge in the (111) direction. While this is noticeable in the bulk bandstructure, it has important consequences for the complex bandstructure. Complex wavevector states start and end at stationary points and these complex states have the real part of the wavevector *on the zone edge* which has consequences for the identification of the non-repeated solutions in the first Brillouin zone.

Figure 5.5 shows the complex bandstructure of zincblende GaN as both the full open representation and "folded" about the plane halfway to the L point. The folded version of the bandstructure allows a comparison with the wurtzite complex bandstructures. The complex bandstructure of zincblende GaN features saddle points in the complex plane. These are at a zone edge maxima in k_r which becomes a minima in k_i. When "folded", these features are clearly recognisable as the minima along the imaginary axis seen in the wurtzite complex bandstructure (figure 3.2). Figure 5.6 shows the complex bandstructure of zincblende GaN in the (100) and (110) directions. Saddle features are not observed in the (110) direction or the (100) direction. For all the complex bandstructures, the imaginary wavevector loop across the band gap is observed and the spin split-off band loops along the imaginary axis to the first conduction band.

5.4.1 Numerical problems

The existence of stationary points at the zone edge presents numerical problems in the calculation of the complex bandstructure of zincblende crystals. The complex wavevector

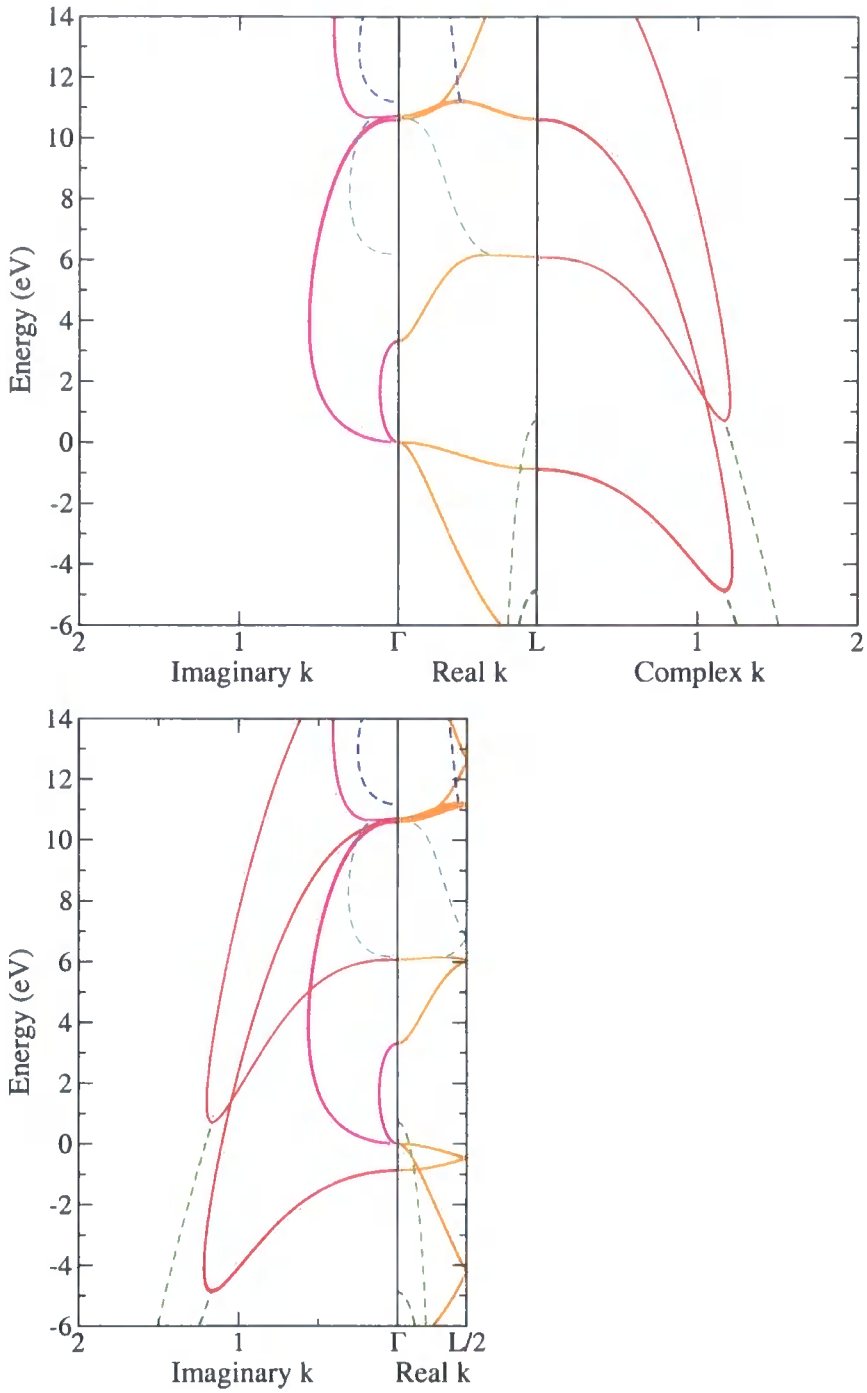

Figure 5.5: Top: Complex bandstructure, with zero in-plane wavevector, in the (111) direction for zincblende GaN. The solid pink lines to the left represent the purely imaginary solutions. The solid orange lines in the middle region are the real bandstructure between Γ and L. To the right the solid red lines are complex solutions with the real component at L. The complex states are represented by pairs of similarly coloured dashed lines. **Bottom**: The above complex bandstructure is 'folded' about $\frac{L}{2}$ to provide a relevant comparison with the complex bandstructure of wurtzite GaN (figure 3.2).

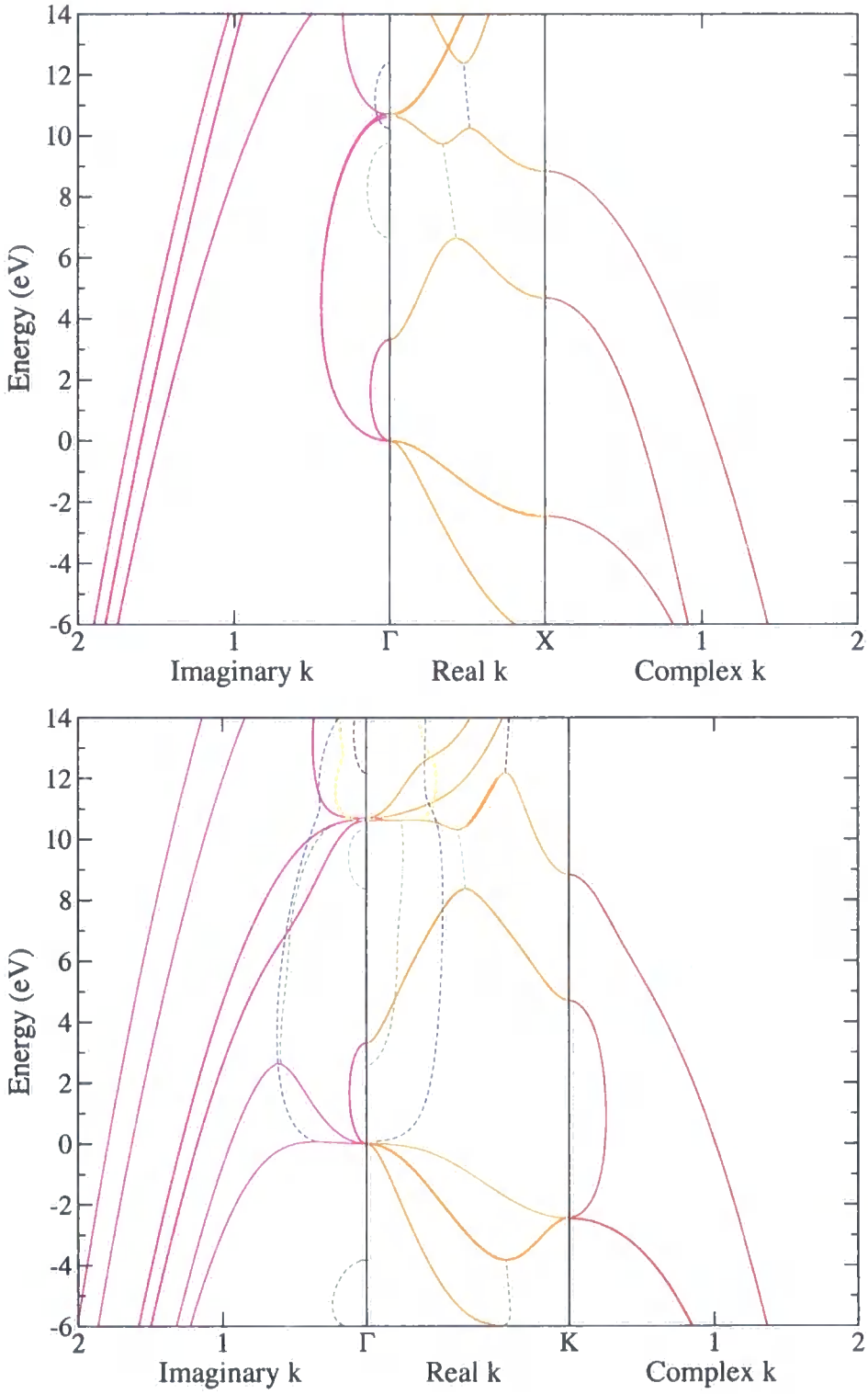

Figure 5.6: The complex bandstructure, with zero in-plane wavevector, in the (100) direction (top) and the (110) direction (bottom).

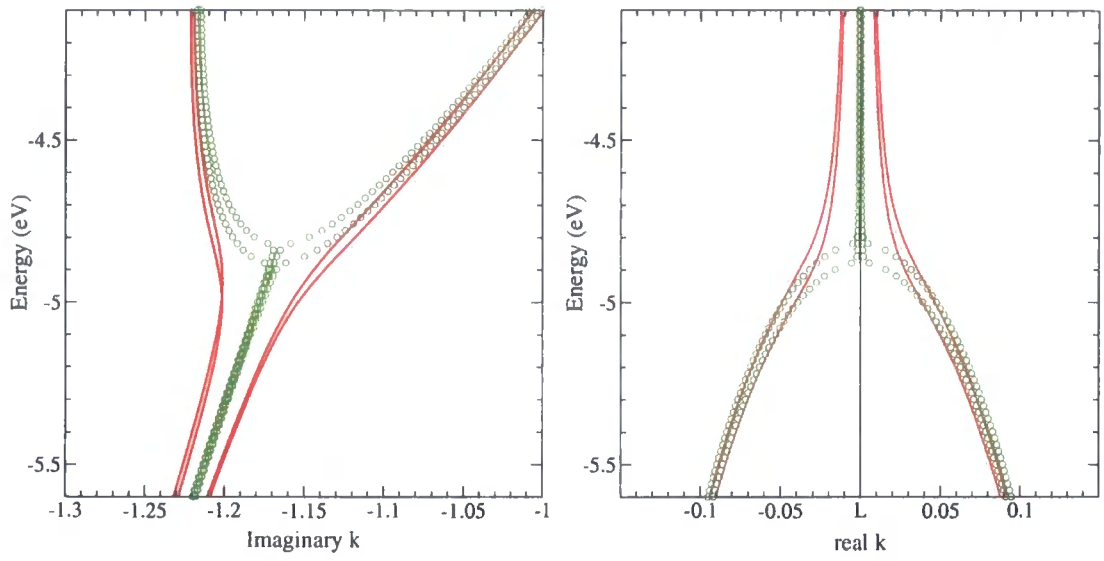

Figure 5.7: A close up of the saddle features of the zincblende GaN complex bandstructure for 137 and 169 plane waves. The solid red line describes the bandstructure for 137 plane waves and the green circles are for 169 plane waves. The addition of the (333) group of plane waves has a significant effect on the convergence in the (111) direction.

solutions arising from these stationary points should ideally be and remain *exactly* at the zone edge. However, a complex solution at the zone edge will have an equivalent solution at the opposite edge of the zone and such repeat solutions have to be identified and discarded or the conservation of number of solutions will be effected. In practice, with a finite basis set, the complex solutions are not exactly at the zone edge and worse still, "wander" away from the zone edge slightly as the energy varies. In addition states may exist that are genuinely inside the zone, but very near the edge. This makes the identification of the set of non-repeated solutions much more difficult. In practice this identification is only really needed over the region of energy being studied in a heterostructure calculation, and some numerical scheme for automatically identifying the non-repeated solutions is usually possible.

The complex bandstructure of zincblende GaN presents an interesting numerical problem in relation to the saddle features. The bandstructures shown in figures 5.5-5.6 were generated with 169 plane waves. This is more than was required for reasonable convergence of the bulk bandstructure. However, it was observed that no consistent scheme could be found to establish the non-repeated solutions over a wide energy range of the complex bandstructure at 137 plane waves. In fact, the complex bandstructure is still not converged at 137

plane waves and a noticeable difference is observed in the saddle features for 137 and 169 plane waves. Figure 5.7 shows this difference. The true nature of the saddle points and the corresponding effect on the identification of non-repeated solutions is only clear if 169 or more plane waves are used. The reason is, the addition of the (333) group of plane waves was required for convergence to be achieved in the (111) direction. To include the next (111) group of g-vectors, the (444) group, requires the use of at least 339 plane waves.

5.5 Wurtzite-Zincblende Interface

The existence of two different crystal structures based on related stacking sequences allows for the possibility of *stacking faults* and even a seamless change in the crystal structure during growth. The geometry of the change in crystal structure from zincblende to wurtzite has been studied as part of the effort to improve the growth of hexagonal semiconductors on cubic substrates [144]. The nitrides are known for the extremely high density of extended defects [21], although the role of the defects in the electronic properties has not yet been determined [145]. As a result of the stacking faults, even high quality crystals are expected to contain regions of zincblende structure. These regions of zincblende structure could be considered to form natural superlattices or quantum wells. Also, the controlled growth through solid source MBE of SiC structures consisting of hexagonal and cubic layers has been demonstrated [146] and continues to be improved. This development opens up new device design possibilities and allows for increased flexibility in the design of current SiC devices [147]. The growth of the nitrides is significantly less mature that that of many other semiconductor systems. Nevertheless it remains a possibility that controlled growth of homostructures of wurtzite and zincblende GaN could very soon be achievable. One possible route that has been suggested is the introduction of Mg doping in wurtzite GaN to induce the formation of zincblende regions [148].

5.5.1 Stacking Sequences

It is instructive to first consider the stacking sequences that give rise to the two different polytypes of GaN. The rotational freedom about the tetrahedral bonds oriented in the growth direction gives rise to three different positions onto which a growth layer can be

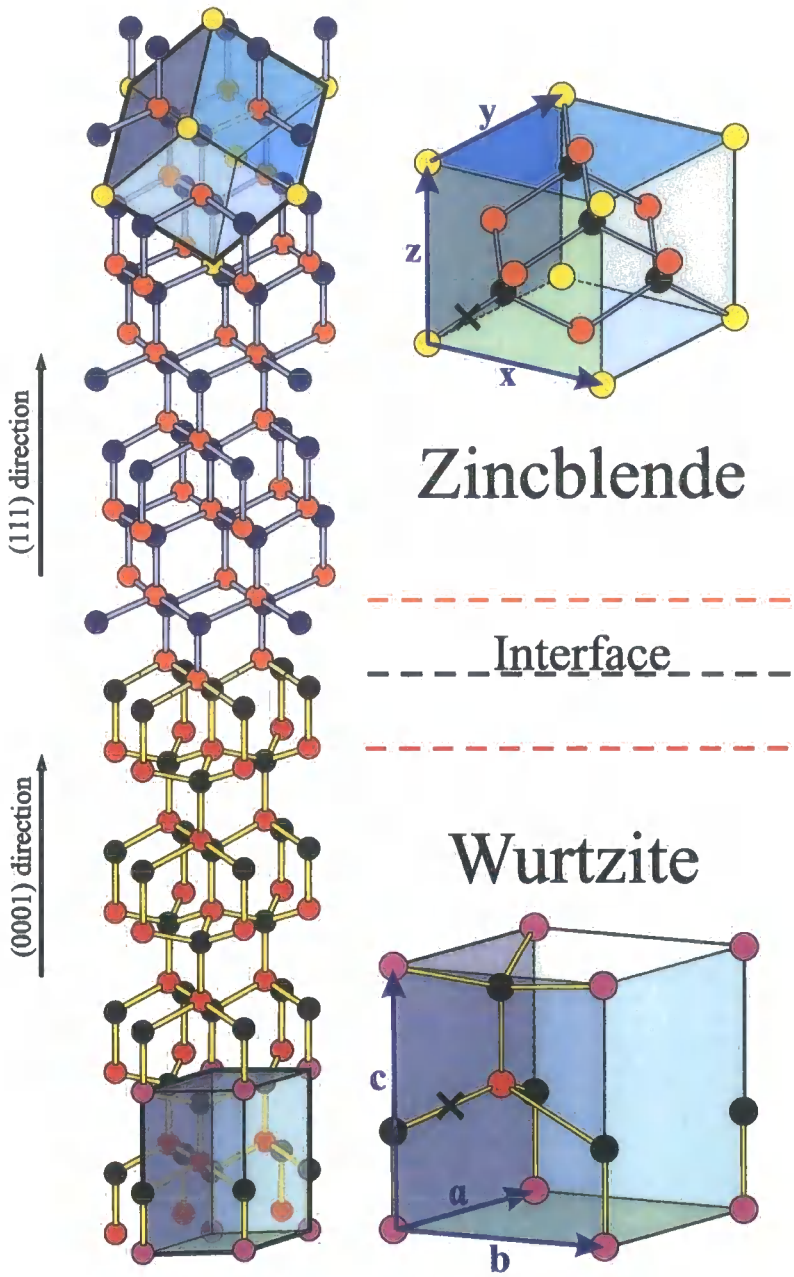

Figure 5.8: The wurtzite and zincblende interface.

"placed" during growth. These three positions are labelled A, B and C. The wurtzite phase is achieved by stacking the sequence $\ldots ABABAB \ldots$ or equivalently $\ldots BCBCBC \ldots$ or $\ldots ACACAC \ldots$. The crystal resulting from an $\ldots ABABAB \ldots$ is related to that resulting from $\ldots BCBCBC \ldots$ by a rotation of 60°. The zincblende phase is then achieved by making use of the third possible stacking location with the sequence $\ldots ABCABC \ldots$. Again the $\ldots ABCABC \ldots$ sequence is equivalent to the $\ldots ACBACB \ldots$ or $\ldots CABCAB \ldots$ sequences, rotated by 60°. It is important to note that each letter, A,B or C, in the stacking sequence corresponds to a cation-anion pair of atoms, i.e. a gallium atom and a nitrogen atom for GaN. The term monolayer (ML) is often used in the literature to refer to a layer formed from a pair of atoms corresponding to one of the letters in the growth sequence [148]. The environment of a single atom in a wurtzite crystal differs from one in a zincblende crystal only by the comparative location of its second and third nearest neighbours. The similarity in the local structure leads to a very small (~10meV/atom) [148,149] difference in the formation energies of the two crystal structures.

5.5.2 Stacking Faults

A stacking fault can be thought of as the result of a misplaced monolayer. The fault then places the monolayer in the only other available location. For an atomic pair in a wurtzite crystal that should go into location B as part of a sequence AB, the fault would then be the sequence AC since C is the only other location permitted while retaining the tetrahedral bonding. The sequence for the fault would then be $\ldots ABABABCBCBCB \ldots$. The stacking fault itself actually contains a zincblende-like sequence of ABC. It is clear that a wurtzite zincblende interface could be formed by continuing this zincblende sequence after the stacking fault $\ldots ABABABCABCABC \ldots$. The zincblende-wurtzite interface would then be formed by the sequence $\ldots ABCABCABABAB \ldots$, noting that there will be an asymmetry between the WZ-ZB and the ZB-WZ interfaces.

A WZ-ZB interface of the sequence $\ldots ABABAB\mathbf{AB}CABCABC \ldots$ represents the only possible crystal geometry without the introduction of further stacking faults. Double stacking faults, or more complicated variations on the stacking sequence, are commonly observed and may well play a role in the geometry of a real WZ-ZB interface. However for the purposes of this work we will restrict the models to the most simple case of an

interface without additional faults. The stacking layers marked in bold type face could be considered part of either the wurtzite or zincblende repeat pattern. Only layers either side of this "interface region" can be unambiguously defined as either wurtzite or zincblende.

Any other combinations of zincblende and wurtzite stacking sequences result in the same interface crystal structure in the same way as the $ABABAB$ sequence results in the same structure as $ACACAC$. This is important, because as a result there is only one type of WZ-ZB interface. To illustrate this consider $\ldots BCBCBC\mathbf{BC}ABCABCA\ldots$ which is related to $\ldots ABABAB\mathbf{AB}CABCABC\ldots$ by a rotation of the whole structure by 60^o. Clearly the same argument holds for the ZB-WZ interface.

5.5.3 Quantum Well

Now consider a quantum well constructed from a structure with WZ-ZB and ZB-WZ interfaces. The wurtzite structure, having a 0.2eV larger band gap, forms the barrier regions around a zincblende well. The growth direction is therefore the (0001) direction in the wurtzite and the (111) direction in the zincblende.

In this chapter we describe the application of the empirical pseudopotential complex bandstructure matching techniques used in chapters 2,3 and 4 to a simple quantum well formed from wurtzite and zincblende GaN. The lattice constants of wurtzite and zincblende GaN are so similar that a quantum well constructed this way would be under very little strain (<0.5%). The effects of distortion of the crystal in the (111)-direction of a zincblende structure would result in a reduction of the crystal symmetry and a resultant splitting of degenerate bands. These effects could be included, but the additional complexity is not justified for the small effect it would have, and is avoided by considering the very nearly lattice matched system to be *exactly matched.* Without strain there will be no piezoelectric fields, although spontaneous polarisation could be present. For the purposes of a demonstration of the calculation the effect of spontaneous polarisation has been ignored.

The band offset between wurtzite and zincblende GaN has not been investigated experimentally. Chapter 6 investigates the WZ-ZB interface, including the band offset, using a first principles calculation based on density functional theory. In this chapter, the band offset calculated in chapter 6 is used.

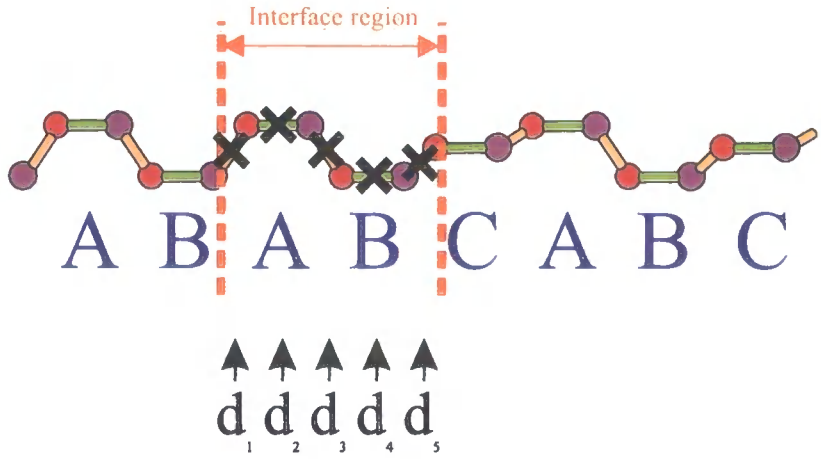

Figure 5.9: Schematic diagram of the 5 possible locations $\mathbf{d}_1 - \mathbf{d}_5$ of the WZ-ZB and ZB-WZ interfaces.

5.5.4 Matching

Figure 5.8 illustrates a WZ-ZB interface and the different unit cells on both sides. The matching of wavefunctions is carried out in a similar way to that for a wurtzite only heterojunction. The zincblende complex bandstructure is required in the (111) direction. The wavefunctions for the WZ and ZB complex bandstructures are described in terms of the two different sets of g-vectors and therefore the appropriate in-plane projections need to be calculated separately for each structure. The origins of the WZ and ZB unit cells are displaced by a vector $\mathbf{d}$ to give the two unit cells the correct alignment for a WZ-ZB and ZB-WZ interface. This displacement can be accounted for by multiplying the wavefunction projections by a phase factor $e^{i\mathbf{g}\cdot\mathbf{d}}$. Having calculated the wavefunction projections for the well and barrier regions over a range of energies, the matching technique described in chapter 4 can then be used to establish the bound state energies.

Location of interface

The exact location of the WZ-ZB (or equivalently the ZB-WZ) interface is not well defined. Over the stacking sequence $\cdots ABABAB\mathbf{ABC}ABCABC\cdots$ the stacking layers marked in bold could equally be considered part of the wurtzite or zincblende repeat sequences. This "interface region" exists to a small extent in a normal heterostructure, in that the nitrogen atoms at the interface between GaN and AlN could be considered part of

either material. However the interface region of 1 atomic layer in the GaN - AlN interface is significantly smaller than the 4 atom region of a WZ-ZB interface. For GaN - AlN, the matching was performed on one side of the nitrogen atom, at the bond centre of the "diagonal" bonds. It could equally have been performed at the centre of the growth direction bonds. Hall [71] has considered the effect of the matching plane for bond-centred and atom-centred matching of zincblende superlattices. Although some differences of the energies and the symmetry of wavefunctions were observed, generally the results were in good agreement. Since the pseudopotential approximation is only valid away from the ionic cores, there is an argument to restrict the matching of the wavefunctions to the bond centre sites. For a WZ-ZB interface that narrows the choice down to 5 locations, shown in figure 5.9,with the most intuitive being at the centre of the "interface region". The choice of matching plane is achieved in practice by choosing an appropriate displacement vector d between the origins of the WZ and ZB unit cells. In the actual calculations the choice of matching plane from these 5 positions had little effect on the final bound state energies or wavefunctions. Figure 5.10 illustrates this point, the bound state energy for a GaN conduction band quantum well is plotted against the location of matching plane. For a given matching plane on the WZ-ZB interface, the complementary one on the ZB-WZ was used to ensure the well width remained constant. The variation of bound state energy with matching plane is found to be very small ($\sim$0.0005eV) with the most noticeable difference being between that of matching on a diagonal bond (d_1,d_3,d_5) and growth direction bond (d_2,d_4).

5.5.5 Bound states

A profile of the quantum well with band offsets calculated by the *ab-initio* density functional theory calculations described in chapter 6 is displayed in figure 5.11. Zero field is assumed in the zincblende region and the conduction band offset is inferred from the empirical difference in band gaps of the two materials. The resulting conduction band well is 0.168eV deep and the valence band well is 0.0314eV deep.

The bound states vs well width of a GaN WZ-ZB conduction and valence band quantum well are plotted in figures 5.12 and 5.13. The conduction band states are typical of a conduction band quantum well and somewhat similar to the results for a WZ well previously discussed in chapter 4. The conduction band state energies are in good agreement with those

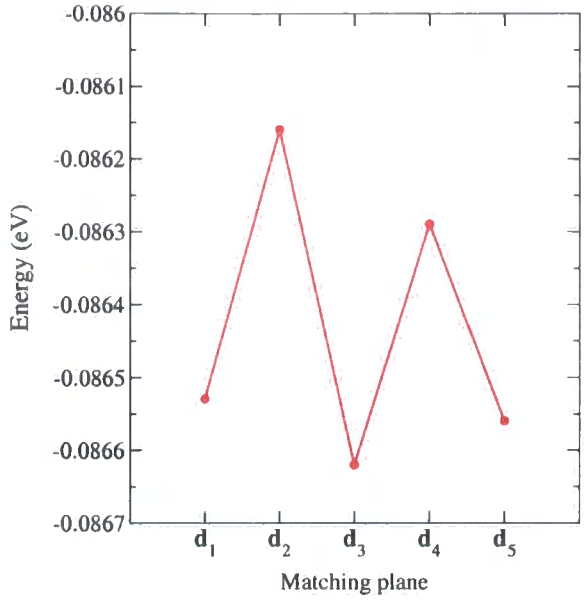

Figure 5.10: The variation of bound state energy for a GaN WZ-ZB conduction band quantum well with the location of matching plane.

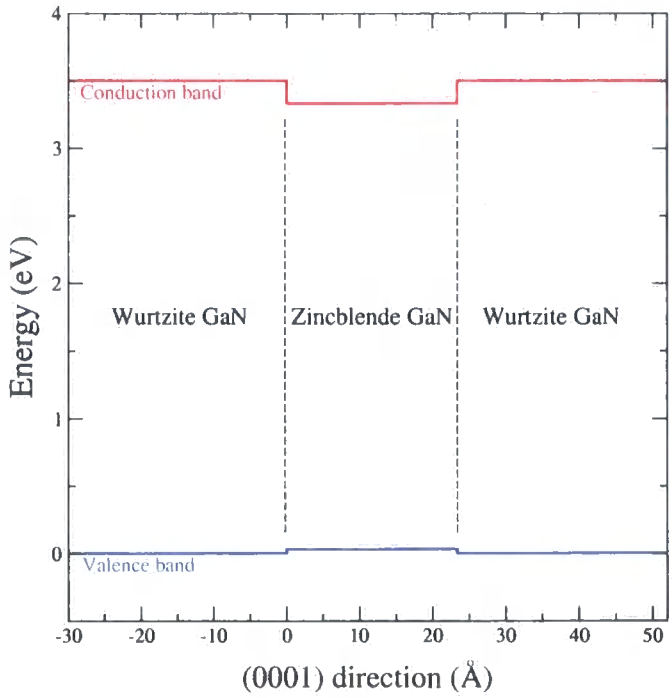

Figure 5.11: The band profile of a 3 unit cell wide zincblende/wurtzite GaN conduction and valence band quantum well

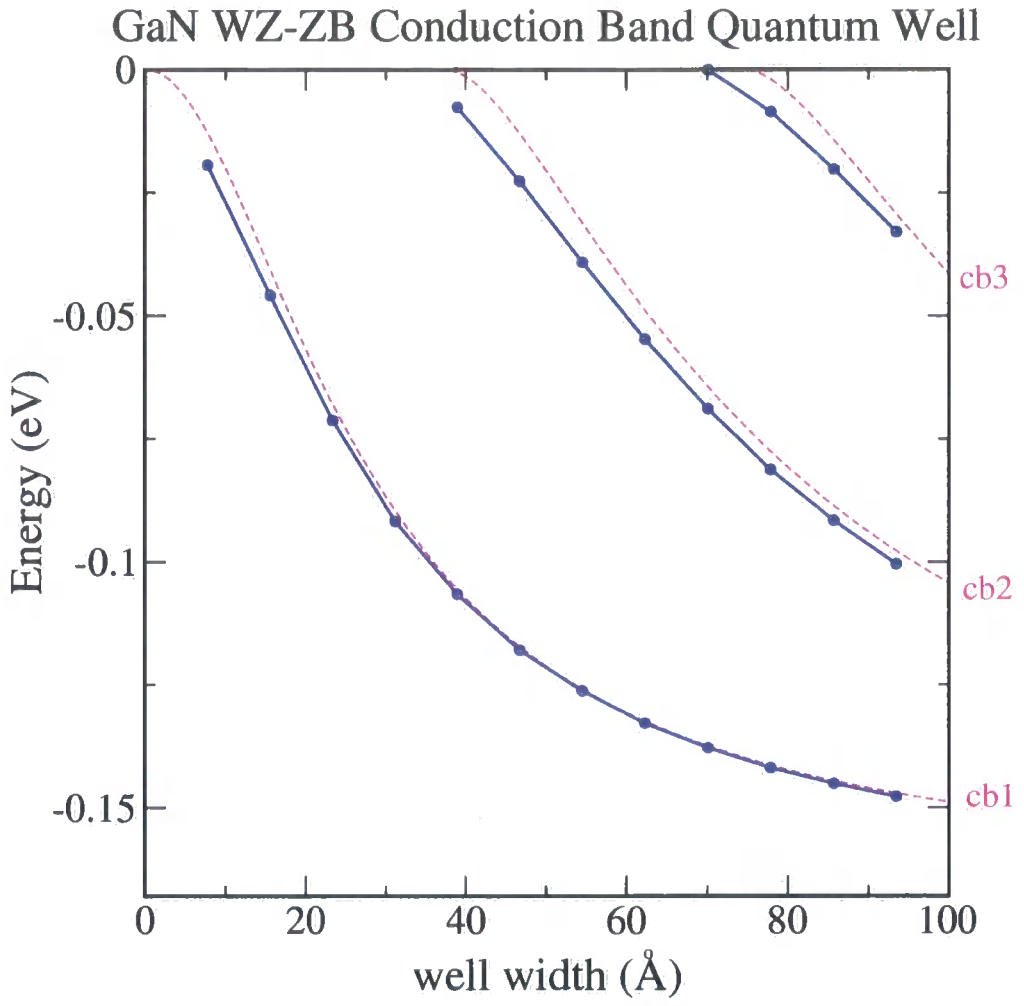

Figure 5.12: The variation of bound state energy with well width of a conduction band WZ-ZB GaN quantum well. Energies are in eV, with 0eV as the top of the well and -0.168eV at the bottom of the conduction band well. Dashed lines illustrate the solutions of an envelope function calculation based on effective masses derived from the pseudopotentials used in the complex bandstructure matching calculation.

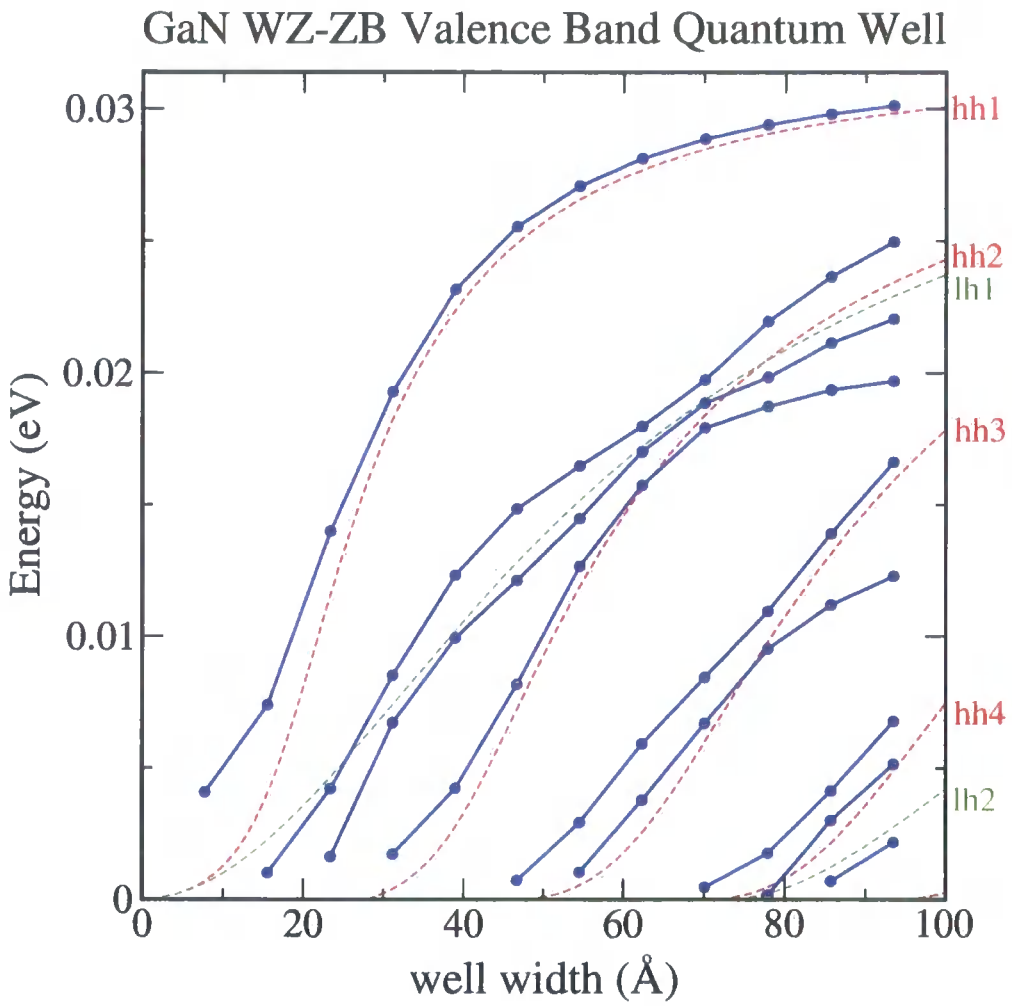

Figure 5.13: The variation of bound state energy with well width of a valence band WZ-ZB GaN quantum well. Energies are in eV, with 0eV as the top of the well, 0.0314eV at the bottom of the valence band well. Dashed lines illustrate the solutions of an envelope function calculation based on effective masses derived from the pseudopotentials used in the complex bandstructure matching calculation.

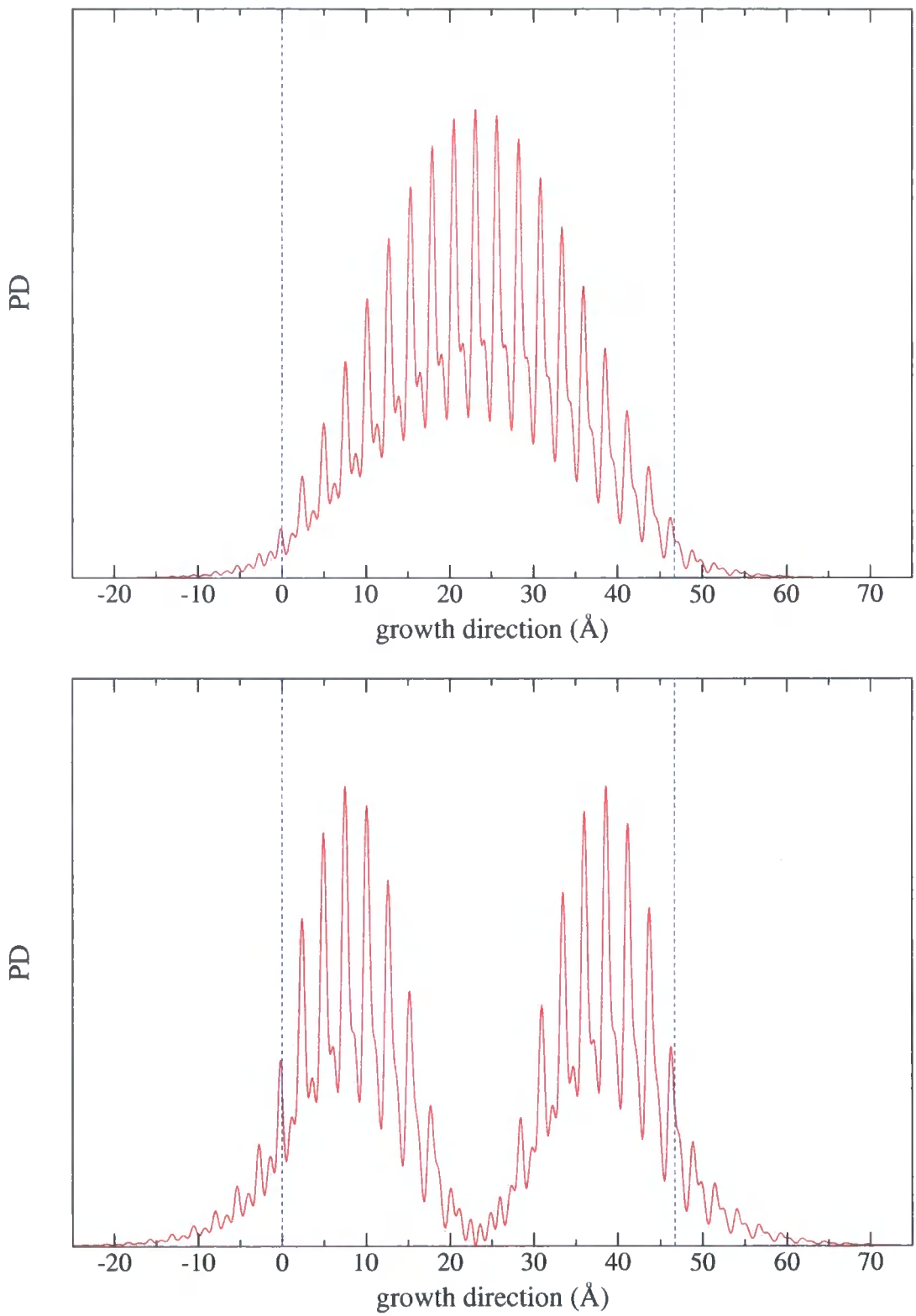

Figure 5.14: The in-plane averaged probability densities for the ground state and 1st excited state of a 46.71Å wide GaN WZ-ZB conduction band quantum well.

based on an effective mass model, with masses derived from the pseudopotential results. For any width above about 4nm we predict more than one conduction subband, and it should be possible to confirm this experimentally using photoluminescence measurements. The in-plane averaged probability densities are displayed in figure 5.14 for the ground state and 1st excited state of a 46.71Å wide GaN WZ-ZB conduction band quantum well.

The valence subband structure is considerably more complicated than for InGaN quantum wells which, because of the nature of the bulk InGaN valence bandstructure, and the small well depth, only possessed one bound state. For the WZ-ZB wells we predict multiple heavy hole, light hole and spin split off subbands. Considerable band mixing is present and the effective mass calculations only broadly reflect the bound state energies as a function of well width. Anti-crossing behaviour is observed, for instance between the 2nd, 3rd and 4th subbands at a well width of 7.5nm. The presence of anti-crossing behaviour would not be predicted by a simple single parabolic band effective mass approach and demonstrates the advantages of the complex bandstructure method for calculating quantum well bound states.

In reality, the well may be under the influence of an electric field. The zincblende region is to a very good approximation unstrained and not prone to pyroelectric effects to quite the same extent of wurtzite materials, but the WZ-ZB and ZB WZ interfaces may well give rise to a polarisation. To properly account for these effects an approach similar to the first principles geometric optimisations discussed in chapter 6 would be required. In fact, an interesting extension to this work would be to use *ab-initio* calculations of the field in a quantum well due to polarisation effects, in a complex bandstructure calculation of the bound states.

5.6 Summary

The bulk local pseudopotential bandstructure and corresponding complex bandstructure of zincblende GaN have been calculated and used in a complex bandstructure study of the electronic states of a wurtzite-zincblende quantum well composed entirely of GaN. The bound state energies and probability densities have been calculated and anti-crossing behaviour has been observed in the states of a valence band quantum well as a function of well width.

Chapter 6

Ab-initio Calculations of Nitride Semiconductors

6.1 Introduction

Ab-initio, total energy calculations have for a number of years been an established and extremely profitable approach in the theoretical toolkit of condensed matter physics. Specifically the combination of density functional theory (DFT), the use of plane waves, and the pseudopotential approximation has proved a particularly effective combination. The approach is often simply referred to as a DFT calculation or as an *ab-initio* plane wave pseudopotential (PWP) calculation. DFT has routinely been applied to solid state problems such as the atomic and electronic structure of crystals, surfaces, interfaces, and the study of defects. More recently DFT has found success in the fields of computational chemistry and the biosciences. This success was formally recognised through the 1998 Nobel prize for chemistry being awarded in part to Walter Kohn "for his development of the density functional theory" [150].

In this chapter, we report total energy calculations using pseudopotentials and plane waves which have been performed on zincblende and wurtzite nitride systems. An overview of the theory and its implementation is given, but many much more detailed reviews are available in the literature [150–162]. The DFT calculations have been used to supply supporting data for the calculations performed in earlier chapters in this thesis and provide an interesting comparison between the empirical and *ab-initio* pseudopotential approaches. Fi-

nally the nature of the wurtzite - zincblende interface is explored by *ab-initio* methods. In particular, the ambiguously defined location of the interface is considered and the degree of structural relaxation is investigated. Estimates are provided for the band offsets which are an important property of a heterointerface.

6.2 Ab-initio Total Energy Calculations

The aim of *ab-initio* total energy calculations is to calculate the total energy of the system without the input of experimental information. For a system of electrons and nuclei, the only information required is a reasonable starting point for the relative positions and atomic numbers of the ions. The calculation of the total energy of a system is in itself not a very useful quantity, but many important physical quantities can be found indirectly from total energy calculations. These physical quantities are often calculated by considering changes in the total energy with system parameters. A simple example of this is the lattice parameter which is found by searching for a minimum in the total energy of a unit cell with a range of lattice parameters. The first principles nature of the calculation enables systems to be investigated where experiments are very expensive, difficult or even impossible to perform. The classic example of the latter is establishing the crystal structure of materials under extremely high pressures. The problems of depending on experimental information for calculation inputs is truly appreciated when the experimental data is inconclusive or unreliable. Within the field of nitride materials, many physical parameters are still poorly known such as band offsets and the built-in electric fields, and more recently even the accepted band gap of InN has been questioned [55,56]. An *ab-initio* approach suffers from none of those problems although it should be noted that that does not mean the results are necessarily any more accurate; that all depends on the strengths and weaknesses of the theory.

6.2.1 Description of the problem

The problem of calculating the total energy of a number of electrons and nuclei is a quantum mechanical many-body problem. Mathematically the Hamiltonian is written as the sum of the kinetic and potential energy operators of the components of the system;

$$\hat{H}_{Many\ Body} = \hat{T}_N + \hat{T}_e + \hat{V}_{NN} + \hat{V}_{eN} + \hat{V}_{ee} \tag{6.1}$$

where the subscripts N refer to the nucleus N and the electrons e. The solution of the Schrödinger equation with the Hamiltonian in (6.1) is clearly impossible without approximation. As with the empirical pseudopotential approach, the Born-Oppenheimer approximation allows the nuclei to be considered stationary so that the nuclear kinetic energy $\hat{T}_N$ term can be ignored, and the nuclear potential term $\hat{V}_{NN}$ will simply be a constant for fixed atomic positions. The problem is now essentially one of an interacting electron gas in the presence of nuclei. The kinetic energy of all the electrons is represented by the operator;

$$\hat{T}_e = \sum_k \frac{-\hbar^2}{2m_e} \nabla_k^2 \tag{6.2}$$

The potential of the nuclei seen by the electrons is represented by

$$\hat{V}_{eN} = -\sum_{k,i} \frac{Z_i e^2}{4\pi\varepsilon_0 |\mathbf{r}_k - \mathbf{R}_i|} \tag{6.3}$$

where Z_i is the atomic number of nucleus i, $\mathbf{R}_i$ denotes the positions of the ions and $\mathbf{r}_i$ denotes the positions of the electrons. This term is usually approximated through the use of pseudopotentials for some of the same reasons as pseudopotentials are used in the empirical pseudopotential approach. The pseudopotential V_{ion} then describes the potential due to the *ionic cores* rather than the nuclei.

The important difference between an empirical and *ab-initio* pseudopotential is the absence of the effects of a mean field in the *ab-initio* pseudopotential. The empirical pseudopotentials include the average effect of all the electron-electron interactions. For this reason the empirical pseudopotentials contribute essential physics to the empirical pseudopotential method whereas in an *ab-initio* calculation they serve only to reduce the computational cost of the calculation. All-electron *ab-initio* calculations in a plane wave basis, without pseudopotentials have been performed, and act as an excellent test of the validity of the

pseudopotential approximation [163]. The *ab-initio* pseudopotentials are generated without experimental input, requiring only the core radius and the ionic charge as input. It should be noted that care must be taken in deciding which electrons are to be considered core electrons, so as not to exclude the effects on bonding of the lower orbitals. This is especially true of some nitrides, in which the upper d-orbitals of Ga and In are known to have an effect on the bonding [164]. For more details on the construction of *ab-initio* pseudopotentials, see the work of Kleinman and Bylander [165] on which many *ab-initio* pseudopotentials are based.

The final term of (6.1) left for consideration is that of the electron electron interactions,

$$\hat{V}_{ee} = \frac{1}{2}\sum_{k\neq l}\frac{e^2}{4\pi\varepsilon_0|\mathbf{r}_k - \mathbf{r}_l|} \tag{6.4}$$

and it is this which presents the greatest challenge because of the many electron interactions. A number of different theoretical frameworks that come under the umbrella of *ab-initio* total energy calculations have been applied to overcoming the difficulties associated with the many electron problem. Two of the most common are the Hartree-Fock (HF) approach and density functional theory (DFT). The Hartree Fock approach is an extension of the mean field Hartree approach, which approximates the actual N electron wavefunction Ψ by a product of single particle orbitals ψ_i. However, only the effect of Coulomb repulsion is included. The Hartree Fock approach improves on this, by including the effects of electron indistinguishability and therefore the Pauli exclusion principle is enforced exactly. However, no further many body effects are included and hence the Hartree Fock theory is not an exact theory. The difference between the actual energy and the Hartree Fock energy is defined as the electron correlation energy

$$E_{Cor} = E - E_{HF} \tag{6.5}$$

This is the effect of all the many body interactions, apart from the exchange interaction. Density functional theory is an exact theory, but practical implementation make use of approximate exchange-correlation functionals to describe the effects of exchange and correlation energy.

6.3 Density Functional Theory

Density functional theory was initially developed as an exact theory for interacting electrons by Hohenberg and Kohn in 1964 [166]. A year later a practical method for using DFT in the calculation of single particle energies was reported [167]. DFT is based on two fundamental theorems [162,166]:

1. *The total energy of a system of electrons and nuclei is a unique functional of the electron density.*
2. *The true ground state energy is exactly equal to the variational minimum of the total energy.*

Equivalent to the first theorem is the observation that the density uniquely determines the overall potential which in turn determines the total energy [162]. This allows a major simplification of the problem without any loss of generality. Now the total energy E can be expressed as a functional $E[\rho(\mathbf{r})]$ of the electronic density $\rho(\mathbf{r})$.

$$E[\rho(\mathbf{r})] = \int V_{ion}(\mathbf{r})\rho(\mathbf{r})d\mathbf{r} + F[\rho(\mathbf{r})] + E_i \tag{6.6}$$

where $V_{ion}(\mathbf{r})$ is the pseudopotential of the ionic cores, $F[\rho(\mathbf{r})]$ is a yet to be determined functional and E_i is a constant energy shift.

DFT avoids the need to describe several interacting electrons by the use of a mean field or effective potential. The concept of a mean field allows N electrons to be described, separately by N Schrödinger-like equations called the Kohn-Sham (KS) equations [167]. The Kohn-Sham equations arise by the application of the second theorem of DFT to the energy functional [162]. The density can now be defined in terms of the wavefunctions of the non-interacting electron-like quasi-particles. That is

$$\rho(\mathbf{r}) = \sum_{n=1}^{N} \psi_n^*(\mathbf{r})\psi_n(\mathbf{r}) \tag{6.7}$$

Where ψ_n are the wavefunctions of n non-interacting electron-like quasi-particles. The functional $F[\rho(\mathbf{r})]$ can now be considered to consist of three components

$$F[\rho(\mathbf{r})] = E_K[\rho(\mathbf{r})] + E_H[\rho(\mathbf{r})] + E_{xc}[\rho(\mathbf{r})] \tag{6.8}$$

$E_K[\rho(\mathbf{r})]$ is the kinetic energy of a system of non-interacting electrons whose electronic density is identical to that of the real system. $E_K[\rho(\mathbf{r})]$ is analogous to $\hat{T}_e$ in equation (6.1), although the expectation value of $\hat{T}_e$ will not correspond to $E_K[\rho(\mathbf{r})]$. $E_H[\rho(\mathbf{r})]$ is the Hartree energy and is analogous to electron interaction operator $\hat{V}_{ee}$, although it also doesn't correspond to the expectation value of $\hat{V}_{ee}$.

$$E_H[\rho(\mathbf{r})] = \frac{1}{2}e^2 \int\int \frac{\rho(\mathbf{r})\rho(\mathbf{r}')}{4\pi\epsilon_0|\mathbf{r}-\mathbf{r}'|} d\mathbf{r}d\mathbf{r}' \tag{6.9}$$

The final term in equation (6.6) is $E_{xc}[\rho(\mathbf{r})]$, the exchange and correlation energy. There is no analogous operator for $E_{xc}[\rho(\mathbf{r})]$ because it arises as a result of the lack of correspondence between the expectation value of the many body operators and the analogous terms in the energy functional. In other words

$$E_H[\rho(\mathbf{r})] + E_K[\rho(\mathbf{r})] \quad \neq \quad < \hat{T}_e + \hat{V}_{ee} > \tag{6.10}$$

$E_{xc}[\rho(\mathbf{r})]$ therefore contains the energy not present in $E_H[\rho(\mathbf{r})] + E_K[\rho(\mathbf{r})]$ that is needed to make $E[\rho(\mathbf{r})]$ exact.

$$E_{xc}[\rho(\mathbf{r})] = E_{exact} - E_H[\rho(\mathbf{r})] - E_K[\rho(\mathbf{r})] \tag{6.11}$$

Effective Potential

The empirical pseudopotential method incorporated the mean field into the empirical pseudopotentials. In an *ab-initio* calculation the mean field is calculated as an effective potential and it is important to consider the form of the effective potential. The Kohn-Sham equations arise as a result of the second theorem which says that the ground state of the

system can be found using the variational principle. Consider the density to be perturbed by a small amount $\delta\rho(\mathbf{r})$ which gives rise to a small change in energy δE.

$$\delta E = \int \delta\rho(\mathbf{r}) \left[V_{ion}(\mathbf{r}) + \frac{\delta E_K[\rho(\mathbf{r})]}{\delta\rho(\mathbf{r})} + \frac{\delta E_H[\rho(\mathbf{r})]}{\delta\rho(\mathbf{r})} + \frac{\delta E_{xc}[\rho(\mathbf{r})]}{\delta\rho(\mathbf{r})} \right] d\mathbf{r} \tag{6.12}$$

Since the number of electrons in the system remains unchanged

$$\int \delta\rho(\mathbf{r}) d\mathbf{r} = 0 \tag{6.13}$$

which ensures that the quantity in square brackets is a constant, which is the chemical potential μ.

$$\mu = V_{ion}(\mathbf{r}) + \frac{\delta E_K[\rho(\mathbf{r})]}{\delta\rho(\mathbf{r})} + \frac{\delta E_H[\rho(\mathbf{r})]}{\delta\rho(\mathbf{r})} + \frac{\delta E_{xc}[\rho(\mathbf{r})]}{\delta\rho(\mathbf{r})} \tag{6.14}$$

The chemical potential is the energy gained as a result of increasing the number of electrons by one. For a ground state system it is equal to the Fermi energy. We can now define an effective potential called the Kohn-Sham potential $V_{KS}(\mathbf{r})$ as the potential seen by the non-interacting electrons.

$$V_{KS}(\mathbf{r}) = V_{ion}(\mathbf{r}) + \frac{\delta E_H[\rho(\mathbf{r})]}{\delta\rho(\mathbf{r})} + \frac{\delta E_{xc}[\rho(\mathbf{r})]}{\delta\rho(\mathbf{r})} \tag{6.15}$$

$$V_{KS}(\mathbf{r}) = V_{ion}(\mathbf{r}) + V_H(\mathbf{r}) + V_{xc}(\mathbf{r}) \tag{6.16}$$

which has also illustrated the definition of the Hartree potential $V_H(\mathbf{r})$ and the exchange-correlation potential $V_{xc}(\mathbf{r})$. The definition of the Kohn-Sham potential is important because it allows the charge density to be constructed from Kohn-Sham single particle orbitals ψ_i. By replacing V with V_{KS} the Schrödinger equation for non-interacting particles can be solved yielding ψ_i .

$$-\frac{\hbar^2}{2m}\nabla^2\psi_i + V_{KS}\psi_i = E_i\psi_i \tag{6.17}$$

The charge density can be constructed from equation (6.7), but it is necessary to know $\rho(\mathbf{r})$ to construct V_{KS}. This circular problem is solved through self-consistency, which we will discuss later.

6.3.1 The Local Density Approximation

The functional for the exchange and correlation energy $E_{xc}[\rho(\mathbf{r})]$ was defined previously in equation (6.11) as the contribution to the total energy from electron-electron interactions not accounted for by the Hartree or kinetic energy terms. $E_{xc}[\rho(\mathbf{r})]$ contains all the "difficult" parts of the many body interaction and as yet we have not considered its form. In general, an exact form for the exchange-correlation functional is not known, and approximations must be employed.

The most common approximation for the exchange-correlation functional is the local density approximation (LDA). The main assumption behind the LDA is that the density is slowly varying. The exchange-correlation energy contribution at a point $\mathbf{r}$ can then be approximated as the exchange-correlation energy of an electron gas of uniform density $\rho(\mathbf{r})$. The exchange-correlation energy per electron in a uniform electron density can be calculated by explicit many body calculations such as quantum Monte-Carlo (see for example [168,169]). Further, a computationally efficient approximation can be achieved by a parameterisation based on these calculations and allows the exchange and correlation energy to be evaluated. The exchange-correlation functional can now be written as

$$E_{xc}\left[\rho(\mathbf{r})\right] = \int \varepsilon_{xc}(\rho(\mathbf{r}))\rho(\mathbf{r})d^3r \tag{6.18}$$

where $\varepsilon_{xc}(\rho(\mathbf{r}))$ is the exact exchange-correlation energy of uniform electron density $\rho(\mathbf{r})$. As part of the definition of the Kohn-Sham potential in equation (6.16), the derivative of exchange-correlation energy with respect to electron density is required. Now

$$\frac{\delta E_{xc}[\rho(\mathbf{r})]}{\delta\rho(\mathbf{r})} = \frac{\partial\left[\rho(\mathbf{r})\varepsilon_{xc}(\rho(\mathbf{r}))\right]}{\partial\rho(\mathbf{r})} \tag{6.19}$$

where

$$\varepsilon_{xc}(\rho(\mathbf{r})) = \varepsilon_{xc}^{hom}(\rho(\mathbf{r})) \tag{6.20}$$

The most common parameterisation for ε_{xc}^{hom} is that of Perdew and Zunger [170] which is based on the quantum Monte Carlo calculations of Ceperly and Alder [169].

Despite its simplicity, the LDA works remarkably well in the context of plane wave pseudopotential calculations based on DFT. Alternatives to the LDA do exist, the most common of which are known as generalised gradient approximations (GGA). In general the exchange-correlation energy is non-local, whereas the LDA is clearly local in nature. By also considering the spatial derivative of the density rather than just the density, GGAs hope to include a little of the non-local nature.

$$E_{xc}\left[\rho(\mathbf{r})\right] = \int \varepsilon_{xc}(\rho(\mathbf{r}), \nabla\rho(\mathbf{r}))\rho(\mathbf{r})d^3r \tag{6.21}$$

Higher and higher order derivatives could in principle be included although presently only the use of first order derivatives is well established. The most commonly used GGAs are that of Perdew and Wang (PW91) [171–173], Perdew, Burke and Ernzerhof (PBE) [174] and a revised form of PBE called RPBE [175]. In this work the well established functionals of Perdew and Wang are used throughout.

Self-consistency

The combination of an approximate form for the exchange-correlation functional, such as the GGA we use in this work, and the definition of an effective potential allows the Kohn-Sham equations to be solved and yield the charge density. However the $E_H[\rho(\mathbf{r})]$, $E_K[\rho(\mathbf{r})]$ and $E_{xc}[\rho(\mathbf{r})]$ are all functionals of the charge density. This leaves a circular problem, which

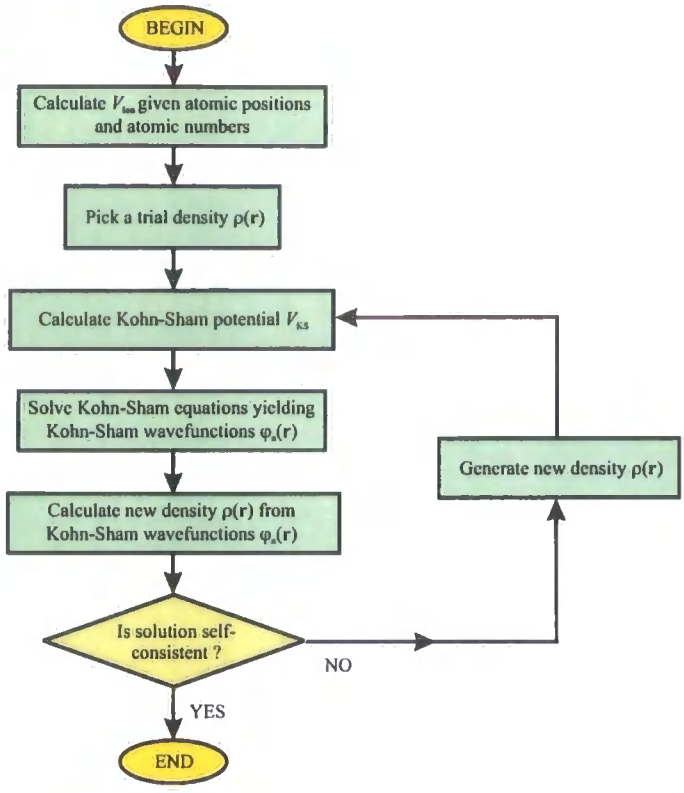

Figure 6.1: Flow chart describing the procedure for finding the self-consistent solutions to the Kohn-Sham equations.

is solved through the concept of self-consistency.

For the densities to be self-consistent, the charge density should give rise to an effective potential that on solution of the Kohn-Sham equations gives rise to Kohn-Sham wavefunctions with the same charge density. In practice this is achieved by starting from an initial guess for the density which is then used to calculate the Kohn-Sham potential and then solve the Kohn-Sham equations. The resultant Kohn-Sham wavefunctions and therefore the density is then hopefully closer to the true ground state than the original guess. This procedure is repeated with the new density and Kohn-Sham wavefunctions until self-consistency is observed. Figure 6.1 describes this process as a flow chart. The computational cost can be significantly reduced with improved iterative schemes for the self-consistent minimisation (see for example [157]).

Expansion using a plane wave basis set

A Kohn-Sham wavefunction is represented as a Fourier expansion in the same way as the empirical pseudo-wavefunctions:

$$\psi_n(\mathbf{r}) = \sum_{\mathbf{g}} c_{n,\mathbf{k}+\mathbf{g}} e^{(i(\mathbf{k}+\mathbf{g})\cdot\mathbf{r})} \tag{6.22}$$

where g are the reciprocal lattice vectors and k is the wavevector of the state. The use of a plane wave expansion implies a periodic system, but by making the cell size large enough, a periodic array of essentially isolated aperiodic systems may also be studied. The unit cell used in a calculation in this way is referred to as a supercell. In theory the calculation of charge density requires an infinite number of k-points to be calculated, however in practice this is approximated by a finite sampling of k-points just as it was in the calculation of the empirical pseudo-charge density. Each k-point involves a separate self-consistent calculation and therefore any reduction in the number of k-points results in a significant saving in computational cost. Usually a relatively small number of k-points, known as *special k-points*, covering the irreducible wedge of the first Brillouin zone are sampled. Several schemes for this sampling exist such as those of Chadi and Cohen [57] and Monkhorst and Pack [58]. These schemes involve the allocation of a weight $w_{\mathbf{k}}$ for the contributions of each special k-point.

$$\rho(\mathbf{r}) = \sum_{n}\sum_{\mathbf{k}} \psi^*_{n\mathbf{k}}(\mathbf{r})\psi_{n\mathbf{k}}(\mathbf{r}) = \sum_{n}\sum_{\mathbf{k}} w_{\mathbf{k}} \sum_{\mathbf{g},\mathbf{g}'} c^*_{n,\mathbf{k}+\mathbf{g}} c_{n,\mathbf{k}+\mathbf{g}'} e^{(i(\mathbf{g}-\mathbf{g}')\cdot\mathbf{r})} \tag{6.23}$$

In this work the Monkhorst and Pack (MP) scheme is used. In addition to the finite sampling of k-points, the plane wave expansion has to be truncated. In contrast to the EPM the number of plane waves is not kept constant, but a kinetic energy cut-off E_{cut} is chosen such that all plane waves k with lower energy that are obeying the inequality

$$E_{cut} > \frac{\hbar^2}{2m_e} |\mathbf{k}+\mathbf{g}| \tag{6.24}$$

are included in the expansion. The use of a kinetic energy cut-off rather than a fixed number of plane waves has the consequence that the number of plane waves, and therefore the computational cost, changes with the size of the supercell. For a larger system it is reasonable to expect more plane waves to be needed to successfully approximate the wavefunction.

The use of a plane wave basis set is advantageous in that the substitution of equation (6.22) into the Kohn-Sham equations yields a particularly simple form:

$$\sum_{\mathbf{g}'} \left[\frac{\hbar^2}{2m} |\mathbf{k}+\mathbf{g}|^2 \delta_{\mathbf{g}\mathbf{g}'} + V_{ion}(\mathbf{g}-\mathbf{g}') + V_H(\mathbf{g}-\mathbf{g}') + V_{xc}(\mathbf{g}-\mathbf{g}') \right] \times c_{n,\mathbf{k}+\mathbf{g}'} = \varepsilon_n c_{n,\mathbf{k}+\mathbf{g}'} \tag{6.25}$$

The simplest approach to finding the self-consistent solution to the Kohn-Sham equations within a plane wave basis is by diagonalisation of the Hamiltonian matrix. The size of the matrix is determined by the kinetic energy cut-off. In all but the most simple systems, the N^3 scaling for the cost of a diagonalisation would make systems with more than a few atoms impossible. In practice, more advanced techniques for minimising the Kohn-Sham energy functional are employed. These typically treat the plane wave coefficients as dynamical variables and iteratively improve the self-consistent solution to the Kohn-Sham energy functional. [157,176–178]

6.4 Structural relaxations

The Kohn-Sham equations can now be solved self-consistently yielding a charge density for each of the n bands and a total energy for the system. The total energy can be minimised for changes in the supercell dimensions or even the ionic positions. This on its own is a powerful tool and can determine bandstructures, lattice parameters, and providing there are not too many degrees of freedom, the crystal structure.

For more complicated systems of ions with many degrees of freedom, there is a need to calculate the forces on the ions and establish a minimum energy set of ionic positions by minimising the forces. This is achieved through the application of the Hellman-Feynman theorem.

6.4.1 Hellman-Feynman theorem

If $\mathbf{F}_i$ is force acting on ion i at position $\mathbf{R}_i$, $\mathbf{F}_i$ is given by the full derivative of the total energy of the system with respect to the ionic position:

$$\mathbf{F}_i = -\frac{dE}{d\mathbf{R}_i} \tag{6.26}$$

The energy depends on all the wavefunctions and atomic positions, and therefore the full derivative must be written in terms of partial derivatives as

$$\mathbf{F}_i = -\frac{\partial E}{\partial \mathbf{R}_i} - \int \frac{\partial E}{\partial \psi_n}\frac{d\psi_n}{d\mathbf{R}_i} - \int \frac{\partial E}{\partial \psi_n^*}\frac{d\psi_n^*}{d\mathbf{R}_i} \tag{6.27}$$

this can be simplified using

$$E = < \psi | H | \psi > \tag{6.28}$$

which enables the final two terms in equation (6.27) to be written as

$$\sum_n E_n \frac{\partial}{\partial \mathbf{R}_i} < \psi_n | \psi_n > \tag{6.29}$$

where E_n is the energy eigenvalue for the electronic eigenstate ψ_n. Equation (6.29) is clearly zero for all n as $< \psi_n | \psi_n >$ is simply the normalisation constant. Hence, the Hellman-Feynman theorem states that if the electronic wavefunctions are eigenstates of the Hamiltonian, the force felt by an ion is just the partial derivative of the total energy with respect to the ionic position.

$$\mathbf{F}_i = -\frac{\partial E}{\partial \mathbf{R}_i} \tag{6.30}$$

This allows the forces on the individual ions to be calculated and the equilibrium structure

to be determined by what is called a "geometric optimisation".

6.4.2 Geometric optimisation

A geometric optimisation involves predicting the equilibrium ionic positions and or the equilibrium lattice constants for the system. Within the Born-Oppenheimer approximation the equilibrium ionic positions can be established through the Hellman-Feynman forces. A self-consistent electronic calculation is performed for a given set of ionic positions and the Hellman-Feynman forces are then obtained. If the forces are not below a given numerical tolerance then the ions are moved in the direction of the forces and the process is repeated until equilibrium is achieved. The same procedure can involve changes to the lattice constants, using stresses, in order to establish their equilibrium value at the same time. With each geometric optimisation iteration the old charge density is used as the initial guess. This gives a starting point that should be close to the new self-consistent density and therefore significantly reduce the computational cost. A flowchart describing the overall procedure is given in figure 6.2. Where possible the symmetry of the system is used to reduce the degrees of freedom for the geometric optimisation.

6.4.3 Lattice relaxations

The geometric optimisation becomes less efficient as the number of degrees of freedom increases. Is is sometimes computationally cheaper to vary manually one of the lattice constants and look for a minimum in the total energy as a function of lattice constant. At each lattice constant, if the symmetry of the system allows the ions to move, a separate geometric optimisation must be performed. The form of total energy as a function of lattice constant is asymmetric and is well described by Murnaghan's equation [176,179,180].

Murnaghan's equation

Murnaghan's equation [179,180] is an equation of state which gives the pressure as a function of the adiabatic bulk modulus and as such can be used to model the change in energy with volume [176] as

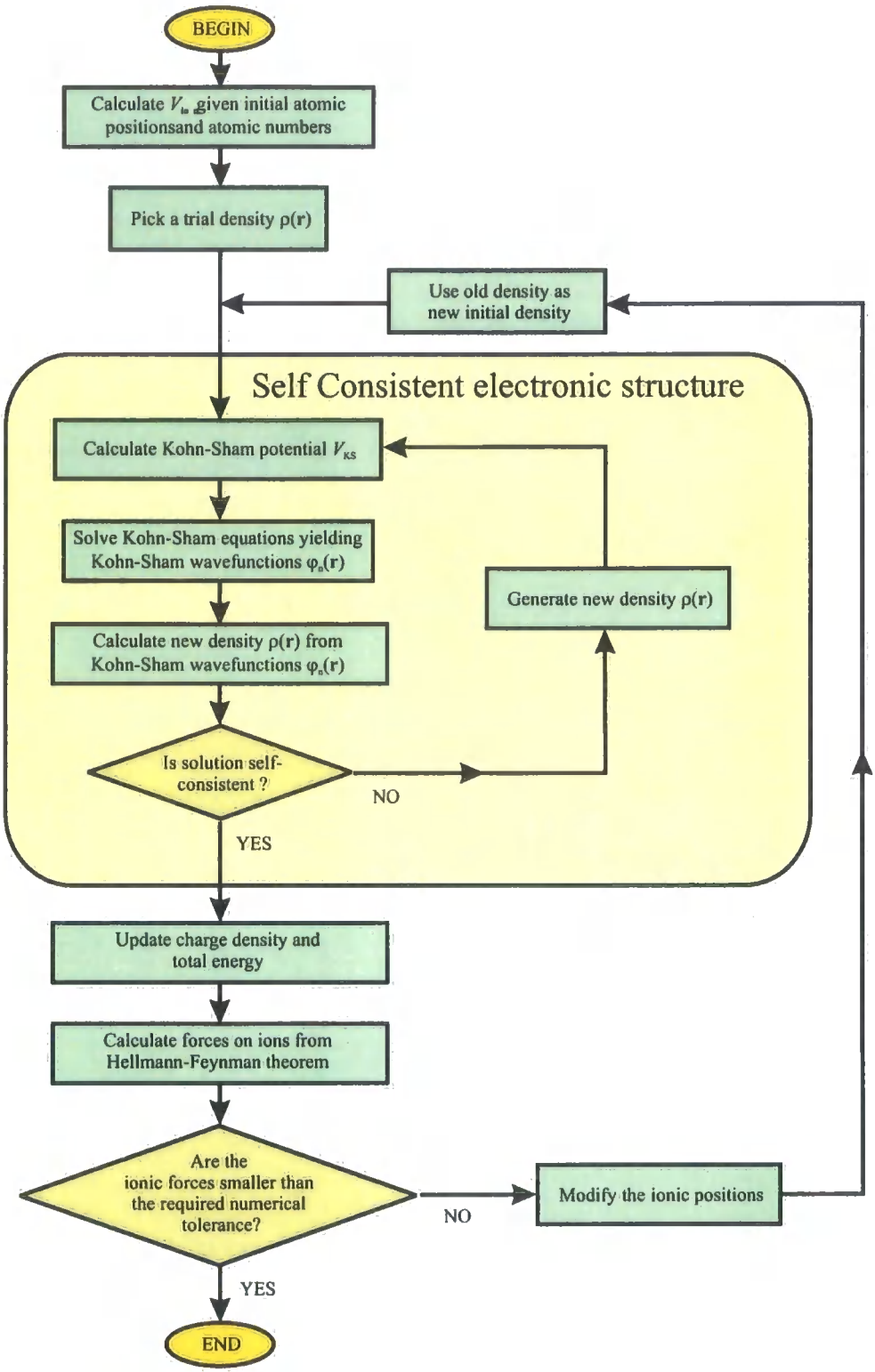

Figure 6.2: Flow chart describing the procedure for establishing the equilibrium ionic positions.

$$E = \frac{\kappa V}{\kappa'}\left[\frac{1}{\kappa' - 1}\left(\frac{V_0}{V}\right)^{\kappa'}\right] + E_0 \tag{6.31}$$

Here κ is the bulk modulus, κ' is the derivative of bulk modulus with pressure and V_0 is the equilibrium volume. By fitting 6.31 to a minimum of five energies computed at different cell volumes (c-lattice parameters), the values of κ, κ' and V_0 can be calculated. For a structural relaxation of a supercell, we are only interested in the equilibrium volume [176,181]. With the equilibrium lattice parameters established a further geometric optimisation of the atomic positions is performed for a supercell with the equilibrium lattice parameters.

6.5 DFT calculations

In this work first principles calculations have been performed on bulk crystals and wurtzite-zincblende superlattices of AlN, GaN, InN. A commercial plane wave density functional code called CASTEP [162] was used for this purpose. Ultra-soft Vanderblit pseudopotentials [182] were used throughout. For GaN and InN, these pseudopotentials treated the *d* electrons as valence rather than core electrons to account for the known effect they have on bonding for the nitrides [164]. An increased computational cost is incurred as a result of the extra electrons and AlN was noticeably quicker in calculations. The GGA of Perdew and Wang [173] was used for all calculations.

6.5.1 Convergence tests

As with the empirical calculations involving plane waves, a confirmation of the convergence of the wavefunction with respect to the plane wave kinetic energy cut-off is important in establishing the validity of the results. Convergence must also be tested against the number of **k**-points within the Monkhorst-Pack scheme used in the self-consistent calculation of the wavefunctions. Finally, if periodicity is not required in one or more directions then the convergence against the size of the supercell must also be tested.

The most convenient test for convergence is the total energy, which can be examined as a function of plane wave kinetic energy cutoff and number of **k**-points. Figure 6.3 describes

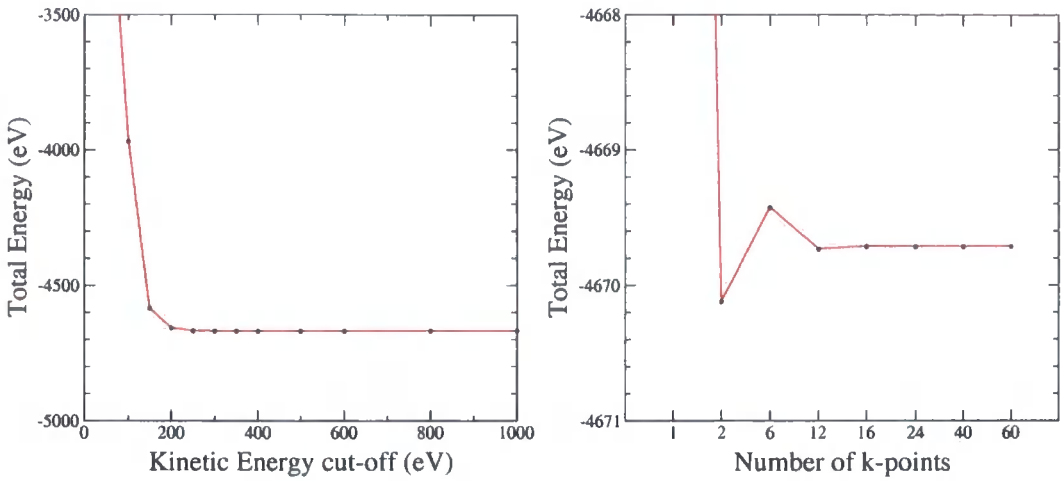

Figure 6.3: i) The convergence of total energy with increasing plane wave energy cutoff for wurtzite GaN. ii) The convergence of total energy with increasing number of k-points for wurtzite GaN.

such a convergence test for a single unit cell of GaN. The total energy is its self an important quantity, but it does not alone provide a good test from which to judge the convergence. It is important to also confirm the convergence against the particular outputs required from the calculation. In this work we calculate and make use of the lattice constants, and therefore it is reasonable to examine the convergence of the predicted lattice constants as well. Figure 6.4 shows the convergence of the lattice constants for wurtzite GaN against kinetic energy cut-off and number of k-points.

Kinetic energy cut-off

The kinetic energy cut-off depends only on the depth of the pseudopotentials and is therefore a function of the species present. Nitrogen has quite a deep pseudopotential and therefore the cut-off needed is higher than for many other elements. From figures 6.3 and 6.4 it is clear that 350eV is adequate and has been used in the calculations in this work. A kinetic energy cut-off of 350eV is sufficient to converge the total energy to within 0.01eV and the lattice constants to within 0.002 Å. Similar tests were performed for AlN and InN, however the deep nitrogen pseudopotential dominates and no significant difference is noticed on the convergence requirements.

The pseudopotentials used in the calculations presented here are 'ultrasoft pseudopo-

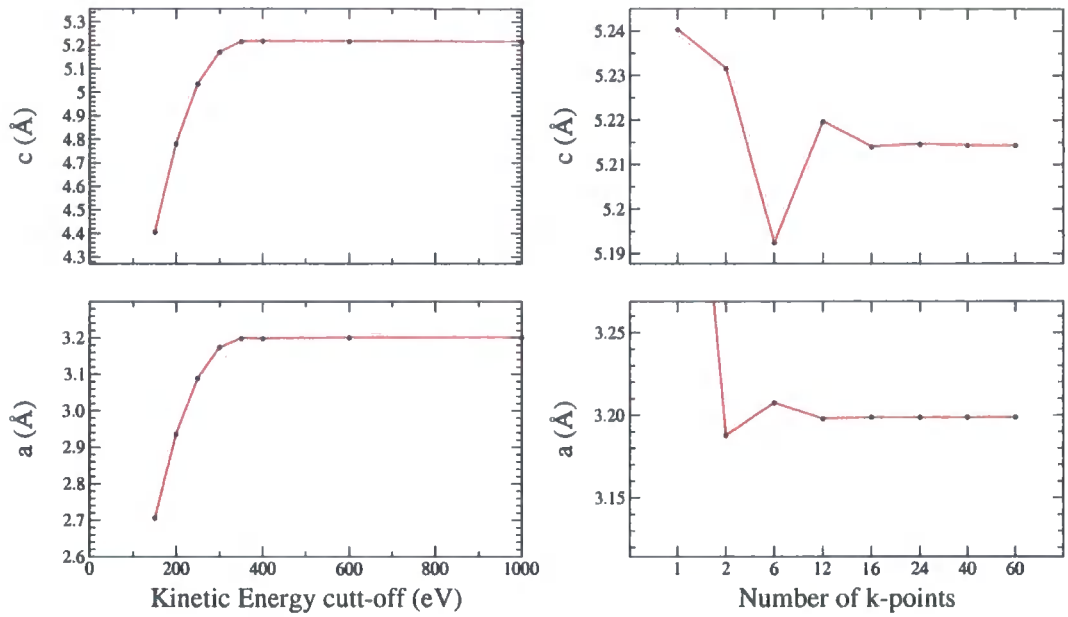

Figure 6.4: i) The convergence of lattice constants with increasing plane wave energy cutoff for wurtzite GaN. ii) The convergence of lattice constants with increasing number of k-points for wurtzite GaN.

tentials' (USP) [182]. USPs are weaker potentials and therefore require a smaller energy cutoff than norm-conserving *ab-initio* pseudopotentials. This is achieved by relaxing the restriction of norm-conservation and accounting for the resulting difference between the exact and the pseudo charge density using localised augmentation functions centred on each atom [182].

It is interesting to compare the convergence requirements of the DFT calculations with the convergence tested for the EPM. The energy cutoff and therefore the number of plane waves required for DFT calculations is significantly greater than those of the empirical pseudopotential approach. This is mainly because the empirical pseudopotentials are weaker than the *ab-initio* pseudopotentials. *Ab-initio* pseudopotentials are a result of only the cancellation of the orthogonalisation potential and the core ionic potential. The empirical pseudopotentials attempts to include the mean field effects of other electrons, through the experimental input, that DFT seeks to calculate self-consistently. This mean field further softens the potential and means that a smaller number of plane waves are required.

Number of k-points

The number of k-points required within the Monkhorst-Pack scheme [58] is a function of the structure and a convergence test should be performed for all structures being studied. Figures 6.3 and 6.4 show that 16 k-points generated from a grid of 7 × 7 × 4, is sufficient to converge the total energy to within 0.002eV and the lattice constants to within 0.001 Å. Similar tests were performed on all the different structures investigated using DFT in this work and a suitable number of k-points corresponding to a similar level of convergence were used.

6.6 Lattice constants

As an initial fundamental test of the DFT calculations and to provide supporting data for other calculations, the lattice constants of the bulk materials were investigated first. GaN, AlN and InN were considered in both the wurtzite and zincblende crystal structures. For the wurtzite crystal structure the same unit cell geometry as was used in the EPM calculations is considered, although to aid visualisation the origin at the bond centre has been located at the centre of the unit cell. For the zincblende structure, calculations were performed on the primitive 2-atom unit cell, the conventional 8-atom cubic unit cell and an alternative 6-atom unit cell that shares the same hexagonal geometry as wurtzite. The 6-atom unit cell has its c-lattice vector in the 111-direction, which corresponds to the 0001 direction in wurtzite. Figures 6.5 and 6.6 illustrate the geometry of the 4 different unit cells.

The convergence tests described in the previous section concluded that a MP grid of 7 × 7 × 4 was sufficient for wurtzite and it was also found to be sufficient for the zincblende 6-atom cell. A grid of 7 × 7 × 7 was used for the primitive zincblende cell and a grid of 4 × 4 × 4 was used for the conventional zincblende unit cell. Table 6.1 contains the calculated lattice constants for wurtzite AlN, GaN and InN. All the calculated values are within 2% of the experimental values. DFT calculations are often quoted as having an accuracy of 1-2% for lattice constants [153], and the values presented here are therefore reasonably accurate.

The lattice constants calculated for the zincblende 6-atom cell have a different a and c as a result of the geometry of the 6-atom cell. Table 6.2 contains the calculated lattice constants for this unusual 6-atom unit cell. Comparisons are made with the experimental

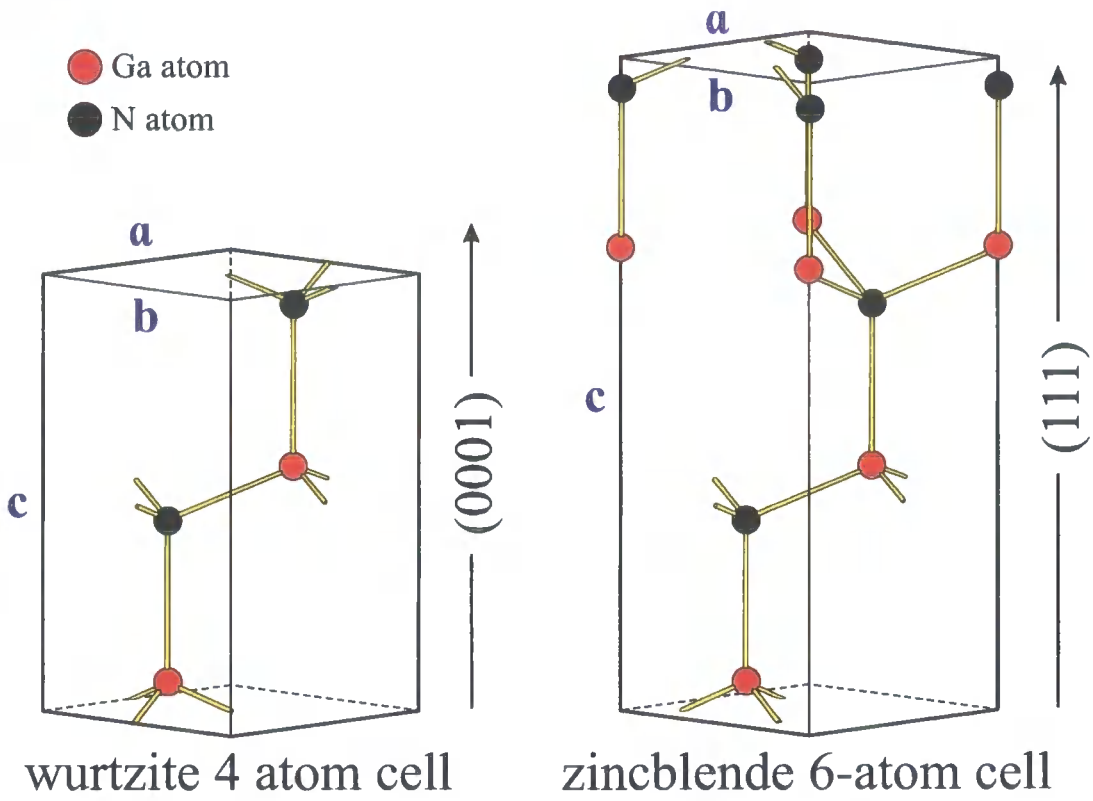

Figure 6.5: The wurtzite unit cell and the corresponding zincblende unit cell, with the same hexagonal geometry. For ideal wurtzite, the zincblende unit cell should be exactly 50% larger in the c-direction

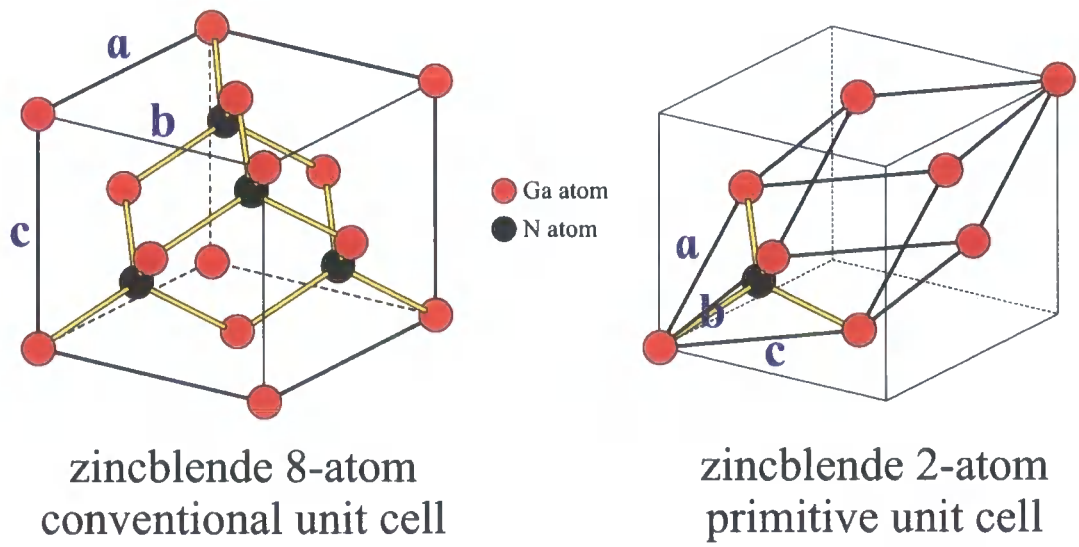

Figure 6.6: The conventional 8-atom unit cell for zincblende and the primitive 2-atom unit cell.

		CASTEP	experimental
wurtzite **AlN**	a_{wz} (a_{zb})	3.0578 (4.324)	3.110 (4.398) [184]
	c	4.9023	4.980 [184]
	u	0.3817	0.3819 [44]
wurtzite **GaN**	a_{wz} (a_{zb})	3.1983 (4.523)	3.190 (4.511) [184]
	c	5.2136	5.189 [184]
	u	0.3760	0.3768 [44]
wurtzite **InN**	a_{wz} (a_{zb})	3.5782 (5.060)	3.544 (5.012) [12]
	c	5.7870	5.718 [12]
	u	0.3785	0.3790 [44]

Table 6.1: The calculated and experimental lattice constants (in Angstroms) for wurtzite GaN, InN and AlN. The values in parenthesis are the wurtzite lattice constants multiplied by $\sqrt{2}$ to provide a meaningful comparison with zincblende.

		CASTEP	experimental
6-atom **AlN**	a_{wz} (a_{zb})	3.0423 (4.3025)	3.10 (4.38) [185]
	c	7.4517	7.59
	u	0.37514	0.375
6-atom **GaN**	a_{wz} (a_{zb})	3.1970 (4.5212)	3.18 (4.50) [186]
	c	7.828	7.80
	u	0.37507	0.375
6-atom **InN**	a_{wz} (a_{zb})	3.5314 (4.9942)	3.52 (4.98) [35]
	c	8.6895	8.63
	u	0.37417	0.375

Table 6.2: The calculated a and c and lattice constants (in Angstroms) for zincblende GaN, InN and AlN. The experimental value of zincblende a_{zb} lattice constant is given in parenthesis with the equivalent wurtzite. The corresponding experimental value of c is then calculated from a_{zb}. For zincblende u should be exactly 0.375.

		CASTEP	experimental
6-atom **AlN**	a_{zb}	4.3020	4.38 [185]
2-atom **AlN**	a_{zb}	4.3019	4.38 [185]
8-atom **AlN**	a_{zb}	4.3018	4.38 [185]
6-atom **GaN**	a_{zb}	4.5212	4.50 [186]
2-atom **GaN**	a_{zb}	4.5219	4.50 [186]
8-atom **GaN**	a_{zb}	4.4943	4.50 [186]
6-atom **InN**	a_{zb}	4.9942	4.98 [35]
2-atom **InN**	a_{zb}	5.0562	4.98 [35]
8-atom **InN**	a_{zb}	5.0464	4.98 [35]

Table 6.3: The calculated and experimental a_{zb} lattice constants (in Angstroms) for three different unit cells of zincblende GaN, InN and AlN.

value for the a-lattice constant and the equivalent c lattice constant that should be exactly $\sqrt{8/3} \times 3/2 \times a_{zb}$, where a_{zb} is the equivalent zincblende conventional unit cell lattice constant. The wurtzite a-lattice constant a_{wz} is always related to the zincblende one by $a_{wz} \times \sqrt{2} = a_{zb}$. The theoretical values of a_{zb} are within the 2% accuracy expected of a DFT calculation. The values of "experimental" c-lattice constant are also in good agreement with those calculated. The wurtzite internal parameter for a zincblende structure should be exactly $\frac{3}{8} = 0.375$ and the calculated values are very close to that.

Table 6.3 contains the calculated lattice constants for the three different unit cells of zincblende AlN, GaN and InN. The various unit cell lengths have been converted to that of a zincblende conventional cell length for comparison purposes. Agreement between the different cells is to better than 1% and again the experimental values all agree within 2%.

6.6.1 Effect of biaxial strain

The relaxation of a crystal under the influence of biaxial strain can be studied from first principles using DFT. The in-plane lattice parameters of the strained unit cell are held

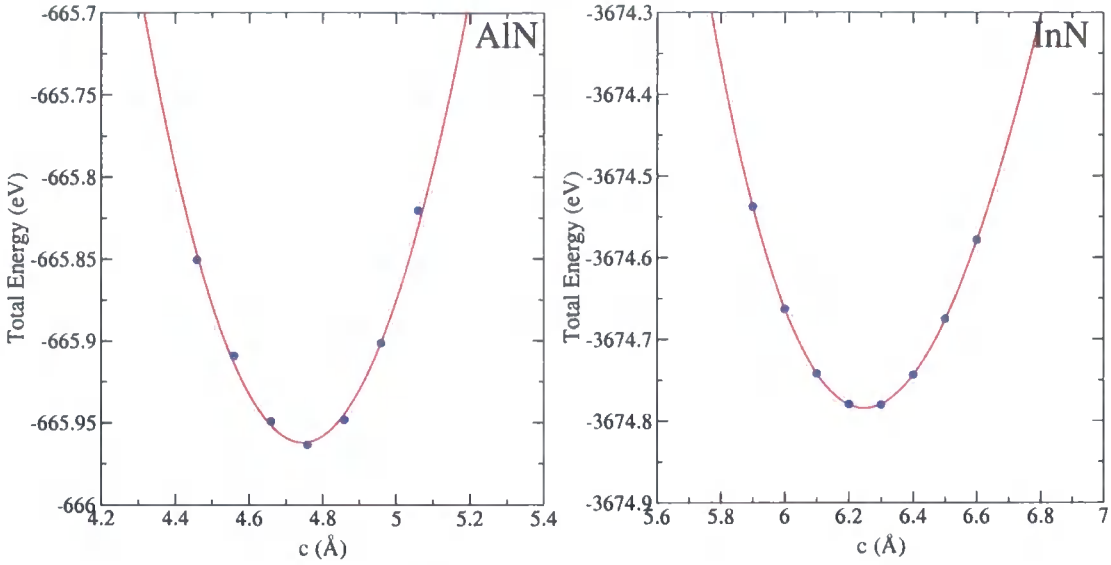

Figure 6.7: Total energy against c-lattice constant for i) Lattice relaxation of wurtzite AlN grown on wurtzite GaN. Minimum at $c = 6.248$Å. ii) Lattice relaxation of wurtzite InN grown on wurtzite GaN. Minimum at $c = 4.736$Å. The dots represent the total energy calculated by DFT and the solid line in the best fit by least squares to Murnaghan's equation.

at the chosen value, which in the case of a pseudomorphic layer, would be those of the substrate. The c-lattice parameter is then varied with a separate geometric optimisation of the ions being performed for each different length of c. The minimum is then found by fitting the data to a Murgnahan.

Wurtzite on wurtzite heteroepitaxy

The EPM calculations of alloy bandstructures relied on known values for the relaxed c-lattice of wurtzite AlN and InN grown with the in-plane lattice of wurtzite GaN. In this section we consider the *ab-initio* calculations used to obtain those values. Figure 6.7 shows plots of total energy against c-lattice constant used to predict the equilibrium relaxation. The c-lattice parameter of AlN has lowered from 4.9023Å to 4.736Å under the biaxial strain appropriate to a GaN substrate. Conversely the c-lattice parameter of InN is increased from 5.7870Å to 6.248Å as the GaN in-plane lattice parameter is smaller than that of InN.

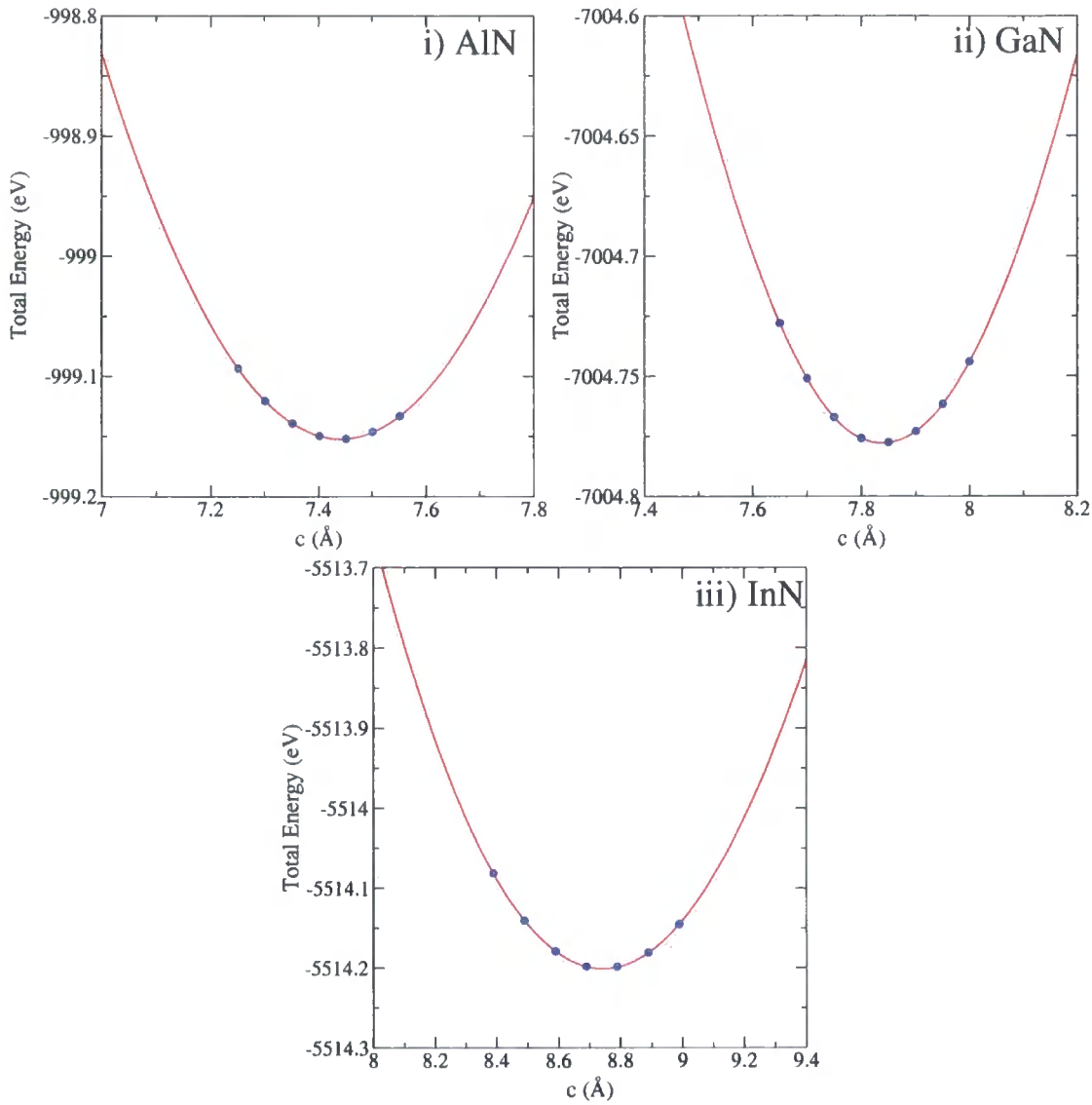

Figure 6.8: Total energy against c-lattice constant for i) Lattice relaxation of zincblende AlN grown on wurtzite AlN. Minimum at $c = 7.4418$Å. ii) Lattice relaxation of zincblende GaN grown on wurtzite GaN. Minimum at $c = 7.8380$Å. iii) Lattice relaxation of zincblende InN grown on wurtzite InN. Minimum at $c = 8.7427$Å. The dots represent the total energy calculated by DFT and the solid line in the best fit by least squares to Murnaghan's equation.

Zincblende on wurtzite homoepitaxy

The small difference in lattice constant between the wurtzite and zincblende crystal structures of the same material suggests that very little relaxation should be observed for zincblende grown on wurtzite. The same approach as was applied to wurtzite heteroepitaxy was used establish the relaxed c-lattice constants. Figure 6.8 contains the plots of total energy against c-lattice constant used to predict the equilibrium relaxation. The calculated values of relaxation were indeed small as would be expected from such little biaxial strain. Relaxations of 0.01Å were observed for GaN and AlN and a larger value of 0.06Å was observed for InN. The values of the relaxed lattice constant for the zincblende nitrides on wurtzite were required as a starting point for the calculation of WZ-ZB band offsets.

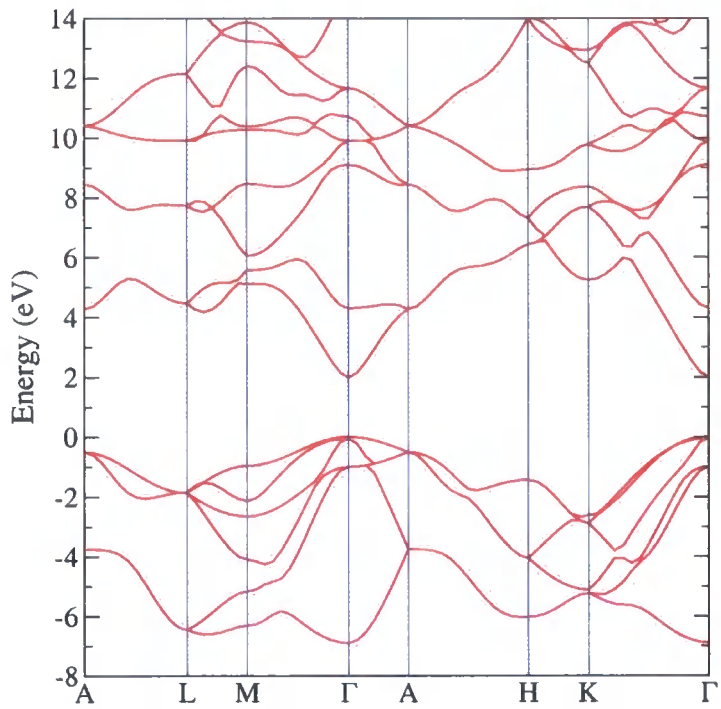

Figure 6.9: *Ab-initio* bandstructure for wurtzite GaN.

6.7 Bandstructure

DFT calculations can be used to produce *ab-initio* bandstructures by simply performing the calculation over the range of **k** required. Figure 6.9 shows the *ab-initio* bandstructure

for wurtzite GaN. The most important difference between the *ab-initio* and empirical bandstructures (see figure 2.8) is in the underestimation of the band gap. DFT is a ground state theory and the lines on the bandstructure above the valence band represent *unoccupied orbitals* rather than *excited states*. It is therefore not surprising that the excited states are not accurately represented. However, apart from the band gap, the *ab-initio* conduction bands are surprisingly accurate.

The *ab-initio* bandstructures of the wurtzite and zincblende nitrides studied in this work are required as part of the calculation of WZ-ZB band offsets.

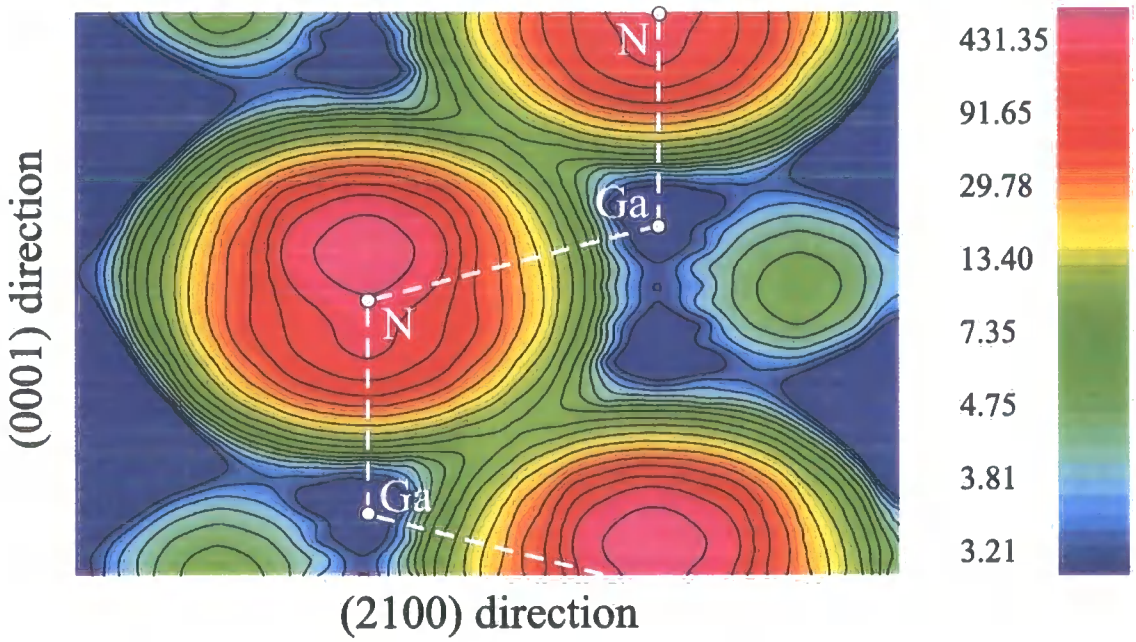

Figure 6.10: *Ab-initio* charge density for wurtzite GaN. The y-axis is the growth direction and the x axis defines a plane cutting through the core sites and bonds between them. The charge density is in units of electrons per unit cell volume.

6.8 Charge densities

As a consequence of the workings of a DFT calculation, the charge densities are always explicitly calculated. For example the *ab-initio* charge density of wurtzite GaN is presented in figure 6.10 which should be compared with the empirical charge density in figure 2.12. Overall the two charge densities are obviously quite different, with the the *ab-initio* density showing more spherically symmetric distribution and steeper peaks. The

cause of the difference in shape is not at present known. The empirical charge densities did not include the d-electrons, but even if the d-electrons are excluded from the *ab-initio* calculation the densities are still very different. A study of the differences in the charge densities produced by the two methods would make an interesting extension to this work.

6.9 Interface calculations

The properties of a semiconductor interface are a result of the change in structure and chemical composition across the interface. As such these properties are determined by the ground state of the system and are therefore a good candidate for study by a DFT calculation. In this section the techniques of DFT are used to determine the band offsets of nitride wurtzite - zincblende homointerfaces, the degree of interface reconstruction and to study the effective "location" of the interface. A general overview of the geometry of the WZ-ZB and ZB-WZ interfaces was given in chapter 5.

6.9.1 Supercell

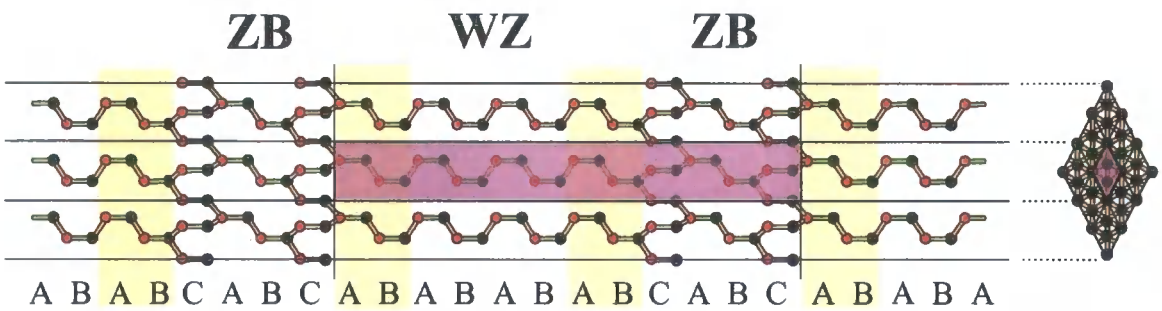

Figure 6.11: Schematic illustration of the supercell used to produce the superlattice from which the interface properties are extracted. This supercell contains 24 atoms, 12 Gallium and 12 Nitrogen. The corresponding stacking sequence used to generate the supercell is illustrated, the yellow bars highlight atoms in the interface region.

The first step in the calculation of interface properties is the construction of a supercell. The supercell has to be periodic in all three dimensions and therefore must contain both a region of wurtzite and zincblende material and both a WZ-ZB and ZB-WZ interface. The periodic supercell is actually a unit cell of a superlattice of alternating wurtzite and zincblende crystals. Figure 6.11 illustrates this approach for a 24 atom supercell. The

supercell must be large enough to include an adequate bulk-like representation of both the wurtzite and zincblende regions. These regions must approximately have the charge densities, potentials and the relaxed atomic positions of the bulk. The computational cost is however very strongly dependent on the number of atoms and size of cell. Previous workers report that for band offset calculations layers 8 to 12 atoms thick are required to achieve bulk-like properties at the layer centre [40,187,188]. However the WZ-ZB superlattice results from an ordering of the stacking sequence rather than a change in chemical composition and there is a region, 4 atoms thick of overlap between the crystal structures. A given atom in the supercell only "knows" it is wurtzite or zincblende from the positions of its second and third nearest neighbours. It is therefore reasonable to assume that the interface regions will be larger than those based around superlattices of chemically different layers. To examine properly the convergence of the bulk-like properties of the layers against the size of supercell, a range of supercell sizes was studied. The smallest conceivable WZ-ZB superlattice could be constructed from 14 atoms and would only contain one instance of the zincblende "*C*" stacking sequence. Larger supercells would contain increasing numbers of "*C*" stacking sequences, for example

14 atom supercell:	*AB***AB***C***AB**
24 atom supercell:	*ABAB***AB***CABC***AB**
34 atom supercell:	*ABABAB***AB***CABCABC***AB**
48 atom supercell:	*ABABABABAB***AB***CABCABCABC***AB**

where the sequence letters in bold represent stacking layers in the interface regions. It should be noted that the lengths of wurtzite and zincblende regions are only equal for the 24 and 48 atoms supercells. Calculations performed using these supercells utilise a MP grid of $7 \times 7 \times 1$ for the **k**-space sampling. The in-plane **k**-space sampling 7×7 is the same as was previously employed for the bulk wurtzite and zincblende calculations. The reduction of the final component to 1 is because we are not interested in the periodic properties of the z-direction.

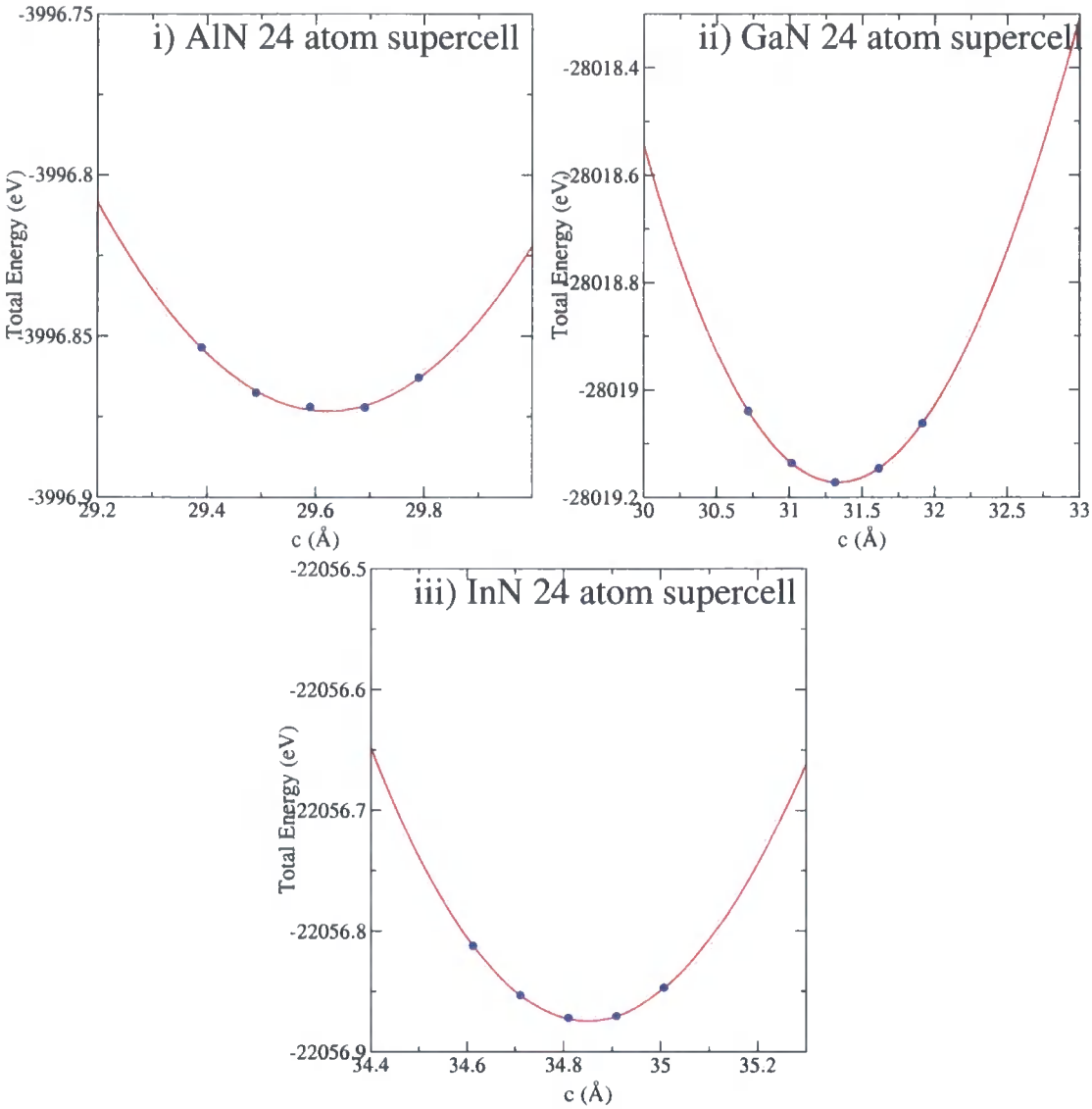

Figure 6.12: Total energy against $c_{supercell}$ for the relaxation of a supercell of a WZ-ZB superlattice held at the in-plane lattice constant of wurtzite. i) AlN 24 atom supercell - $c_{supercell} = 29.622$Å ii) GaN 24 atom supercell - $c_{supercell} = 31.339$Å iii) InN 24 atom supercell - $c_{supercell} = 35.851$Å . The dots represent the total energy calculated by DFT and the solid line in the best fit by least squares to Murnaghan's equation.

Before any calculations of the properties of an interface can be considered, the supercell must be relaxed to establish the equilibrium length for the in-plane lattice constant used. For the materials studied here the in-plane lattice parameter used was that of wurtzite, as calculated previously in a bulk DFT calculation. For example, in an AlN WZ-ZB supercell, the in-plane lattice parameter was held at that of wurtzite AlN, as listed in table 6.1. The calculated lattice parameters were used rather than the experimental values to keep the calculation consistent; an experimental value or even one from a different calculation may introduce unwanted strain [189]. However, the zincblende parts of the superlattice are however under small strain as they are forced into the in-plane lattice constants of the wurtzite phase. The resultant relaxation of a zincblende structure under these conditions was examined in section 6.6.1. The results of those calculations enabled the atomic positions in the supercell to be constructed and a length to be estimated. The estimated length was based on the relaxed length of the zincblende unit cells and the equilibrium length of the wurtzite unit cells. However, the equilibrium supercell length may be different as a result of reconstruction at the interfaces. Figure 6.12 shows the calculated total energy against $c_{supercell}$. The supercell calculations for each value $c_{supercell}$ involved a separate geometric optimisation of the atomic positions to ensure the structure was in the relaxed geometry.

6.9.2 Relaxation of atoms at interface

A final geometric optimisation of the atomic position for the equilibrium $c_{supercell}$ was performed and the structure was then considered relaxed, including the effects of any interface reconstruction. The in-plane symmetry of the lattice restricts the atomic movements to the z-axis. Looking at the absolute movement of the atoms as a result of the optimisation can be misleading as whole superlattice layers may have been moved due to expansion or contraction at the interfaces. Any movement relative to nearest neighbours along the z-axis will affect the bond-lengths, which may result in different bond-lengths for the "straight" bonds, parallel to the z-axis, and the "diagonal" bonds. Figures 6.13-6.15 show plots of both bond-lengths against position for the 24-atom superlattices of AlN, GaN and InN. The diagonal and the straight bond-lengths for the zincblende regions are not equal because the zincblende regions are under biaxial strain. Clear differences in bond length behaviour can be seen between the zincblende regions and the wurtzite regions, and evidence of interface

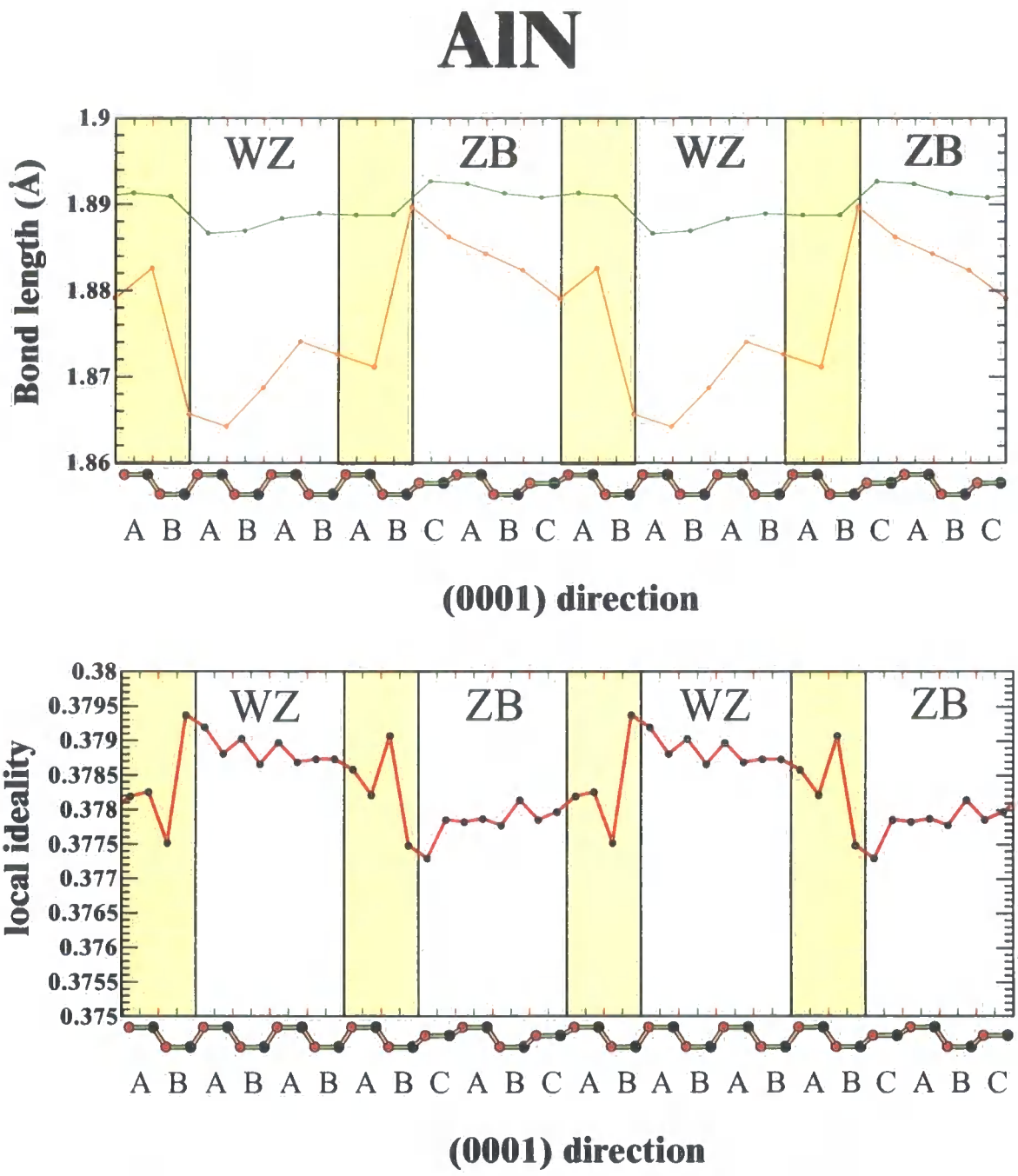

Figure 6.13: Top Bond lengths for straight (green) and diagonal (orange) bonds along the length of the AlN WZ-ZB superlattice. **Bottom** The local ideality as a function of position in the AlN WZ-ZB superlattice.

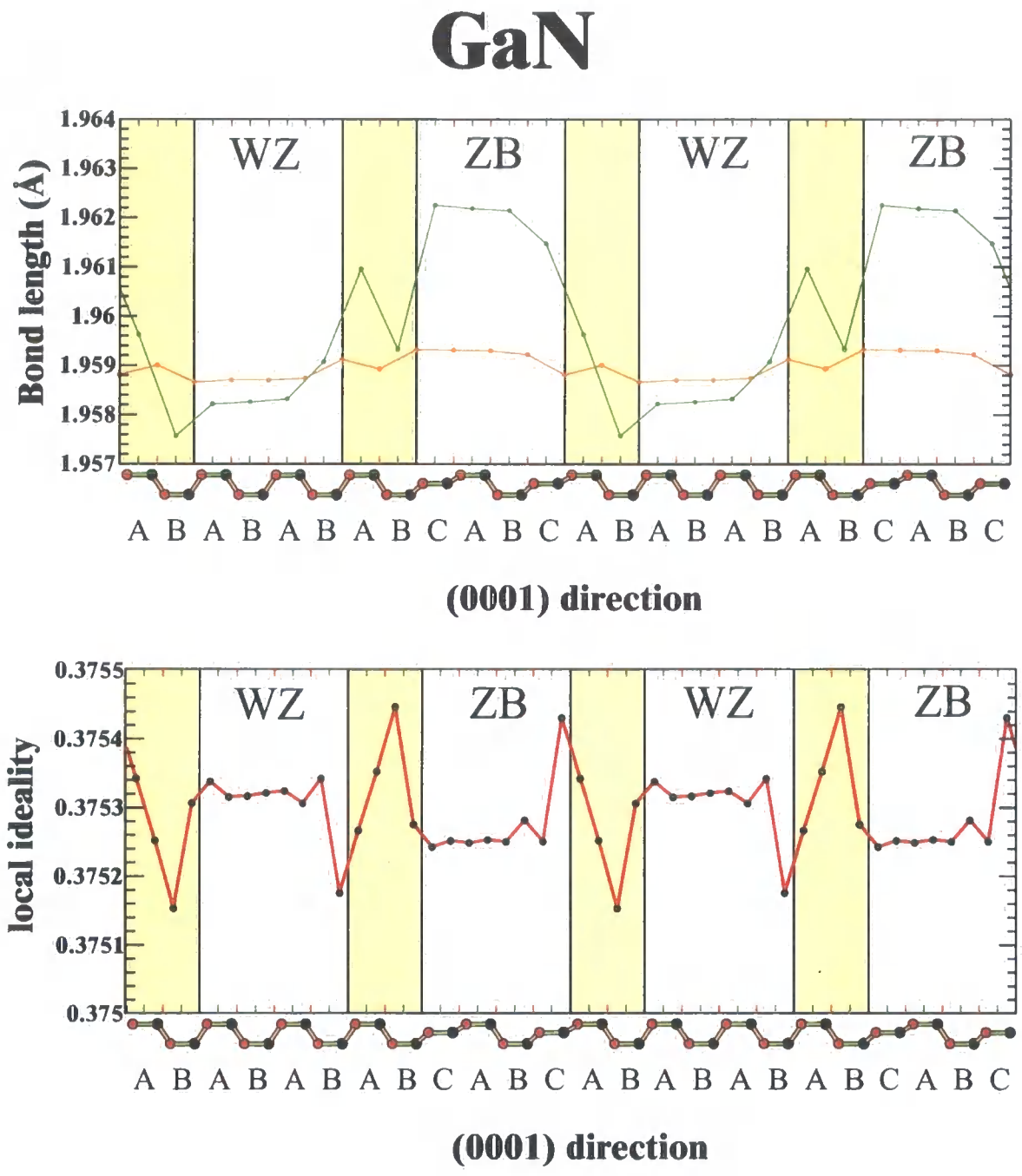

Figure 6.14: Top Bond lengths for straight (green) and diagonal (orange) bonds along the length of the GaN WZ-ZB superlattice. **Bottom** The local ideality as a function of position in the GaN WZ-ZB superlattice.

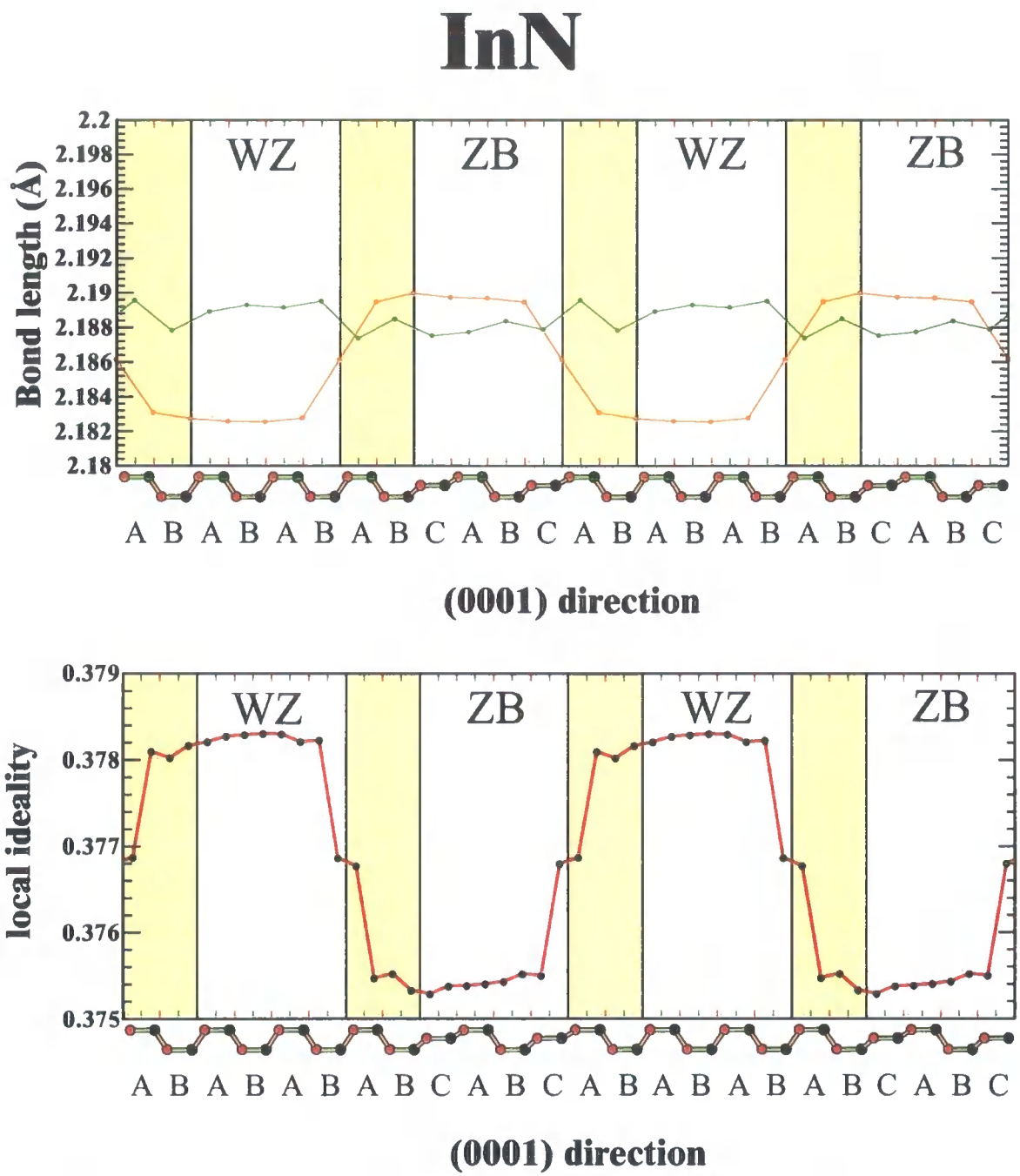

Figure 6.15: Top Bond lengths for straight (green) and diagonal (orange) bonds along the length of the InN WZ-ZB superlattice. **Bottom** The local ideality as a function of position in the InN WZ-ZB superlattice.

reconstruction is observed.

For wurtzite materials the internal parameter u measures the ideality of the crystal structure. An ideal structure has diagonal and straight bonds of equal length and $u = 3/8 = 0.375$. An analogous internal parameter *local* to a given atom j in the superlattice can be defined, which we will call the local ideality U_j. Atom j has in general two different types of bond, the straight bond, represented by vector α with a z-component α_z and the diagonal bond β with z-component β_z. The local ideality can simply defined as

$$U_j = \frac{\alpha_z}{2\alpha_z + 2\beta_z} \tag{6.32}$$

A value of U_j is then available for each atom in the superlattice. Figures 6.13-6.15 also contain graphs of U_j for all of the atomic positions in the superlattice. A clear difference between the wurtzite regions and the zincblende regions becomes very apparent. The difference is more pronounced for InN than for AlN and GaN, but in all three case the zincblende regions are more ideal (closer to 0.375) than the wurtzite regions. Again the zincblende regions are not completely ideal because they are under strain, which breaks the crystal symmetry of zincblende. It is interesting to note that the position of the transition between zincblende-like U_j and wurtzite-like U_j occurs progressively closer to the $(000\bar{1})$ edge of the interface region when going from AlN to GaN to InN. The pattern of the change-over is also different in each case, although in all cases some kind of symmetry is observed between the WZ-ZB interface and the ZB-WZ interface.

Overall the scale of any reconstruction is quite small, with bond lengths varying by no more than 0.03Å. The change in ideality is most marked for InN, but is still less than 1%. In fact, very little reconstruction is to be expected, since the atoms in the interface regions still have the same nearest neighbours as they do in the bulk. Nardelli [190] states that the residual relaxation of atoms at an AlN-GaN heterointerface is *negligible* and that it does not affect the band offset [191]. This is relevant since an AlN/GaN interface is likely to face much more severe reconstruction than the WZ-ZB interfaces studied here.

Over the range of $c_{supercell}$ scanned during the relaxation of the supercell the bond length and ideality profiles change surprisingly little. There is a general increase in the straight bonds with increasing $c_{supercell}$ and a corresponding lowering in the ideality with

increasing $c_{supercell}$. The reconstruction at the interface takes much the same form for each of the materials at all the values of $c_{supercell}$.

6.9.3 Convergence of structure with supercell size

The appearance of interface reconstruction and "plateaus" of constant bond-length and local ideality provide some evidence that the layers of the superlattice contain bulk-like regions. Complete convergence of the structure with respect to supercell size can only really be confirmed by studying a range of supercell sizes. Figure 6.16 shows the variation of local ideality against supercell size for four different supercells. The scale on the x axis is kept the same to allow a fair comparison of the four different superlattices. It is immediately apparent that the 14 atom supercell is unlikely to represent accurately the bulk regions of wurtzite or zincblende. The 14 atom supercell only contains one "C" stacking location and is still interesting as a model of a stacking fault, but is probably too small for determining the band offset. The 24 atom and larger supercells show very similar reconstructions at the interface regions, with larger and larger sections of constant bulk-like structure. The 24 atom contains regions 6 atoms wide that could be described as bulk-like and therefore could be used to extract the band offsets. The computational cost of the calculations increases very strongly with increasing size of supercell because of the additional number of electrons involved and the additional plane-waves required for a larger unit cell.

6.9.4 Band offset

Having calculated the relaxed structure of the interface, the electronic properties such as the band offset can be determined. The valence band offset is defined as the difference in energy between the top of the valence bands of the two materials. However, this quantity cannot be determined from separate bulk calculations because the band energies are determined with respect to a macroscopic average potential of the bulk $\overline{\overline{V}}$. Instead the difference in the microscopic average $\Delta\overline{\overline{V}}^{B-A}$ between the two materials A and B, is extracted from a supercell calculation containing both materials. The band offset is then derived from the relative energies of the top of the valence bands, when the bulk bandstructures of the two materials have been shifted relative to each other by $\Delta\overline{\overline{V}}^{B-A}$. Figure 6.17 describes the procedure schematically. In mathematical terms the valence ΔE_{VBO}^{B-A} and conduction band

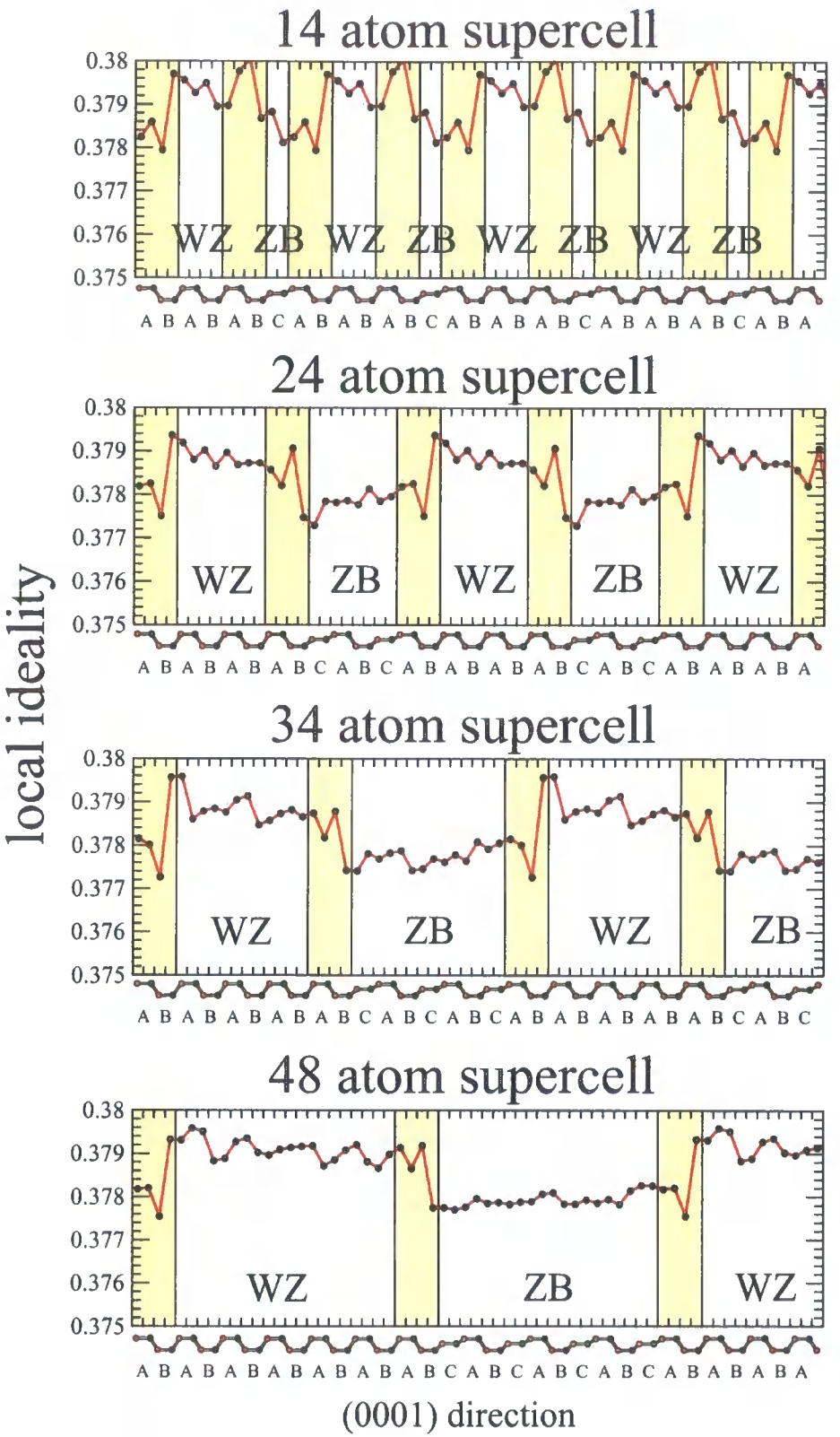

Figure 6.16: The local ideality as a function of position in the AlN WZ-ZB superlattice for various different supercells. The interface regions are marked by yellow rectangles.

ΔE_{CBO}^{B-A} offsets are given by

$$\Delta E_{VBO}^{B-A} = \Delta \overline{\overline{V}}^{B-A} + \Delta E_V^{B-A} \tag{6.33}$$

$$\Delta E_{CBO}^{B-A} = \Delta \overline{\overline{V}}^{B-A} + \Delta E_V^{B-A} + \Delta E_G^{B-A} \tag{6.34}$$

where ΔE_V^{B-A} is the relative difference in the bulk valence band maximum energies and ΔE_G^{B-A} is the difference in band gaps. Note the conduction band offset cannot reliably be calculated from first principles entirely because the GGA-based method does not predict the correct band gap.

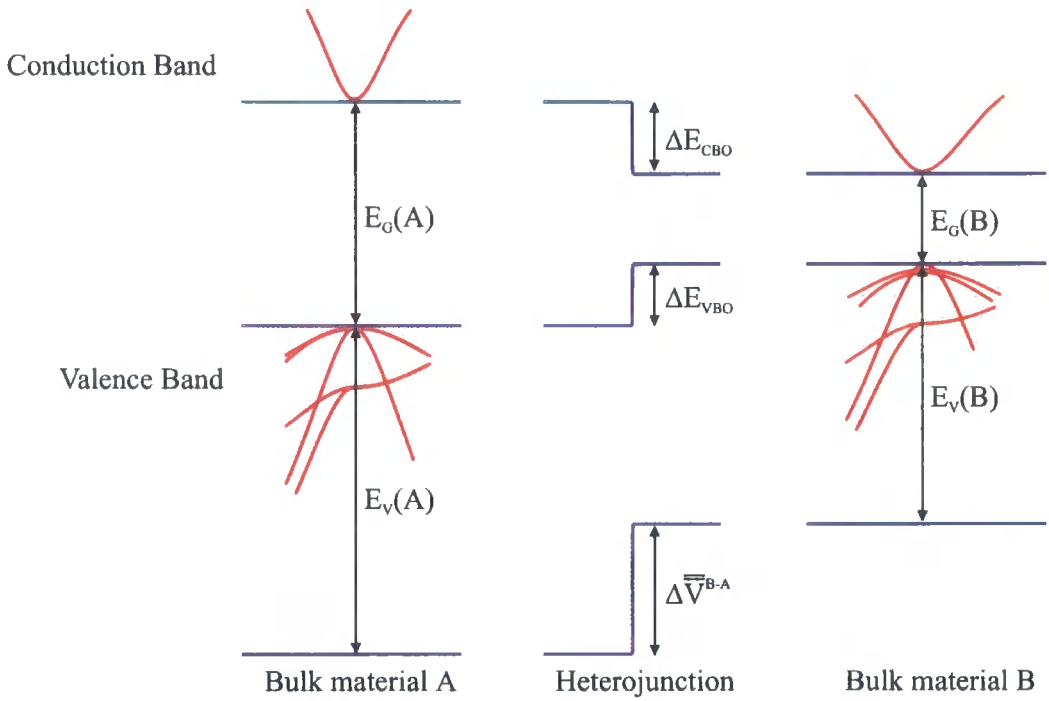

Figure 6.17: Schematic illustration describing the evaluation of the band offset from knowledge of i) the bandstructure $E_V(A)$,$E_V(B)$,$E_G(A)$,$E_G(B)$ and ii) the relative difference in the effective potentials $\Delta \overline{\overline{V}}^{B-A}$. The red lines illustrate the relative positions of the bandstructures of materials A and B.

Macroscopic Averaging

To extract the macroscopic average from the superlattice calculations, the microscopic potential must first be considered. In a DFT calculation this microscopic potential

is generated as part of the self-consistent calculation and is given by the sum of the Hartree, exchange-correlation and ionic potentials

$$V(\mathbf{r}) = V_H(\mathbf{r}) + V_{xc}(\mathbf{r}) + V_{ion}(\mathbf{r}) \tag{6.35}$$

The microscopic potential can be integrated in the plane perpendicular to the growth direction to produce a planar microscopic average $\overline{V}(z)$. The periodic character of the potential at any z is eliminated by integrating $\overline{V}(z)$ over a region centred on z with width of the same period Υ as the potential [192,193]. This has the effect of averaging the periodicity of period Υ over a "slab" that moves along the z-axis, resulting in the macroscopic average $\overline{\overline{V}}(z)$. This integral needs to be performed twice since the wurtzite and zincblende parts of the superlattice will have different potential periods, Υ and Υ' [194].

$$\overline{\overline{V}}(z) = \frac{1}{\Upsilon\Upsilon'} \int_{z'=z-\frac{\Upsilon}{2}}^{z'=z+\frac{\Upsilon}{2}} \int_{z''=z'-\frac{\Upsilon'}{2}}^{z''=z'+\frac{\Upsilon'}{2}} \overline{V}(z'')dz''dz' \tag{6.36}$$

In practice the DFT calculation is performed with the self-consistent potential and charge density sampled on a finite grid. The in-plane averaging is then calculated on this grid and the resultant planar potential is interpolated before the macroscopic averaging is performed. The same procedure can be employed to average the in-plane charge density ($\overline{\rho}(z)$) and then to obtain the macroscopically averaged charge density ($\overline{\overline{\rho}}(z)$).

Electric Fields

If there are no electric fields present as a result of polar interfaces then the difference in macroscopic potential is easily extracted from $\overline{\overline{V}}(z)$. However, the presence of a field causes a spatial variation in the potential in the wurtzite and zincblende layers and the difference in macroscopic potential is then ill-defined. Figure 6.18 illustrates this point.

The difficulty in extracting the relative difference in potentials lies in the lack of an abrupt discontinuity. The problem then becomes one of locating the interface, or equivalently, locating the middle of the bulk-like regions. This is not an easy problem to solve and as yet no perfect solution has been found. Binggeli *et al* [195] used the theoretical positions

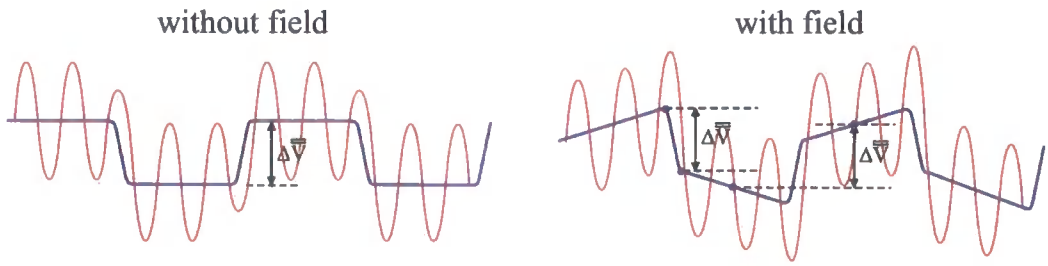

Figure 6.18: Schematic description of the periodic potential $\overline{V}(z)$ (red line) and its macroscopic average $\overline{\overline{V}}(z)$ (blue line) used to define the band offset. The band offset for a superlattice with an electric field is ill-defined unless a consistent location relative to the period of the superlattice can be defined, such as the middle or edge of the layer.

of the interface planes in the calculation of band offset of an AlN/GaN superlattice. The location is not well defined even in an AlN/GaN interface and the location of the WZ-ZB interface is even less certain. Other workers [134,196] have attempted to locate the centre of the bulk-like regions by decomposing the macroscopically averaged charge density into two components, containing the odd and even multipoles. This does not make the problem any less ill-defined as the decomposition can be performed in an infinite number of ways [134]. In fact, the decomposition approach is of most use when the fields are particularly strong and the corresponding polarisations well defined, such as the wurtzite AlN-GaN and InN-GaN heterostructures. For the WZ-ZB interface the fields are not particularly strong, but they do tend to obscure what is a very small offset. Figure 6.19 shows the self-consistent potential, the in-plane average potential and the macroscopic average potential for a 24 atom GaN WZ-ZB superlattice. Figure 6.20 shows the resulting charge density over the bond plane, the in-plane average charge density and macroscopic average charge density. Note that the red line of the macroscopic average is also shown on the plot of the planar potential (and charge density) to give an indication of the small scale of the variation in macroscopic average. The bulk-like regions can only just be made out as regions of constant gradient in $\overline{\overline{V}}(z)$ and plateaus of constant value in $\overline{\overline{\rho}}(z)$.

It is tempting to use the measured atomic reconstruction to define the middle of the interfaces or the bulk-like regions from figures 6.13-6.15 and measure the band offset from there. Another possibility is to use the macroscopically averaged charge density to define the interface or bulk-like regions. However, using either the charge density or the structural

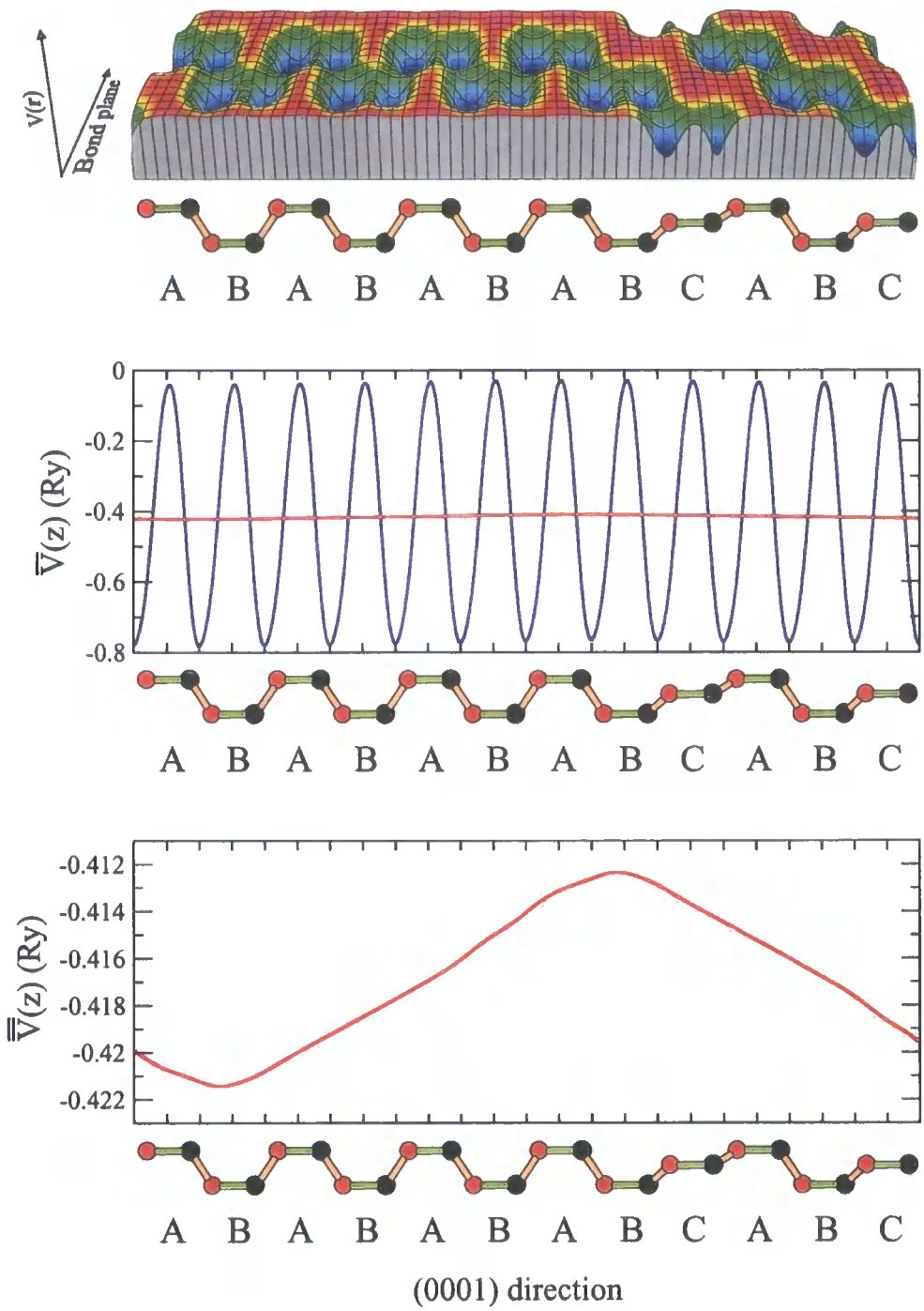

Figure 6.19: Top The self-consistent potential $V(\mathbf{r})$ as a function of position in the bond plane for a GaN 24 atom WZ-ZB superlattice. **Middle** The resulting in-plane average potential $\overline{V}(z)$ (blue) and the macroscopically averaged potential $\overline{\overline{V}}(z)$ (red). **Bottom** The macroscopically averaged potential $\overline{\overline{V}}(z)$.

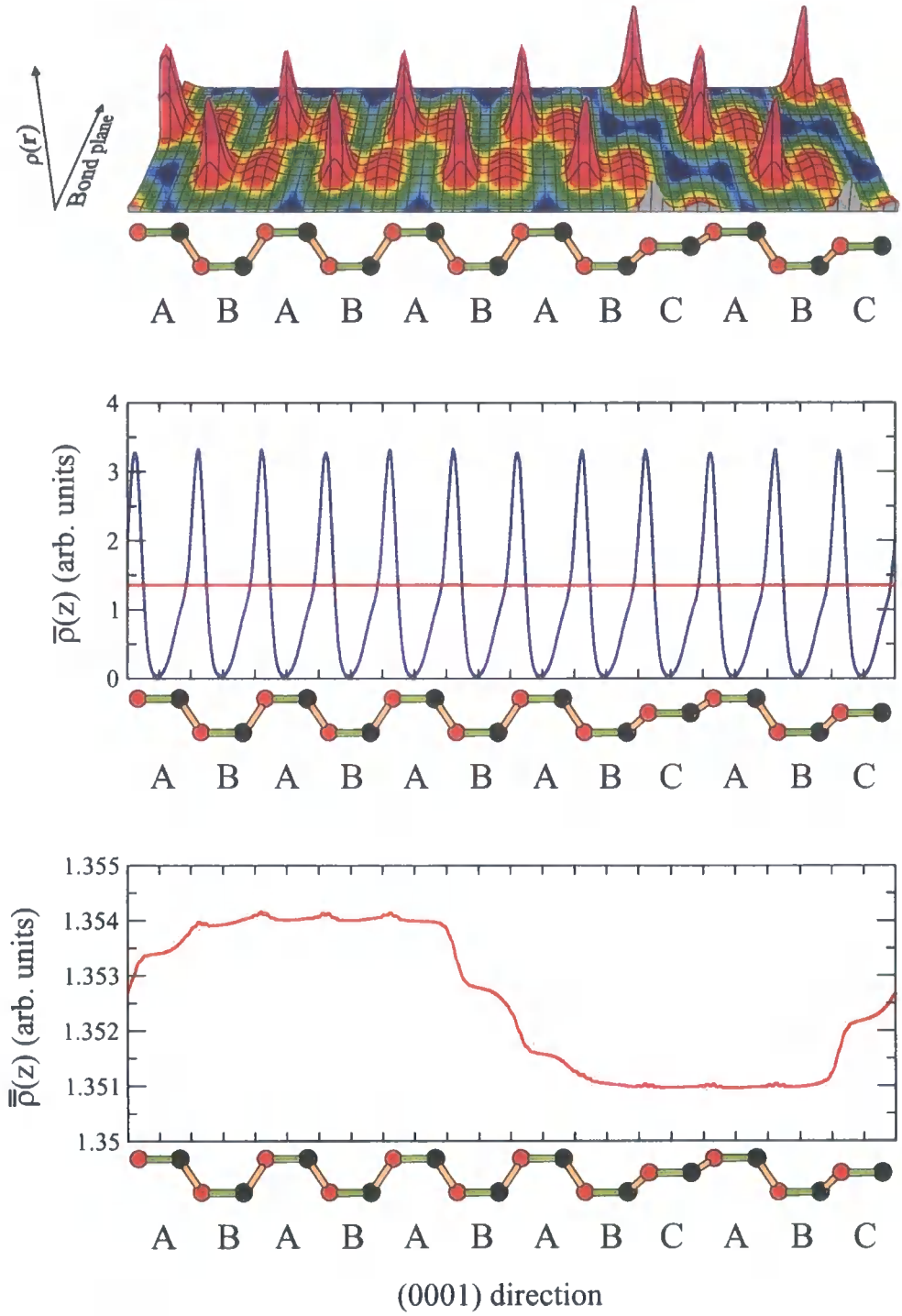

Figure 6.20: Top The charge density of the GaN 24 atom WZ-ZB superlattice as a function of position in the bond plane. **Middle** The resulting in-plane average charge density $\overline{\rho}(z)$ (blue) and the macroscopically averaged charge density $\overline{\overline{\rho}}(z)$ (red) **Bottom** The macroscopic average of the periodic charge density. $\overline{\overline{\rho}}(z)$

	$\Delta\overline{\overline{V}}^{ZB-WZ}$	ΔE_v^{ZB-WZ}	ΔE_{VBO}^{ZB-WZ}	ΔE_{CBO}^{ZB-WZ}	
				ab-initio E_G	empirical E_G
AlN	0.326eV	-0.268eV	**0.0587eV**	-1.12eV*	-1.24eV*
GaN	0.0824eV	-0.0510eV	**0.0314eV**	-0.150eV	-0.268eV
InN	0.0823eV	-0.130eV	**-0.0480eV**	-0.0406eV	-0.398eV

Table 6.4: The calculated values of difference in macroscopic average potential $\Delta\overline{\overline{V}}^{ZB-WZ}$, difference in bulk valence band energy ΔE_v^{ZB-WZ}, calculated valence band offset ΔE_{VBO}^{ZB-WZ} and predicted conduction band offset ΔE_{CBO}^{ZB-WZ} based on the *ab-initio* band gaps and experimental band gaps [5,7,8]. * The band gap of zincblende AlN is indirect $\Gamma \rightarrow X$ which gives rise to the larger difference in band gap between wurtzite and zincblende and therefore a larger conduction band offset.

reconstruction still results in an ambiguous definition of the interface and therefore the band offset. The location of the interface for the charge density might not necessarily coincide with the location for the potential or the structure. Probably the most consistent approach would be to use the potential itself in the estimation of the interface locations.

The bulk-like regions provide the most well defined parts of the macroscopically averaged potential in that they are regions of constant gradient. This is illustrated by the first and second derivate of $\overline{\overline{V}}(z)$ in figure 6.21, which provide a clear indication of the extent of the bulk-like regions and therefore an estimate for their centre. Given the location of the centre of the bulk like regions the difference in macroscopic potentials can be inferred and used to estimate the band offset. The location of the centre of the bulk-like regions can then be defined as the centre of the region for which the second derivative of $\overline{\overline{V}}(z)$ remains less than a given numerical tolerance. A tolerance of 5% of the maximum value of second derivative was found to be adequate for all three material systems.

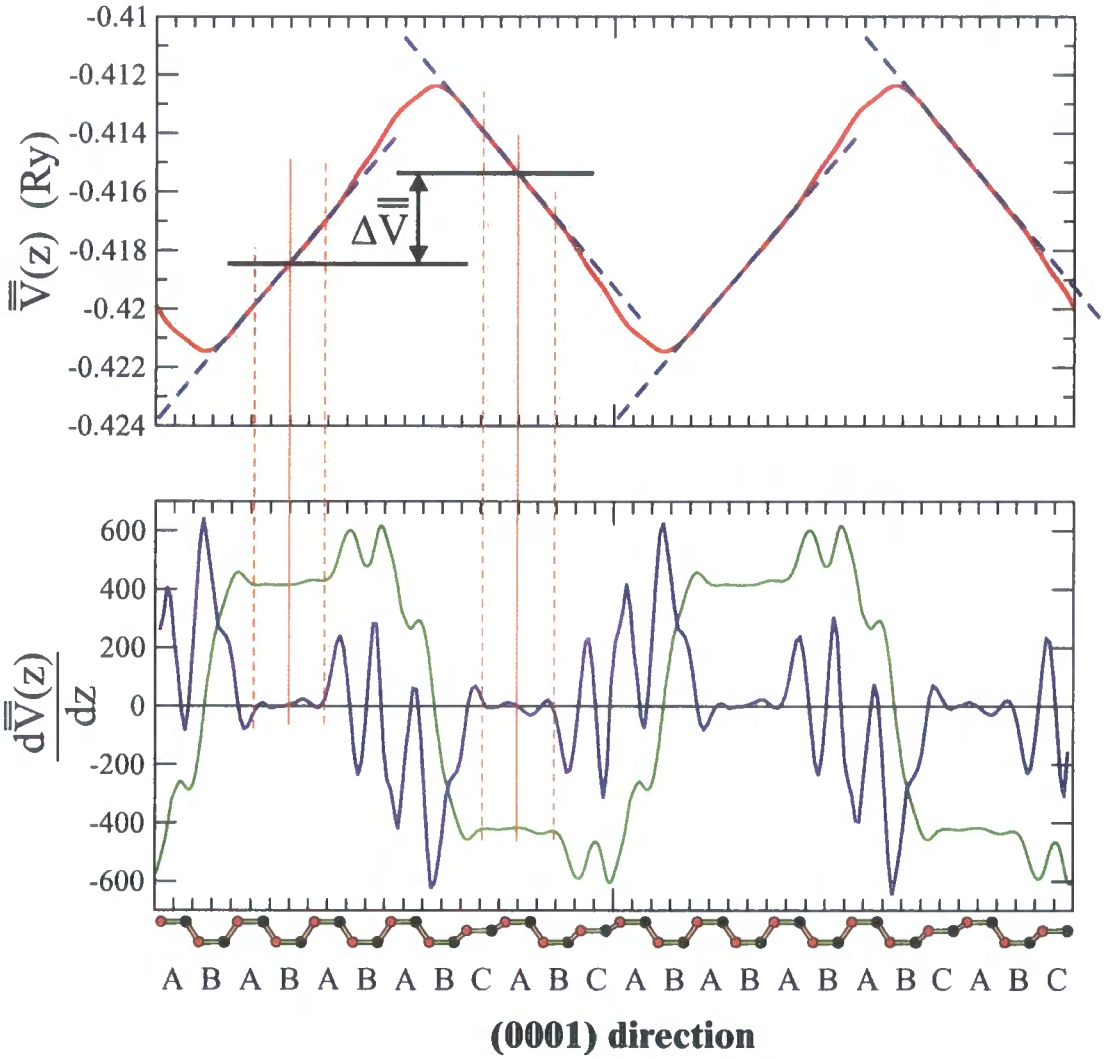

Figure 6.21: Top The macroscopically averaged potential for two repeat units of the 24 atom GaN WZ-ZB superlattice. Locations of constant gradient corresponding to bulk-like regions are used to identify the band offset. **Bottom** The first derivative (green line) and second derivative (blue line) with respect to z are used to establish the bulk-like regions of constant gradient.

6.9.5 Discussion

The calculated values for the valence and conduction band offset for the three wurtzite-zincblende interfaces investigated are presented in table 6.4. The difficulty in determining the bulk-like regions from which to extract the macroscopic averages, and therefore the band offset, gives rise to large uncertainties in the values presented. An upper limit of the error in the difference in the macroscopic average of the potential is estimated at $\pm 20\%$.

It is apparent that the calculated valence band offsets are very small. Experimental measurements are currently unable to resolve such small band offsets [8] and values for WZ-ZB interfaces are often quoted as zero. Murayama and Nakayama [197] estimated the VBO of WZ-ZB interfaces for many materials, by comparing the valence band maxima of separate bulk calculations. The values of -0.034eV for GaN and -0.056eV for AlN therefore assume that the difference in macroscopic potential is negligible, which these calculations here show it is not the case. Murayama and Nakayama's estimates are also based on an ideal wurtzite structure lattice matched to a zincblende structure without any relaxation due to strain. In contrast to the results of Murayama and Nakayama, the offsets of GaN and AlN calculated in this work predict type I interfaces and heterostructures. This is confirmed by examination of the macroscopically averaged charge densities which locate the greater average charge densities in the wurtzite region. Murayama and Nakayama's values imply a type II interface for AlN and GaN. The calculated band offset of InN is negative and does give rise to a type II interface, but unfortunately no direct data is available in the literature for comparison. It should be noted that the superlattices were modelled at the in-plane lattice constant of the wurtzite phase of the material. Any future experimental measurements may be made at the lattice constant of the zincblende phase or even the lattice constant of a GaN substrate. Band offsets this small are likely to be very sensitive to changes in the strain of the materials.

Wei and Zunger [44] calculated the difference in band offset for wurtzite and zincblende forms of the AlN/GaN interface to be 0.03eV. The results presented here predict a value of 0.027eV. Similarly Wei and Zunger calculate the difference for the InN/AlN interface to be -0.21eV, and here the results suggest a value of -0.11eV. For the GaN/InN interface Wei and Zunger calculate a difference of -0.22eV, compared to -0.079eV from the results in this work. Wei and Zunger's interfaces are under considerable strain which explains the difference in the numbers, although qualitatively the results are in agreement.

The calculated conduction band offsets suffer from the additional uncertainty in the band gap of the two phases. The experimental band gap is typically known to within ~0.1eV, which leaves uncertainties in the difference of gaps which are large relative to the band offsets. The *ab-initio* values of band gap are clearly not correct, especially for InN for which DFT calculates to be very close to zero (0.0075eV (ZB) and 0.00018eV (WZ)). The *ab-initio* calculation would therefore predict the InN WZ-ZB superlattice is of type II - broken gap, whereas the use of experimental band gaps suggests the superlattice is type II - staggered. In all cases, the difference in band gap is mostly accommodated by the conduction band offset. Physically this is reasonable, since the designation of an atom in the crystal to be part of a wurtzite or zincblende crystal depends on the location of its next nearest neighbours. The valence bands are considered to be more localised and are influenced by the effect of the next nearest neighbours less than the delocalised conduction bands.

The use of larger supercell sizes resulted in no significant improvement in the calculated value of band offset. The middle of the bulk-like regions was *more* difficult to locate in a larger supercell to the same absolute level of accuracy because the bulk-like regions were longer. Clearly the band offset remained the same but was obscured by larger regions of electric field. Given that the structural relaxation, potential and charge density all showed evidence of constant bulk-like regions, the 24-atom supercells can be considered large enough to extract bulk-like properties.

The location of the interface was shown to be an integral part of the problem of calculating the band offset, but is also an interesting question in its own right. The matching techniques applied in chapter 5 relied on an estimate of the "effective" location of the interface at which to match the wavefunctions. The effective interface as defined by the location used to extract the band offsets of GaN is closest to the d_2 (see fig 5.9) mid-straight bond matching location. The atomic reconstruction agrees with this location. However, the macroscopic charge density seems shifted to the left when compared to the potential and would suggest that the d_1 (see fig 5.9) matching location of the first diagonal bond at the edge of the interface region. All the estimates of the effective location of the interface agree that it is to the left ($(000\bar{1})$ direction) of the "theoretical" location at the centre of the interface region. AlN has an effective interface in a more central location with respect to the interface region, whereas the interface for InN seems to be even more shifted in the $(000\bar{1})$ direction.

6.10 Summary

In this chapter the techniques of DFT within the GGA approximation were applied to the wurtzite and zincblende structures of AlN, GaN and InN. Lattice constants were calculated and compared with experiment. The relaxation as a result of biaxially strained InN and AlN on GaN was predicted and was used as part of the input to the empirical pseudopotential calculations of alloys. The relaxation of zincblende nitrides grown on wurtzite substrates was used to set up supercell calculations of WZ-ZB superlattices. The superlattices were observed to show some small interface reconstruction and bulk-like regions were also observed. From these bulk-like regions the band offsets were extracted after accounting for the dominating effects of the electric fields present. The resulting band offsets were, as expected, very small and the error in their value was estimated at $\sim$20%. For AlN and GaN the interfaces were predicted to be of type I and for InN of type II. No direct comparison was available with other work as the calculated offsets are below the current uncertainty of experimental measurement and no other comparable calculations have been performed. The magnitude of the calculated band offsets is within that which is generally expected [8] and therefore this author believes the band offsets presented in this work to be at least a reasonable first estimate.

Chapter 7

Conclusions and suggestions for further work

In this thesis, work investigating the electronic structure of group III - nitride quantum wells in the wurtzite crystal structure has been presented. A complex bandstructure matching technique, previously applied to zincblende structure materials has been used to calculate the bound state energies of wurtzite structure quantum wells. The wurtzite-zincblende interface has also been studied by an adapted complex bandstructure matching technique and through *ab-initio* calculations using density functional theory.

Bulk nitrides in the wurtzite crystal structure form the focus of chapter 2. The empirical pseudopotential method with a plane wave basis was presented as an effective method for the calculation of semiconductor bandstructures. The bandstructures of AlN, GaN and InN were presented including the effects of spin-orbit coupling. An example of the density of states and a plot of the charge density of GaN were also presented. The virtual crystal approximation and a parameterisation of the pseudopotential form factors allowed the effects of alloying and biaxial strain to be incorporated into the pseudopotential calculations. These calculations involved the alloys, AlGaN and InGaN being modelled as biaxially strained to the a-lattice constant of GaN. The demonstration of the empirical pseudopotential method for the nitrides provided a foundation upon which subsequent chapters built.

In chapter 3 the empirical pseudopotential method was used to produce complex band-structures and associated pseudo-wavefunctions for wurtzite materials. To our knowledge, wurtzite complex bandstructures have not previously been reported, and therefore the topo-

logical features were compared to the (111) zincblende complex bandstructures which is expected to have similarities. The complex bandstructure was also demonstrated for non-zero values of in-plane wavevector.

The complex bandstructures were then used to construct the bulk states of heterostructures. By matching the general complex states at the interfaces of a heterostructure, calculations of the bound state energies and wavefunctions of wurtzite InGaN and AlGaN quantum wells were carried out. The electronic structure of quantum wells of various widths were studied for a range of in-plane wavevectors, and for a range of built-in electric fields and alloy compositions. The strong built-in electric fields, due to piezoelectricity and pyroelectricity, were found to dramatically affect the bound state energies and wavefunctions. The wavefunctions and therefore the probability densities were observed to show a noticeable asymmetry as a result of the electric field and the bound state energies were increased, with respect to the bottom of the well, as a result of the increased confinement the electric fields introduced. The inter subband transitions of AlGaN conduction band quantum wells were studied and the results compared with experiment. In addition the issues involved in any comparison with experiment were considered including the problem of estimating the electric field strength. It was suggested that the complex bandstructure approach demonstrated could provide a better method than the usual effective mass models for estimating the field strengths from experimental spectroscopy data. The joint density of states and optical matrix elements were calculated from the bound state energies and wavefunctions and used to calculate the absorption spectra of an AlGaN quantum well.

Chapter 5 considered the widely investigated zincblende crystal structure and demonstrated the use of the empirical pseudopotential method and the production of complex bandstructures for zincblende GaN. Local pseudopotential form factor were needed and had to be generated using a Monte-Carlo scheme. The bandstructures produced from local pseudopotentials were found not to be as accurate as the non-local calculations, but were sufficient for the purposes of this work. The concept of an interface between a wurtzite and zincblende region of GaN was considered and the existence of homostructure quantum wells as a result of stacking faults was put forward. The matching procedure used in chapter 4 was adapted to generate the bound states of this type of quantum well as a function of well width. The valence band states were observed to exhibit anti-crossing behaviour when their energies were

plotted as a function of well width. This illustrated one of the advantages of the complex bandstructure approach, because this anti-crossing behaviour would not be predicted by the simpler effective mass-based methods.

Chapter 6 reviewed the techniques based on *ab-initio* calculations using density functional theory and a plane wave basis. The method was used to calculate supporting data for the other calculations described in earlier chapters and to provide a comparison to the empirical pseudopotential method. The nature of the wurtzite-zincblende interface was investigated from first principles. The location of the interface was found to be poorly defined and some interface reconstruction was observed. The band offsets were found to be very small and were difficult to accurately extract from the self consistent potentials because of the presence of comparatively strong electric fields. However, the values of the band offsets were successfully extracted and their magnitude was found to be in agreement with the general expectation. In the absence of any more accurate values, the band offsets presented in this work provide at least a good first estimate.

7.1 Suggestions for further work

The complex bandstructure matching techniques for wurtzite-wurtzite and wurtzite-zincblende structures developed in this work could be employed in the study of other systems. For the nitrides, the InGaN - GaN - AlGaN laser diode has already been a commercial success, and there is also considerable interest in nitride multiple quantum wells which could be modelled with the complex bandstructure approach, as could a superlattice constructed from nitride semiconductors. Other semiconductor systems that have wurtzite crystal structures would make interesting subjects for study using the complex bandstructure approach, such as many II-VI semiconductors. Equally, other systems of heterostructures or homostructures based on the wurtzite-zincblende interface, such as SiC homostructures which have already been demonstrated experimentally, would make interesting subjects for further work. For any study of heterostructures with a wurtzite-zincblende interface, strain is likely to be present and must be accounted for in the zincblende regions.

The techniques presented here focus on bound states, but the matching approach can be adapted to unbound states and would provide a valuable extension to the results presented

within this work. In addition to the inter subband transition studied in chapter 4, inter band transitions including excitonic effects are of both fundamental and device interest in the nitrides and would provide an interesting and challenging theoretical problem.

The effects of band bending due to space charge effects were not included in this work. These effects could be incorporated by the introduction of a self-consistent calculation of the well potential. However, this would make the calculation of bound state energies and wavefunctions significantly more computationally expensive.

The first principles calculations provided results for WZ-ZB interfaces of the same material, however heterostructures with a WZ-ZB interface could also be investigated and can be expected to give substantially larger band offsets in some cases. Such work would enable a more convincing verification of the band offset results presented in this work through the property of transitivity.

Bibliography

[1] P Y Yu and M Cardona, *Fundamentals of Semiconductors*, Springer, Berlin (1995)

[2] C Wetzel, T Takeuchi, H Amano and I Akasaki, Phys. Rev. B, **61** 2159 (2000)

[3] F Bernardini, V Fiorentini and D Vanderbilt, Phys. Status Solidi **216**, 319 (1999)

[4] R A Matzger, Compound Semiconducters, **1** 26 (1995)

[5] O Ambacher, J. Phys. D. Appl. Phys. **31** 2653 (1998)

[6] J-Y Duboz, Phys. stat. sol. (a) **176** 5 (1999)

[7] S C Jain, M Willander, J Narayan and R Van Overstraeten, Appl. Phys. Rev. **87** 965 (2000)

[8] I Vergaftman, J R Meyer and L R Ram-Mohan J. Appl. Phys. **89** 11 (2001)

[9] R Juza and H Hahn, Z. Anorg. Allg. Chem. **234** 232 (1938)

[10] R Juza and H Hahn, Z. Anorg. Allg. Chem. **244** 233 (1940)

[11] H P Maruska and J J Tietjen, Appl. Phys. Lett. **15** 377 (1969)

[12] K Osamura, S Naka, Y Murakama, J. Appl. Phys. **46** 3432 (1975)

[13] B Monemar, Phys. rev. B **10** 676 (1974)

[14] J I Pankove, A Miller and J E Berkeyheiser, J Lumin. **5** 84 (1972)

[15] H Amano, N Sawaki, I Akasaki and T Toyoda, Appl. Phys. Lett. **48** 353 (1986)

[16] H Amano, I Akasaki, T Kozawa, K Hiramatsu, N Sawak, K Ikeda and Y Ishi, J Lumin. **40-41** 121 (1988)

[17] H Amano, H Kito, K Hiramatsu and I Akasaki, Japn. J. Appl. Phys. Part 2 **28** L2112 (1989)

[18] T Matsuoka, H Tanaka, T Sasaki and A Katsui, Inst. Phys. Conf. Ser. **106** 141 (1990)

[19] M A Khan, R A Skogman and J M Van Hove, Appl. Phys. Lett. **56** 1257 (1990)

[20] K Itoh, T Kawamoto, H Amano, K Hiramatsu and I Akasaki, Japn. J. Appl. Phys. Part 1 **30** 1924 (1991)

[21] S S Lester, F A Ponce, M G Craford, D A Steigerwald, Appl. Phys. Lett. **66** 1249 (1995)

[22] N Grandjean, B Damilano and J Massies, J. Phys. Condens. Matt. **13** 6945 (2001)

[23] F A Ponce, MRS Bull **22** 51 (1997)

[24] O Lagerstedt, B Monebar, Phys. Rev. B, **19** 3064 (1979)

[25] Cohen and Chelikowsky, *Electronic structure and optical properties of semiconductors*, Springer-Verlag, Berlin (1988)

[26] O Ambacher, J Majewski, C Miskys, A Link, M Hermann, M Eickhoff, M Stutzmann, F Bernardini, V Fiorentini,V Tilak, B Schaff and L F Eastman, J. Phys. Condens. Matter **14**, 3399 (2002)

[27] E S Hellman1998, MRS Internet J. Nitride. Semicon. Res., **3** 11 (1998)

[28] M Born and R Oppenheimer. Zur Quantentheorie der Molekeln. Ann. Phys. (Leipzig) **84**, 457 (1927)

[29] P Y Yu and M Cardonas, *Fundamentals of Semiconductors*, Springer-Verlag, Berlin (1996)

[30] F Bloch, Z. Physic, **52** 555 (1928)

[31] E Fermi, Nuovo Cimento **11** 157 (1934)

[32] H Hellmann, J. Chem. Phys. **3** 61 (1935)

[33] J C Phillips, Phys. Rev. **112** 3 (1958)

[34] E Antoncik, J. Phys. Chem. Solids **10** 314 (1959)

[35] M L Cohen and V Heine, Solid State Physics **24** 37 (1970)

[36] W A Harrison, *Pseudopotentials in the theory of metals*, W A Benjamin., New York (1966)

[37] J C Phillips, Phys. Rev. **116** 287 (1959)

[38] J P Walter and M L Cohen, Phys. Rev. B, **2** 1821 (1970)

[39] J R Chelikowsky and M L Cohen, Phys. Rev. B., **14** 556 (1976)

[40] D J Dugdale, *Electronic structure calculations on nitride semiconductors and their alloys* (PhD Thesis), Durham University (2001)

[41] G Weisz, Phys. Rev. B, **149** 504 (1966)

[42] A O E Animalu, Phil. Mag., **13** 53 (1966)

[43] S Bloom and T K Berstresser, Solid State Commun., **6** 465 (1968)

[44] S H Wei and A Zunger, Appl. Phys. Lett. **69** 2719 (1990)

[45] Y Yeo, C Chong and M F Li, Appl. Phys. **83** 1429 (1998)

[46] R Coles, *Theory of the electronic structure of quantum wells* (PhD Thesis), Durham University (1998)

[47] S K Pugh, D J Dugdale, S Brand and R A Abram, Semi. Sci. Tech., **14** 23 (1999)

[48] L M Falicov and P J Lin, Phys. Rev. **141** 562 (1966)

[49] M Goano, E Bellotti, E Ghillino, G Ghione and K F Brennan, J. Appl. Phys., **88** 6467 (2000)

[50] S K Pugh, D J Dugdale, S Brand and R A Abram, J. Appl. Phys., **86** 3768 (1999)

[51] D J Dugdale, S Brand and R A Abram, Physica Status Solidi. B, **216** 351 (1999)

[52] S Bloom, J. Phys. Chem. Solids, **32** 2027 (1971)

[53] A P Dmitriev, N V Evlakhov and A S Furman, J. Semiconductors, **30** 60 (1996)

[54] C P Foley and T L Tansley, Phys. Rev. B, **33** 1430 (1986)

[55] J Wu, W Walukiewicz, K M Yu, J W Ager III, E E Haller, H Lu and W J Schaff, Proceedings for 26th Conference on the physics of semiconductors, Abstracts Part **II** 48 (2002)

[56] T Inushima et al, J. Crystal Growth. **227-228** 481 (2001)

[57] D J Chadi and M L Cohen, Phys. Rev. B, **8** 5747 (1973)

[58] H J Monkhorst and J D Pack , Phys. Rev. B **13** 5188-5192 (1976)

[59] J W D Connolly and A R Williams, Phys. Rev. B, **27** 5169 (1983)

[60] M van Schilfgaarde, A Sher and A-B Chen, J. Crystal Growth., **178** 8 (1997)

[61] Toshio Saito and Yasuhiko Arakawa, Phys. Rev. B **60** 1701 (1999)

[62] S-H Wei, L G Ferreira, J E Bernard and A Zunger, Phys. Rev. B **42** 9622 (1990)

[63] H Angerer et al, Appl. Phys. Lett. **71** 1504 (1997)

[64] T Peng, J Piprek, G Qiu, J O Olowolafe, K M Unruh, C P Swann and E F Schubert, Appl. Phys. Lett. **71** 2439 (1997)

[65] L Bellaiche, S-H Wei and A Zunger, Phys. Rev. B **56** 13872 (1997)

[66] N A El-Masry, E L Piner, S X Liu and S M Bedair, Appl. Phys. Lett., **72** 40 (1998)

[67] D Doppalapudi, S N Basu, K F Ludwig and T D Moustakas, J. Appl. Phys., **84** 1389 (1998)

[68] L Bellaiche, T Mattila, L W Wang, S H Wei and A Zunger, Appl. Phys. Lett. **74** 1842 (1999)

[69] N N Ledentsov, V M Ustinov, V A Shchukin, P S Kop'ev, Z I Alferov and D Bimberg, semiconductors **32** 343-365 (1998)

[70] E Anastassakis, paper at European Physical Society Condensed Matter Division conference, Lisbon (1990)

[71] D O Hall, *Calculations of the electronic structure and optical properties of strained II-VI supperlattices* (PhD Thesis), Durham University (1991)

[72] D R Lovet, *Tensor Properties of Crystals*, Adam Hilger, Bristol and Philadelphia (1989)

[73] J F Nye, *Physical properties of crystals*, Oxford University Press, London (1957)

[74] S C Jain, A H Harker and R A Cowley, Philos. MAg. A **75** 1461 (1997)

[75] S C Jain, Germanium-Silicon Strained Layers and Heterostructures, Advances in Electronics and Electron Physics series, Supplement **24** Academic, Boston (1994)

[76] F C Frank and J H van der Merwe, Proc. R. Soc. London **198** 205 (1949)

[77] J Jacobsen, L Pleth Nielsen, F Besenbacher, I Stensgaard, E Laegsgaard, T Rasmussen, K W Jacobsen and J K Norskov, Phys. Rev. Lett. **75** 489 (1995)

[78] J W Matthews and A E Blakeslee, J. Crystal Growth **27** 118 (1974).

[79] A Braun, K M Briggs and P Boni, J. Cryst. Growth **241** 231-234 (2002)

[80] N Grandjean and J Massies, Appl. Phys. Lett. **71** 1816 (1997)

[81] G Martin, A Botchkarev, A Rockett and H Morkoç, Appl. Phys. Lett. **68** 2541 (1996)

[82] I Akasaki and H Amano in *GaN*, edited by J I Pankove and T D Moustakas, Vol1, 459-72, Academic, New York (1998)

[83] C Wetzel, T Takeuchi, H Amano and I Akasaki, MRS Internet J. Nitride Semicond. Res., **4S1** G3.66 (1999)

[84] T Takeuchi, S Sota, M Katsuragawa, M Komori, H Takeuchi, H Amano and I Akasaki, Jpn. J. Appl. Phys., **36** L382 (1997)

[85] L R Saravia and D Brust, Phys. Rev, **178** 1240 (1969)

[86] Y-C Chang and J N Schulman, Phys. Rev. B **25**, 3975 (1982)

[87] S Monaghan and S Brand, Supperlattices and Microstructures, **3** 697 (1987)

[88] S Brand and D T Hughes, Semi. Sci. Tech., **2** 607 (1987)

[89] S Brand, S Monaghan and P P Szydlik, Semi. Sci. Tech., **2** 123 (1987)

[90] V Heine, Proc. Phys. Soc. London **81**, 300 (1963)

[91] Y-C Chang, Phys. Rev. B **25**, 605 (1982)

[92] J R Waldrop, E A Kraut, C W Farley and R W Grant, J. Appl. Phys. **69**, 372 (1991)

[93] A Nakagawa, H Kroemer and J H English, Appl. Phys. Lett. **54**, 1893 (1989)

[94] S-H Wei and A Zunger, Phys. Rev. Lett. **59** 144 (1987)

[95] G H Wannier, Phys. Rev. **52**, 191 (1937)

[96] J C Slater, Phys. Rev. **76**, 1592 (1949)

[97] J M Luttinger and W. Kohn, Phys. Rev. **97**, 869 (1955)

[98] M G Burt, J. Phys. Condens. Matt., **4**, 6651 (1992)

[99] M G Burt, J. Phys. Condens. Matt., **11**, R53 (1999)

[100] G Bastard, *Wave Mechanics Applied to Semiconductor Heterostructures*, John Wiley and Sons, New York (1988)

[101] A P French and E F Taylor, *Introduction to Quantum Physics*, Chapman and Hall, London (1993)

[102] C Mailhiot and D L Smith, J. Appl. Phys., **59** 200 (1986)

[103] S-P Wan and J-B Xia, Solid State Commun., **122**, 287 (2002)

[104] J L Sánchez-Rojaz, J A Garrido and E Muñoz, Phys. Rev. B, **61** 2773 (2000)

[105] F D Sala, A D Carlo, P Lugli, F Bernardini, V Fiorentini, R Scholz and J-M Jancu, Appl. Phys. Lett., **74** 2002 (1999)

[106] T Taliercio, P Lefebvre, M Gallart and A Morel, J. Phys. Condens. Matt., **13** 7027 (2001)

[107] O Gfrörer, C Gemmer, J Off, J S Im, F Scholz and A Hangleiter, Phys. Status Solidi B, **216** 405 (1999)

[108] J P Ibbetson, P T Fini, K D Ness, S P DenBaars, J S Speck and U K Mishra, Appl. Phys. Lett., **77** 250 (2000)

[109] G Traetta, A Di Carlo, A Reale, P Lugli, M Lomascolo, A Passsaseo, R Cingolani, A Bonfiglio, M Berti, E Napolitani, M Natali, S K Sinha and A V Drigo, J. Cryst. Growth, **230** 492 (2001)

[110] R Resta, Rev. Mod. Phys., **66**, 899 (1994)

[111] R M Martin, Phys. Rev. B **9**, 1998 (1974)

[112] F Bernardini, V Fiorentini and D Vanderbilt, Phys. Rev. B **56**, R10024 (1997)

[113] F Bernardini, V Fiorentini and D Vanderbilt, Phys. Rev. Lett. **79**, 3958 (1997)

[114] A D Carlo, F D Sala, P Lugli, F Bernardini, V Fiorentini, R Scholz and J-M Jancu, Appl. Phys. Lett., **76** 3950 (2000)

[115] S-P Wan, J-B Xia and K Chang, J. Appl. Phys., **90** 6210 (2001)

[116] S F Chichibu, A C Abare, M P Mack, M S Minsky, T Deguchi, D Cohen, P Kozodoy, S B Fleischer, S Keller, J S Speck, J E Bowers, E Hu, U K Mishra, L A Coldren, S P DenBaars, K Wada, T Sota and S Nakamura, Matt. Sci. Eng. **B59** 298 (1999)

[117] T Mukai, H Narimatsu, S Nakamura, Jpn. J. Appl. Phys., **37** 479 (1998)

[118] M Kneissl, D P Bour and N M Johnson, Appl. Phys. Lett., **72** 1539 (1998)

[119] C Wetzel, S Nitta, T Takeuchi, S Yamaguchi, H Amano and I Akasaki, MRS Internet J. Nitride Semicond. Res., **4S1** G3.66 (1999)

[120] E Berkowicz, D Gershoni, G Bahir, E Lakin, D Shilo, E Zolotoyabko, A C Abare, S P Denbaars and L A Goldren, Phys. Rev. B **61**, 10994 (2000)

[121] T Takeuchi, C Wetzel, S Sota, M Katsuragawa, M Komori, H Takeuchi, H Amano, I Akasaki, Y Kaneko, S Nakagawa, Y Yamaoka and N Yamada, Appl. Phys. Lett., **73** 1691 (1998)

[122] L-H Peng, C-W Chuang and L-H Lou, Appl. Phys. Lett., **74** 795 (1999)

[123] Y D Jho, J S Yahng, E Oh and D S Kim, Appl. Phys. Lett., **79** 1130 (2001)

[124] F Bernardini and V Fiorentini, Phys. Rev. B **64**, 085207 (2001)

[125] Ch. Manz, M Kunzer, H Obloh, A Ramakrishnan and U Kaufmann, Appl. Phys. Lett. **74** 3993 (2000)

[126] K Hoshino, T Someya, K Hirakawa and Y Arakawa, Phys. Stat. Sol., **192** 27 (2002)

[127] B F Levine and G Hasnain, C G Bethea and N Chand, Appl. Phys. Lett., **54** 2704 (1989)

[128] J Faist, F Capasso, D L Sivco, C Sirtori, A L Hutchinson and A Y Cho, Science, **264** 553 (1994)

[129] A Liu, S-L Chuang and C Z Ning, Appl. Phys. Lett., **76** 333 (2000)

[130] R Langer, J Simon, V Ortiz, N T Pelekanos, A Barski, R André and M Godlewski, Appl. Phys. Lett., **74** 3827 (1999)

[131] N Grandjean, J Massies and M Leroux, Appl. Phys. Lett. **74** 2361 (1999)

[132] N Suzuki and N Iizuka, Jpn. J. Appl. Phys., **38** L363 (1999)

[133] N L Thomas and N T Pelekanos, Microelectronics Journal, **1** 24 (2002)

[134] F Bernardini and V Fiorentini, Phys. Rev. B, **57**, R9427 (1998)

[135] D M Ryan, *Electronic States and Optical Properties of Quantum Well Heterostructures with Strain and Electric Field Effects* (PhD Thesis), Durham University (1997)

[136] A C G Wood, *Strain Effects in Semiconductor Quantum Wells* (PhD Thesis), Durham University (1990)

[137] W J Fan, M F Li, T C Chong and J B Xia, J. Appl. Phys., **79** 188 (1996)

[138] W J Fan, M F Li, T C Chong and J B Xia, Solid State Commun., **97** 381 (1996)

[139] K Kassali and N Bouarissa, Solid State Electronics, **44** 501 (2000)

[140] T Lei, T D Moustakas, R J Graham, Y He and S J Berkowitz, J. Appl. Phys., **71** 4933 (1992)

[141] C R Eddy, T D Moustakas and J Scanlon, J. Appl. Phys., **73** 448 (1993)

[142] M J Paisley, Z Sitar, J B Posthill and R F Davis, J. Vac. Sci. Technol. A, **7** 701 (1989)

[143] A Rubio, J L Corkill, M L Cohen, E L Shirley, and S G Louie, Phys. Rev. B., **48** 11810 (1993)

[144] S N Mohammad and H Morkoc, Prog. Quant. Elect.. **20** 361 (1996)

[145] C Stampfl and C G Van der Walle, Phys. Rev. B, **57** R15052 (1998)

[146] A Fissel, B Schröter, U Kaiser and W Richter, **77** 2418 (2000)

[147] M Ruff, H Hitlehner and R Helbig, IEEE Trans. Electron Devices, **41** 1040 (1994)

[148] Z Z Bandić, T C McGill and Z Ikonić, Phys. Rev. B, **56** 3564 (1997)

[149] C-Y Yeh, Z W Lu, S Froyen and A Zunger, Phys. Rev. B, **46** 10087 (1992)

[150] Nobel prize for Chemistry 1998 : W Kohn and John A Pople. Lecture : W Kohn, Rev. Mod. Phys., **71** 1253 (1999)

[151] G Kresse and J Furthmüller, Phys. Rev. B, **54** 11169 (1996)

[152] J R Chelikowsky, J. Phys. D: Appl. Phys., **33** R33 (2000)

[153] R O Jones and O Gunnarsson, Rev. Mod. Phys., **61** 689 (1989)

[154] A K Rajagopal, Adv. Chem. Phys., **41** 59 (1980)

[155] R G Parr, Annu. Rev. Phys. Chem., **34** 631 (1983)

[156] J Callaway and N H March, Solid State Phys., **38** 135 (1984)

[157] M C Payne, M P Teter, D C Allan, T A Arias and J D Joannopoulos, Rev. Mod. Phys., **64** 1045 (1992)

[158] J Ihm, A Zunger and M L Cohen, J Phys C, **12** 4409 (1979)

[159] P Denteneer and W van Haeringen, J Phys C, **18** 4127 (1985)

[160] M J Gillan, J Phys.: Condens. Matter, **1** 689 (1989)

[161] M L Cohen, Int. J. Quantum Chem., **29** 843 (1986)

[162] M D Segall, P J D Lindan, M J Probert, C J Pickard, P J Hasnip, S J Clark and M C Payne, J. Phys. : Condens. Matter, **14** 2717 (2002)

[163] M Fuchs, J L F Da Silva, C Stampfl, J Neugebauer and M Scheffler, Phys. Rev. B, **65** 245212 (2002)

[164] C Stampfl and C G Van de Walle, Phys. Rev. B, **59** 5521 (1999)

[165] L Kleinman and D M Bylander, Phys. Rev. Lett., **48** 1425 (1982)

[166] P Hohenberg and M L Cohen, Int. Phys. Rev., **136** 864 (1964)

[167] W Kohn and L J Sham, Phys. Rev., **140** 1133 (1965)

[168] D M Ceperley, Phys. Rev. B, **18** 3126 (1987)

[169] D M Ceperley and B J Alder, Phys. Rev. Lett.,**140** 1133 (1965)

[170] J P Perdew and A Zunger, Phys. Rev. B, **23** 5048 (1981)

[171] J P Perdew, Phys. Rev. B,**33** 8822 (1986)

[172] J P Perdew and Y Wang, Phys. Rev. B, **33** 8800 (1986)

[173] J P Perdew and Y Wang, Phys. Rev. B, **45** 13244 (1991)

[174] J P Perdew, K Burke and M Ernzerhof, Phys. Rev. Lett., **77** 3865 (1996)

[175] B Hammer, L B Hansen and J K Norsekov, Phys. Rev. B, **59** 7413 (1999)

[176] S Clark, *Complex Structures in tetrahedrally Bonded Semiconductors* (PhD Thesis), University of Edinburgh (1994)

[177] S Pugh, *First-principles simulation of molecular adsorption at oxide surfaces* (PhD Thesis), University of Keele (1997)

[178] R Car and M Parrinello, Phys. Rev. Lett., **55** 2471 (1985)

[179] F D Murnaghan, Am. J. Math., **49** 235 (1937)

[180] F D Murnaghan, Proc. Nat. Acad. Sci., **30** 244 (1944)

[181] D L Anderson, Theory of the Earth, Blackwell Scientific Publications, Boston (1989)

[182] D Vanderbilt, Phys. Rev. B **41** 7892 (1990)

[183] G Kresse and J Hafner, J.Phys. Condens. Matt. **6** 8245 (1994)

[184] H Schulz and K H Thiemann, Solid State Commun., **23**, 815 (1997)

[185] R Miotto, G P Srivastava and A C Ferraz, Physica B., **292**, 97 (2000)

[186] M L Cohen and T K Bergstresser, Phys. Rev., **141**, 789 (1966)

[187] N E Christensen, Phys. Rev. B, **37**, 4528 (1988)

[188] C G V de Walle and R M Martin, Phys. Rev. B, **35**, 8154 (1987)

[189] V Fiorentini, Solid State Commun., **83**, 871 (1992)

[190] M B Nardelli, K Rapcewicz and J Bernholc, J. Vac. Sci. Tech. B **15** 1144-1147 (1997)

[191] M B Nardelli, K Rapcewicz and J Bernholc, Phys. Rev. B **55** R7323 (1997)

[192] H M Al-Allak and S J Clark, Phys. Rev. B, **63**, 033311 (2001)

[193] A Franciosi and C G V de Walle, Surf. Sci. Rep., **25**, 1 (1996)

[194] L Colombo, R Resta and S Baroni, Phys. Rev. B, **44**, 5572 (1991)

[195] N Binggeli, P Ferrara and A Baldereschi, Phys. Rev. B, **63**, 245306 (2001)

[196] A Balderschi, S Baroni and R Resta, Phys. Rev. Lett., **61**, 734 (1988)

[197] M Murayama and T Nakayama, Phys. Rev. B, **49** 4710 (1994)